UQAR

Université du Québec
à Rimouski

CONNECTIVITÉ HYDROLOGIQUE ET GÉOCHIMIQUE DANS LE CONTINUUM AQUIFÈRE-RIVIÈRE EN RÉGION SUBARCTIQUE

Thèse présentée

dans le cadre du programme de doctorat en sciences de l'environnement

en vue de l'obtention du grade de *philosophiæ doctor*

PAR

© ANTOINE BIEHLER

Décembre 2022

Composition du jury :

André Pellerin, président du jury, Université du Québec à Rimouski

Gwénaëlle Chaillou, directrice de recherche, Université du Québec à Rimouski

Paul Baudron, codirecteur de recherche, Institut pour la Recherche et le

Développement

Thomas Buffin-Bélanger, codirecteur de recherche, Université du Québec à Rimouski

Genevieve Bordeleau, examinatrice externe, Institut National de la Recherche

Scientifique

Vincent Cloutier, examinateur interne, Université du Québec en Abitibi-

Témiscamingue

Dépôt initial le 11 juillet 2022   Dépôt final le 09 décembre 2022

UNIVERSITÉ DU QUÉBEC À RIMOUSKI
Service de la bibliothèque

Avertissement

À tous les curieux des Sciences qui, la tête dans les étoiles, s'intéressent à ce qui se trouve sous leur pieds…

« Je suis de ceux qui pensent que la Science a une grande beauté. Un savant dans son laboratoire n'est pas seulement un technicien : c'est aussi un enfant placé en face des phénomènes naturels qui l'impressionnent comme un conte de fées. Nous ne devons pas laisser croire que tout progrès scientifique se réduit à des mécanismes, des machines, des engrenages, qui, d'ailleurs, ont aussi leur beauté propre. […] Si je vois autours de moi quelque chose de vital, c'est précisément cet esprit d'aventure qui me paraît indéracinable et s'apparente à la curiosité… »

Marie Curie, congrès sur l'Avenir de la Culture, Madrid, 1933

REMERCIEMENTS

place de citer ici et avec qui j'ai tant partagé, tant rit, tant discuté : Merci ! Enfin à ceux qui outre Atlantique m'ont tant supporté : ma famille et mes amis en France : Merci !

Je me répète, mais c'est important : « Tant de personnes devraient avoir leur nom cité ici ». Chacune de ces personnes formidables ont, à leur manière délicieusement personnelle, constitué les piliers qui m'ont permis de construire et d'achever ce travail. Merci pour ces années !

Et maintenant à vous lecteur : merci de me lire. C'est peut-être inusuel, mais permettez-moi de vous demander une faveur : prenez votre café, thé ou toute autre boisson à votre convenance et trinquez à toutes ces personnes qui m'ont aidé, à ces années inoubliables passées à leur côté, et à toutes les années qui suivront en leur compagnie. Ils le méritent.

Merci !

AVANT-PROPOS

Cette thèse portant sur la connectivité hydrologique et géochimique dans le continuum aquifère-rivière en région subarctique a été réalisée sous la direction de la professeure Gwénaëlle Chaillou et sous la co-direction des professeurs Thomas Buffin-Bélanger et Paul Baudron. L'auteur de la thèse est le contributeur principal. Le détail des contributions individuelles est présenté sur les pages titre de chacun des chapitres.

Cette thèse de doctorat est composée d'une introduction, de trois chapitres rédigés sous forme d'articles scientifiques et d'une conclusion générale. Le premier chapitre de cette thèse a été publié dans la revue à comité de lecture *Journal of Hydrology*. Le second chapitre a été soumis dans la revue scientifique avec comité de lecture *Biogeochemestry* et le troisième chapitre sera soumis prochainement. La section bibliographie à la fin de cette thèse regroupe les références insérées dans chaque chapitre. Les deux articles scientifiques présentés en annexes à ce manuscrit inclus l'auteur de la thèse en tant que co-auteur.

RÉSUMÉ

L'évolution climatique actuelle et l'usage intensif des ressources en eau dans notre société placent la protection des ressources d'eau douce, et donc la compréhension des processus contrôlant sa qualité, au cœur des problématiques de recherche actuelles. Parmi ces processus, les flux de matières entre les rivières et les eaux provenant des bassins versants, dont les processus de subsurface, contrôlent l'état chimique des eaux de rivière et leur contribution comme source de CO_2 à l'atmosphère. Plusieurs techniques sont disponibles pour comprendre et quantifier ces flux. Dans ce cadre, l'utilisation du radon en tant que traceur géochimique permet de spécifiquement cibler les eaux souterraines dans leur mélange avec les eaux de surface.

Cette thèse cherche à approfondir les connaissances portant sur cette connectivité en qualifiant et en quantifiant les flux d'eaux souterraines et de surface basé sur une combinaison d'approches géochimiques et hydrogéologiques. La rivière Matane (Québec, Canada) a été choisie dans ce cadre comme modèle d'étude. À travers le suivi pluriannuel à haute résolution spatiale et temporelle des niveaux piézométriques dans un méandre de la rivière, couplé à des campagnes d'échantillonnage d'eau de surface et d'eaux souterraines, cette recherche vise d'une part à estimer l'influence de la rivière sur les eaux de l'aquifère alluvial, et d'autre part à quantifier les flux d'eau souterraine et de carbone inorganique dissous à la rivière. Ce travail est accompagné d'une réflexion sur l'optimisation de l'usage des bases de données acquises.

Dans le chapitre 1, les variations géochimiques des eaux souterraines et des eaux de surfaces (radon, température, pH, conductivité électrique, et isotopes stables de l'eau) ont été analysées au cours du temps en parallèle avec les variations de température de l'air, du débit dans la rivière, et des niveaux piézométriques. Une analyse multivariée par redondance a permis d'établir que le débit de la rivière contrôle la géochimie dans les eaux souterraines jusqu'à une distance de plus de 200 m du rivage. Un mélange d'eau souterraine avec les eaux de surface se produit ainsi dans l'aquifère alluvial à plus large échelle que ne le laissait penser la littérature scientifique. Le calcul des temps de résidence de l'eau souterraine dans la plaine alluviale, à partir d'un modèle basé sur l'activité de radon, montre des apports d'eau souterraine transversaux et verticaux à l'aquifère alluvial qui répondent aux variations de débit dans la rivière.

Le chapitre 2 s'intéresse à quantifier les décharges d'eau souterraine à la rivière. Ces apports, appliqués aux paramètres du système des carbonates, a permis d'estimer les flux de carbone inorganique dissous à la rivière et de CO_2 à l'atmosphère aux échelles infra- et pluri-kilométriques. Dans un contexte d'étiage, des transects longitudinaux à hautes et à basses

résolutions spatiales d'activités en radon, de carbone inorganique dissous, d'alcalinité totale et de pression partielle en CO_2 ont été réalisés. Un modèle utilisant l'activité en radon révèle une hétérogénéité spatiale des décharges d'eau souterraine. Ces apports s'accompagnent d'un flux de carbone inorganique dissous correspondant à moins de 13 % de celui soutenu par la rivière. Ces apports externes induisent pourtant un important flux de CO_2 vers l'atmosphère traduisant un dégazage extrêmement rapide du CO_2 dès l'arrivée de l'eau souterraine en surface.

Le troisième chapitre porte sur l'optimisation de l'usage de bases de données hydrogéologiques via leur partage public et normalisé. Au travers d'exemples tirés de la base de données piézométriques pluriannuelle acquise sur la rivière Matane entre 2011 et 2019, l'étude montre qu'une ré-exploitation d'une base de données existante peut permettre de peaufiner, d'étendre ou de limiter des conclusions obtenues au cours d'études précédentes d'une part, mais aussi de réinvestir les données au sein d'études connexes portant sur des problématiques différentes. Le partage de bases de données selon les principes FAIR est une approche efficace pour préserver et donner accès aux données de recherche à une communauté scientifique large. Cette disponibilité se traduit par des opportunités de mise en valeur des données scientifiques préexistantes dans une optique de maximisation des connaissances et des avancées scientifiques.

L'originalité de ce travail réside sur le développement et l'utilisation de bases de données hydrogéologiques et géochimiques, rendues ouvertes et accessibles. En faisant le portrait de la connectivité entre les eaux souterraines et les eaux de surface à travers l'exemple de la rivière Matane, cette thèse souligne l'importance des échanges hydrogéochimiques au sein du continuum aquifère-rivière et leur rôle dans le cycle du carbone.

Mots clés : Eau souterraine ; Rivière ; Continuum hydrologique et géochimique ; Radon ; Traceurs géochimiques ; CO_2 ; Publications de bases de données ; Région subarctique

ABSTRACT

Due to climate change and of the intensive uses of water in our society, the protection of freshwater and the processes related to its quality are one of the key research topics in science. These processes include water fluxes between river and groundwater flowing from the catchment. Subsurface exchanges drive the chemical condition in riverine surface water and their contribution as a source of CO_2 to the atmosphere. Several methods are available to understand and quantify these fluxes. The use of radon as a geochemical tracer allow to specifically target groundwater in the mixing process with surface water.

The objective of this thesis is to intensify the knowledge of this connectivity by describing and quantifying groundwater and river water fluxes using a mix of geochemical and hydrogeological approaches. To investigate this problematic, the Matane River (Quebec, Canada) was used as a model. A pluriannual survey with high temporal and spatial resolution of piezometric levels was conducted in an alluvial floodplain of the river. This survey, combined with sampling campaigns of surface water and groundwater, aim to evaluate the influence of the river on alluvial groundwater, and to quantify groundwater and dissolved inorganic carbon fluxes to the river. The study goes along a discussion about the optimal use of the acquired databases.

In the first chapter, geochemical variations of groundwater and surface water (radon, temperatures, pH, electrical conductivity and stable isotopes of water) were analyzed over time and compare with air temperature variations, river discharges, and piezometric levels in the alluvial aquifer. A redundancy multivariate analysis established that river discharges impact groundwater geochemistry up to 200 m from the riverbank. Groundwater and surface water are mixed in the alluvial aquifer on a longer distance than previously estimated. The calculation of groundwater residence time in the floodplain from a model based on radon activity shows transversal and vertical groundwater inputs in the alluvial aquifer. These inputs are controlled by the river discharge variations.

The second chapter deals with the quantification of groundwater discharges in the river. These calculated fluxes applied to carbonate chemistry allow the evaluation of dissolved inorganic carbon (DIC) fluxes to the river and CO_2 fluxes to the atmosphere at infra- and pluri-kilometric scales. High and low-resolution sections of radon activity, dissolved inorganic carbon concentration, total alkalinity, and CO_2 partial pressure had been undertaken in the river at its baseflow. A model based on radon showed spatial heterogeneity of groundwater discharges in the river. These inputs come with a DIC flux that only represents a maximal contribution of 13 % of the river flux. However, these external inputs

cause a considerable CO_2 flux to the atmosphere. This flux evidence nearly immediate outgassing of CO_2 as soon as groundwater discharge in the river.

The third chapter focuses on the optimal use of hydrogeological databases through their public and normalized publication. Examples from the pluriannual hydrogeological database collected on the Matane River alluvial aquifer between 2011 and 2019 were used to demonstrate that a database can be reused with other objectives in order to refine, extend or limit previous conclusions of different studies. These databases can also be included in related studies with different purposes. Sharing databases according to the FAIR principles is effective in preserving and providing access to research data to a broad scientific community. This availability results in opportunities to add value to pre-existing scientific data in order to maximize scientific knowledge and progress.

The study's originality is on the development and the use of hydrogeological and geochemical databases. By describing the connectivity between groundwater and surface water through the Matane River example, this thesis highlights the importance of hydrogeochemical exchanges in the aquifer-river continuum and their role in the carbon cycle.

Keywords: Groundwater ; River ; Hydrological and geochemical continuum ; Radon ; Geochemical tracers ; CO_2 ; Databases publications ; Subarctic region

TABLE DES MATIÈRES

LISTE DES TABLEAUX

LISTE DES FIGURES

LISTE DES ABRÉVIATIONS, DES SIGLES ET DES ACRONYMES

DIC   Carbone inorganique dissous *(de l'anglais Dissolved Inorganic Carbon)*

EC   Conductivité électrique *(de l'anglais Electrical Conductivity)*

FAIR   Trouvable *(Findable)*, disponibles *(Accessible)*, interopérables *(Interoperable)*, et réutilisables *(Reusable)*

GS   Station de jaugeage *(de l'anglais Gauging Station)*

GW   Eau souterraine *(de l'anglais Groundwater)*

PCO2   Pression partielle en CO_2

Q   Débit

RDA   Analyse de redondance

TA   Alcalinité totale *(de l'anglais Total Alkalinity)*

xxx

INTRODUCTION GÉNÉRALE

Au cours des dernières décennies, les modifications globales du climat et l'empreinte importante qu'impriment nos sociétés sur l'environnement nous ont poussés à mieux comprendre la manière dont nous interagissons avec ce qui nous entoure. La notion de développement durable, apparue dès 1987 dans le rapport Brundtland, a permis d'affirmer cette interaction de l'être humain avec son environnement dans la durée : les besoins nécessaires à nos sociétés se doivent d'être protégés à la fois pour la génération actuelle et pour les générations futures (World Commission on Environment and Development, 1987). Dans ce contexte, les eaux douces potables (rivières, lacs, et eaux souterraines) représentent un enjeu primordial. Mis en avant lors de la *Déclaration du millénaire de l'Organisation des Nations Unies* en 2000, puis dans le sixième objectif du *Programme de développement durable à l'horizon 2030*, l'accès universel à des eaux douces de qualité doit être assuré, protégé, et restauré (Organisation des Nations Unies, 2019, 2008). Une compréhension des processus physiques et chimiques affectant ces eaux est donc nécessaire. Cette thèse cherche ainsi à approfondir les connaissances scientifiques portant sur la connectivité physique et chimique entre les eaux souterraines et les rivières.

1. LA PROTECTION DES EAUX DE SURFACE PAR LA PRÉSERVATION DES ZONES RIPARIENNES

De manière à réduire les risques sur les cours d'eau, des politiques prenant en compte une gestion intégrée des ressources en eau ont été proposées de manière à mieux contrôler les types de pesticide utilisés en milieu agricole, la quantité de produits ajoutés aux sols, ainsi que leurs méthodes et leurs périodes d'application (Baker et Mickelson, 1994). Dans cette

optique d'optimisation de la protection des eaux de surface, les zones interfaces entre les milieux aquatiques de surface et le milieu terrestre, aussi appelé zones ripariennes (Fig. 1), ont été mis de l'avant dans les pratiques de gestion. Ces zones sont hydrologiquement et géochimiquement plus actives que le reste du bassin versant et ont ainsi un impact extrêmement important sur la chimie des rivières (Broder et Biester, 2017; Tiwari et al., 2017). Ces zones assurent naturellement des processus physico-chimiques permettant de tamponner les flux de matières ponctuels ou diffus aux rivières (Vidon et al., 2010). Elles permettent de transformer ou de piéger l'azote, le phosphore, les herbicides, et les sédiments provenant des terres avant qu'ils ne puissent atteindre les cours d'eau (Lovell et Sullivan, 2006; Vidon et al., 2010). Elles piègent les polluants de surface et de subsurface, et filtrent les particules issues de l'érosion du bassin versant (Uusi-Kämppä et Jauhiainen, 2010) grâce à des processus de dépôt, d'absorption, et de dénitrification (Li et al., 2009; Peterjohn et Correll, 1984). En surface, la végétation arbustive et boisée des zones ripariennes permet d'intercepter les polluants transportés par le vent qui pourraient potentiellement se déposer dans les eaux de surface (Mander et al., 2005). Les zones ripariennes ont donc un rôle direct sur les concentrations en nutriments, en cations, en métaux, et en éléments traces dans les cours d'eau (Broder et Biester, 2017; Zaharescu et al., 2017). Par ailleurs, en plus de préserver la qualité des eaux de surface, les zones ripariennes présentent de nombreuses autres fonctions dans le domaine physique (e.g. protection des berges de l'érosion ; stabilisation du lit des cours d'eau ; réduction des pics de crue ; optimisation de la recharge des aquifères adjacents ; régulation de la température de l'eau), écologique (e.g. maintien de la biodiversité à travers son rôle d'écotone), et sociétal (e.g. création de lieux de récréation ; amélioration de la qualité de vie des habitants) (Fischer et al., 2000; Golkowska et al., 2016; Kuglerová et al., 2014; Lovell et Sullivan, 2006; Mander et al., 2005, 1997; MDDELCC, 2015; Xue et al., 2014). De fait, la préservation et la restauration des zones ripariennes sont devenues des éléments clés dans les schémas de gestion des bassins versants (Gagnon et Gangbazo, 2007; Vidon et al., 2010).
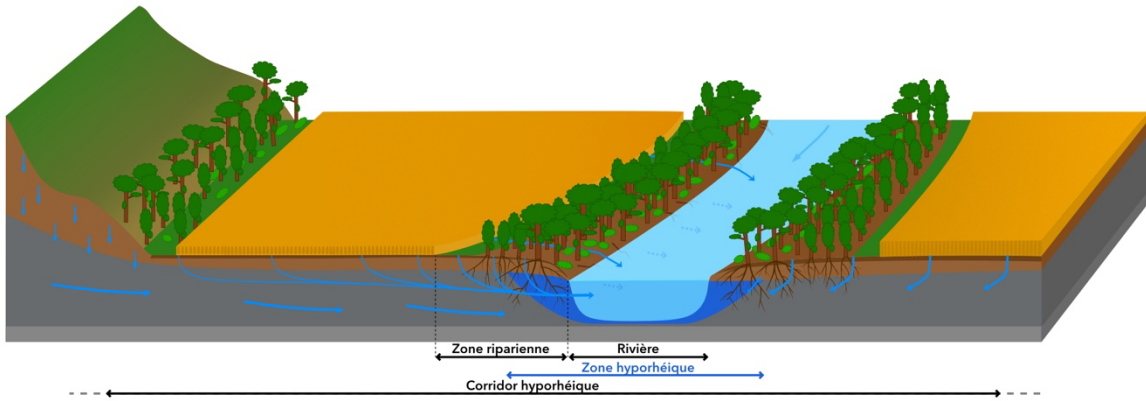
Figure 1. Délimitation schématique de l'étendue des zones ripariennes, de la zone hyporhéique, et du corridor hyporhéique par rapport à une rivière.

L'efficacité de ces interfaces est cependant largement dépendante de leurs dimensions, du type de végétation qui les compose, de leur topographie et de leur positionnement au sein des bassins versants (Fischer et al., 2000; Syversen, 2005). Trois études indépendantes portant sur la capacité de zones ripariennes de 35 à 38 m de largeur ont montré des capacités de dénitrification différentes lors du transit des eaux souterraines. Les concentrations en nitrate diminuaient de 92 à 99% pour une zone riparienne forestière au Royaume-Uni (Haycock et Pinay, 1993), tandis que des efficacités de dénitrification de l'ordre de 83% et de 56% ont été observées lors d'études sur des zones ripariennes herbacées dans le Connecticut (Clausen et al., 2000) et dans le Maryland (Correll et al., 1997) respectivement. Une réglementation fondée sur une taille fixe de protection des zones riparienne n'est donc pas adaptée d'un point de vue géochimique et aurait des répercussions sur les objectifs écologiques et économiques attribués à ces zones (Kuglerová et al., 2014). Une approche alternative basée sur l'hydrogéomorphologie des cours d'eau et intégrant la mobilité des rivières, les plaines d'inondations, et les zones ripariennes dans la gestion des rivières a été proposée par Biron et al., (2014). Cette approche par « espace de liberté » permet d'établir trois niveaux de protection de plus en plus large autours des rivières : des espaces de liberté minimum, fonctionnels, et rares. L'étendue de ces espaces de libertés varient le long des rivières. Elle peut être très restreinte autours des chenaux ou inclure une zone très large sur des centaines de mètres autour de la rivière.

2. PLACE DU CARBONE DANS LA CONNECTIVITÉ AQUIFÈRE - RIVIÈRE

Les eaux souterraines de la zone riparienne, concentrées en carbones dissous (inorganiques et organiques), alimentent les rivières. La connectivité entre les aquifères de surface et les rivières est un élément important du cycle du carbone au sein du continuum continent-océan. Pendant longtemps, la place des rivières dans ce cycle du carbone a été réduite à un simple vecteur passif où transite directement l'intégralité du carbone continental vers les océans. Cette vision des rivières impliquait que les 0,9 Pg·C·an^{-1} arrivant à l'océan correspondait à un export global de 0,9 Pg·C·an^{-1} depuis le milieu continental (Kempe, 1991; Meybeck, 1982). Cette hypothèse néglige cependant les transferts verticaux de carbone à la faveur d'un simple transfert horizontal des continents vers les océans (Cole et al., 2007). Ces transferts verticaux incluent le stockage de carbone vers les sédiments, son utilisation par la biosphère aquatique (croissance végétale) et son dégazage vers l'atmosphère (sous forme de CO_2). Ce modèle plus complet implique un apport continental minimal de carbone aux eaux de surface de 1,9 Pg·C·an^{-1}. D'autres études ont par la suite repris ce modèle exposé par Cole et al. (2007) en réévaluant le bilan de carbone au niveau des rivières. Raymond et al. (2013) estimait un dégazage global de 1,80 ± 0,25 Pg·C·an^{-1} pour les seuls ruisseaux et rivières et de 2,10 Pg·C·an^{-1} pour l'ensemble des eaux de surface (Raymond et al., 2013). Plus récemment, Abril et Borges (2019) ont repris le modèle de transferts verticaux et horizontaux de carbone développé par Cole et al. (2007) en s'interrogeant sur le rôle des zones humides dans ce système. Dans leur étude, Abril et Borges (2019) avancent que le système actif développé par Cole et al. (2007) devrait être un système à double entrée. Ce dernier est alimenté comme dans le modèle de Cole et al. (2007) par les zones continentales drainées, mais aussi par les zones humides. Une bonne compréhension des flux de carbone continental vers les eaux de surface doit être acquise pour obtenir un bilan réaliste du dégazage de carbone des eaux de surface vers l'atmosphère.
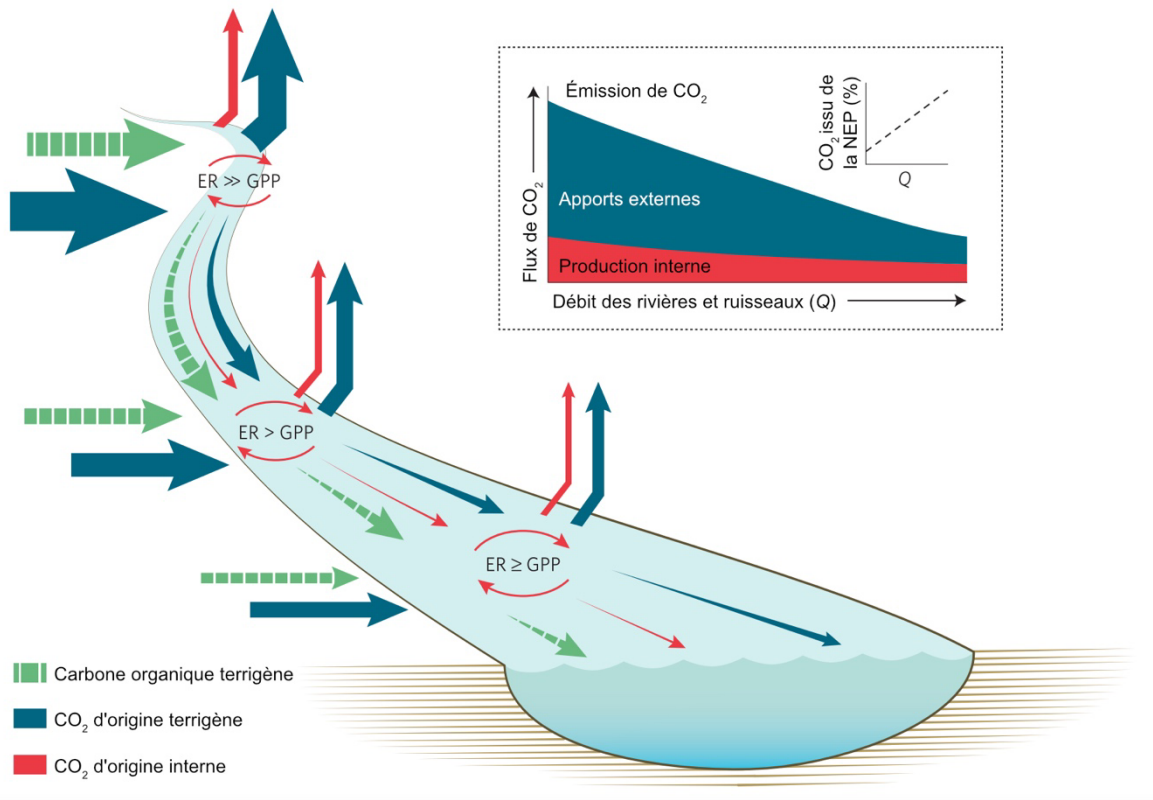
Figure 2. Sources et ampleur relatives des émissions théoriques de CO_2 le long d'une rivière (modifié d'après Hotchkiss et al. 2015). ER : Respiration Hétérotrophe ; GPP : Production primaire brute ; NEP : Production nette de l'écosystème.

Seuls, les processus internes d'hétérotrophie et de photo-oxydation de la matière organique ne permettent pas d'expliquer les flux de CO_2 des rivières vers l'atmosphère (Hotchkiss et al., 2015). Une part importante du CO_2 participant au dégazage par les rivières est issu d'apports externes aux rivières via les décharges d'eaux souterraines, à savoir le carbone inorganique dissous (DIC) issu de l'altération chimique des roches du bassin versant et des processus de dégradation microbienne dans les zones ripariennes et le reste des bassins versants (Macklin et al., 2014; Polsenaere et Abril, 2012; Regnier et al., 2013). Cette contribution des eaux souterraines évolue le long des cours d'eau (Hotchkiss et al., 2015). Elle est très importante en amont lorsque la rivière est principalement alimentée par les eaux souterraines, et diminue vers l'aval jusqu'à *in fine* devenir comparable avec la contribution des apports internes de carbone (Fig. 2). Du fait de l'apport de nutriments et de la

modification des paramètres physico-chimiques de l'eau résultant du mélange eau de surface - eau souterraine, les décharges d'eau souterraine dans les rivières créent des *hot-spots* biogéochimiques au sein des rivières (McClain et al., 2003; Vidon et al., 2010). La position et l'intensité de ces décharges d'eau souterraine sont dépendantes du type de connexion entre l'aquifère alluvial et la rivière. Une quantification de ces flux de carbone vers la rivière et vers l'atmosphère nécessite d'estimer de manière précise les apports d'eaux souterraines aux rivières.

3. LA CONNECTIVITÉ EAUX SOUTERRAINES – EAUX DE SURFACE

Si le niveau piézométrique est supérieur au niveau de l'eau dans la rivière, cette dernière est alimentée par des décharges d'eau souterraine (Fig. 3a.). À l'inverse si le niveau de l'eau dans la rivière est supérieur à celui de l'aquifère, c'est l'eau de surface qui va s'infiltrer dans le chenal et alimenter l'aquifère (Fig.3b.). La zone de mélange à l'interface entre ces deux environnements, appelée zone hyporhéique (Fig. 1), est généralement délimitée par des considérations écologiques et/ou géochimiques. L'influence de la rivière sur le niveau piézométrique ne se limite cependant pas à un simple échange de matière le long du chenal. Lors des crues, l'augmentation rapide du niveau des rivières induit une pression sur les berges qui se propage dans l'aquifère sous forme d'onde de crue (Fig. 3c. et d.). L'augmentation du niveau piézométrique est uniquement liée à l'entrechoquement des molécules d'eau entre elles lors du passage de l'onde de pression (Sophocleous, 1991) ainsi qu'à l'accumulation d'eau souterraine en provenance du bassin versant (Jung et al., 2004). Ces fluctuations du niveau piézométrique sans transport de matière peuvent être observées jusqu'à plusieurs centaines de mètres de la rivière (Cloutier et al., 2014; Lewandowski et al., 2009; Sophocleous, 1991). L'absence de mélange d'eau est supportée par la vitesse de propagation des ondes de crue qui peut être supérieure de deux à trois ordres de magnitude de plus que la vitesse de circulation des eaux souterraines dans l'aquifère (Buffin-Bélanger et al., 2015c; Jung et al., 2004; Vidon, 2012). Cette influence mutuelle à large échelle entre

la rivière et l'aquifère nécessite d'élargir le concept de zone hyporhéique vers celui, spatialement plus étendu, de corridor hyporhéique (Stanford et Ward, 1993). La zone interface n'est alors plus limitée à quelques mètres de part et d'autre du chenal. Elle forme un continuum de subsurface qui inclut les zones ripariennes (Fig. 1), les paléochenaux, et les aquifères alluviaux (Boulton et al., 1998).

L'étude de cette connectivité entre les eaux souterraine et les eaux de surface peut être réalisée par des suivis des niveaux piézométriques dans les aquifères alluviaux et des débits enregistrés dans les rivières (Marchand et al., 2022). Ces données peuvent également servir à quantifier les apports souterrains en utilisant les travaux de Darcy sur les écoulements en milieu poreux (e.g. Hunt et al., 1996), ou en calculant des différentiels de débits en différents points de la rivière (e.g. Hatch et al., 2006 ; Ruehl et al., 2006). D'autres méthodes de suivi des eaux souterraines dans les eaux de surface impliquent l'utilisation de traceurs géochimiques tels que les concentrations en chlorures, en brome, ou en silice (e.g. Constantz et al., 2003 ; Herczeg et Edmunds, 2000 ; Winterdahl et al., 2016) ; l'activité en radium (e.g. Raanan Kiperwas, 2011) ; les rapports isotopiques du strontium (e.g. Rose et Fullagar, 2005) ou des isotopes stables de l'eau (e.g. Cook et al., 2008 ; Gurrieri et Furniss, 2004) ; l'évolution de la température des eaux (e.g. Constantz et al., 2003 ; Hatch et al., 2006) ; l'évolution des éléments majeurs de l'eau (e.g. Gurrieri et Furniss, 2004) ; ou encore l'évolution d'éléments artificiels ajoutés au milieu (e.g. Bencala et al., 1990 ; Clark et al., 1996 ; Cook et al., 2003 ; Ruehl et al., 2006). L'isotope 222 du radon est un autre traceur géochimique naturellement présent dans les eaux souterraines. En tant que gaz radioactif à courte demi-vie ($t_{1/2}$ = 3,8 jours), son activité décroît rapidement lorsque l'eau souterraine arrive en surface et que sa production n'est plus supportée par la désintégration du ^{226}Ra présent dans la matrice aquifère (Cook et al., 2006). Communément utilisé pour localiser et quantifier les décharges d'eau souterraine en milieu côtier (Burnett et al., 2010 ; Chaillou *et al.*, 2018 - Annexe I ; Dulaiova *et al.*, 2005), le radon est également utilisé en milieu continental en tant qu'indicateur des échanges entre l'aquifère et les rivières (Cook, 2015; Hoehn et Von Gunten, 1989). Sa présence naturelle dans l'aquifère (Cecil et Green, 2000), la possibilité d'analyse *in-situ* de son activité (Kluge et al., 2007), et le fort contraste

d'activité entre les eaux souterraines et les eaux de surface, font de l'utilisation du radon un traceur extrêmement pertinent pour cibler les eaux souterraines dans un contexte d'étude de la connectivité entre les eaux souterraines et les rivières (Cook et al., 2006).
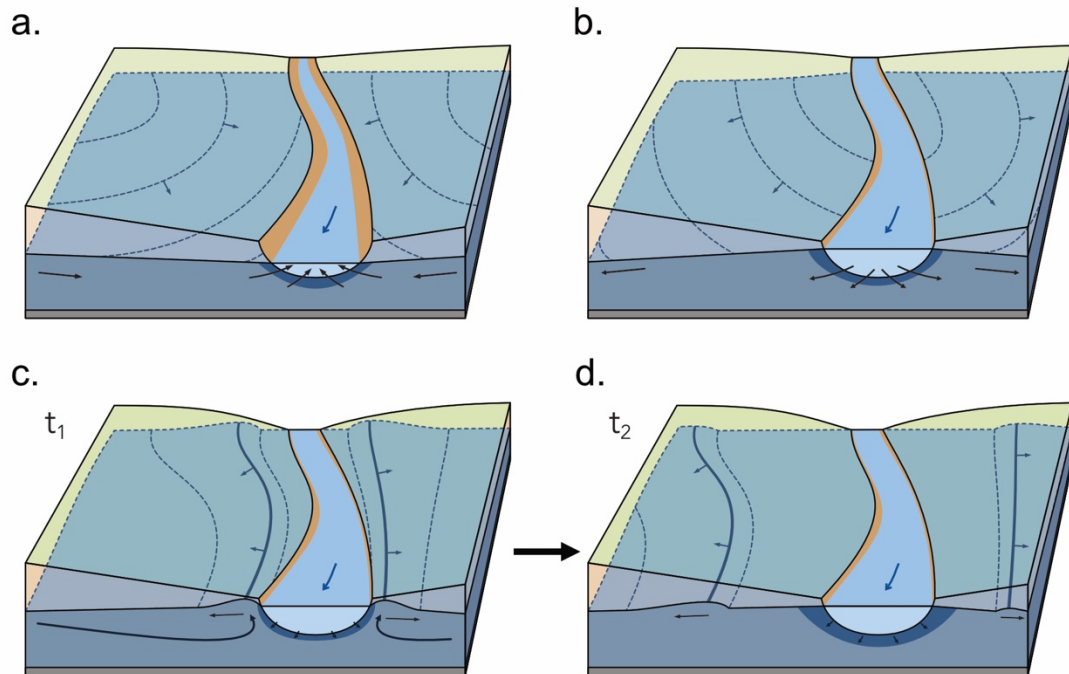
Figure 3. Situation théorique où (a.) la rivière est alimentée par l'aquifère, et où (b.) la rivière alimente l'aquifère. (c. et d.) Propagation théorique d'une onde de crue dans l'aquifère alluvial adjacent à la rivière à la suite d'une augmentation brutale du débit dans la rivière . La vitesse de propagation de l'onde est très supérieure à celle de l'infiltration des eaux de surface vers l'aquifère alluvial (bleu foncé).

4.   CONTEXTE DE L'ÉTUDE

Au Québec, les eaux de surface couvrent 22 % du territoire, soit plus de 365 000 km^2 (lacs, rivières, et fleuve – (MDDELCC, 2018). Soixante-quinze pourcents de la population utilise les eaux de surface comme source d'approvisionnement en eaux potables. Le reste de la population utilise les eaux souterraines au travers de puits collectifs ou individuels. La protection de la ressource en eau de surface y fait ainsi l'objet d'une protection particulière notamment avec l'obligation de conservation à l'état végétalisé de bandes de terrain dans la

zone riparienne directement autour des rivières. Ces zones, connues sous le nom de bandes riveraines, sont légalement protégées par l'article 3.2. de la Loi sur la qualité de l'environnement (MELCC, 2018):

> « *Dans la rive, sont en principe interdits toutes les constructions,*
> *tous les ouvrages et tous les travaux.* »

La rive y est définie comme une bande de terre commençant à partir de la ligne de hautes eaux des rivières et qui s'étend sur une largeur minimale de 10 à 15 m suivant la morphologie du plan d'eau. Les bandes riveraines sont cependant réduites à une largeur de 3 m dans le cas d'activité agricole (MELCC, 2018). En plus de l'objectif de maintien et d'amélioration de la qualité des cours d'eau, la mise en place de bandes riveraines par le gouvernement du Québec a également pour but de protéger la biodiversité dans et autour des rivières. Dans cette optique, l'article 28.2 de la Loi sur les forêts étend la largeur des bandes riveraine à 60 m autour des cours d'eau définis comme étant des rivières à saumon (Ministère des Forêts de la Faune et des Parcs, 1986).

En complément de ces mesures, dans sa *Stratégie québécoise de l'eau 2018-2030*, la protection de la ressource en eau passe également par l'acquisition de nouvelles connaissances sur les eaux souterraines. Dans cette optique, les Programmes d'Acquisition des Connaissances sur les Eaux Souterraines (PACES) ont été déployés pour étudier et cartographier les eaux souterraines dans le Québec municipalisé (MELCC, 2020). Dans ce cadre, des études sur la connectivité aquifère-rivière ont été réalisées au niveau de rivières telles que la Rivière Matane (Fig. 4a.) dans le Nord-Est du Bas-Saint-Laurent (PACES-NEBSL). Une étude de Cloutier *et. al* (2014) a ainsi permis de mettre précisément en évidence la propagation d'ondes de crue dans l'aquifère alluvial de la rivière grâce à une étude à haute résolution de la variation des niveaux piézométriques dans une plaine d'inondation de la rivière Matane. La forte connectivité observée entre l'aquifère et la rivière (ondes de crues dans l'aquifère ; occurrence d'inondation par débordement de nappe ; présence de sédiments alluvionnaires grossiers (Buffin-Bélanger et al., 2015b; Marchand et al., 2014) permettant une conductivité hydraulique importante dans l'aquifère) et la qualité

de l'instrumentation déjà en place nous ont conduits à sélectionner la rivière Matane pour illustrer ce travail de doctorat sur la connectivité hydrogéologique et géochimique dans le continuum aquifère-rivière.

5. LA RIVIÈRE MATANE COMME MODÈLE D'ÉTUDE

La rivière Matane est située dans la région du Bas-Saint-Laurent (Qc, Canada) (Fig. 4a. et b.). Son aquifère alluvial est le plus important du Nord-Est du Bas-Saint-Laurent et alimente en eau les villes de Matane et de Saint-René-de-Matane (Buffin-Bélanger et al., 2015b) respectivement à hauteur de 38 % et 100 % de leur approvisionnement en eau (Rapport PACES-NEBSL). Pour ces deux villes, ces prélèvements représentent une consommation annuelle d'eau souterraine de plus de 3 600 000 m^3 soit un volume correspondant à environ 970 piscines olympiques !

La rivière Matane est un affluent du fleuve Saint-Laurent qui prend sa source dans les monts Chic-Chocs et s'écoule sur une distance de plus de soixante-dix kilomètres dans la péninsule gaspésienne au sein d'un bassin versant principalement forestier (82 % - Atlas de l'eau Québec) de 1 678 km² (Fig. 4b). Sa roche mère est composée d'argile, de mudstones, de siltstones, et de quartzite (Marchand, 2013). Les monts Chic-Chocs font partie des massifs des Appalaches. Ils sont constitués principalement de séries volcaniques, de schistes ardoisiers, et d'arkoses et forment la limite approximative de partage des eaux entre l'estuaire du Saint-Laurent au Nord et la Baie-des-Chaleurs au Sud (Lebuis et David, 1977; Marchand, 2013). Cette zone fut recouverte par l'Inlandsis Laurentidien issu de la glaciation Wisconsinienne jusqu'à sa déglaciation débutée il y a environ 15 000 ans (Dyke, 2004). La vallée de la rivière Matane a alors été occupée par une langue glaciaire inactive qui a permis l'accumulation d'un volume important de cailloutis fluvio-glaciaires à l'amont de la rivière. La déglaciation a par la suite permis l'invasion de la vallée par la mer de Goldthwait et le dépôt de sédiments fins (argiles et silts) dans la partie aval de la vallée (Fig. 4d.). Cette

histoire géologique récente a ainsi conduit à la formation d'un aquifère libre dans la partie amont de la rivière et à un aquifère confiné dans sa partie aval (Buffin-Bélanger et al., 2015b).

Figure 4. (a.) Localisation du site d'étude à l'échelle du Québec avec (b.) le tracé et l'altitude LiDAR de la vallée de la rivière Matane. Le rectangle rouge situe (c.) le méandre instrumenté (depuis 2011) à Saint-René-de-Matane. (d.) La coupe stratigraphique simplifiée de la vallée est issue du rapport final du Programme d'Acquisition des Connaissances sur les Eaux Souterraines (PACES) du Nord Est du Bas-Saint-Laurent (Buffin-Bélanger et al., 2015b). La coupe suit le lit de la rivière depuis l'entrée de la ville de Matane à l'aval (**A**) jusqu'à 25 km plus en amont (**B**).

Aujourd'hui, la rivière Matane s'écoule au sein d'un climat avec des températures de type subpolaire et un niveau de précipitation de type humide à subhumide (Gerardin et McKenney, 2001). La rivière se situe ainsi dans une région avec un contraste climatique saisonnier fort entre l'hiver et l'été[1] avec une température annuelle moyenne de 3,4 °C. De novembre à avril, la température moyenne est de -6.2 °C et les précipitations sont majoritairement neigeuses avec une hauteur précipitée moyenne mensuelle de 46 cm. De mai à octobre, la température moyenne est de 13.2 °C et les précipitations sont sous forme liquide pour une hauteur précipitée moyenne mensuelle de 84 cm. La rivière Matane présente un régime d'écoulement nivo-pluvial avec un débit moyen annuel de 39 $m^3 \cdot s^{-1}$. Son débit maximum est globalement enregistré au début du mois de mai et son débit à plein bord est de 350 $m^3 \cdot s^{-1}$ pour une largeur de chenal d'environ 55 m (Cloutier et al., 2014). La rivière est encaissée dans une vallée d'environ 475 m de large en phase d'accrétion. Elle présente une morphologie de type méandriforme caractérisée par une divagation latérale du chenal principal. Cette situation explique le fait que les plaines d'inondation de la rivière Matane sont entièrement constituées de dépôts sablo-graveleux (Fig. 4d., Touchette *et al.,* 2013).

Le site instrumenté étudié par Cloutier et al. (2014) puis par Buffin-Bélanger et al. (2015) est un méandre situé sur la municipalité de Saint-René-de-Matane, dans le hameau de Village-à-Dancause au point de coordonnées 48°40'4.48''N ; 67°21'10.82''O (Fig. 4c. et d.). Au printemps, pendant la fonte des accumulations neigeuses, cette plaine alluviale graveleuse est partiellement inondée (Fig. 5a. et e.) du fait de la remontée du niveau piézométrique de l'aquifère au-dessus du niveau du sol (Fig. 5a. et c.). En dehors de ces périodes d'inondation, le niveau piézométrique dans l'aquifère de surface reste sous le niveau topographique (Fig. 5b. et d.)

---

[1] La station météorologique la plus proche de la rivière Matane avec les données de température les plus complètes est la station d'Amqui mais cette station n'enregistre pas les précipitations à l'échelle quotidienne. Les données de température sont ainsi issues de la station d'Amqui sur la période 2010-2019 tandis que les données de précipitation présentées ici sont issues de la station de Rimouski sur la période 2010-2017. Les données sont issues des archives climatiques d'Environnement et Changement climatique Canada, 2021.
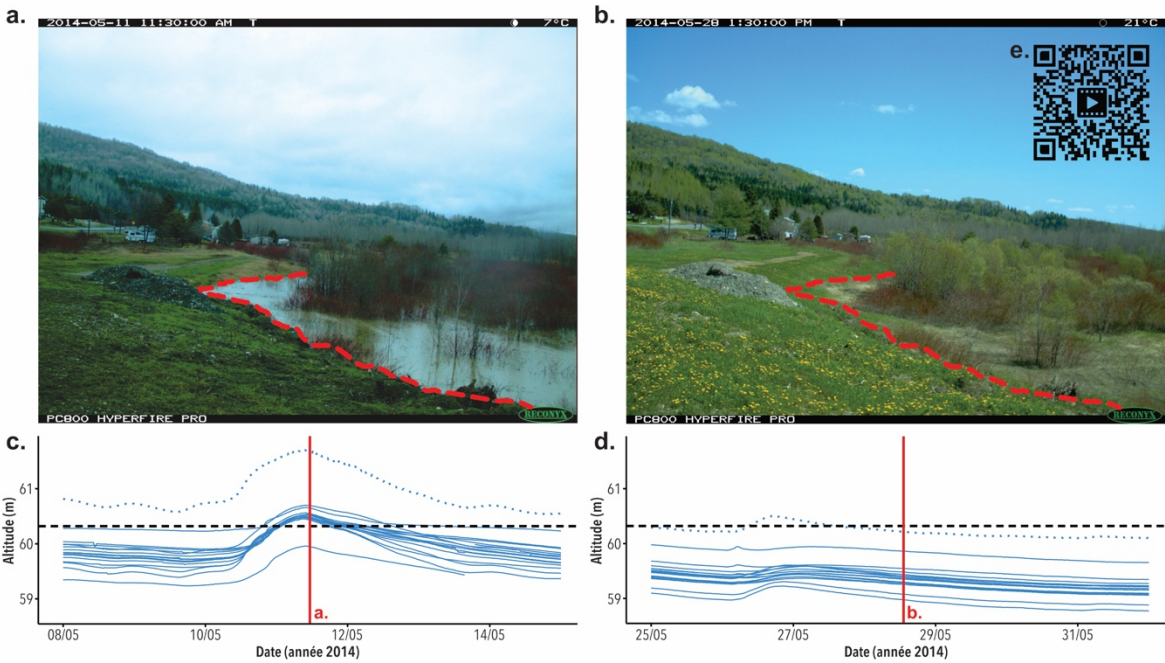
Figure 5. Exemple d'une inondation par remontée de la nappe phréatique au niveau du site instrumenté de Dancause. La première photo (a.) a été prise au maximum de l'inondation le 11/05/2014 alors que la seconde photo (b.) a été prise quelques jours plus tard le 28/05/2014. Sur les photos (a. et b.) la ligne rouge représente l'étendue maximale de la zone submergée lors de l'inondation du 11/05/2014. Les graphiques représentent les variations des niveaux piézométriques dans chaque piézomètre (lignes bleues pleines) entre (c.) les 08 et 15/05/2014 et entre (d.) le 25/05 et le 01/06/2014. Les lignes bleues pointillées représentent le niveau dans la rivière en amont du méandre. Les lignes pointillées noires indiquent l'altitude moyenne des piézomètres sur le site. Il est à noter que l'altitude du site au niveau de la mesure du niveau de la rivière en amont est d'environ 62 m. Les indicateurs rouges sur les graphiques (c. et d.) indiquent le moment où les photos ont été prises. Le QR code à scanner avec un téléphone ou une tablette (e.) renvoie à la vidéo accélérée de l'inondation du méandre entre le 12 avril 2014 et le 1er juin 2014 : https://youtu.be/E-GWsOjMAFY

Le site a été instrumenté avec vingt et un piézomètres (Fig. 6) : 15 en places depuis 2011 issus de l'étude de Cloutier et al. (2014), et 7 ajoutés en juillet 2014. Tous les piézomètres, à l'exception de D771, ont été installés à une profondeur d'environ 3 m. Le piézomètre D771 a lui été installé jusqu'à une profondeur d'environ 6 m. Une station de jaugeage du niveau de la rivière a également été installée en amont du site. La station de jaugeage et l'ensemble des piézomètres sont équipés de sondes permettant la mesure autonome de la température et de la pression (Hobo U20-001) à une fréquence d'une mesure

réalisée toutes les 15 minutes. Comparées à la pression atmosphérique mesurée en surface, ces mesures de pression permettent d'enregistrer les variations de niveaux piézométriques et du niveau de la rivière. Ces mesures sont converties en altitude grâce à une mesure précise de leur position au GPS différentiel (DGPS - Magellan ProMark III differential) de l'altitude de chacun des piézomètres et de leurs sondes. Le système est en place depuis juin 2011 et a été démantelé en juin 2021. La quantité de données générée par cette étude et celles qui l'ont précédée est donc extrêmement importante avec environ 12.3 millions de données spatialisées (niveaux piézométriques et températures de l'eau souterraine).
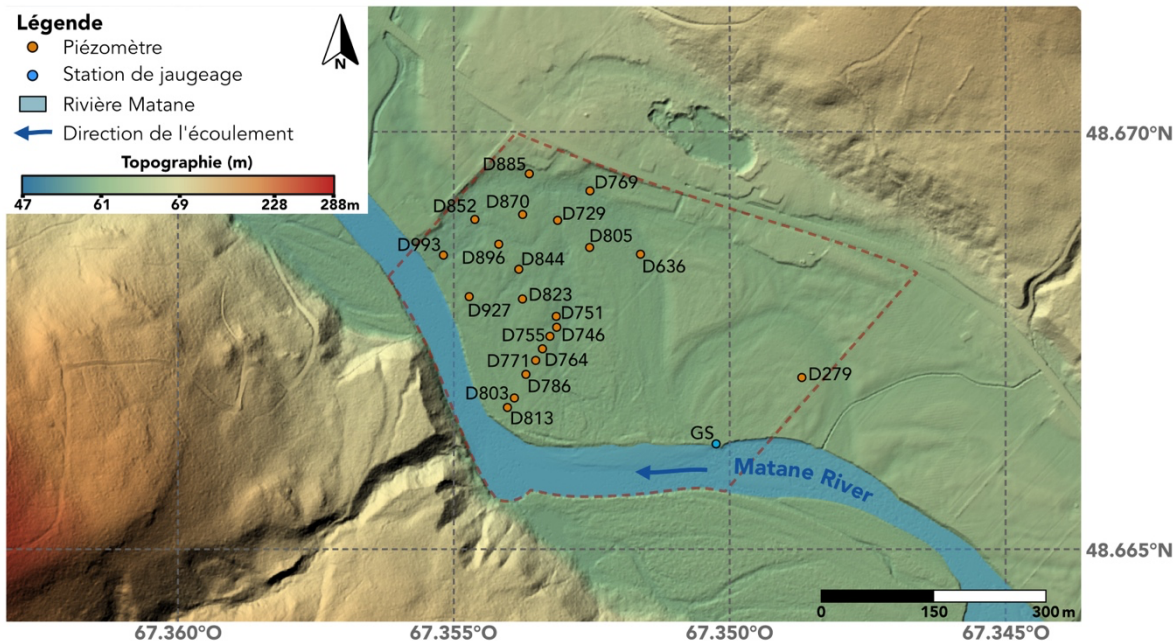
Figure 6. Position des piézomètres et de la station de jaugeage (GS) dans le méandre instrumenté de la rivière Matane servant à cette étude. La topographie est issue d'un relevé LiDAR de la vallée de la Matane réalisé en 2011.

6. DES BASES DE DONNÉES À VALORISER

Cette base de données, acquise au cours des projets de recherche successifs sur le méandre de la rivière Matane ainsi qu'au cours du travail de thèse présenté ici, présente un caractère exceptionnel du fait de sa résolution spatiale, de la longueur de la période de mesure, et du type de données obtenues. Avec le retrait sur le site des piézomètres et des instruments de mesure, on peut légitiment se questionner sur la conservation de cette base de données dans le temps et sur sa réutilisation avec les bases de données géochimiques associées dans le cadre d'autres problématiques. Par ailleurs, à travers le monde, les progrès technologiques et l'augmentation des capacités de stockage de l'information ont permis l'émergence d'études de ce type, générant des quantités impressionnantes d'autres données physique et chimique spatialisées. Chacune de ces bases de données est classiquement traitée en interne par un seul laboratoire ou institut de recherche et donc avec un nombre limité d'expertises (Diepenbroek et al., 1999). Ce système non optimisé de production et de traitement de données apporte ainsi de nouvelles problématiques sur l'intérêt et les infrastructures nécessaires à un partage ouvert des masses de données acquises dans le but d'optimiser l'avancée des connaissances sur la connectivité entre les eaux souterraines et les rivières.

Pour répondre à ces questions, différents projets ont vu le jour en sciences naturelles. En 1993, par exemple, le système d'information PANGAEA (Institut Alfred Wegener (AWI), Centre de sciences environnementales marines de l'Université de Bremen (MARUM)) a été développé dans le but d'héberger et de diffuser en libre accès des bases de données spatialisées et structurées avec leurs métadonnées issues de la recherche sur le système terrestre (Diepenbroek et al., 2017). Hébergeant plus de 360 000 bases de données pourvues d'un DOI, cette plateforme a reçu l'accréditation de Centre de Données Mondiales (*World Data Center*) par le conseil international pour les systèmes de bases de données scientifiques mondiales (*International Council for Science World Data System*). L'objectif de ces centres de données mondiales est de permettre un accès universel et équitable à des données scientifiques dont la qualité est assurée. Les bases de données hébergées par de telles

instances sont gérées et diffusées sur le long terme (Diepenbroek et al., 2017; International Science Council, 2021). D'autres initiatives plus ciblées sur un domaine précis, comme le projet européen KINDRA (European Inventory of Groundwater Research, 2021; Tomaszewska et al., 2018) lancé en 2015, se proposent de diffuser des bases de données hydrogéologiques en les intégrant dans un système de classification harmonisé gravitant autour de trois thèmes : le domaine de recherche ; sa mise en œuvre ; et le défi sociétal dans lequel la recherche s'intègre. Le but de cette classification est d'avoir une vue d'ensemble des différentes bases de données et projets européens tout en servant de support aux objectifs de gestion et de protection des ressources en eaux définies par l'Union Européenne. Ces systèmes de stockage et de diffusion de bases de données peuvent également conserver une dimension plus locale. Au Québec, c'est par exemple le cas de l'Observatoire Global du Saint-Laurent (OGSL). Ce regroupement d'organisations provinciales et fédérales canadiennes publie ainsi en libre accès sur son site internet les bases de données permettant la compréhension, et la gestion durable de l'écosystème global du Saint-Laurent (Observatoire Global du Saint-Laurent, 2021). Ces différents exemples sont conformes aux principes FAIR (*Findability*, *Accessibility*, *Interoperability*, et *Reuse*) de partage de la donnée scientifique, assurant que cette dernière puisse être trouvée facilement, qu'elle soit disponible et réutilisable, et qu'elle puisse être utilisée sur différentes plateformes. Un partage généralisé des bases de données pourrait potentiellement aider à augmenter les connaissances sur les échanges entre les aquifères et les rivières.

7. OBJECTIFS ET STRUCTURE DE LA THÈSE

Cette thèse a pour objectif général de **qualifier et de quantifier la connectivité hydrogéologique et géochimique aquifère-rivière en combinant des approches géochimiques et hydrogéologiques**. Plus spécifiquement nous nous proposons ici de répondre à cet objectif en trois étapes principales (Fig. 7). Nous avons d'abord (**Chapitre 1**) cherché à vérifier si de l'eau de rivière s'infiltrait ou non dans l'aquifère alluvial en analysant

l'influence de l'état hydrique des rivières (i.e. crues, étiages) sur la géochimie des eaux souterraines d'une plaine d'inondation. Les variations observées de la géochimie des eaux (radon, conductivité électrique, température, pH, isotopes stables de l'eau) nous ont permis d'évaluer l'extension spatiale de la zone hyporhéique au cours du temps et de supporter le concept de corridor hyporhéique. Dans un second temps (**Chapitre 2**), la quantification des eaux souterraines se déchargeant vers la rivière à l'aide d'un modèle fondé sur les activités en radon nous a permis d'estimer les flux de carbone inorganique dissous (DIC) vers la rivière et de CO_2 vers l'atmosphère. Enfin, étant donné l'ampleur de la base de données hydrogéologique et géochimique acquises dans le cadre de cette étude, la question de son potentiel de valorisation s'est posée (**Chapitre 3**) dans le cadre de sa réutilisation pour d'autres problématiques et de son partage à la communauté scientifique. Toutes les bases de données associées à cette thèse ont été publiées sur le répertoire de bases de données Pangaea.
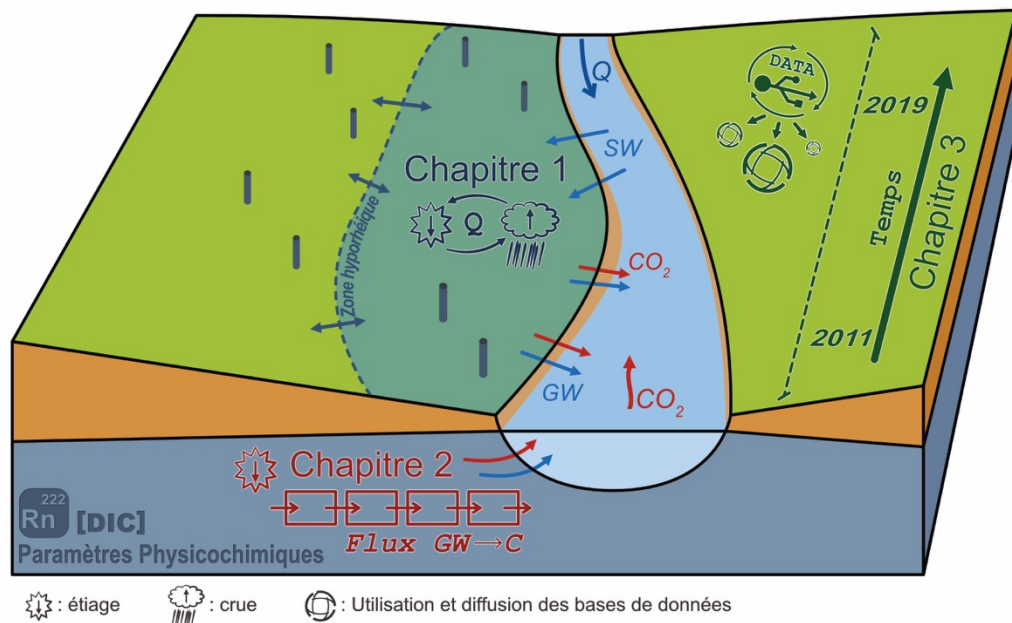
Figure 7. Représentation schématique des trois chapitres proposés dans cette thèse au sein du continuum aquifère-rivière.

CHAPITRE 1
CONNECTIVITÉ HYDROLOGIQUE DANS LE CONTINUUM AQUIFÈRE - RIVIÈRE : IMPACT DU DÉBIT DE RIVIÈRE SUR LA GÉOCHIMIE DES EAUX SOUTERRAINES DE LA PLAINE D'INONDATION

1.1 RÉSUMÉ

L'étude est basée sur une base de données complexe et unique d'activité en radon, d'isotopes stables de l'eau, et de paramètres physicochimiques (température, conductivité électrique, et pH) produite pour mieux comprendre la connectivité hydrogéochimique entre les eaux souterraines et les eaux de rivières dans une plaine d'inondation de la rivière Matane (Québec, Canada). À l'aide d'un réseau de 21 piézomètres implanté dans un méandre de 18 ha, les propriétés géochimiques des eaux souterraines de subsurface ont été étudiées au cours de neuf campagnes d'échantillonnage entre 2011 et 2017. La rivière est alimentée par les eaux souterraines pendant la majorité de l'année, mais peut également alimenter les eaux souterraines lorsque le débit de l'eau dans la rivière est important. L'objectif de cette étude était d'explorer les variations géochimiques saisonnières des eaux souterraines en réponse aux variations de débit dans la rivière en regardant tout particulièrement l'étendue spatiale de la zone hyporhéique. Un examen approfondi des températures, du $\delta^{18}O$, de la conductivité électrique, et de l'activité en ^{222}Rn dans les eaux souterraines indique que les propriétés géochimiques des eaux souterraines de subsurface varient dans l'espace et au cours du temps. Des analyses statistiques multivariées (clustering et analyse canonique par redondance) ont montré que le débit des rivières est un facteur déterminant de contrôle de la géochimie des eaux souterraines de subsurface, quelle que soit la saison. La zone hyporhéique, où les eaux souterraines se mélangent avec les eaux de rivières, s'étend loin de la rivière. Ces résultats appuient le concept de corridor hyporhéique et de gestion intégrée des rivières en apportant un point de vue géochimique sur la connectivité entre les aquifères et les rivières.

Cet article, intitulé « *Hydrological connectivity in the aquifer–river continuum: Impact of river stages on the geochemistry of groundwater floodplains* » (doi : doi.org/10.1016/j.jhydrol.2020.125379) a été publié dans la revue *Journal of Hydrology* et est disponible en ligne depuis le 5 août 2020. La publication de cet article s'accompagne d'une publication conjointe de la base de données géochimique traitée dans ce chapitre dans le répertoire de base de données Pangaea.de sous le titre « *Geochemical data collected in shallow groundwater and river water in a subpolar environment (Matane river, QC, Canada)* » (doi : doi.pangaea.de/10.1594/PANGAEA.908290).

Contribution des auteurs :

Cet article a été corédigé par moi-même ainsi que les professeurs Gwénaëlle Chaillou, Thomas Buffin-Bélanger, et Paul Baudron. En tant que premier auteur, j'ai contribué à l'essentiel de la recherche de conceptualisation de la problématique, de développement de la méthodologie, de prélèvements sur le terrain, d'analyse des données, de leur interprétation, de productions de figures, et de rédaction de la première version de l'article. Ce travail de conceptualisation a été réalisé en collaboration avec l'ensemble des coauteurs qui ont tous contribués par leurs révisions et propositions à la version finale de l'article.

Communications :

Une version préliminaire et abrégée de cet article a été présentée sous forme d'affiche scientifique au 28e congrès de la Goldschmidt à Boston en aout 2018 :

Biehler, A., Tremblay, C., Baudron, P., Buffin-Bélanger T., & Chaillou, G. (2018). *Seasonal variation in chemical exchanges between a river and a meander floodplain*. 28th Goldschmidt Conference, Boston (MA, USA), Août 2018

1.2 HYDROLOGICAL CONNECTIVITY IN THE AQUIFER–RIVER CONTINUUM: IMPACT OF RIVER STAGES ON THE GEOCHEMISTRY OF GROUNDWATER FLOODPLAINS

Antoine Biehler[a], Gwénaëlle Chaillou[b], Thomas Buffin-Bélanger[a], Paul Baudron[c]

[a] *Université du Québec à Rimouski, 300 allée des Ursulines, Rimouski, Québec G5L 3A1, Canada*
[b] *Institut des Sciences de la Mer de Rimouski, Université du Québec à Rimouski, 310 allée des Ursulines, Rimouski, Québec G5L 3A1, Canada*
[c] *École Polytechnique de Montréal, 2500 chemin de polytechnique, Montréal, Québec H3T 1J4, Canada*

Abstract: The study is based on a complex and unique data set of ^{222}Rn activity, water stable isotopes, and physicochemical parameters (i.e., temperature, electrical conductivity, pH) produced to better understand the hydrogeochemical connectivity between groundwater and river water in a meander floodplain of the Matane River, QC, Canada. Using an array of 21 piezometers implanted into an 18 ha meander floodplain, the geochemical properties of shallow groundwater were investigated over nine sampling campaigns between 2011 and 2017. The river is in gaining conditions most of the year, although losing conditions are temporally observed along high river discharge. The objective was to explore the seasonal geochemical variations in response to river discharge with a specific focus on the spatial extent of the hyporheic zone. A thorough examination of temperature, δ^{18}O, electrical conductivity, and ^{222}Rn in groundwater indicated that the geochemical properties of shallow groundwater varied in space and time. Multivariate statistical analyses (i.e., clustering and canonical redundancy analysis) showed that river discharge is a key factor controlling shallow groundwater geochemistry, whatever the season. The hyporheic zone, where groundwater mixes with river water, extended far from the riverbank. These results support the concept of the hyporheic corridor and integrated river management by providing a geochemical viewpoint on river-aquifer connectivity.

Keywords: Groundwater–river connectivity; River discharge; Hyporheic corridor; Radon-based model; Groundwater mixing zone

1.3 INTRODUCTION

The hydrology and water quality of rivers are mainly controlled by the exchange of water and solutes with surrounding groundwater. These exchanges can be of three types (Cook, 2015): groundwater from the catchment can discharge in rivers (gaining streams); river water can flow into the aquifer (losing streams); or river water can flow into the aquifer, transit in it for hours or days, then return to the river. At the river-aquifer interface, the hyporheic zone, where downwelling surface water mixes with discharging groundwater, is a key zone that controls stream ecosystems by regulating water flow and biogeochemical processes. It is a critical zone in the conservation and management of freshwater resources, influencing both surficial and groundwater quality and availability. Then determining the extent of hyporheic zones is critical when making management decisions for stream and riparian systems.

The spatial extent of the hyporheic zone is, however, highly dependent on the chosen definition. From a biological point of view, the hyporheic zone is defined by a specific distribution of hypogean and epigean invertebrates (White, 1993; Williams, 1989; Xu et al., 2012). In hydrogeology, the hyporheic zone is defined by the volume of sediment with a specific proportion of infiltrated surface water mixed with groundwater (Lewandowski et al., 2019; Triska et al., 1989; White, 1993). Schindler and Krabbenhoft (1998) proposed, however, the use of geochemical characteristics of water masses to discriminate between ground and surface water allowing to delimit the spatial extent of the mixing zone. The extent of this zone can also be seen in terms of water residence time and timescale of exchanges (Bayani Cardenas, 2008; Gooseff, 2010). These timescales range from hours to days. In this way, stable isotopes of water ($\delta^{18}O$, δ^2H) and radio-isotopes (^{222}Rn) would be useful environmental tracers to better understand groundwater - surface water interactions (Baskaran et al., 2009).

The impact of floods on the hydrological connectivity between surface water and groundwater have been studied extensively over the last decades mainly for flood risk

planning and infrastructure damages (Macdonald et al., 2012). River discharge intensity controls over-bank flooding events as well as water table levels in the adjacent aquifer. In response to flood events, rapid variations in piezometric levels surrounding the rivers occur (Buffin-Bélanger et al., 2015c; Lewandowski et al., 2009; Sophocleous, 1991; Vekerdy and Meijerink, 1998). However, because the propagation velocities of this groundwater floodwave cannot be explained by Darcy's law (Jung et al., 2004; Lewandowski et al., 2009; Vidon, 2012), one might assume that direct recharge from the river within floodplains remains limited (Lewandowski et al., 2009). The groundwater floodwave is a pressure wave that propagates into the surrounding aquifer. It is detected up to several kilometers from the riverbed (Lewandowski et al., 2009; Vekerdy and Meijerink, 1998). The groundwater floodwave is considered as a kinematic or dynamic wave depending on its dispersive or diffusive behaviour, respectively (Buffin-Bélanger et al., 2015c). The groundwater floodwave induces new flowpaths (Cloutier et al., 2014; Gooseff, 2010). Moreover, Buffin-Bélanger et al. (2015c) pointed out that the velocity and the amplitude of this dynamic waves changed seasonally in response to river discharge variations. These findings highlight the hydrodynamic connectivity between river and aquifer at a reach to catchment-scale, in the so-called "hyporheic corridor zone" as defined by Stanford and Ward (1993).

Most studies have focused on the temporal and spatial evolution of surface water quality in response to hyporheic geochemical conditions (e.g. Aguiar Jr. et al., 2015; Cook et al., 2003; Dragon et al., 2015; Hill, 1996; Ledesma et al., 2013; Mayer et al., 2007) but the temporal and spatial geochemical variations in hyporheic zone and adjacent aquifers have received little attention. This is surprising given the importance of the hyporheic zone as a functional entity for groundwater and dependent ecosystems (see Boulton et al., 1998) and the use of alluvial aquifer as freshwater resources in some region as in Canada and Québec province particularly (Buffin-Bélanger et al., 2015b; Chaillou et al., 2016; Masse-Dufresne et al., 2019; Patenaude et al., 2020). Further knowledge is needed on the temporal and spatial extent of hyporheic exchanges in order to improve the understanding of the functioning of catchment and the use of freshwater resources for water management authorities and political decision-makers (Bencala et al., 2011).

The present study focused on the spatial and temporal variations of geochemical characteristics of shallow groundwater in a ~18 ha meander floodplain on the Matane River (Québec, Canada). The objectives were to use a multi-geochemical parameters approach to determine whether the geochemical characteristics of shallow groundwater is controlled by hydrological conditions, e.g. river discharge and river–aquifer connectivity. Specifically, we analyzed the distribution of pH, temperature, radon (^{222}Rn), electrical conductivity, and stable isotopes of water (δ^{18}O, δ^{2}H) to locate the lateral extent of the hyporheic zone in the aquifer floodplain. Using multivariate statistical analyses, we explored the role of river discharge as a key factor that controls subsurface geochemistry. By proposing a model based on ^{222}Rn for the calculation of groundwater residence time, we discussed the role of river discharge in the internal hydrodynamic flows of the surrounding aquifer.

1.4 MATERIAL AND METHODS

1.4.1 Study site

Matane River Valley is located in the northwest Gaspé Peninsula (Quebec, Canada; Fig. 8a) between the Chic-Choc Mountains (Appalachian orogen) and the St. Lawrence Estuary. The river drains a 1 678 km^2 catchment that is mainly forested (~90%). Catchment is composed of shales, fine sandstones, and limestones (Marchand, 2013; Ollerenshaw, 1967). In the valley, these rocks are overlaid by a ~48 meters layer of Quaternary sediments composed of pebbles, gravels, and coarse sands (Cloutier, 2013) that are from the late Holocene deglaciation of the valley followed by alluvial filling (Marchand et al., 2014). The river channel has an average width of 55 meters and is included in a semi-alluvial valley with a mean width of 475 meters and an average slope of 0.2 m·100 m^{-1} (Buffin-Bélanger et al., 2015a; Marchand, 2013). The study site is located 30 km from the mouth of the river and is a 17.8 ha meander at an average elevation of 60.4 meters (Fig. 8a). At the study site location, Matane River is mainly a gaining stream. The floodplain shows signs of contemporary lateral

migration dynamics as well as an ancient meander that was cut off. The action of this remnant subsurface structure on the floodplain hydraulic is still not clear. Based on high-frequency time series of piezometric levels in observation wells in the study site, Cloutier et al. (2014) and, more recently Buffin-Bélanger et al. (2015c) didn't found any preferential subterranean flow paths related to this structure.

The mean annual discharge of Matane River is 39 $m^3 \cdot s^{-1}$ (1929–2009), and bankfull discharge is 350 $m^3 \cdot s^{-1}$ (Buffin-Bélanger et al., 2015c; Cloutier et al., 2014). The nivo-pluvial hydrologic regime is characterized by strong seasonal contrasts between summer and winter (Fig. 8b), with baseflow periods in winter (February and March) and in summer (from mid-July to the end of September). From December to early April, mean temperatures are negative and ice covers the river. In April and May, river discharge increases rapidly to reach a mean maximum value of ~380 $m^3 \cdot s^{-1}$ (this mean value is calculated from maximum discharges from 1926 to 2017) in response to snow melt in the catchment. During snow melt as well as during significant flood events, the alluvial plains adjacent to the study site are flooded by overbank flooding and groundwater exfiltration resulting from the rapid propagation of a dynamic groundwater floodwave (Cloutier et al., 2014). Based on the analyses of 54 flood events in observation wells located in the study site, Buffin-Bélanger et al. (2015c) calculated groundwater floodwave propagation velocities ranging from 8 to 13 $m \cdot h^{-1}$, and they reported some waves propagating up to 230 m from the main river channel. These propagation velocities are higher than Darcy's Flow calculation that suggests a median velocity of 4.95 $m \cdot h^{-1}$ (i.e. calculations were based on an effective porosity of 0.25 and hydraulic conductivities from Cloutier et al., 2014). The authors concluded that the groundwater floodwaves are kinematic or dynamic waves whose amplitudes and velocities would be controlled by the river discharge. They then proposed, based on the groundwater temperature analyses that the propagation of this wave induces no or limited mixing between surface water and groundwater.
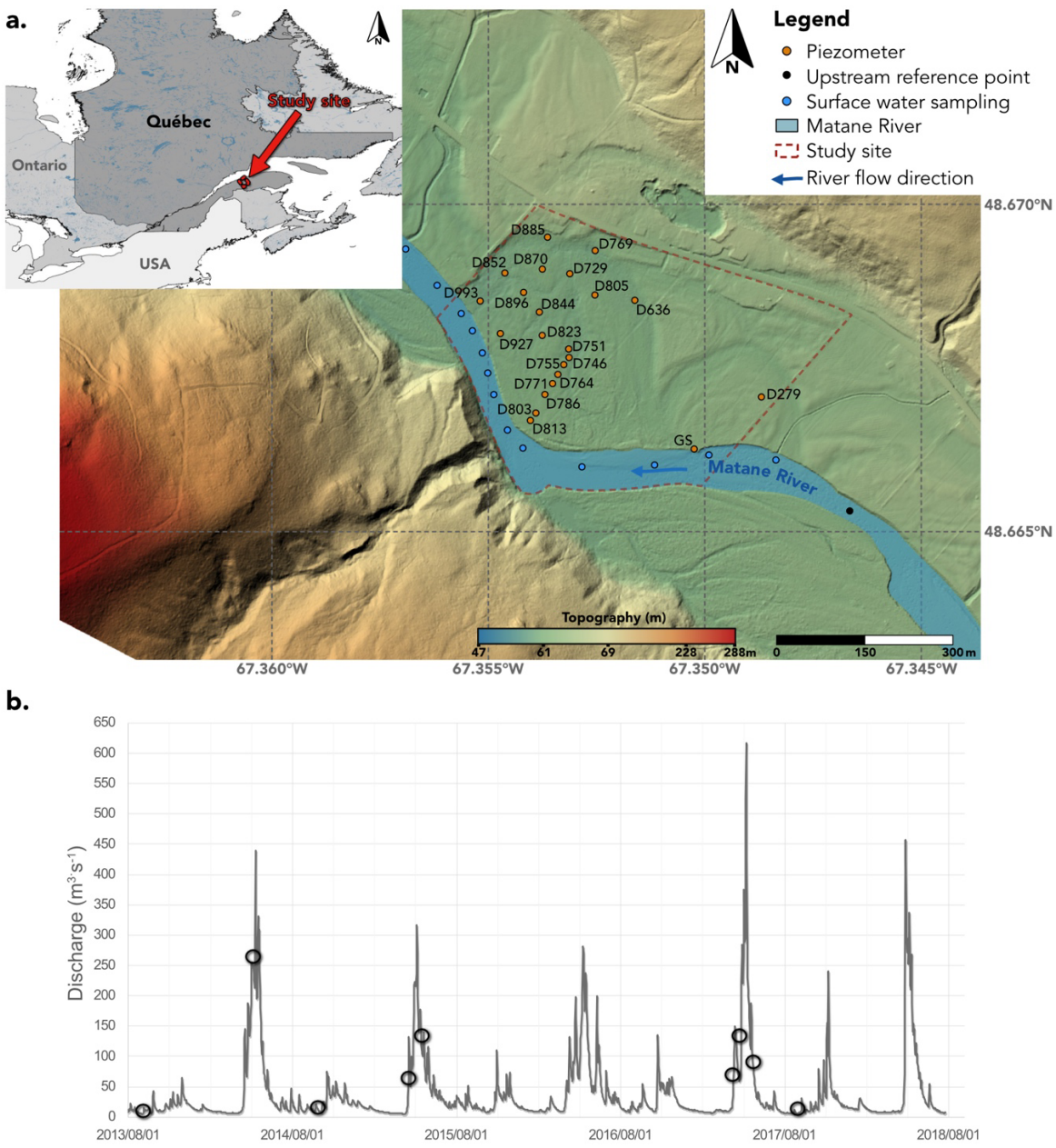
Figure 8. Location of Matane River (red square in inset) and the studied meander. The location of the different piezometers (Table 1) and the river gauging station (GS) are shown along with the upstream reference point (black dot; see text for details). Blue arrow represents the flow direction. Blue dots represent river water sampling from riverbank. (b) Water level fluctuations at station #021601, 25 km downstream of the sample site (data from the Government of Québec). Black circles represent water sampling periods (yyyy/mm/dd). The number of sampled piezometers during each campaign is given in Table 2.

1.4.2   Sampling approach

In 2011 and 2014, an array of 21 piezometers was randomly inserted in the floodplain to depths of ~3 m below the surface (from GS to D993; Fig. 8a). They correspond to the observation wells used by Cloutier et al. (2014) and Buffin-Bélanger et al. (2015a) to study the hydrological connectivity between river and the surrounding floodplain aquifer. Piezometers were made from 38 mm polymerized vinyl chloride pipes sealed at the base and equipped with a 0.3 m screen at the bottom end. The elevation of the bottom end of the different tubes ranged from 56.57 to 59.07 m above sea level (Table 1), near or below the position of the riverbed (58.40 m). Piezometer locations and elevations were determined using a Magellan ProMark III differential global positioning system (DGPS). Buffin-Bélanger et al. (2015) reported hydraulic conductivities (K) derived from slug tests using the Hvorslev method (Hvorslev, 1951) ranging from 13 to 275 m·day^{-1} with a mean value of 53 m·day^{-1}. These data are reported in Table 1. Piezometers were named according to their distance from a reference point chosen upstream of the study site (48.665364°N, 67.346850°W; Fig. 8a) irrespective to preferential groundwater flow paths in the floodplain. For example, D885 is located 885 m from the upstream reference point. Automated level and temperature loggers (Hobo U20-001) were inserted in each piezometer and in the gauging station (GS). Time series were corrected for barometric pressure from a barologger located at the study site.

Tableau 1. Location and features of the piezometer array. The N column refers to the number of times each piezometer have been sampled. The perpendicular distance refers to the shortest distance between each piezometer and the river bank; the distance from upstream (used to label the piezometer) was calculated as the distance of each piezometer from a reference point chosen upstream of the study site (48.665364°N; 67.346850°W; Fig. 8a); and screen bottom elevation refers to the DGPS (Differential Global Positioning System) elevation of the bottom of the piezometer. Hydraulic conductivity values are from Buffin-Bélanger et al. (2015c). GS refers to the piezometer located just under the surface in the riverbed.

Piezometer ID	Longitude (°W)	Latitude (°N)	N	Screen bottom elevation (mASL)	Perpendicular distance (m)	Distance from upstream (m)	Hydraulic conductivity (m·day^{-1})	DGPS elevation on the ground (mASL)
D885	67.353633	48.669497	5	56.72	233	885	18.14	59.511
D870	67.353753	48.669009	7	57.89	191	870	73.27	60.825
D852	67.354619	48.668950	5	56.61	109	852	57.11	59.615
D993	67.355189	48.668522	8	56.57	30	993	17.19	59.651
D927	67.354722	48.668025	6	57.79	41	927	16.76	60.55
D823	67.353756	48.667997	5	57.97	135	823	77.58	60.965
D786	67.353694	48.667094	6	58.13	80	786	24.02	61.178
D751	67.353144	48.667789	2	57.82	171	751	109.73	59.995
D746	67.353136	48.667658	4	58.39	153	746	203.04	59.902
D844	67.353822	48.668353	7	56.76	142	844	70.33	59.876
D896	67.354186	48.668653	4	57.92	127	896	274.75	60.957
D729	67.352539	48.668614	6	58.11	263	729	12.55	61.035
D805	67.353119	48.668939	5	56.99	245	805	29.72	60.034
D636	67.351617	48.668533	8	57.28	254	636	17.88	60.312
D769	67.352533	48.669292	4	57.30	322	769	53.40	59.947
D813	67.354028	48.666697	5	57.58	22	813	-	60.546
D803	67.353903	48.666811	4	57.57	41	803	-	60.383
D771	67.353517	48.667261	5	54.52	105	771	-	60.460
D764	67.353394	48.667400	4	57.32	125	764	-	60.256
D755	67.353258	48.667550	3	57.47	144	755	-	60.461
D279	67.348692	48.667056	3	59.07	83	279	-	62.141
GS	67.350164	48.666478	3	-	0	207	-	-

Nine groundwater sampling campaigns were carried out (Fig. 8b) in spring and summer to study high flow and baseflow periods. In each piezometer, groundwater was continuously pumped to the surface using a submersible pump connected to an on-line flow cell where electrical conductivity, temperature, and pH were continuously monitored using a calibrated multiparameter probe (600QS, YSI Inc.). After these parameters stabilized, groundwater samples were collected without filtration for measurements of stable isotopes of water ($\delta^{18}O$, δ^2H) and radon (^{222}Rn). For stable isotopes, groundwater was collected in 30 ml scintillation vials, hermetically sealed, and stored at room temperature. For radon, a detailed description of the measurement is presented below. Unfortunately, various meteorological and technical constraints did not make it possible to sample all the piezometers in each campaign. The information for each campaign is reported in Table 2. In addition to groundwater samples, surface water samples were also collected to obtain mean values for the river endmember. River water samplings were collected in the gauging station GS (Table1, Fig. 8a) and at different points along the meander. Surface waters were collected using a submersible pump connected to the on-line flow cell where multiparameter probe (600QS, YSI Inc.) measured physico-chemical parameters. Water for stable isotopes and radon analyses were done as explained below.

Tableau 2. Number of sampled piezometers during each campaign.

Sampling campaign	Number of sampled piezometers
20–30 August 2013	14
8–16 May 2014	15
3–14 September 2014	19
16 April 2015	14
14 May 2015	9
25 April 2017	1
16 May 2017	19
24 May 2017	3
22–24 August 2017	12

1.4.3 Stable isotopes of water

Stable isotopes of water ($\delta^{18}O$, δ^2H) were analyzed by EA-IRMS (Triple Liquid Water Isotope Analyzer; T-LWIA-45-EP) at the GEOTOP-UQAM Laboratory. Accuracies are ±0.05 ‰ (at the 2σ level) and ±0.21 ‰ (at the 2σ level) for $\delta^{18}O$ and δ^2H, respectively. Isotopic analyses are reported compared to the international Vienna Standard Mean Ocean Water (VSMOW) as defined by Gonfiantini (1978). Reference materials were used throughout the isotopic water analyses to ensure high-quality data. Results are expressed using the delta (δ) notation $\delta^{18}O$ (‰ relative to VSMOW).

1.4.4 Radon isotope

^{222}Rn is a radioactive isotope produced in the aquifer material by the decay of radium-226 (^{226}Ra), which is part of the uranium-238 (^{238}U) decay chain. ^{222}Rn activity in water and groundwater samples were analyzed using RAD7 alpha spectrometers (Durridge Inc.) with two different techniques (i.e. RAD *Aqua* and RAD *H₂O-BigBottle*) to outgas radon. The RAD7 alpha spectrometer was originally designed to the in-situ measurements of radon in coastal water to map and quantify submarine groundwater discharges (e.g., Baudron et al., 2015; Burnett and Dulaiova, 2003; Santos et al., 2012). But it is now commonly used in freshwater systems (Burnett et al., 2010; Hofmann et al., 2011; Kluge et al., 2007; Ortega et al., 2015; Schmidt et al., 2008).

During the 20–30 August 2013, 8–16 May 2014, and 3–14 September 2014 campaigns, we used the *in situ* RAD*Aqua* technique (showerhead-type air-water exchanger, RAD*Aqua*, Durridge). Surface and groundwater were continuously pumped into a spray chamber at a rate of 3 L·min⁻¹ where the degassed radon is injected through a Drierite dessicant to the radon detector for a minimum of 60 minutes. ^{222}Rn values were corrected with sample water temperature. Mean analytical uncertainties (2σ) based on counting statistics were 5% for groundwater samples (N=4) and 13% for surface water samples (N=16). For the other

campaigns (16 April 2015, 14 May 2015, 25 April 2017, 24 May 2017, and from 22–24 August 2017) we used the RAD *H₂O-BigBottle* technique. This technique is based on laboratory analyses of water samples collected in 2L plastic bottles tightly sealed. This technique has been preferred for groundwater analysis to increase the numbers of samples by campaign. Water was bubbled to allow ^{222}Rn degassing in a 30 mL headspace. As for RAD*Aqua* technique, the equilibrated air flows through a Drierite dessicant to the detector. ^{222}Rn values were corrected with air and water volumes, sample water temperature, and radioactive decay between the sampling and the analysis (globally between 2 and 30 hours). Mean analytical uncertainties (2σ were 19% for groundwater samples (N=54) and 29% for surface water samples (N=42). The two technics gave similar results with an error of $\pm$ 7 %.

Assuming the short half-life of ^{222}Rn (3.8 days) and anisotropic conditions in the aquifer, the ^{222}Rn activities should be constant and only controlled by the balance between production and decay. Radon can then be used as a chronometer whatever the origin of water masses introduced into the aquifer.

1.4.5   Statistical analysis

To regroup samples over space and time, the database was submitted to a hierarchical clustering. The database included water temperature, pH, electrical conductivity, ^{222}Rn activity, and δ^{18}O, for a total of 87 observations. One observation corresponds to one sample in one piezometer at a given moment, and for which the five target parameters were measured. Dendrogram analysis was performed on the Euclidian distance matrix with the Ward method (Murtagh and Legendre, 2014).

To determine the most significant environmental factors that control groundwater geochemistry, a canonical redundancy analysis (RDA) was performed using the Vegan 2.5-4 package in R (Oksanen et al., 2019). As was the case for clustering analysis, the physico-chemical parameters included water temperature, pH, dissolved oxygen, electrical

conductivity, ^{222}Rn activity, and δ^{18}O. The tested environmental parameters included river discharge, air temperature, piezometer elevations in the floodplain, water level in piezometers at the sampling period, as well as the distances of the piezometers to the upstream reference point, and the perpendicular distances to the riverbed. Note that air temperature values were included because they represent seasonal variations in the system: the seasons would affect geochemical reactions and groundwater inputs. For these statistical analyses, all data were standardized using the "decostand" function of the "vegan" package.

Correlation tests were conducted on tested parameters to select only independent parameters, based on variance inflation factors (VIF) greater than 3.5. Finally, environmental factors were selected by permutation tests in constrained ordination using a maximum of 1000 iteration steps. RDA model significance was then tested by ANOVA (999 permutations). Statistical analyses were conducted with R software v.3.5.2 "Eggshell Igloo" using RStudio.

1.5 RESULTS

1.5.1 Groundwater elevation in the shallow aquifer

Groundwater elevations in the floodplain varied from 58.00 to 61.20 m during the nine sampling campaigns. Fig. 9 illustrates three piezometric maps obtained at two baseflow conditions (September 2014 and August 2017), and at higher flow conditions (May 2015). For all those flow conditions, a regional north-west to south-east gradient was observed. The amplitude and direction of the gradient are relatively similar between flow conditions. The elevation of the piezometric surface was, however, higher during the high flow conditions (Fig. 9b). The minimum elevation for all flow conditions was obtained near the river in the downstream part of study site at piezometer D993 while groundwater elevations at piezometer D279 were always higher than mean elevation in the east of the floodplain.
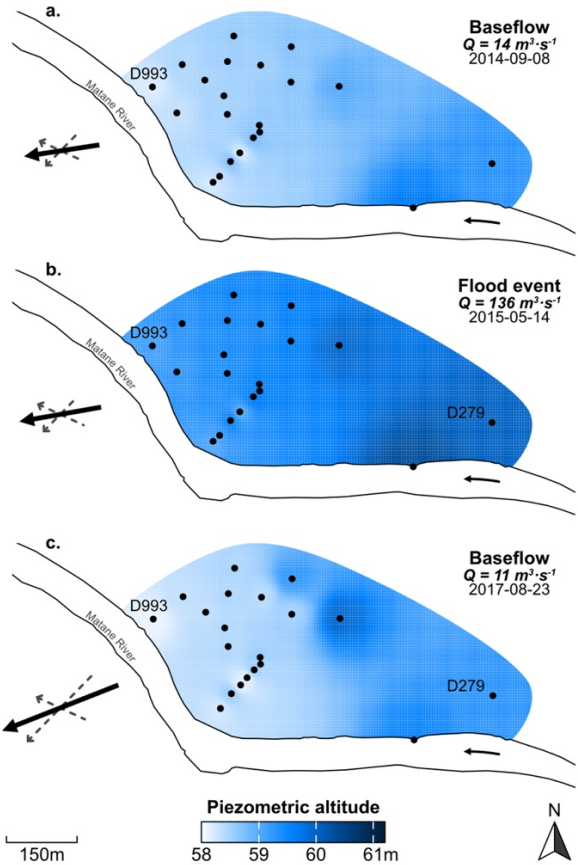
Figure 9. Altitudes of the piezometric surface during the (a.) September 2014, (b.) May 2015, and (c.) August 2017 campaigns. Piezometric maps were generated by the interpolation of piezometric altitudes in the piezometers (black dots). Curved black arrows indicate river flow direction. Crossed arrows show the resultant (black arrow) of the two gradients (grey dotted arrows) in the floodplain for each campaign.

1.5.2   Hydrogeochemical properties of floodplain groundwater

Fig. 10 shows the $\delta^{18}O$ and δ^2H compositions of groundwater and river water collected in the study site during each sampling campaign. Whatever the origin of the sample (surface or groundwater), there isotopic compositions remained parallel and exhibited similar average compositions with differences of less than 1% for both $\delta^{18}O$ and δ^2H. Except for April 2015 and May 2015, samples are in the line with the regional meteoric water line defined by Buffin-Bélanger et al., (2015b). For April 2015 and May 2015, even if values diverged from

the regional meteoric water line, the behaviors of surface and groundwater were similar suggesting they were affected by the same processes.

The average composition of groundwater samples over the 9 sampling campaigns was -12.9 ± 0.7 ‰ and -91.5 ± 3.5 ‰ for $\delta^{18}O$ and δ^2H respectively. These values were very close to the regional average values reported by Chaillou et al. (2017) for regional shallow aquifers (i.e. -12.4 ± 1.0 ‰ and -86.6 ± 8.3 ‰ for $\delta^{18}O$ and δ^2H respectively).
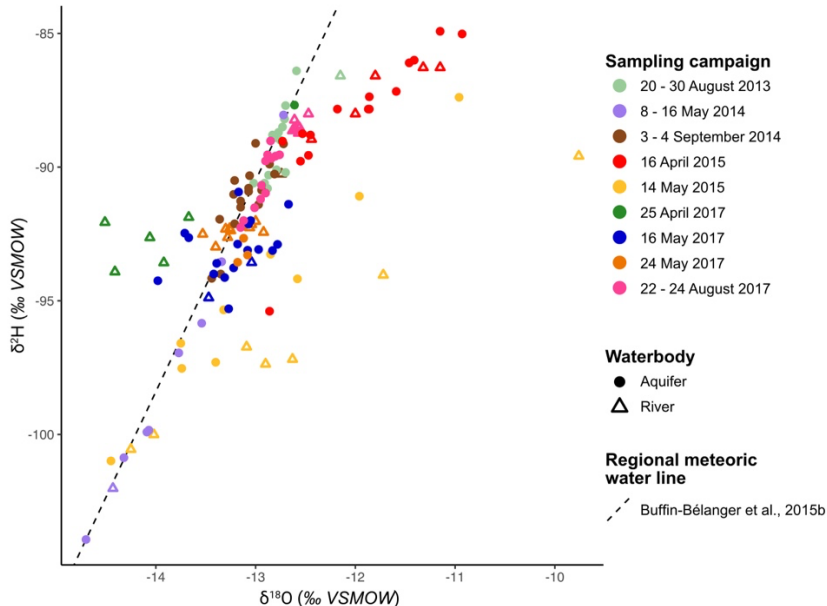
Figure 10. Deuterium *vs* oxygen-18 concentrations for river water and groundwater samples in the studied meander for each campaign. Regional meteoric water line was determined by Buffin-Bélanger et al. (2015b).

Fig. 11 shows the variability of groundwater temperature, electrical conductivity, $\delta^{18}O$, and ^{222}Rn activity over the sampling periods for all piezometers. Temperature ranged from 1.67°C at D279 to a maximum of 15.99°C at D813 (N=100; Fig. 11a). The median temperature for all sampling campaigns was 7.12°C with an interquartile range of 3.97°C. The temperature values exhibited high temporal variations (mean interquartile range of 5.18°C), and the highest differences between the median values and the global median value (i.e. 7.12°C) were in the first ~820 m from the upstream point. The piezometers in the downstream portion of the field site (D844 to D993) presented temperature medians around

the global median independent of the sampling period (mean interquartile ranges of 2.75°C). Piezometer D885, in the most downstream part of the floodplain, had a slightly higher median temperature (i.e., 9.85°C, with a minimum value of 8.38°C).

The median value of the $\delta^{18}O$ stable water isotope was -12.94‰ in the floodplain with the exception of three piezometers that exhibited more depleted values of ~-14‰ (D746 and D870–D896; Fig. 11b). This is similar to what was observed in the river, where a median $\delta^{18}O$ value of -13.98‰ was measured. In the upstream part of the study site (from GS to D755), variations of $\delta^{18}O$ values were higher than in the rest of the floodplain. Two piezometers, D885 and D771, had extremely low variations (interquartile ranges < 0.1 ‰) between sampling campaigns. Piezometer D771 had the deepest porous section in the floodplain and may have been less affected by near-surface processes.

Electrical conductivity increased from GS to D729 to reach a median value of 271 $\mu S \cdot cm^{-1}$ (Fig. 11c). Further downgradient, electrical conductivities were near the median value except around piezometers D852 and D885, where electrical conductivity suddenly increased (median = 302 $\mu S \cdot cm^{-1}$). The database shows high inter-campaign variability for piezometers D279, D748, and D786 to D813. The minimum and maximum electrical conductivity measurements are 97 $\mu S \cdot cm^{-1}$ (river piezometer GS) and 358 $\mu S \cdot cm^{-1}$ (D885) respectively.

^{222}Rn activities in the river (piezometer GS) are lower than activities in the floodplain piezometers (median values of 1.06 and 5.15 $Bq \cdot L^{-1}$, respectively; Fig. 11d). ^{222}Rn activities ranged from a minimum of 1.84 $Bq \cdot L^{-1}$ (D636, September 2014) to a maximum of 9.93 $Bq \cdot L^{-1}$ (D769, September 2014). Piezometers D729, D769, D786, and D823 had high inter-campaign variability, with an interquartile value higher than 2.10 $Bq \cdot L^{-1}$. ^{222}Rn activities measured in the shallow aquifer were two to 10 times lower than the mean activity reported in Appalachian-type aquifers. Pinti et al. (2014) found that the mean ^{222}Rn activity in Appalachian Mountain aquifers and in the St. Lawrence River platform aquifers were 31.3 $Bq \cdot L^{-1}$ and 16.1 $Bq \cdot L^{-1}$ respectively. Our radon data are in the range of median values reported for groundwater around Montreal and in some places in the province of Quebec

(e.g., 2.30 Bq·L^{-1} reported by Roireau and Zikovsky, 1989; 3.20 Bq·L^{-1} by Chah and Zikovsky, 1990).
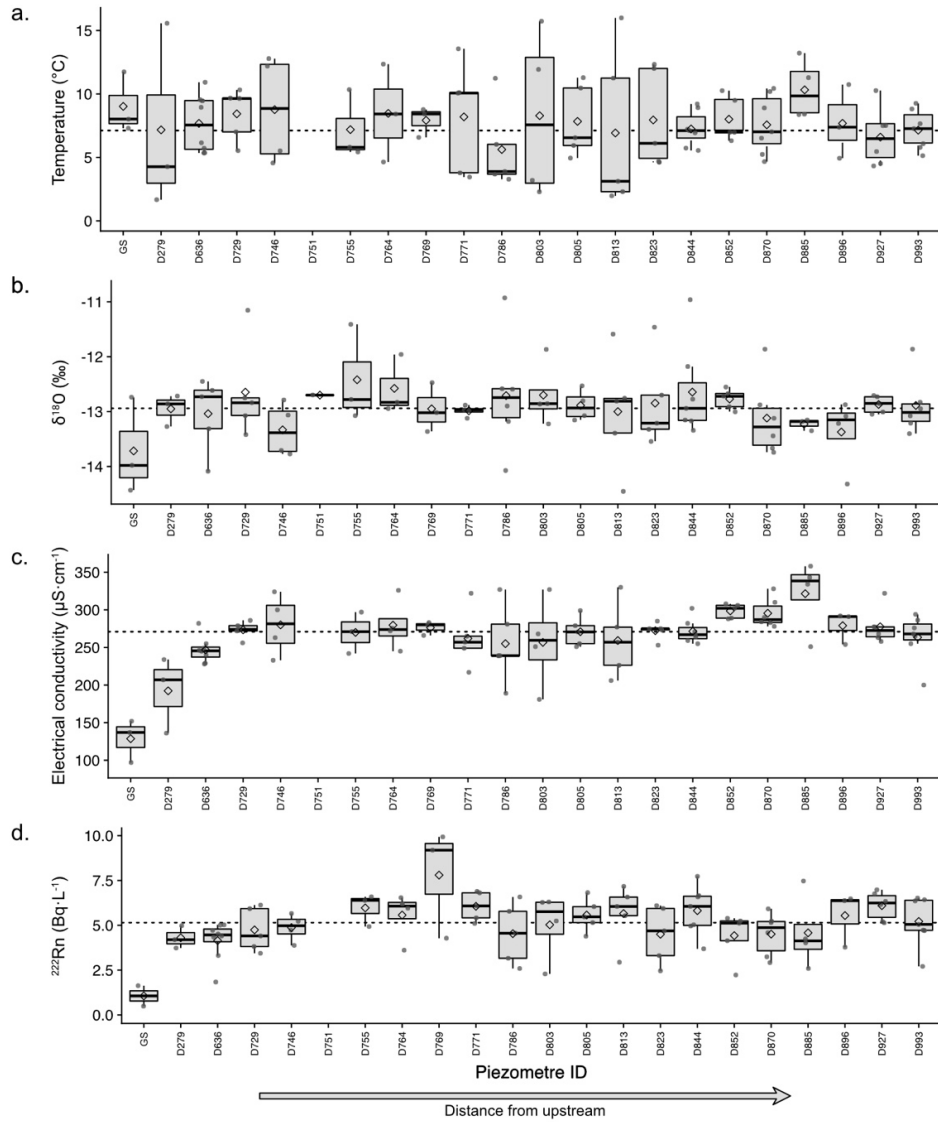
Figure 11. Groundwater data measured in the river (GS) and in the shallow aquifer (D279 to D993). Boxplots include measurements of (a) temperature (°C), (b) δ^{18}O (‰ VSMOW), (c.) electrical conductivity (μS·cm^{-1}), and (d) ^{222}Rn activity (Bq·L^{-1}) for all sampling campaigns. Black diamonds represent the mean values for each piezometer, black solid lines represent median values, and grey dots represent measured values. Grey boxes represent second and third quartiles and whiskers represent the first and fourth quartiles. The horizontal dotted lines are median values calculated in the groundwater floodplain (river piezometer GS was excluded from the calculation). Piezometers are identified as a function of the distance from upstream (Table 1).

The distribution of medians and interquartile ranges are reported in Fig. 12. There is no significant spatial pattern in the distribution of median values of temperature, electrical conductivity, water stable isotopes, and radon in the shallow aquifer. Nevertheless, the inter-campaign variability, as presented by interquartile value, tends to decrease from the upstream point, in the southeast part of the floodplain, to the northwest part of the floodplain.
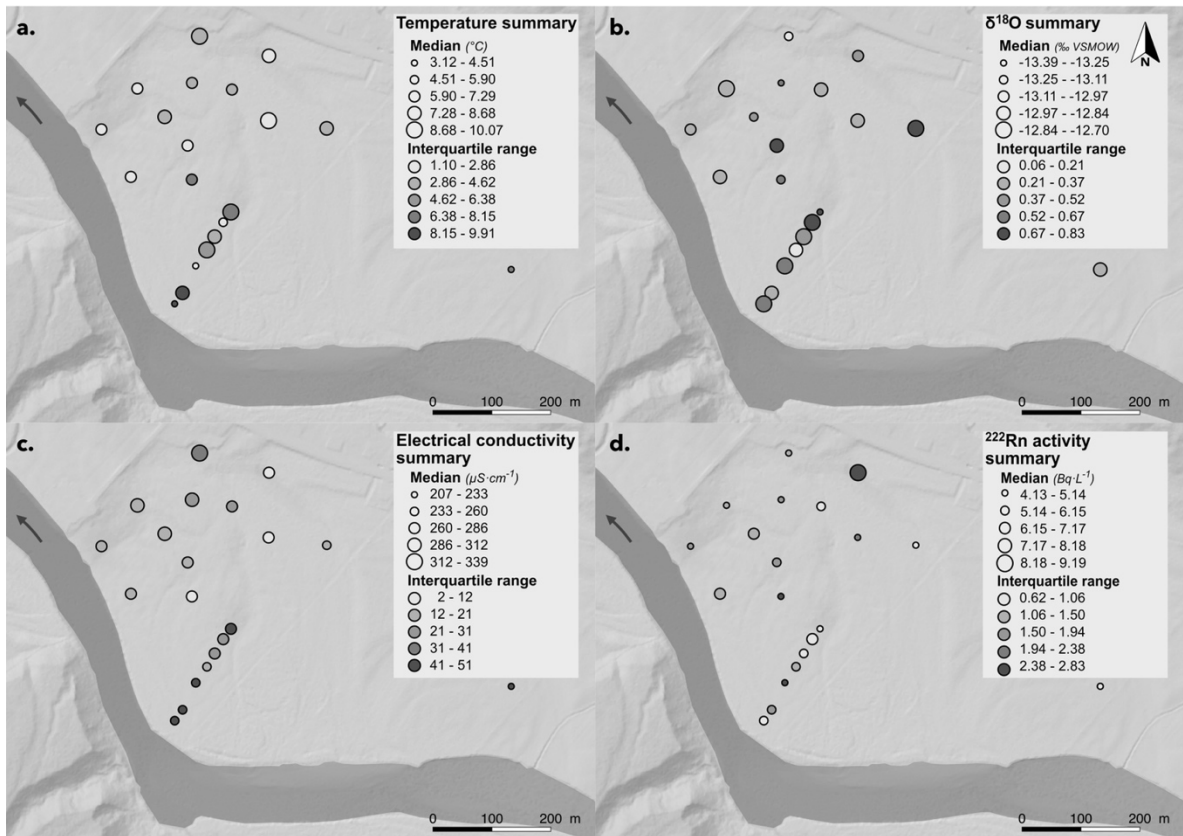
Figure 12. Median and interquartile ranges for floodplain piezometers (GS is not included) calculated using the overall database for (a) temperature (°C), (b) $\delta^{18}O$ (‰ VSMOW), (c) electrical conductivity ($\mu S \cdot cm^{-1}$), and (d) ^{222}Rn activity (Bq L^{-1}). Grey arrow represents the flow direction.

1.5.3 Hierarchical clustering on hydrogeochemical properties of groundwater floodplain

Parameters for hierarchical clustering were selected after a principal component analysis. The first three PCA axes calculated with water temperature, pH, electrical conductivity, ^{222}Rn, and $\delta^{18}O$ data explained 77.1% of the total variance in the geochemical database (34.4%, 27.2%, and 15.5% for PC1, PC2, and PC3, respectively). Electrical conductivity and ^{222}Rn activity mainly depend on water interaction with the aquifer matrix, and ^{222}Rn can be used as a groundwater tracer. Water temperature, pH, and $\delta^{18}O$ allow us to interpret the geochemical proximity of sampled groundwater with surface water. Hierarchical clustering using these target parameters led to the identification of four hydrogeochemical groups based on the 87 observations (Table 3). Group 1 (N=9) is characterized by both low median values and large interquartile ranges for electrical conductivity and ^{222}Rn values. Group 1 presents the most depleted values of $\delta^{18}O$ and includes all samples collected in the riverbed (piezometer GS). Group 2 (N=18) presents the highest median values for both temperature and electrical conductivity. The interquartile range for $\delta^{18}O$ is the lowest of all groups. Group 3 (N=22) is an intermediate group characterized by the highest pH values and the most enriched $\delta^{18}O$ signature. However, these parameters also exhibit large interquartile ranges. Group 4 is the largest group, with 38 observations. It has the highest ^{222}Rn activities and the highest interquartile range for temperature. In terms of median values, electrical conductivity is the most variable parameter among the four groups. In contrast, the median values for pH are quite stable, ranging between 7.80 and 7.90.

Tableau 3. Median hydrogeochemical features of the four groups revealed by the hierarchical clustering analysis performed on ^{222}Rn, δ^{18}O, temperature, pH, and electrical conductivity. Uncertainty is given as the interquartile range. N represents the number of samples included in each group.

Cluster ID	N	^{222}Rn (Bq·L^{-1})	δ^{18}O (‰ VSMOW)	Temperature (°C)	pH	Electrical conductivity (μS·cm^{-1})
Group 1	9	4.20 ± 3.49	-13.22 ± 0.44	4.27 ± 3.85	7.80 ± 0.48	189 ± 54
Group 2	18	5.24 ± 1.49	-13.01 ± 0.25	10.18 ± 3.97	7.81 ± 0.37	322 ± 25
Group 3	22	4.95 ± 1.54	-12.86 ± 0.85	5.53 ± 1.37	7.90 ± 0.81	247 ± 15
Group 4	38	6.11 ± 1.74	-12.90 ± 0.46	8.04 ± 4.72	7.86 ± 0.17	277 ± 13

Figure 13 exposes the spatial distribution of the relative occurrence of the four groups. Only four piezometers were consistently affiliated with the same group (black circles in Fig. 13e): GS, D885, D636, and D769 belonging to groups 1, 2, 3, and 4, respectively. These piezometers can be interpreted as the most representative points of their respective groups. Group 1 represented groundwater geochemically close to river water and is generally composed of samples collected near the riverbank. Groups 2 and 3 included piezometers far from the riverbank that were located in the downstream and upstream parts of the meander, respectively. Group 4 comprised the rest of the samples and included samples collected over the entire the floodplain.
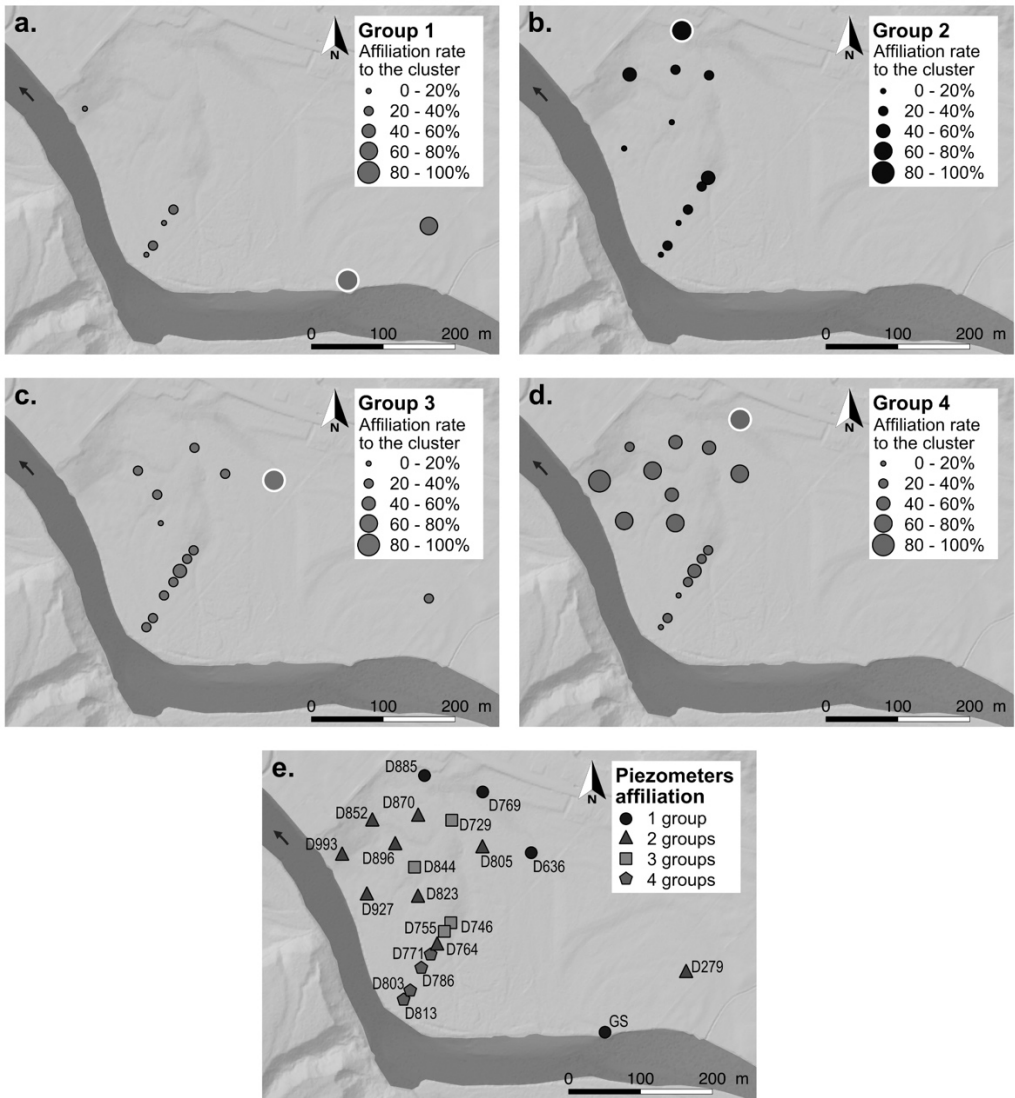
Figure 13. Affiliation of each piezometer in the different groups obtained by hierarchical clustering. Affiliation rates for each cluster are the percent of samples from each piezometer included in the cluster. Circles with white outline correspond to a 100% affiliation rate (maps a. to d.). In map e., shapes represent the number of groups to which each piezometer belongs (e.g., D729 is present in three of the four groups = grey square). Grey arrow represents the flow direction.

1.5.4 RDA on hydrogeochemical properties

We used canonical analysis by redundancy (RDA) to characterize how environmental parameters control groundwater chemistry in the shallow aquifer. After permutation tests in

constrained ordination, the significant environmental parameters that were identified for the final model were i) river discharge, ii) air temperature, and iii) distance from the upstream reference point (Fig. 14a). The RDA model explained 32% of the variance. The first RDA axis was mainly driven by river discharge and, to a lesser extent, the distance from upstream, while the second axis was mainly explained by air temperature (used as a proxy of seasonality). In this model, river discharge explained 45% (P-value <0.001) of the geochemical pattern (i.e., 16% of the total variance). Air temperature and distance from upstream explained 42% and 12% (P-value <0.001), contributing to 14% and 4 % of the total variance, respectively.

To further examine river discharge magnitude patterns, we repeated the RDA tests on different sets of data. The first test was performed on a database that only included the 35 groundwater samples collected near baseflow (e.g., river discharge < 50 $m^3 \cdot s^{-1}$). The second test used 42 samples collected during higher flows (e.g., river discharge > 50 $m^3 \cdot s^{-1}$). The ordination test was done to select the parameters for each RDA. For baseflow, air temperature and distance from the upstream point were statistically selected as environmental factors. For higher flow, piezometric levels, air temperature, and distance from the upstream point were statistically selected. Fig. 14b and Fig. 14c present the different RDA models. In both cases, the RDA models were significant (P-value < 0.001) explaining 37% of the variance for higher flows but only 20% of the variance for baseflow. The RDA model indicated that piezometric level (36% of the constrained variance; P-value < 0.001) and distance from the upstream point (34% of the constrained variance; P-value < 0.001) were the main environmental factors controlling the distribution of geochemical parameters during higher flow. During baseflow however, the main environmental factor was external temperature (61% of the constrained variance; P-value < 0.001).
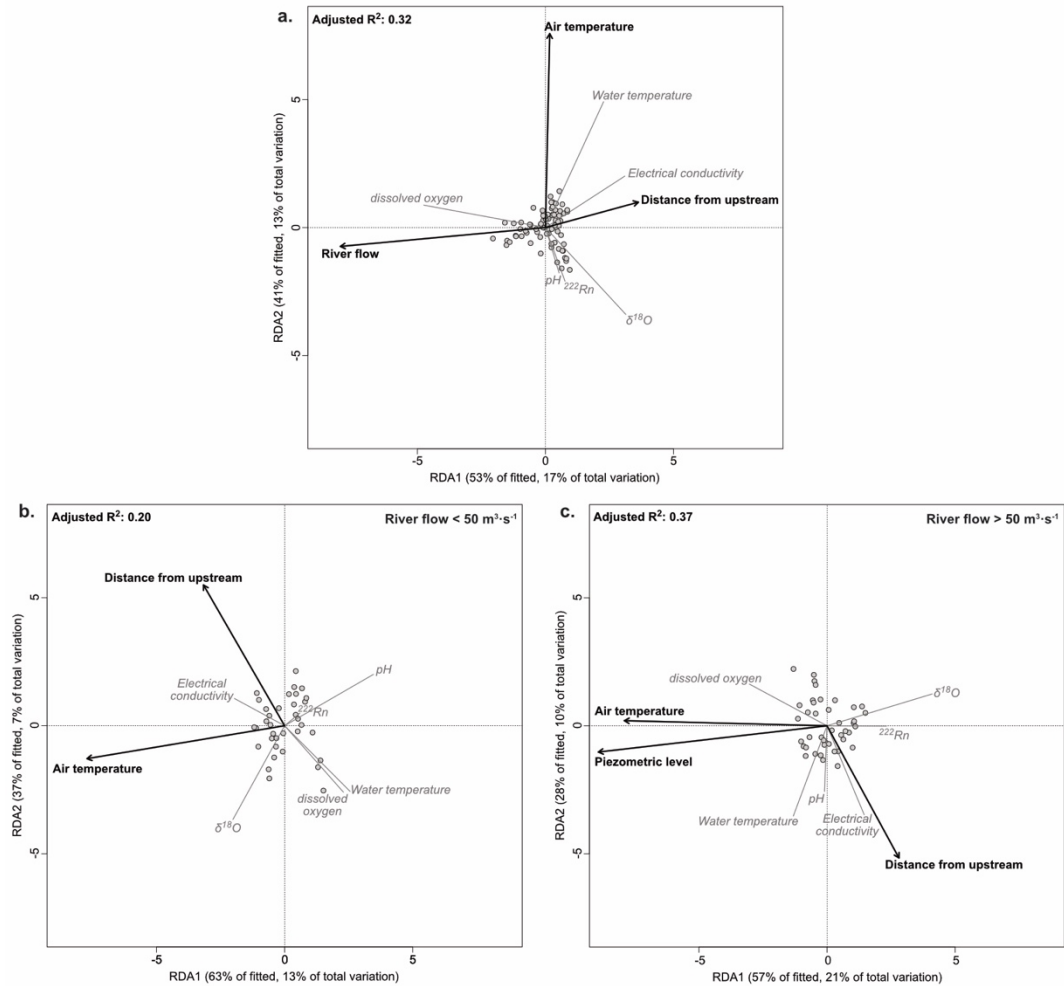
Figure 14. RDA biplots performed (a) on the entire groundwater database, (b) on the groundwater database for campaigns undertaken when river discharge was lower than 50 $m^3 \cdot s^{-1}$, and (c) on the groundwater database for campaigns undertaken when river discharge was higher than 50 $m^3 \cdot s^{-1}$. Grey dots represent observations located in the two-axis environment, grey lines represent the influence of each physicochemical parameter, and black arrows represent the importance of the considered environmental parameters.

1.6 DISCUSSION

The floodplain is a highly dynamic system where groundwater geochemistry changes in space and time. Most studies have focused on the impact of alluvial groundwater quality on surface water and river ecosystems (Aguiar et al., 2015; Cook et al., 2003; Dragon et al.,

2015; Hill, 1996; Ledesma et al., 2013; Mayer et al., 2007). However, our results show that, in Matane River, surface water controls significantly the geochemistry and flowpath of groundwater in adjacent alluvial aquifers. These findings support the concept of hyporheic corridor proposed by Stanford and Ward (1993).

1.6.1 Changing hydraulic conditions in the floodplain in response to river discharge

During the sampling campaigns, the piezometric gradients revealed a regional hydraulic gradient from the catchment to the floodplain, with the dominance of an NE-SW direction (Fig. 9). This local piezometric gradient in direction of the river valley is a common observation in the region, where the regional aquifer supports baseflow river discharge (Buffin-Bélanger et al., 2015c). However, at the scale of the meander, an additional hydraulic gradient parallel to the river flow is established in the floodplain. This additional gradient was already observed by Cloutier et al. (2014) in the same study site. So, whatever the river discharge, this upstream – downstream gradient suggests that surface water infiltrates into the meander without flowing via the remnant subsurface structures of ancient meanders. The nature and the high permeability of the aquifer matrix probably explain the absence of preferential flowpaths via these structures. During flood events (defined as discharges higher than 60 % of bankfull ~350 $m^3 \cdot s^{-1}$) however, Cloutier and co-workers (2014) showed that this NE-SW gradient can reverse, leading to a dominant upstream - downstream gradient. During these episodic events, the gradient is in the same direction as the Matane River and surface water could infiltrate faster and further into the aquifer floodplain.

1.6.2 Spatial and temporal variations of groundwater geochemical properties

1.6.2.1 Geochemical features of shallow groundwater in the floodplain

Groundwaters in the shallow aquifer did not exhibit distinct isotopic compositions with respect to surface water (Fig. 10). The similarity between the water stable isotopes in surface and groundwater, coupled with a common Ca-HCO3 facies (N = 14, data not shown), suggest that infiltration and recharge of the shallow aquifer occurred under modern climatic conditions, as it was already observed for regional groundwaters (see Chaillou et al., 2017).

1.6.2.2 Key factors that control the geochemical properties of shallow groundwater

The physico-chemical parameters (Fig. 11) over the 9 sampling campaigns revealed that the geochemistry of groundwater in the floodplain has changed over time. Only three piezometers indicated a low variability for all the target physico-chemical parameters (D852, D927, D993). These piezometers were located in the downstream part of the floodplain. For all the piezometers, the target parameters exhibited high to very high variations. For example, radon activities ranged from 4.5 to 9.9 $Bq \cdot L^{-1}$ in D769 whereas activities were between 4.0 and 6.0 in D764. Based on a multivariate statistical approach, we tested different combinations of environmental factors (including river discharge, air temperature, piezometer elevations in the floodplain, water level in piezometers at the sampling period, distances of the piezometers to the upstream reference point, and perpendicular distances to the riverbed) to discriminate the key factors that explain the distribution of geochemical parameters in the floodplain over the sampling campaigns. The redundancy analysis (RDA) reveals that these variations are mainly controlled by river discharge and air temperature (as a proxy for seasonal variations - Fig. 14a). Piezometer elevations, water levels, and perpendicular distances, however, had no impact on the RDA model distribution. River discharge and air temperature are both closely linked to seasons. Thus, the geochemistry of groundwater appears to directly respond to the strong seasonal variations of subpolar climate.

During higher flow river discharge (e.g., >50 $m^3 \cdot s^{-1}$ in Matane River), piezometric gradient parallel with the river would increase. Surface water probably recharges the alluvial aquifer from the upstream of the meander and geochemical properties of groundwater are modified by dilution. Since the stable isotopes of water were similar between the surface and groundwater samples (Fig. 10), $\delta^{18}O$ and δ^2H indicated no significant change. In contrast, radon activities and electrical conductivity values decreased in response to a mix with surface water with low radon activities and low electrical conductivity values. Such dilution effects have been already observed for nitrate by Baillieux et al. (2014) in the Alte Aare River (Switzerland) where they noted an attenuation of nitrate concentration in groundwater up to 2 km from the riverbank.

In addition to hydroclimatic conditions, RDA model indicates a relationship between distance from the upstream reference point and groundwater geochemistry (Fig. 14). The geochemical variations observed in the shallow aquifer indicate a geochemical gradient from the upstream part of the floodplain where we observed high temporal variations of the geochemical parameters. In the downstream part of the floodplain, the geochemical parameters were less subject to temporal variation. In this zone, D852, D927, and D993 exhibited no variability, for example. This variability pattern coupled with the gradient observed for electrical conductivity from GS to D748 (Fig. 11c) were consistent with an active recharge from the river to the shallow aquifer which mixed surface water with low electrical conductivity to groundwater with higher electrical conductivity values. The figure 15 presents a conceptual model of the different factors that control groundwater geochemistry in the studied floodplain. According to our results, when the discharge was low (<50 $m^3 \cdot s^{-1}$), the hydraulic indicated a gradient toward the shallow aquifer that induced weak river water inputs in the floodplain (Fig. 15a and 15c). These conditions are dominant in the Matane catchment (Fig. 8b) and they limit the mixing between surface water and groundwater near the riverbank. However, when the discharge is high (> 200 $m^3 \cdot s^{-1}$), the hydraulic gradient in the floodplain reverses (Cloutier et al., 2014) and the gradient parallel to the riverbed enhances the intrusion of surface water within the shallow aquifer (Fig. 15b and 15d). These conditions are likely to be accentuated when the discharge increases. Surprisingly, the ancient

meanders do not act as preferential flowpaths under these conditions. This is in agreement with the results of Cloutier et al. (2014) that observed that, during flood events, the floodwave propagates up to 250 m from the riverbank, with no influence of these subsurface structures in the direction and velocity of the floodwave. Despite the conditions of higher flows and flood events are episodic (Fig. 8b), they significantly imprint the geochemistry of groundwater in almost all piezometers.
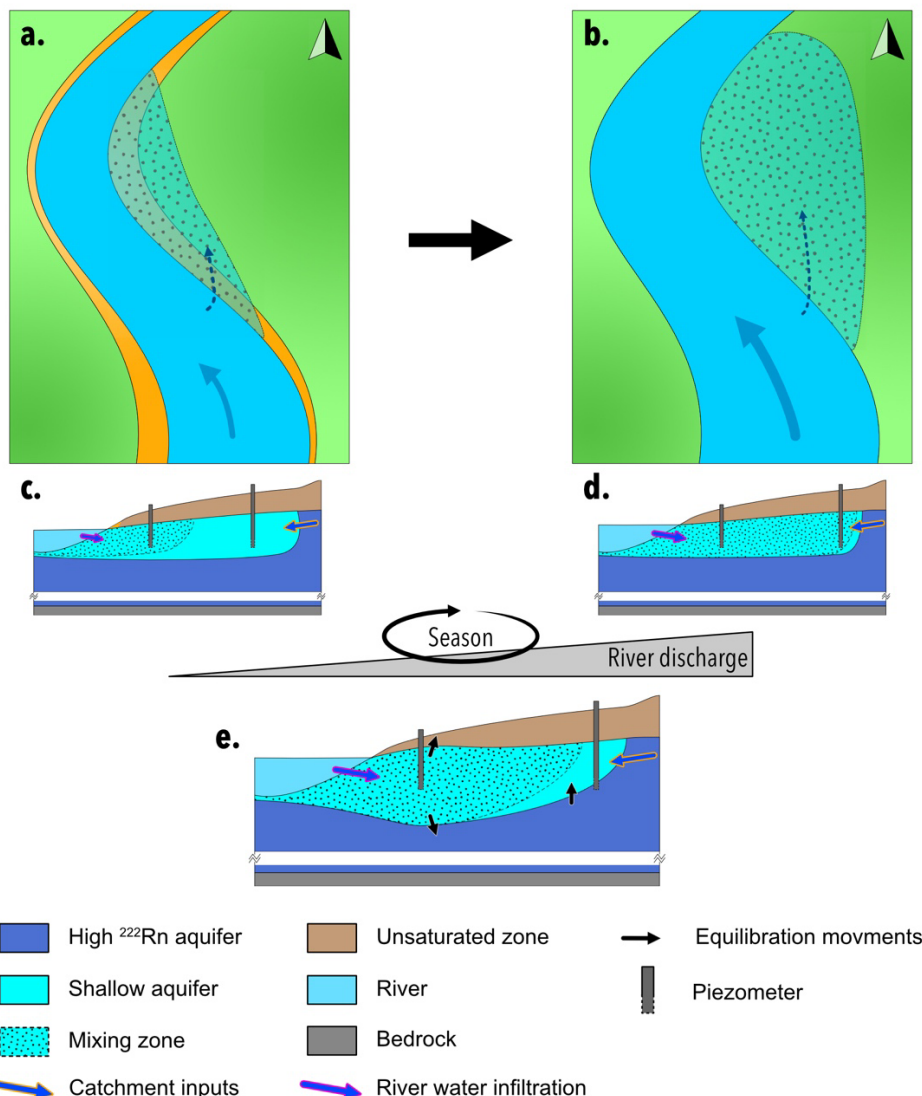
Figure 15. Schematic view of the floodplain and the associated section with the infiltration of groundwater for low (a. and c.) and high (b. and d.) river discharges. Floodplain section for transitional river stage (e.) represent the scenario from the ^{222}Rn model.

1.6.2.3 Spatial extent of the hyporheic zone

In a site similar to Matane River (e.g. low-land rivers meandering through extended floodplains), Lewandowski et al. (2009) also observed that infiltration of surface water into the adjacent floodplain aquifer occurs only periodically, under short periods of flooding. They concluded, however, that although the surface water level fluctuations propagated fast and far away from the river into the aquifer, infiltration events were short and only limited to the first ~4 m near the bank. In contrast, our results support the idea that infiltration of surface water into the shallow aquifer was sufficiently long to obtain detectable radon activities variations at all piezometer locations supporting a larger extent of flow mixing within the floodplain.

Spatial repartition of the groups defined by hierarchical clustering analysis supports the finding that surface water inputs affect a major part of the shallow aquifer. The piezometers included in group 1 were located near the riverbank at 100 m (Fig. 13a). This group exhibited low radon activity and low electrical conductivity, that indicated shorter water – aquifer matrix interactions. Radon activities varied greatly in this group (interquartile range of 3.49 Bq·L^{-1}) probably in response to the rate of mixing and residence time of infiltrated water and groundwater due to the proximity of the riverbank (Cartwright et al., 2014). In contrast, samples included in group 2 were located in the downstream part of the floodplain and far from the riverbank (Fig. 13b). This group exhibited the highest electrical conductivities and temperatures, and high radon activities resulting from prolonged water – aquifer matrix interactions. The groups 1 and 2 discriminated two contrasted geochemical poles in the floodplain, i.e., respectively a geochemical pole highly influenced by episodic surface water infiltrations, and a geochemical pole weakly influenced by surface water infiltrations and with geochemical characteristics similar to the geochemistry of the regional aquifer. Groups 3 and 4 represent two intermediate groups that result from different rates of mixing between groups 1 and 2. Both groups constituted the main part of the shallow aquifer and can be observed up to 270 m from the riverbank (Fig. 13c and Fig 13d), almost 5 times the average width of the Matane River.

Several piezometers located in the neck of the meander (i.e. D746 to D813; except D764) were included in at least three of these groups (G1, G3, and G4) highlighting the very high temporal variation of the geochemical properties in this zone (Fig. 13e). These results were consistent with the establishment of hydraulic gradients parallel to the stream flow and were in agreement with an inflow of surface water through the meander neck as observed by Peterson and Sickbert (2006).

The spatial distribution of groundwater temperature, $\delta^{18}O$, electrical conductivity, ^{222}Rn, the piezometric gradients and the clustering analysis indicate that water infiltration in this meandering river occurs in the downstream end of the concave bank. This freshly infiltrated water is then mixed with floodplain groundwater before flowing out to the river. Such a flowpath is consistent with the idealized conceptual models of a simple, low-radius meander with hyporheic exchange flow traversing a floodplain (Wondzell and Gooseff, 2013). In this model, the distance to the upstream river point is a key factor that controls the dilution rate and the geochemical properties in the shallow groundwater floodplain.

1.6.3 Deep implications for groundwater flowpaths?

1.6.3.1 A radon mass balance-based model

Surface infiltration from the river to the shallow aquifer impacts both water levels and geochemical properties of shallow groundwater. These hyporheic flowpaths are likely to have an impact on the dynamics of exchanges within the aquifer system. During the propagation of the floodwave, the fast and far propagation of the dynamic wave within the floodplain may enhance piston flow transport inducing vertical transport and water exchange between the shallow aquifer and the deep underlying aquifer. In the next section, we propose to use the radon dataset in order to explore the impact of hyporheic flowpaths on the dynamic of the aquifer system. Considering the properties of the radon isotope, ^{222}Rn activities allow the estimation of groundwater residence time in aquifers.

Based on previous stratigraphic data (Marchand et al., 2014), the studied floodplain system is depicted as an anisotropic aquifer connected to the river, the catchment (e.g. the Appalachian bedrock) and a deep underlying aquifer with several meters (~40 m) of Quaternary sediments (Fig. 15 c., d., and e.). The shallow groundwater sampled at 3 m depth in the floodplain likely originates from transversal flows from the river and catchment and from vertical exchanges with the underlying aquifer. Based on slurry experiments performed on homogenized sediments collected in the floodplain and in the riverbed, we determined a mean ^{222}Rn production of 0.329 ± 0.104 Bq·L^{-1} (N=5) in the shallow aquifer. This value is lower than the groundwater ^{222}Rn activities measured in the floodplain (median values = 5.15 Bq·L^{-1}, N=97), suggesting that the floodplain aquifer matrix cannot support the activities measured in the groundwater samples. To explain these higher radon activities, we assume that groundwater with higher radon activities has been introduced into the shallow aquifer, probably in connection with the catchment and the underlying aquifer. The specific secular equilibrium of radon is not known for these two aquifer systems, but we will assume that the maximum radon value measured in the floodplain reflects the advected radon activity. Over the 9 sampling campaigns, the maximum of radon was measured in D769 and reach 9.93 Bq·L^{-1}. This value is 3 times lower than activities reported in Appalachian bedrock (Pinti et al., 2014) but it is in the range of activities recently measured in Bas St-Laurent region in Appalachian bedrocks (mean ^{222}Rn activity = 14.0 Bq·L^{-1}, Tommi-Morin, pers. comm.) and in Quaternary sediments (mean ^{222}Rn activity = 10.2 Bq·L^{-1}, Tommi-Morin, pers. comm.). The time between the start of the imbalance and the sampling of groundwater can then be obtained from the radioactive decay equation of ^{222}Rn.

^{222}Rn activity in the aquifer is the partitioning between the ^{222}Rn radioactive decay, the production rate by the shallow aquifer matrix (supported Rn), and the dilution by "young" groundwater newly supplied by the river with low ^{222}Rn activity.

To integrate the dilution between surface water and groundwater, a factor of dilution (f_{GW}) was calculated by a mixing equation model using the mean electrical conductivity values of groundwater (i.e. 358 µS·cm^{-1}, N=98), and surface water (i.e. 97 µS·cm^{-1}, N=55).

In addition to the dilution factor, the model must consider the time (τ) since the surface water infiltrated the floodplain. Based on the mean hydraulic conductivity (53.40 m·day^{-1}; Table 1) and the maximum distance in the floodplain (530 m), τ varies between 0 and 10 days.

The following mass balance (Eq. 1) allow the estimation of the groundwater residence time within the shallow aquifer (Eq. 2):

(1) $$^{222}Rn_t = f_{GW}\left({}^{222}Rn_{GW_0}e^{-\lambda t} + {}^{222}Rn_{sup}\left(1 - e^{-\lambda t}\right)\right)$$
$$+(1 - f_{GW})\left({}^{222}Rn_{sup}\left(1 - e^{-\lambda \tau}\right)\right)$$

(2) $$t = -\frac{1}{\lambda} \times ln\left(\frac{{}^{222}Rn_t - {}^{222}Rn_{sup}(1 - f_{GW})\left(1 - e^{-\lambda \tau}\right) - f_{GW} \times {}^{222}Rn_{sup}}{f_{GW}\left({}^{222}Rn_{GW_0} - {}^{222}Rn_{sup}\right)}\right)$$

where λ is the ^{222}Rn decay constant ($\lambda = 0.181$ day^{-1}); ^{222}Rn$_t$, ^{222}Rn$_{sup}$, and ^{222}Rn$_{GW0}$ correspond to ^{222}Rn activity at sampling time t, where ^{222}Rn$_{sup}$ is the Rn produced by the aquifer material in the floodplain and ^{222}Rn$_{GW0}$ is the radon activity in the groundwater entering in the floodplain by the regional flow. Because τ is not fixed, the calculated results have an incertitude that is relatively large for f_{GW} that tend toward 0 and is negligible for f_{GW} that tend toward 1. Due to its exponential form in the equation, incertitude is well delimited even if τ tends to the infinite. The figure 16 summarizes the approach to resolve the equation and estimate t. Residence times are thus independent of the hydraulic gradients and they combine lateral and vertical groundwater movements indiscriminately.
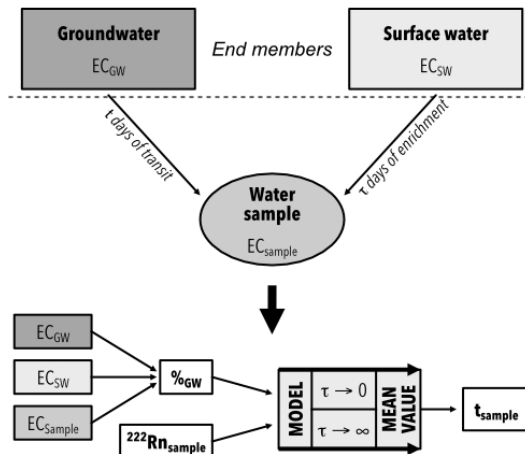
Figure 16. Schematic representation of the residence time model taking into account the dilution rate by surface water obtained with electrical conductivity (EC).

1.6.3.2   Groundwater residence time within the shallow aquifer

Fig. 17 illustrates groundwater residence time variability in both time and space. Groundwater residence times in the floodplain vary from a minimum of 1.4 days near the upstream reference point (D279 collected in May 2017) to a maximum of 14 days in D885 and D852 in the downstream part of the floodplain (samples collected in September 2014). The mean estimated residence time is 7.6 ± 2.6 days. These values are in the range as those obtained with minimum and maximum hydraulic conductivities for the maximum distance in the floodplain (530 m) between 1.9 and 42.3 days and with a mean value of 9.9 days. These calculated residence times show heterogeneous temporal variations among piezometers (Fig. 17b). Except for D755 with a very low interquartile value of 0.48 days, all piezometers from the upstream point to D786 showed medium interquartile ranges of 1.5 to 2.6 days.
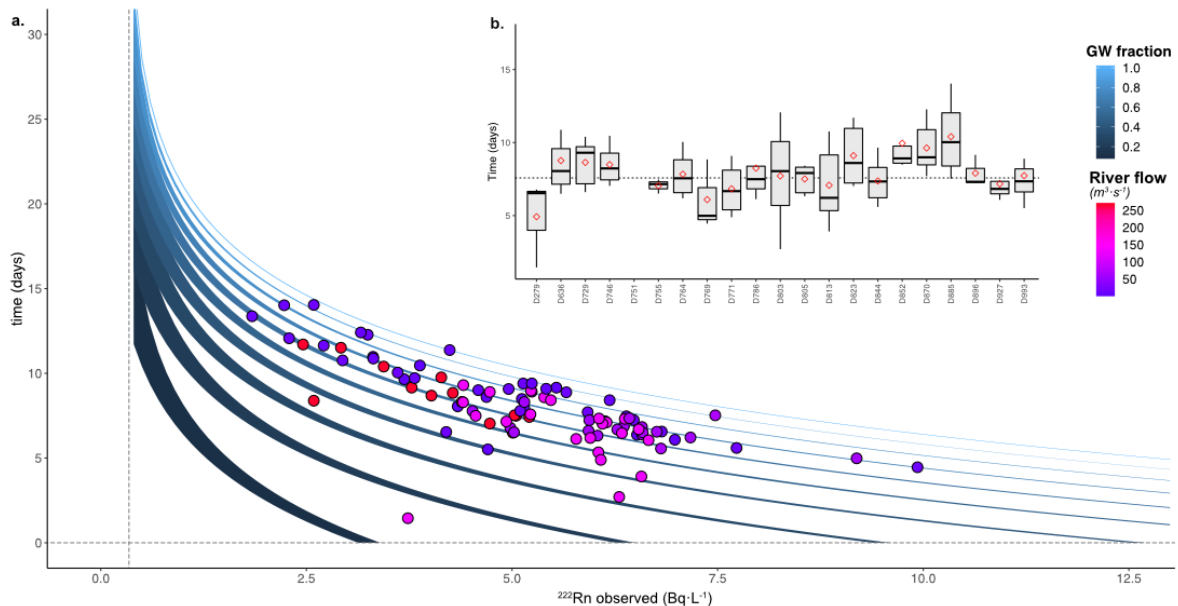
Figure 17. Residence time model based on equation (2). (a) The blue curved areas represent the theoretical times since groundwater entered the floodplain system, with the lighter blue shades representing higher fractions of groundwater. The colored points represent calculated residence times of groundwater in the floodplain for each sample collected at a known river discharge of Matane River. (b) Variations for each piezometer are represented by box plots. The red diamonds represent the mean values for each piezometer, and the black solid lines represent the median values. The horizontal dotted line is the median value calculated in the groundwater floodplain (gauging station GS was excluded).

Piezometers D803 to D885 (except for D805 and D852) had medium and large interquartile ranges, with values from 2.1 to 4.3 days. Piezometers D896 to D993, which are far from the reference upstream point and near the river shore, had low residence time variations, with interquartile values ranging from 0.86 to 1.58 days.

1.6.3.3 Implications for groundwater flowpath in the shallow aquifer and water resource management.

Variations in river discharge involve both wave propagation and mass transfer that directly control the geochemistry and the dynamic of groundwater exchanges in the aquifer system. Such a superposition of floodwave propagation and groundwater displacement has already been proposed to explain differences between estimated groundwater velocities and calculated Darcy velocities in the Matane shallow aquifer (Larocque et al., 2016a). Groundwater residence times in the shallow aquifer are not constant over time. Variations of residence time concerned the entire floodplain up to 200 m from the riverbank as observed with geochemical parameters.

An interesting and counter-intuitive subdivision emerges in the distribution of residence times in respect to river discharge. The range of groundwater residence times in the floodplain system is similar for baseflow (e.g., < 50 $m^3 \cdot s^{-1}$ – 14 % of bankfull discharge) and extremely high (e.g., 250 $m^3 \cdot s^{-1}$ – 71 % of bankfull discharge) river discharges, with residence time ranging from 5 to 14 days. However, the model reveals that for intermediate higher flow — between 28 % and 57 % of bankfull discharge — the minimum and maximum residence times of water in the entire floodplain are inferior to 9 days (Fig. 17a). This decrease of groundwater residence time could be explained by hydrologic equilibration processes. When river discharge rises, surface water infiltrates the shallow aquifer. At the same time, the groundwater in the catchment still feeds the shallow aquifer, leading to modifications in groundwater flow paths or in the magnitude of hydraulic exchanges in order to accommodate both water fluxes. The volume of mixed waters increases and puts pressure

on the deeper aquifer. In reaction, vertical fluxes toward the shallow aquifer could be enhanced after a floodwave propagation (Fig. 15c.). This kind of piston flow movement has been already observed at the boundary of costal aquifer, where the propagation of the tidal dynamic wave (with no mass displacement) induced an upward pumping of fresh groundwater from deeper aquifer (Chaillou et al., 2016; Martin et al., 2007). According to our radon mass balance model, the dynamic of exchanges between shallow and adjacent aquifers also respond to the river discharge. O'Brien and Hendershot (1993) studied the contribution of such groundwater upwelling on the total groundwater discharge to the river and highlighted its importance considering the geochemical composition of river water.

River discharge is a key factor that contributes to control piezometric surface of the shallow aquifer, its geochemistry and the hydrodynamic of surrounding aquifers. The scope of this control is laterally and vertically much larger than the scale of the riverbank. In this way, the results of this study strongly support the hyporheic corridor idea and the freedom space river management approach (Biron et al., 2014; Buffin-Bélanger et al., 2015a). A better understanding of hyporheic corridor dynamics requires the combination of both hydrogeological and geochemical measurements at different sites in the floodplains, not only close to riverbanks. Furthermore, because of the variations in geochemistry in response to river discharge fluctuations, assessments must be repeated for different river stages. This is particularly important for water quality management in individual private and municipal wells.

1.7 CONCLUSION

The objective of this study was to determine how river stage magnitude controls the spatiotemporal variations of shallow floodplain groundwater geochemistry. We conducted a multi-parametric analysis that included discrete measurements of temperature, $\delta^{18}O$, electrical conductivity, and ^{222}Rn activity in a highly instrumented area over nine field campaigns from 2013 to 2017.

A thorough examination of temperature, $\delta^{18}O$, electrical conductivity, and ^{222}Rn in groundwater indicated that the geochemical properties of shallow groundwater varied in space and time. Multivariate statistical analyses (i.e., clustering and canonical redundancy analysis) showed that river discharge is a key factor controlling shallow groundwater geochemistry, whatever the season. Surface water infiltrates into the shallow aquifer in the downstream end of the concave bank leading to a local upstream – downstream hydraulic gradient parallel to the riverbed. This hyporheic zone, as defined as the zone where groundwater mixes with river water, can extend up to 200 m, far from the riverbank and almost 5 times the Matane River width. As for geochemical parameters, groundwater residence times calculated based on a radon mass balance model varied greatly, for 2 to 14 days in the entire floodplain and do not result from the dilution with surface water. Additional inputs from adjacent regional aquifers, including both transversal and vertical groundwater flows, appears to respond to river discharge too. The results of this site-specific scale study strongly support the hyporheic corridor concept. They highlight the need to combine geochemical analysis to hydraulic approaches to protect water resources in private and municipal wells often deployed in alluvial aquifers.

1.8 CREDIT AUTHORSHIP CONTRIBUTION STATEMENT

Antoine Biehler: Conceptualization, Methodology, Validation, Formal analysis, Investigation, Writing - original draft, Writing - review & editing, Visualization. **Gwénaëlle Chaillou:** Conceptualization, Validation, Resources, Writing - review & editing, Supervision. **Thomas Buffin-Bélanger:** Writing - review & editing, Supervision. **Paul Baudron:** Writing - review & editing, Supervision.

1.9 DECLARATION OF COMPETING INTEREST

The authors declare that they have no known competing financial interests or personal relationships that could have appeared to influence the work reported in this paper.

1.10 ACKNOWLEDGEMENT

CHAPITRE 2

CONTRIBUTION DES DÉCHARGES D'EAU SOUTERRAINE AU CARBONE INORGANIQUE DISSOUS ET AUX EMISSIONS DE CO_2 DEPUIS LES RIVIÈRES

2.1   RÉSUMÉ

Les rivières agissent comme des sources de CO_2 à l'atmosphère et une part du carbone inorganique impliqué dans ce flux provient de la connectivité entre les aquifères et les rivières au travers de décharges d'eau souterraine vers les eaux de surface. L'objectif de cette étude est de quantifier les décharges d'eau souterraine vers la rivière et d'estimer les apports externes associés de carbone, à la fois sous forme de carbone inorganique dissous (DIC) et sous forme de CO_2 gazeux au niveau de la rivière Matane (Qc, Canada). Deux approches basées sur des bilans de masses de radon, et sur des mesures de concentration en DIC, d'alcalinité totale, de pH, et de pressions partielles en CO_2 ont été développées pour quantifier les décharges d'eau souterraine et des flux de DIC et de CO_2 associés à hautes (< 1km), et basses (> 1km) résolutions. Les décharges d'eau souterraine sont hétérogènes le long des chenaux avec des apports moyens normalisés de 2,9 à 54,7 $m^3 \cdot jour^{-1} \cdot m^{-1}$ selon l'échelle de mesure. Les flux associés de DIC varient de 6,8 à 140,3 $mol \cdot jour^{-1} \cdot m^{-1}$ et correspondent à moins de 13 % du DIC total transporté par la rivière. Cependant, concernant le CO_2, la contribution des eaux souterraines aux flux de dégazage atteint de 73 % à 300 % du flux mesuré dans la rivière. La comparaison du flux excédentaire de CO_2 issu des eaux souterraines avec le flux total de CO_2 mesuré dans la rivière souligne un probable dégazage instantané de CO_2 dès que l'eau souterraine se décharge dans les eaux de surface. Ces résultats mettent en évidence le rôle fondamental des eaux souterraines dans le cycle du carbone inorganique en rivière en région subarctique, et particulièrement dans le dégazage du CO_2 vers l'atmosphère. De telles quantifications sont particulièrement importantes dans

les systèmes nordiques où d'importants changements dans les conditions hydroclimatiques et dans le stockage du carbone terrestre sont en cours.

Cet article, intitulé « *Groundwater discharge contribution to DIC and riverine carbon emissions* » a été soumis pour publication dans la revue *Biogeochemistry*. L'article est en révision suite à son acceptation par l'éditeur sous réserve de modifications majeures. Cet article s'accompagnera de la publication de la base de données géochimique traitée ici dans le répertoire Pangaea.de sous le titre « *Geochemical data collected in river water and shallow groundwater in a subarctic region (Matane river, QC, Canada)* » (doi : doi.pangaea.de/10.1594/PANGAEA.944092). Cette base de données a déjà passé le processus de révision, mais son accès reste cependant restreint dans l'attente de l'acceptation définitive de cet article pour publication.

Contribution des auteurs :

Cet article a été corédigé par moi-même ainsi que les professeurs Gwénaëlle Chaillou, Thomas Buffin-Bélanger, et Paul Baudron. En tant que premier auteur, j'ai contribué à l'essentiel de la recherche de conceptualisation, de développement de la méthodologie, de prélèvements sur le terrain, d'analyse des données, de leur interprétation, de productions de figures, et de rédaction de la première version de l'article. Ce travail de conceptualisation et de prélèvement de terrain a été réalisé en collaboration avec l'ensemble des coauteurs qui ont tous contribué par leurs révisions et propositions à la version finale de l'article.

Communications :

Une version préliminaire et abrégée de cet article a été présentée sous forme d'une présentation orale lors du 44e congrès annuel de l'IAH à Dubrovnik en septembre 2017 :

Biehler, A., Chaillou, G., Baudron, P., & Buffin-Bélanger T. (2017). *Biogeochemical connectivity in aquifer-river continuum - Use of in situ ^{222}Rn and PCO_2 measurements in the study of CO_2 outgassing induced by groundwater discharges in river*. 44th Annual Congress of the International Association of Hydrogeologists, Dubrovnik (Croatia), September 2017

2.2 GROUNDWATER DISCHARGE CONTRIBUTION TO DIC AND RIVERINE CARBON EMISSIONS

Antoine Biehler[a], Thomas Buffin-Bélanger[a], Paul Baudron[b], Gwénaëlle Chaillou[c]

[a] *Université du Québec à Rimouski, 300 allée des Ursulines, Rimouski, Québec G5L 3A1, Canada*
[b] *Institut pour la Recherche et le Développement, UMR G-EAU, 34090 Montpellier, France ; Polytechnique Montréal, 2500 chemin de Polytechnique, Montréal (Québec), Canada, H3T 1J4*
[c] *Institut des Sciences de la Mer de Rimouski, Université du Québec à Rimouski, 310 allée des Ursulines, Rimouski, Québec G5L 3A1, Canada*

Abstract: Rivers act as a source of CO_2 to the atmosphere and some of the implied inorganic carbon comes from the aquifer-river connectivity through groundwater discharges to surface water. This study aims to quantify groundwater discharge entering the stream and to estimate this external input to the riverine inorganic carbon cycle, as both dissolved inorganic carbon (DIC) and CO_2 in the Matane River (Qc, Canada). Two approaches based on radon (^{222}Rn) mass balance models, DIC, total alkalinity, pH and $P$$CO_2$ measurements were developed to quantify groundwater discharges and associated DIC and CO_2 fluxes at a high- (<1km) and low- (>1km) resolution scales. Groundwater discharges were heterogeneous along the riverbed with mean linear inputs varying from 2.9 to 54.7 $m^3 \cdot day^{-1} \cdot m^{-1}$ depending on the scale. The associated fluxes of DIC ranged between 6.8 and 140.3 $mol \cdot day^{-1} \cdot m^{-1}$ and corresponded to only less than 13% of the total DIC transported by the river. Regarding CO_2, however, the contribution of groundwater to CO_2 outgassing fluxes reached 73% to 300%. Exceeding groundwater-derived CO_2 flux compared to the total CO_2 flux from the river probably highlights the instantaneous outgassing of CO_2 as soon as groundwater discharges to the surface water. These results shed light on the key role of groundwater in the riverine inorganic carbon cycle in a subarctic region, and specifically in the CO_2 evasion to the atmosphere. Such quantifications are particularly important in northern systems where important changes in hydroclimatic conditions and terrestrial carbon storage are undergoing and are expected to continue to undergo.

Keywords: Groundwater discharges; River; CO_2 emission; Radon-based model; Dissolved inorganic carbon

2.3 INTRODUCTION

In the land to sea continuum, fluvial systems encompasse complex terrestrial carbon dynamics by which it can be sequestered in the sediment, exported to the ocean, or exchanged directly with the atmosphere (Cole et al., 2007). Estimated to be in the order of 0.75 Pg·C·year^{-1} of CO_2 by Cole et al. (2007), global emissions from inland waters to the atmosphere have been re-evaluated in 2013 to be almost three times higher at 2.1 Pg·C·year^{-1} (Raymond et al., 2013). Over the past decades, there is an increasing interest to accurately quantify the global degassing flux from inland water to the atmosphere, and especially from rivers and their catchment. Nevertheless, a better global quantification requires local-scale studies under different geological and climatic conditions, specifically in regions where hydroclimatic changes have so far been more intense than the global average as in subarctic regions (Milly et al., 2005; St Jacques and Sauchyn, 2009).

In streams, CO_2 is mainly produced by in-stream heterotrophic mineralization and photo-oxidation of organic carbon (Cole and Caraco, 2001; Duarte and Prairie, 2005; Hotchkiss et al., 2015) as well as by CO_2 input via groundwater discharge (Crawford et al., 2014; Deirmendjian and Abril, 2018; Duvert et al., 2018). The advection and production of dissolved inorganic carbon (DIC) in streams likely induce CO_2 oversaturation (Hope et al., 1994; Hotchkiss et al., 2015; Kling et al., 1991). Based on a database of around 12 000 sampling locations in rivers and lakes around the world describing inorganic carbon cycle (from Hartmann et al., 2019) and PCO_2 values derived from alkalinity-pH calculation, Regnier et al. (2013) estimated that 96 % of inland surface waters are CO_2 oversaturated. Whatever the climatic conditions, *in-situ* studies carried out at a site-specific scale globally report a CO_2 oversaturation of waters in rivers found in subarctic (Kling et al., 1991; Rasilo et al., 2017; Wallin et al., 2013), temperate (Butman and Raymond, 2011; Deirmendjian and Abril, 2018), and tropical (Mayorga et al., 2005; Richey et al., 2002) regions. Discriminating the origin of CO_2 is, however, not trivial, but it is a necessary step to future carbon cycle

modelling exercises. Because of the large inputs of groundwater and of the high organic carbon content in soils, the contribution of external CO_2 is supposed to be high in headwater streams (Battin et al., 2008; Hotchkiss et al., 2015; Jones and Mulholland, 1998). In addition, the groundwater chemistry may greatly influence the CO_2 saturation in drought season as seeping groundwater supports stream baseflow.

Several studies have already shown that groundwater supersaturated in CO_2 could be the main source of surface water CO_2 to rivers (Butman and Raymond, 2011; Jones and Mulholland, 1998; Öquist et al., 2009; Teodoru et al., 2009). Most of this carbon (10 to 100% according to Cole et al., 2007) quickly escapes to the atmosphere within a couple of hundred meters from entering the stream (Öquist et al., 2009). Such data supports the idea of high connectivity between streams, their catchment and the global carbon cycle (Maberly et al., 2013). It implies that CO_2 emissions from streams are highly sensitive to terrestrial processes such as subsurface processes (*e.g.* aquifer recharge, groundwater geochemistry and weathering) together with catchment and land use management. Quantifying groundwater discharge to rivers is then needed to determine the fraction of the CO_2 flux to the atmosphere attributable to aquifer-river connectivity.

Different methods are used to quantify the groundwater entering the stream (Cook, 2015). Differential gauging along a stream is a common one (Deirmendjian and Abril, 2018; Duvert et al., 2018). However, its accuracy depends on the precision of river flow measurements and on a robust quantification of all the other fluxes including evapotranspiration, runoff, and potential pumping (Cook, 2015; Schmadel et al., 2010). Over the last decades, geochemical groundwater proxies have been developed to map and quantify groundwater discharge. These geochemical proxies include, for example, the use of temperature, electrical conductivity, the mass balance of silica concentrations (Winterdahl et al., 2016), and the determination of chlorofluorocarbon concentrations (Bohlke and Denver, 1995; Cook et al., 2003) and radon activities (Baudron et al., 2015; Cook et al., 2006; Duvert et al., 2019; Genereux and Hemond, 1990). Radon (^{222}Rn, $T_{1/2}$ = 3.82 days) is a natural radioactive isotope produced in the aquifer material as a result of a-recoil from the decay of

its parent isotope radium (^{226}Ra). Its conservative and chemically stable nature, together with its higher activities in groundwater than in most surface waters (~2 - 3 orders of magnitude) allow it to be used as a tracer of exchange processes between groundwater and surface water (Burnett et al., 2010). The concomitant use of ^{222}Rn activities with DIC concentrations and carbonate buffering capacity is useful to quantify the terrestrial CO_2 input to stream and its contribution to CO_2 degassing to the atmosphere (Duvert et al., 2019; Sadat-Noori et al., 2015; Taillardat et al., 2018).

Most groundwater discharge studies are conducted using large spatial resolutions, with surface water samples taken every kilometer or tens of kilometers, and over large river corridors or catchments (Fleckenstein et al., 2010). In doing so, these studies apply a single value over a large portion of the river corridor, regardless of local hydrogeomorphologic changes. Nonetheless, streambed attributes (Calver, 2001; Kennedy et al., 2008) and geochemical parameters can vary greatly along the stream with some geochemical hotspots where chemical reactions are higher (see McClain et al., 2003 and Vidon et al., 2010 for hotspot definition). These locations are crucial for stream water chemistry and need to be integrated into a mass balance approach to quantify groundwater-derived CO_2 fluxes. Thus, depending on the measurement resolutions and the sampling location (*i.e.* proximity to potential hot spots), interpolating the data to large corridors could induce overestimation or underestimation of fluxes on the transect.

The objective of this study is to estimate the contribution of the aquifer-river connectivity to stream inorganic carbon as both DIC and gaseous CO_2 in a subarctic river. To do so, we determined groundwater-derived DIC fluxes at two spatial configurations having different scales and resolutions along the Matane River (Qc, Canada): the first estimation was done along a ~800 m long meander at a high spatial resolution, and the second was along a ~60 km long corridor at a low spatial resolution. Based on ^{222}Rn activities and carbonate parameters (DIC, total alkalinity (TA) and pH_{NBS}) measured in groundwater and surface water samples, we explored the spatial variability of groundwater fluxes entering the stream at the two studied spatial configurations. The results were compared and validated

with hydrologic flows obtained by hydrodynamic calculations. Finally, carbonate parameters were used to calculate $P\text{CO}_2$ in surface waters, and CO_2 degassing was estimated using an empirical approach. These results are the first methodological step to directly determine the contribution of groundwater to riverine CO_2 emissions. According to our knowledge, it is also the first estimation shedding light on the Matane River, a subarctic river acting as a source of CO_2 to the atmosphere.

2.4   MATERIEL AND METHOD

2.4.1   Study sites and hydrogeological context

This study was conducted in the Matane River Valley, located in the northwest of Gaspe Peninsula (Quebec, Canada, Fig. 18) between the Chic-Chocs Mountain (Appalachian orogen) and the St. Lawrence Estuary. The river drains a 1 678 km² catchment that is mainly forested (~90 %) and composed of shales, fine sandstones, and limestones (Marchand, 2013; Ollerenshaw, 1967). In the valley, these rocks are overlaid by on average 50 m of quaternary fluvial and glaciofluvial deposits composed of pebbles, gravel and coarse sands (Buffin-Bélanger et al., 2015c). This thick sedimentary layer acts as an unconfined aquifer with relatively high hydraulic conductivity (13 to 265 m·day⁻¹) and is recognized as one of the most productive aquifers in the Bas-Saint-Laurent region (Buffin-Bélanger et al., 2015c). Groundwater is characterized by a Ca-HCO_3 geochemical facies with a neutral pH (Biehler et al., 2020; Buffin-Bélanger et al., 2015b). Most of this groundwater originated by recharge from modern precipitations, mostly from the spring melting of the snow cover (Chaillou et al. 2018).

The Matane river channel has an average width of 55 m with a mean floodplain width of 475 m and an average slope of 0.2 m·100 m⁻¹ (Biron et al., 2014; Marchand, 2013). Its mean annual discharge is 39 m³·s⁻¹ (in the 1929-2021 period). The estimated bankfull discharge reaches 350 m³·s⁻¹ and occurs mostly during the spring period (Buffin-Bélanger et

al., 2015c; Cloutier et al., 2014). The baseflow discharge is on the order of ~5 m^3·s^{-1} and can occur during the winter or summer low-flow period (Buffin-Bélanger et al., 2015c).

Recent studies have examined closely the dynamics of groundwater - surface water connectivity in a meandering zone of the Matane river where groundwater springs were observed through the river bed sediment (as shown in Online Ressource 1[2]) suggesting strong connectivity (Biehler et al., 2020; Buffin-Bélanger et al., 2015c; Cloutier et al., 2014).
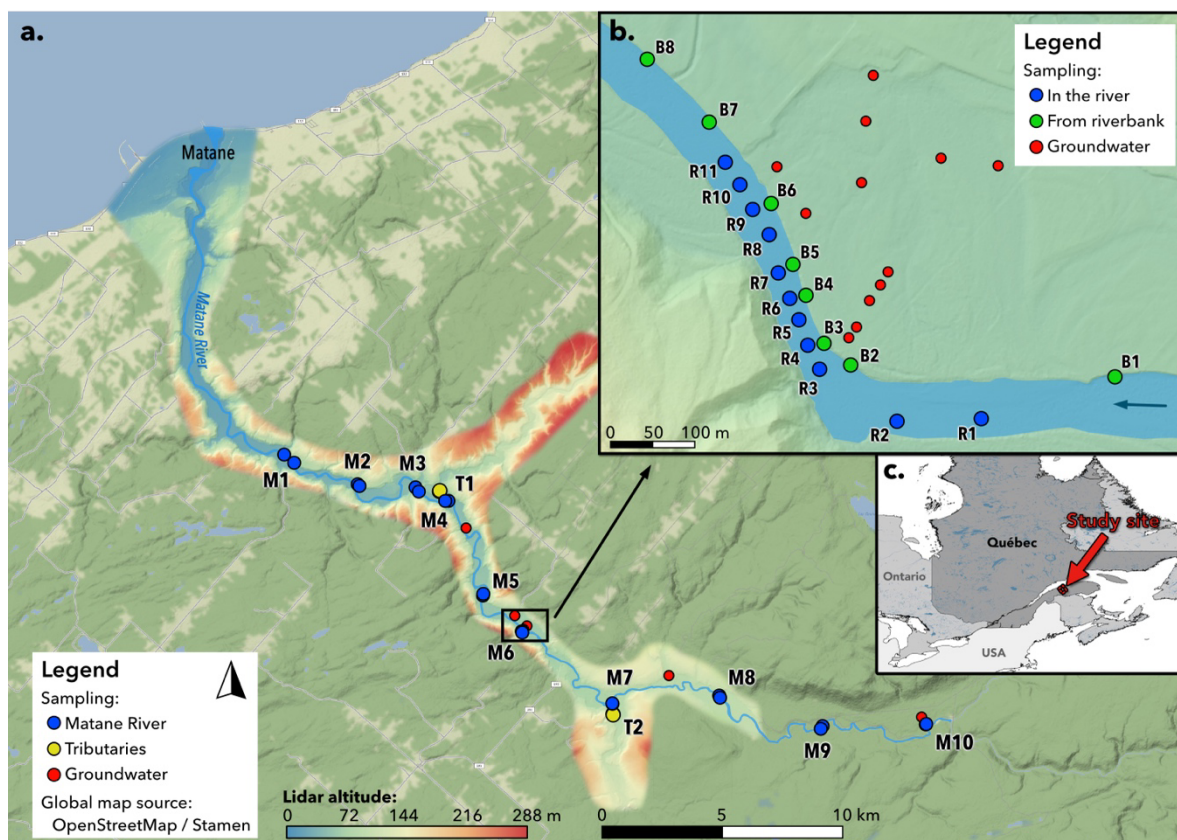
Figure 18. Location of the different sampling sites in the Matane River (a.) for the July campaign at a river corridor scale and (b.) for the August campaign at the meander scale. Topography of Matane and mains tributaries valleys have been determined by a Lidar survey undertaken in 2009 (24 cm resolution). Matane River is located in the Quebec province in Canada (c.).

---

[2] See the Online Ressource at :
https://youtu.be/b8CzFts_LwQ

2.4.2 Sampling approaches

Our study focused on the summer baseflow river stage when groundwater contributions dominate the river flow and when the hyporheic extension is minimal (Biehler et al., 2020). Groundwater discharges and their impact on the river CO_2 degassing fluxes were studied at two different spatial configurations (Fig. 19) with dedicated sampling campaigns in July 2017 (corridor scale; low spatial resolution) and August 2017 (meander scale; high spatial resolution). For both campaigns, the average external temperature was 17.6 °C and the mean river discharges of the Matane River were similar, i.e. 6.3 $m^3 \cdot s^{-1}$ in July 2017 (07/26 to 07/27) and 6.8 $m^3 \cdot s^{-1}$ in August 2017 (08/23 to 08/25). River water levels remained stable a week before each campaign. The Strahler order (6) remains the same along the studied river corridor.
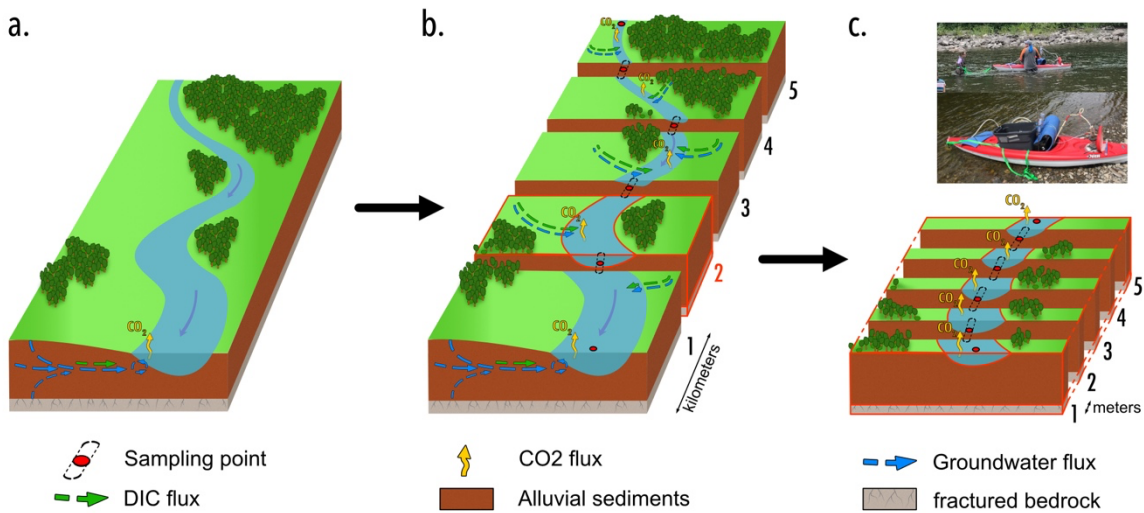
Figure 19. Schematic diagrams presenting the theoretical division of the river (a) in two spatial configurations (panels b and c) where the ^{222}Rn-based model was applied. (b) The river corridor scale in which subsystems are river sections of several km in length. (c) The meander scale in which subsystems are river sections of several m in length. Red circle represents the location of the sampling that determine the inputs and outputs of each subsystem. In c. the photographs illustrated the measurement method in the meander.

2.4.3 Corridor scale and low-resolution study

For this spatial configuration, the groundwater discharge quantification was performed along 64 km of the river (from kilometers 26 to 84 upstream from the mouth of the Matane River; Fig. 18a) at eleven sampling sites dividing the river corridor into 10 river sections. The locations of the sampling sites were determined based on the geomorphology of the river sections (grain sizes, morphologies and river planform geometry) in order to have geomorphologically homogeneous reaches. River sections length varied from 2 to 10 km (Fig. 19b). At each sampling site, river discharge was measured and was used to represent both discharges at the downstream end of a river section (output: Q_o in $m^3 \cdot s^{-1}$) and discharge at the upstream end of the next river section (input: Q_i in $m^3 \cdot s^{-1}$). Discharges were measured using a RiverSurveyor (M9 mounted on a trimaran accessory, SonTek Inc., 4 to 6 transect repetitions by measurement with an accuracy of 5%). Ancillary parameters including electrical conductivity (EC), temperature (T), and pH (NBS calibrated pH probe) were measured *in-situ* at each site using a calibrated multiparametric probe (600QS, YSI Inc.). Surface water samples (~50 cm below the surface) were pumped in the center of the stream for measurements of radon isotope (^{222}Rn), and total alkalinity (TA). For radon isotope (^{222}Rn), water samples were collected in 2 L plastic bottles that were tightly sealed for further analysis (see next section for details). For TA samples, water was filtered on-line onto a 0.45 µm Whatman Polycap cartridge and stored in 250 mL polyethylene bottles. At each sampling site (from M1 to M10, Fig. 18a), these measures were carried out both in a pool (deep stretch with low water velocity) and in a riffle (high depth with high water velocity) and the results were averaged to better represent the geochemistry of river sections extremities. Two tributaries (the *Petite Rivière Matane* and the *Tamagodi* river, T1 and T2 respectively in Fig. 18a) were also sampled near their mouth. The ancillary parameters, ^{222}Rn, and TA were sampled as described above.

In addition, groundwater was collected in four private surface wells and in two piezometers (Fig. 18a). These piezometers were located in the top 3 meters of the unconfined aquifer and allowed to collect shallow groundwater only. The sampling followed the protocol

from Biehler et al. (2020) and can be summarized by 3 steps. First, wells and piezometers were purged for 10-15 minutes to ensure the complete renewal of the groundwater in the well. Groundwater was then pumped into an online flow cell where EC, pH, and temperature were monitored using a calibrated multiparametric probe (600QS, YSI Inc.). Finally, after these parameters stabilized, groundwater was sampled like surface water to further analyze dissolved inorganic carbon, TA, and ^{222}Rn activity. The latter were sampled as described earlier.

2.4.4   Meander scale and high-resolution study

For this spatial configuration, a well-known meander section of the Matane River was sampled to quantify groundwater discharges (sample site M6, Fig. 18b, Fig. 19c). This 17.8 ha meander is located 30 km from the mouth of the Matane River. River discharge was measured upstream and downstream the meander with a Flow Tracker (Handheld-ADV, SonTek Inc.) at the beginning of the campaign. Flow velocity measurements were undertaken at a meter resolution along a transversal transect at 0.4 of the flow depth and partial discharges were added across the transect to calculate the total river discharge. Nineteen surface water samples were collected along the 844 m-long meander to measure ^{222}Rn, TA, $P\mathrm{CO_2}$ and DIC. Samples from R1 to R11 were continuously measured for ^{222}Rn and $P\mathrm{CO_2}$ in the middle of the river while B1 to B8 were sampled near the point bar (i.e. the concave riverbank where sedimentary deposits accumulate; Fig. 18b). In both cases, a submersible pump was used to collect surface water at 50 cm below the surface. Physico-chemical parameters and TA were sampled as described above. In addition, DIC samples were hermetically closed with a Teflon rubber cramped with an aluminum ferrule. A 0.2 mL of HgCl$_2$ solution (7 mg·L^{-1}) was added into the bottle. In parallel, *in-situ* and continuous measurements of ^{222}Rn and $P\mathrm{CO_2}$ were also performed for R1 to R11. The *in-situ* technique is detailed in the next section. For B1 to B8, ^{222}Rn was also measured in 2 L-plastic bottles as described above.

In this meander site, the array of 21 shallow piezometers (< 3 m depth) was previously inserted in the floodplain (Buffin-Bélanger et al., 2015c; Cloutier et al., 2014). Details on the exact position, depth and hydraulic conductivities are reported in Biehler et al. (2020). Briefly, piezometers were made from 38 mm polymerized vinyl chloride pipes sealed at the base and equipped with a 0.3 m screen at their bottom end (~3 m below the surface). They were inserted to depths ranging from 56 to 59 m near or below the altitude of the riverbed (located at 58 m). Each piezometer was instrumented with automated level loggers (Hobo U20-001 – one measurement by piezometers every 15 minutes). Groundwater was collected in 12 piezometers (Fig. 18b) as described earlier to analyze ^{222}Rn, TA, and DIC.

2.4.5   Analytical methods

2.4.5.1   Radon measurements

Radon is considered as a tracer of groundwater interaction with the aquifer matrix (Burnett et al., 2001; Ortega et al., 2015). ^{222}Rn activities were measured using RAD7 Radon Detector (Durridge Inc.) equipped with the RAD*Aqua* or the RAD*H$_2$O BigBottle* accessories. With these techniques, radon is outgassed from water by continuous pumping in a showerhead-type exchanger, or sampled in discrete 2 L plastic bottles (see Biehler et al., 2020 for details on the RAD7 techniques). For discrete samplings (*BigBottle* technique), radon activities were corrected for radioactive decay between the sampling and the analysis. Mean analytical uncertainties (2σ) for RAD*Aqua* and RAD*H$_2$O Bigbottle* techniques were 5 % (N=4) and 19 % (N=54) respectively for groundwater. In surface water, those uncertainties increased to 13 % (N=16) and 29 % (N=42) respectively. Biehler et al. (2020) showed that for samples with radon activities higher than 1 Bq·L^{-1}, the two techniques gave similar results with a relative error of ± 7%. However, for samples with low radon activity (< 1 Bq·L^{-1}), as in surface water samples, the relative error reached ± 27%.

2.4.5.2   Carbonate system

pH was measured using the multiparameter probe 600QS (YSI Inc.) equipped with a glass combination electrode pH sensor. Accuracy of the sensor is ± 0.2 pH units with a resolution of 0.01 pH units. The probe was regularly calibrated with three NBS (National Bureau of Standards) buffers with known pH values (4.00, 7.00, and 10.00). pH values have then been converted from NBS to free scale for latter calculations.

Dissolved inorganic carbon ($DIC = CO_2 + HCO_3^- + CO_3^{2-}$) was analyzed using the flow injection analysis technique based on the method proposed by Hall and Aller, (1992). A gas-permeable membrane is used to remove CO_2 from acidic reagent streams to a basic receiving stream and conductivity detector. The calibration was done using a reagent grade sodium bicarbonate ($NaHCO_3$) solution, and the conductivity response was linear for samples over DIC concentrations from < 0.2 to 20 mmol/L with a precision of ~1 %.

Total alkalinity was measured by a GRAN titration on 50 mL water samples with a Metrohm 848 Titrino Plus device. The internal standard used to correct raw alkalinity data was calibrated by comparison with a Dickson certified reference material (Batch 154). Mean analytical uncertainties were 0.2 % (N=27) and 3.0 % (N=20) for July and August campaigns, respectively.

PCO_2 was measured *in-situ* for a part of the samples, including most of the surface water samples. A PCO_2 logger (CM-0001, CO2Meter, Inc) was inserted in the RAD*Aqua* closed loop as proposed by Santos et al., (2012). Briefly, CO_2 has outgassed in a showerhead-type gas exchanger and the resulting air was drying out in a drierite unit and pumped into a closed loop including the RAD7 detector and the CO_2 data logger. The PCO_2 logger is equipped with a non-dispersive infrared sensor (Hunt et al., 2011) with a measuring range of 0 to 10 000 ppm and a ± 3 % accuracy.

2.4.5.3   Data processing and calculations

A mixture of inorganic and organic bases and acids make up the total alkalinity. It is calculated as follows (equation 1):

$$TA = [HCO_3^-] + 2[CO_3^{2-}] + [B(OH)_4] + [OH^-] + [HPO_4^{2-}] + 2[PO_4^{3-}] +$$
$$[H_3SiO_4^-] + 2[H_2SiO_4^{2-}] + [HS^-] + 2[S^-] + [NH_3^+] + [Org^-] - [H^+] - [H_3PO_4] \ (1)$$

In freshwater, where dissolved organic matter and fulvic acids concentrations are high, the non-carbonated fraction of TA (also labelled NCA for non-carbonated alkalinity) may be an important component of TA (Abril et al., 2015). In natural systems where concentrations of organic matter are expected to be high, the quantification of NCA is then necessary to accurately estimate DIC speciation, PCO$_2$ and thus CO$_2$ degassing fluxes from TA. NCA can be indirectly estimated as the difference between TA measured by direct titration and TA calculated theoretically from the DIC-pH pair corrected with temperature (Hunt et al., 2011).

When *in-situ* PCO$_2$ measurements could not be undertaken, calculated values were calculated as follows. Measured pH, DIC, and TA were input to the freshwater compatible R package "Aquaenv" (Hofmann et al., 2016) for experimental aquatic chemistry, a program that focused on acidification and CO$_2$ air-water exchange. The dissociation constants of carbonic acid (K1 and K2) used are from Millero et al. (2006). The range of salinity for these constants is 0.1 to 50 and between 1°C and 50°C for temperature. According to Abril et al. (2015), because the contribution of NCA to TA is not known, the use of DIC and pH pair was prioritized for PCO$_2$ calculation. Nevertheless, when DIC was absent (i.e. for the low spatial resolution approach), the TA – pH pair was used. Based on the meaning gap between measured and calculated TA (from DIC and pH) for our entire database (N=90 samples collected in 2017 including other sampling campaigns), we assumed a 23 % of uncertainty on the calculated result linked to an unknown NCA contribution in the water samples. Calculated PCO$_2$ using the two couples were significantly correlated (N=55; p-value < 0.01) with a spearman correlation coefficient of 0.89. For the entire database, calculated and

measured PCO_2 are significantly correlated (p-value < 0.01) with correlation coefficients of 0.67 and 0.41 for calculation made by TA – pH and DIC – pH pairs, respectively.

A [222]Rn mass balance was used to quantify the groundwater discharge (Q_{GW}) to the surface water. Radon-based models were developed in several river studies such as in the Mundo River (Spain, Ortega et al., 2015) and the Ichetucknee River (USA, Khadka et al., 2017). In these latter studies, the authors quantified spatial variations of groundwater inputs after conducting a longitudinal radon survey at a catchment scale and at a fine-scale, respectively. Here, we used two spatial configurations (corridor scale and low spatial resolution; meander scale and high spatial resolution) and we assumed steady-state conditions in each river section. For both spatial configurations, each sampling site is the downstream end of a river section and the upstream end of the river section downstream (Fig. 19). Following a proposition by Khadka et al. (2017), groundwater discharges (Q_{GW}) were calculated in each river section as follows:

$$Q_{GW} = \frac{Q_0 Rn_0 + F_{atm} + F_{dec} + F_{evp} + F_{dif} - Q_i Rn_i - Q_{sp} Rn_{sp} - F_{pro} - F_h}{Rn_{GW}} \quad (2)$$

where Q_0 is the river discharge at the downstream end of the river section; Q_i the discharge at the upstream end of the river section; Q_{sp} is the river discharge from tributaries; and Q_{GW} is the groundwater discharge. All of those are expressed in $m^3 \cdot s^{-1}$. Rn_0, Rn_i, Rn_{sp}, and Rn_{GW} are radon activities measured downstream, upstream, in tributaries, and in groundwater respectively. Radon activities are expressed in $Bq \cdot m^{-3}$. Radon fluxes linked to radioactive decay (F_{dec}), outgassing (F_{atm}), river water evaporation (F_{evp}), diffusivity from riverbed sediment (F_{dif}), production in the water column (F_{pro}); and hyporheic water exchanges to the river (F_h) were calculated for each river section and expressed in $Bq \cdot s^{-1}$.

F_{dec} was calculated from [222]Rn activity measured upstream with the decay constant of [222]Rn (lambda$= 2.098 \times 10^{-6}$ s^{-1}) and the volume of water in the considered river section. F_{atm} was calculated using the volume of water and the gas transfer velocity for radon. This parameter was empirically calculated as a function of physical characteristics of rivers and depends on the diffusivity constant of radon, water velocity, water temperature, and river

depth (Khadka et al., 2017). F_{dif} was calculated from riverbed sediment porosity (0.25 for gravel sediments; Leopold et al., 1964) and molecular diffusion coefficient of radon (Khadka et al., 2017; Ullman and Aller, 1982). Because of the large width of the hyporheic zone along the Matane River (Biehler et al., 2020), hyporheic fluxes of radon is largely mixed with radon inputs from shallow groundwater in the floodplain. Then here, F_h were included as part of the total groundwater discharge flux to river. Here, as in Ortega et al. (2015), radioactive production from dissolved radium (F_{pro}) was not considered due to the expected small concentration of dissolved radium in fresh water. In the same way, the loss of ^{222}Rn by evaporation (F_{evp}) is considered as negligible because of its extremely low value compared to the gas transfer velocity value for radon (Cook et al., 2006). Parameters used in the ^{222}Rn mass-balance models are reported in Table 4 and Table 5 for the corridor and meander scales respectively.

2.4.6   Calculations of carbon fluxes

Total dissolved inorganic carbon fluxes from groundwater to the river ($F_{C_{GW \to R}}^{syst}$ in g·C·day^{-1}) were calculated using groundwater discharge (Q_{GW} in m^3·s^{-1}) obtained by equation 2 and the mean concentration of DIC (in g·m^{-3}) measured in the surrounding aquifer ($[\widetilde{C}]_{GW}$):

$$F_{C_{GW \to R}}^{syst} = Q_{GW} \times [\widetilde{C}]_{GW} \text{ (3)}$$

This value was then normalized to the length of the river section to obtain a DIC flux from groundwater to the river by unit of river length (in g·C·day^{-1}·m^{-1}).

Carbon flux from river to the atmosphere was calculated from gas transfer velocity (k_{CO_2} in m·day^{-1}) and the difference between mean carbon concentration (from CO$_2$) in the river ($[\widetilde{C_{CO_2}}]_R$) and carbon concentration in the atmosphere ($[C_{CO_2}]_{Atm}$):

$$F_{C_{R \to Atm}}^{syst} = k_{CO_2} \times \left([\widetilde{C_{CO_2}}]_R - [C_{CO_2}]_{Atm} \right) \text{ (4)}$$

Tableau 4. Measured parameters used in the ^{222}Rn-based model and calculated groundwater discharges at the corridor scale for each river section. Width is the average width of each river section (in m). Lengths are in meter and T in °C. Discharges (Q_{riv}, Q_{trib}, and Q_{GW}) are given in m^3·s^{-1} and ^{222}Rn activities (Rn_{riv}, and Rn_{trib}) in Bq·L^{-1}.

Transect	M10 →	M9 →	M8 →	M7 →	M6 →	M5 →	M4 →	M3 →	M2 →	M1
Width	39	47	51	47	51	61	59	54	59	
Length	9193	9917	8637	9149	4313	9112	2149	6282	5363	
T°$_{riv}$	14.86	17.19	19.83	20.11	18.61	18.67	19.12	18.12	17.51	
Q_{riv}	5.1	5.6	6.0	6.0	6.9	6.6	6.6	6.8	6.9	6.9
Rn_{riv}	0.127	0.127	0.267	0.156	0.156	0.397	0.282	0.170	0.176	0.449
Q_{trib}	-	-	-	*0.4*	-	-	*0.9*	-	-	
Rn_{trib}	-	-	-	*0.416*	-	-	*0.030*	-	-	
Q_{GW}	*0.11*	*0.40*	*0.06*	*0.15*	*0.44*	*0.24*	*0*	*0.14*	*0.59*	

Tableau 5. Measured parameters used in the ^{222}Rn-based model and calculated groundwater discharges at the meander scale for each subdivision. Width was set at 46 m for each subdivision. Lengths are in meter and T in °C. Discharges (Q_{riv}, Q_{trib}, and Q_{GW}) are given in m^3·s^{-1} and ^{222}Rn activities (Rn_{riv}, and Rn_{trib}) in Bq·L^{-1}.

Transect	R1 →	R2 →	R3 →	R4 →	R5 →	R6 →	R7 →	R8 →	R9 →	R10 →	R11
Length	209	184	33	66	32	60	65	50	47	98	
T°$_{riv}$	17.78	17.85	18.22	18.36	18.47	18.23	18	17.1	17.1	18	
Q_{riv}	6.08	6.34	6.57	6.61	6.69	6.73	6.81	6.89	6.95	7.01	7.13
Rn_{riv}	0.363	0.333	0.506	0.451	0.390	0.392	0.434	0.406	0.395	0.463	0.470
Q_{GW}	*0*	*0.29*	*0*	*0*	*0.01*	*0.07*	*0*	*0*	*0.12*	*0.04*	

k_{CO_2} was calculated from CO_2 Schmidt number (Raymond et al., 2012; Wanninkhof, 1992) and k_{600} model number 7 of Raymond et al. (2012). This model considers water velocity, riverbed slope, river discharge and river depth. It shows the greatest correlation coefficient between predicted and measured values (see Table 2 in Raymond et al., 2012) and is suitable for river with Strahler order greater than 1. Atmospheric PCO$_2$ was assumed to be 405 ppm. Used parameters value are reported in Table 6.

Tableau 6. Parameters used for the k_{600} calculation and calculated CO_2 emissions (according to Equation 4) for each resolution approach. PCO$_{2\ atm}$ was defined equal to 405 ppm according to the NOAA - globally averaged marine surface 2017 mean data.

Parameter	Unit	Meander scale	Corridor scale
Schmidt Number	$cm^2 \cdot s^{-1}$	662.93	660.22
k_{600}	$m \cdot day^{-1}$	3.57	3.27
[C_{atm}]	ppm	405	405
Flow velocity	$m \cdot s^{-1}$	0.39	0.32
Discharge	$m^3 \cdot s^{-1}$	6.8	6.3
Slope	$m \cdot m^{-1}$	0.0015	0.002
River depth	m	0.4	0.4
CO_2 emission	$mg\ C \cdot day^{-1} \cdot m^{-2}$	529	88

2.5 RESULTS

2.5.1 Geochemical properties for the high-resolution study in the meander

For this spatial configuration, river discharges measured by a flow tracker ranged from 6.4 $m^3 \cdot s^{-1}$ at the upstream end to 7.1 $m^3 \cdot s^{-1}$ at the downstream end of the river section. The statistical calculated uncertainties (Huhta and Sloat, 2007) were of 8% and 11%, respectively. Based on the difference between upstream and downstream flow rate, calculated groundwater discharge was 0.7 $m^3 \cdot s^{-1}$, i.e. ~72 $m^3 \cdot day^{-1}$ by linear meter of river along the 844 m long meander.

The spatial distribution of ^{222}Rn activity, temperature, electrical conductivity, pH, DIC, TA, and PCO$_2$ along the studied meander is shown in Fig. 20. ^{222}Rn activities (Fig. 20a) ranged from 0.22 Bq·L^{-1} to 1.03 Bq·L^{-1}, with a median value of 0.43 Bq·L^{-1} and an interquartile range of 0.15 Bq·L^{-1}. Activities were lowest in the upstream part (maximum of 0.54 Bq·L^{-1} near R1), significantly increased downstream from the meander apex (maximum close to 1 Bq·L^{-1} at the riverbank), and then dropped back at the downstream end of the studied site (0.32 Bq·L^{-1}). ^{222}Rn activities measured in groundwater were higher with a median value of 4.83 Bq·L^{-1} and an interquartile range of 1.59 (Table 7). River water temperatures (Fig. 20b) ranged from 19.3 °C to 17.1 °C, with median value and interquartile range of 18.0 °C and 0.9 °C, respectively and an overall evolution pattern similar to ^{222}Rn. Electrical conductivity (Fig. 20c) increased along the meander, upstream and along the meander apex. The median value was 197 µS·cm^{-1} with an interquartile range of 13 µS·cm^{-1} and a minimum of 175 µS·cm^{-1} near the riverbank. Downstream from the apex, electrical conductivity ranged from 200 to 210 µS·cm^{-1} and continued to increase until a maximum of 217 µS·cm^{-1} at the downstream end of the meander section (median value = 208 µS·cm^{-1}; interquartile range = 5 µS·cm^{-1}). In groundwater, median electrical conductivity was 325 µS·cm^{-1} (interquartile range = 30 µS·cm^{-1}, Table 7). The values of pH in river water (Fig. 20d) weakly decreased from the upstream end to meander apex where a minimum value of 8.1 was reached. Downstream from the meander apex, pH increased with higher values found at the downstream end of the meander section (maximum value = 8.85). The median pH in river water was 8.26 with an interquartile range of 0.12. DIC values in the river (Fig. 20e) at the upstream end and at the downstream end of the meander were 1.5 mmol·L^{-1}. A peak of DIC concentration occurred downstream of the meander apex, reaching a maximum of 2.0 mmol·L^{-1}. The median DIC concentration in the river was 1.8 mmol·L^{-1} (interquartile range = 0.4 mmol·L^{-1}). In contrast to electrical conductivity and to a lesser extent to pH values, total alkalinity (TA; fig. 20f) exhibited higher values in the upstream part of the meander with a median value of 2 091 mmol·L^{-1} (interquartile range = 207). Downstream from the meander apex, total alkalinity decreased rapidly to a minimum value of 1 479 mmol·L^{-1} before slightly increasing at the downstream end of the meander section.

In this downstream part of the meander, the median value stayed lower than values measured upstream (median value = 1 526 mmol·L^{-1}; interquartile range = 234 mmol·L^{-1}). For the entire studied meander, the median value of measured and calculated PCO_2 was 849 ppm (interquartile range = 300 ppm) with a maximum value of 1 151 ppm (Fig. 20g). The median value was twice larger than the global atmospheric PCO_2 value (405 ppm). The only location where PCO_2 was lower than atmospheric value was the downstream part of the meander where the value dropped to 123 ppm.
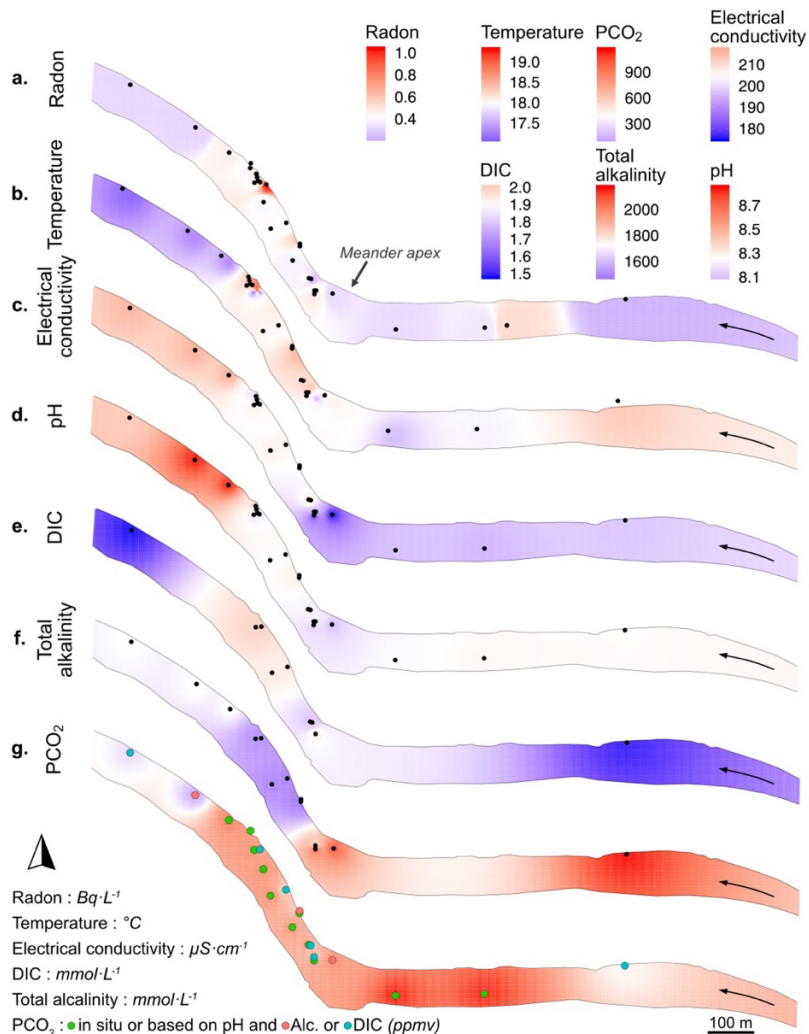
Figure 20. Interpolation of a. ^{222}Rn (Bq·L^{-1}), b. temperature (°C), c. electrical conductivity (μS·cm^{-1}), d. pH, e. dissolved inorganic carbon (mmol L^{-1}), f. total alkalinity (mmol L^{-1}), and g. $PCO2$ (ppm) in a meander of the Matane River from data collected during the August 2017 campaign. Arrows in the river indicate the direction of the river flow.

Tableau 7. Median values of chemical parameters in water sampled in groundwater and in river for the meander and corridor scales (interquartile ranges are indicated in parenthesis). Note that the corridor scale DIC values were obtained according to carbonate chemistry calculations (see text for the details on the calculations).

Location	^{222}Rn $(Bq·L^{-1})$	Temperature $(°C)$	Specific electrical conductivity $(\mu S·cm^{-1})$	pH	DIC $(mmol·L^{-1})$	TA $(mmol·L^{-1})$	PCO_2 (ppm)
Meander Groundwater	4.83 (1.59)	9.55 (3.04)	325 (30)	7.77 (0.26)	2.56 (0.92)	2 618 (442)	2 109 (1 983)
Meander River water	0.43 (0.15)	18.00 (0.89)	208 (5)	8.26 (0.12)	1.80 (0.44)	1 731 (234)	849 (300)
River corridor Groundwater	6.07 (2.17)	10.1 (2.58)	245 (17)	7.93 (0.30)	2.36 (0.63)	2 360 (379)	1 904 (1 438)
River corridor River water	0.18 (0.14)	18.08 (2.53)	203 (28)	8.34 (0.13)	1.89 (0.29)	1 909 (303)	430 (152)

2.5.2 Geochemical properties for the low-resolution study at the corridor scale

For this spatial configuration, river discharge linearly increased (Spearman correlation value = 0.88, p-value < 0.05) from 5.1 $m^3·s^{-1}$ in M10 to 6.9 $m^3·s^{-1}$ in M1 (64 km distance). This increase corresponds to a mean normalized groundwater input of 2.5 ± 0.1 $m^3·day^{-1}$ by linear meter of the river.

The evolution of ^{222}Rn, temperature, pH, electrical conductivity, TA and PCO_2 along the river corridor is presented in Fig. 21. Radon activities (Fig. 21a) varied from 0.13 $Bq·L^{-1}$ in the upstream sites (M10 and M9 in Km 0 and 9, respectively; Fig. 18a) to 0.45 $Bq·L^{-1}$ at the end of the transect (M1, Km 64; Fig. 18a). Median radon activity was 0.17 $Bq·L^{-1}$ (interquartile space of 0.12 $Bq·L^{-1}$). This value contrasted with the much higher one obtained in groundwater samples (median = 6.07 $Bq·L^{-1}$; interquartile range = 0.14 $Bq·L^{-1}$, Table 7). Along the stream corridor, four sites showed, however, slightly higher values (M1, M4, M6, and M8), suggesting higher groundwater discharges at these locations. Surface water temperature (Fig. 21b) was minimum at the upstream end of the corridor in M10 (T=14.5 °C) and increased to a maximum of 20.5 °C in M7. The temperatures rose significantly between

M9 and M8 where it increased from 15.2 °C to 19.2 °C over a short 10 km distance. Downstream from M7, temperatures tended to decrease slowly to reach 17.1 °C in M1. We noted a temperature drop between M6 and M5, with a decrease of ~2.3 °C in less than 5 km. In M4, however, the temperature exhibited a sharp increase to 19.9 °C before decreasing to values lower than 18°C. In groundwater, the median temperature was 10.1 °C (interquartile range = 2.6 °C, Table 7). Surface water pH (Fig. 21c) paralleled temperature distribution. It increased from M10 (pH = 8.26) to M7 where pH values reached a maximum of 8.49. Downstream M7, pH globally decreased until a minimum value of 8.19 at M1. As for temperature, a sharp increase was observed at M4 where the value reached 8.41 and then dropped to a pH value lower than 8.30. Electrical conductivity (Fig. 21d) linearly increased with the distance from the upstream of the transect (Spearman correlation value = 0.98, p-value = 2.2×10^{-16}). The mean increase rate was 0.8 $\mu S \cdot cm^{-1}$ by kilometer of the river. The minimal electrical conductivity value was observed at M9 (170 $\mu S \cdot cm^{-1}$) and the maximal value at M1 (225 $\mu S \cdot cm^{-1}$). The median electrical conductivity in groundwater was 245 $\mu S \cdot cm^{-1}$ (interquartile range = 17, Table 7) near the maximum value in the river. Total alkalinity (TA; Fig. 21e) exhibited a different distribution pattern along the transect. TA was relatively low in the upstream part of the river, between M10 and M8, with a median value of 1677 $mmol \cdot L^{-1}$ (interquartile range = 11 $mmol \cdot L^{-1}$). Downstream, TA increased from M8 to M6 and reached a plateau to a median value of 1968 $mmol \cdot L^{-1}$ (interquartile range = 36 $mmol \cdot L^{-1}$) that was maintained up to M1. Groundwater was more concentrated with a TA median value of 2360 $mmol \cdot L^{-1}$ (interquartile range = 379, Table 7). The global distribution pattern of PCO_2 (Fig. 21f) looked like TA with the low PCO_2 values (< atmospheric PCO_2) in the upstream of the transect and higher values (> atmospheric PCO2) in the downstream portion. The values varied along the river corridor from a minimum of 308 ppm in M7 to a maximum of 595 ppm in M1. The water samples were oversaturated relative to atmospheric PCO_2 only at three locations in M10, M5, and between M2 and M1). At M6 and M4, the water samples were near equilibrium with the atmosphere. In groundwater, PCO2 was much higher with a median value of 1904 ppm (Table 7). Groundwater values were highly variable with an interquartile range of 1438 ppm.
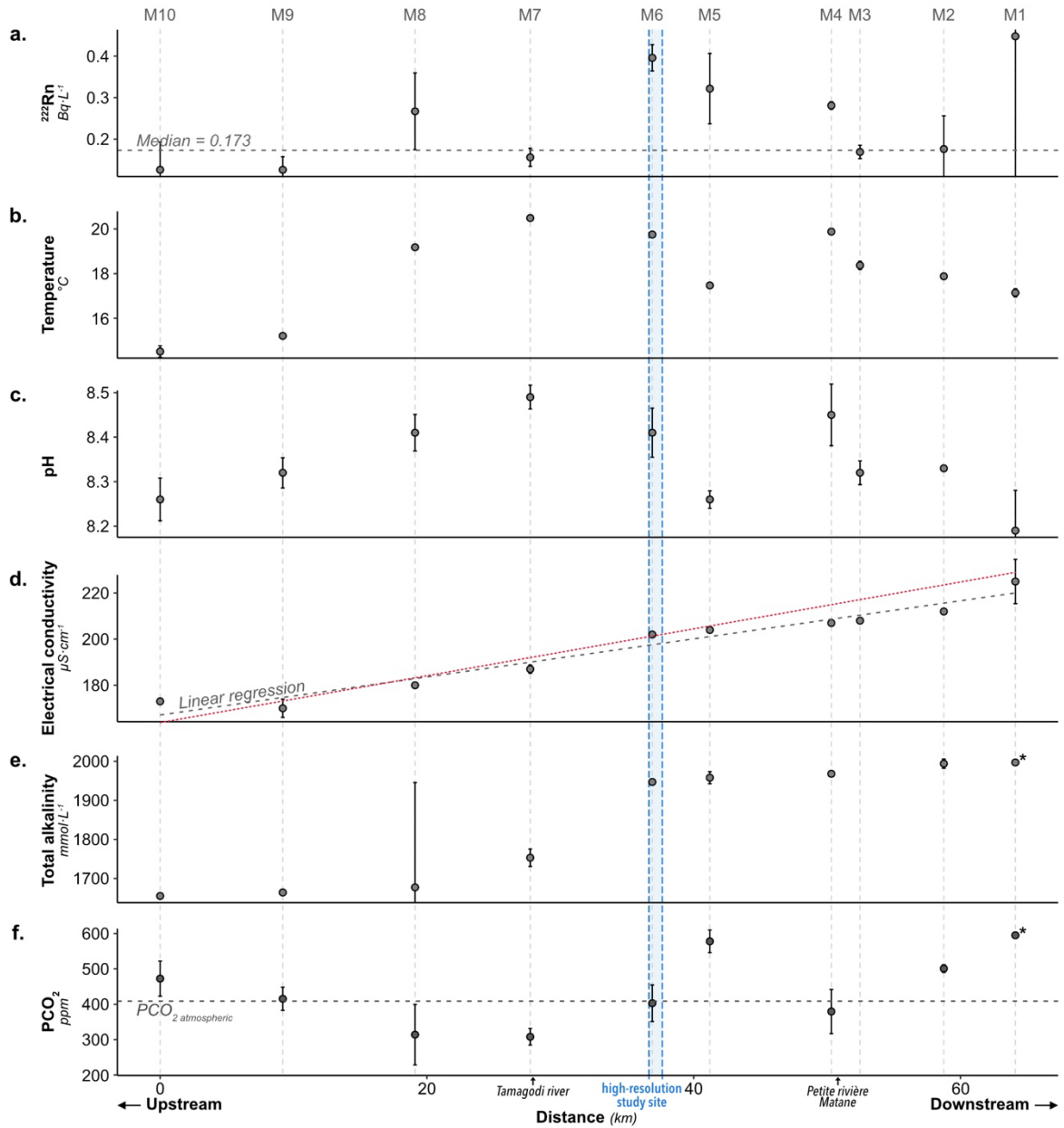
Figure 21. a. ^{222}Rn activity $(Bq·L^{-1})$, b. temperature (°C), c. pH, d. electrical conductivity $(\mu S·cm^{-1})$, e. total alkalinity $(mmol·L^{-1})$, and f. PCO_2 (ppm) data measured in the river during the July 2017 survey. Error bars represent the standard deviations. In electrical conductivity graph, grey linear regression is based on direct measurement in the river while red linear regression is based on Rn-based groundwater fluxes (see the discussion for details). Blue area indicates the location of the high-resolution study site.

2.6 DISCUSSION

2.6.1 Geochemical changes along the stream

During summer, stream baseflow is mainly supported by groundwater seeps. These non-point source discharges are diffuse through the river bed and banks (Exner-Kittridge et al., 2016) but they are mainly controlled by local conditions that include local piezometric levels (Cloutier et al., 2014), riverbed hydraulic conductivity (Brunner et al., 2017; Tang et al., 2017), morphology and structures (Käser et al., 2014; Wondzell and Gooseff, 2013), and river stage (Biehler et al., 2020). The spatial variations of groundwater discharges control geochemical heterogeneities along the stream. Groundwater presents both relatively high electrical conductivity and high nutrient concentrations that support algal community abundance and the presence of grazing organisms (Brunke and Gonser, 1997; Valett et al., 1994). Moreover, groundwater temperature stability during the year creates thermal refugia in the rivers for fishes providing cold water habitats during summer and warm water spots during winter (Dugdale et al., 2013; Meisner et al., 1988). These exfiltration spots have an influence on the behavior, the migration, the reproductive success, and the survival of fishes (Malcolm et al., 2003; Power et al., 1999). Groundwater may also act as a diffuse source of dissolved inorganic carbon and carbonate parameters that create hot spots of CO_2 degassing (Hotchkiss et al., 2015; Johnson et al., 2008).

In the Matane River, the contrasted concentrations of the target parameters between groundwater and surface water (Table 7), for both spatial configurations explored in this study, allow to evaluate the groundwater contribution to the stream carbon cycle. In the meander, ^{222}Rn, electrical conductivity and DIC concentrations reveal that groundwater mainly enters the surface water downstream from the meander apex. This is supported by the piezometric levels measured in the adjacent floodplain (Fig. 22) that revealed a sharp southwest piezometric gradient toward the river. During the summer season, when the river discharge is low (i.e., < 15 m^3·s^{-1}), the regional groundwater flow mainly controls the piezometric levels as well as the concentration of solutes in the floodplain groundwater

(Biehler et al., 2020). This gradient induced shallow groundwater seeps downstream from the apex, which also corresponds to the highest ^{222}Rn activities measured along the meander (Fig. 22).
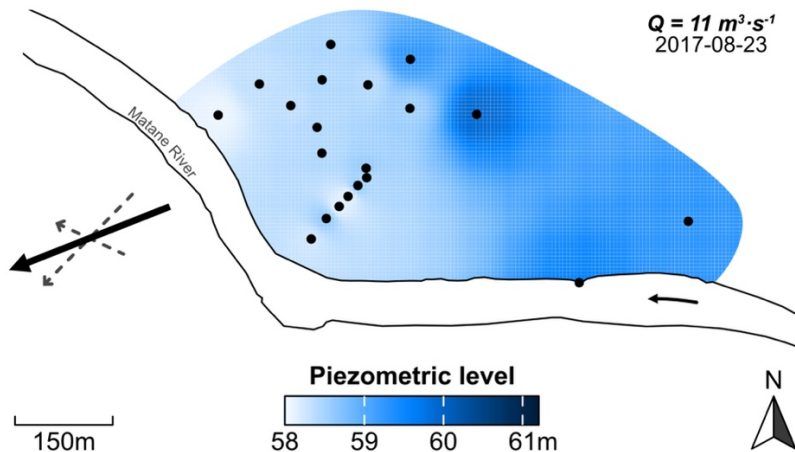
Figure 22. Piezometric levels in the studied meander on August 23rd, 2017. Piezometric map results from spatial interpolation of piezometric altitudes in each piezometer (black dots). Q (in m^3.s^{-1}) is the river discharge at this date and the curved black arrows indicates the direction of the discharge. Crossed arrows show the resultant (black arrow) of the two gradients (grey dotted arrows) in the floodplain as discussed in Biehler et al. (2020).

This spatial heterogeneity in river water geochemistry observed at the meander scale has been evidenced at the corridor scale too. Sharp variations in river water geochemistry occurred mainly between M6 and M3 for ^{222}Rn, temperature, and pH. The confluence between the Petite Matane River and the Matane River lies between M4 and M3 and it could be tempting to explain these variations by a mix between the two sampling points. However, mean temperatures of the Petite Matane River were higher in this affluent (24.4 °C) than in M4 (19.9 °C). The mixing of the two rivers should induce an increase in temperature from M4 to M3 and not the sharp decrease observed there (Fig. 21). Additional processes such as subsurface seeps are therefore needed. In addition, the peaks of radon activity observed in M8, M6, M4, and M1 revealed the input of ^{222}Rn-rich water likely as groundwater discharges. Based on the collected data, however, there is no clear correlation between the presence of ^{222}Rn and the values of temperature, pH, electrical conductivity, total alkalinity and PCO$_2$.

However, those subsurface inputs likely contributed to the geochemical evolution of river water all along the sections.

2.6.2   Groundwater discharges to surface water

2.6.2.1   Meander scale

Along the meander, groundwater discharges estimated based on a radon mass balance (equation 2) reveal high variabilities between river sections (Fig. 23a). From the upstream part of the meander (R1 in Fig. 18b) to the upstream of the meander apex, 200 m further on (from R1 to R2), the model shows no measurable groundwater discharge. The first positive groundwater discharges appear at the meander apex, on a ~180 m long transect (from R2 to R3) with a flux (normalized to river section length) of 137.6 $m^3 \cdot day^{-1} \cdot m^{-1}$. Downstream from the apex, positive groundwater inputs are found from R5 to R7, with calculated discharges ranging from 27.7 to 111.5 $m^3 \cdot day^{-1} \cdot m^{-1}$. Downstream, the discharge drops to zero over 115 m-long river section. The maximum groundwater discharges are estimated near the end of the meander with a peak of 213.6 $m^3 \cdot day^{-1} \cdot m^{-1}$ and the values finally reach a flux of 33.3 $m^3 \cdot day^{-1} \cdot m^{-1}$ at the outlet of the studied zone. On average, along the meander, the ^{222}Rn mass balance model calculates a positive groundwater discharge of 54.7 $m^3 \cdot day^{-1} \cdot m^{-1}$ that corresponds to a volumetric flux of 0.54 $m^3 \cdot s^{-1}$ representing nearly 8% of the river discharge at the downstream end of the river section. These results agree quite well with hydrological calculations. Considering the mean hydraulic conductivities measured in the floodplain (~53 $m \cdot day^{-1}$) and the depth of the aquifer at this site (~46 m - Buffin-Bélanger et al., 2015b), and the hydraulic gradient in the floodplain during the sampling campaign, Darcy volumetric flux to the river was equal to 0.30 ± 0.30 $m^3 \cdot s^{-1}$. This value is slightly lower but still consistent with the ^{222}Rn-based estimation (i.e., 0.54 $m^3 \cdot s^{-1}$). In the same way, assuming there was no additional water input along the meander, groundwater flux estimated by the difference of river discharges between upstream and downstream (Q_i-Q_0) gives a value of

0.70 $m^3 \cdot s^{-1}$ (i.e. around 10% of the river discharge at the downstream end of the river section) which strongly supports the [222]Rn mass balance calculation. All these results show that this meandering river section is then likely in gaining conditions at the time of the sampling, as it was expected in baseflow conditions.

2.6.2.2   Corridor scale

Gaining conditions were also observed at the corridor scale, as the [222]Rn model for the 64 km-long transect showed significant groundwater discharges ranging from 0.6 to 9.5 $m^3 \cdot day^{-1} \cdot m^{-1}$ (Fig. 23b), excepted from M4 to M3 (km 50 to 52). The mean discharge was about 2.9 $m^3 \cdot day^{-1} \cdot m^{-1}$ that corresponds to a total groundwater volumetric input of 2.17 $m^3 \cdot s^{-1}$. Note that 48 % of the river corridor presented groundwater discharge values lower than the mean value, while two major discharge peaks, localized from M7 to M6 and from M2 to the end of the corridor, represented 53 % of the total groundwater discharge. In these river sections (M7-M6 and M2-M1), calculated groundwater discharges were two to three times higher than the mean value, with 6.0 and 9.5 $m^3 \cdot day^{-1} \cdot m^{-1}$ respectively. The flow direction of groundwater in the hyporheic corridor, the heterogeneity of riverbed hydraulic conductivities (Brunner et al., 2017; Tang et al., 2017), and the structure and morphology of the riverbed (Käser et al., 2014; Wondzell and Gooseff, 2013) mainly contribute to the spatial heterogeneity of groundwater discharge at this scale.

At this scale, the mass balance results are still in agreement with other approaches. For example, the differential discharges measurement led to a water input of 2.5 $m^3 \cdot day^{-1} \cdot m^{-1}$, very close to the [222]Rn-based value of 2.9 $m^3 \cdot day^{-1} \cdot m^{-1}$. Moreover, based on EC as a quantitative tracer for groundwater discharge, as proposed by Gilfedder et al. (2015), where minimum EC values in the river (i.e. 167 $\mu S \cdot cm^{-1}$) and maximum EC in the aquifer (i.e. 383 $\mu S \cdot cm^{-1}$) are used as endmembers, the linear increase of EC supports a groundwater discharge of 2.3 $m^3 \cdot day^{-1} \cdot m^{-1}$ along the corridor. As EC values in surface water could be impacted by evapoconcentration, this value, close to the [222]Rn-based calculation, could be

overestimated. The inverse approach, however, where the EC endmembers values and ^{222}Rn-based groundwater discharges are used calculating theoretical electrical conductivities along the river corridor, led to a linear increase of 1.0 µS·cm^{-1} per kilometer ($r^2 = 0.98$; p-value = 1.4 x 10^{-6}). This linear regression was similar to the one obtained with measured EC values (i.e. 0.8 µS·cm^{-1}·km^{-1}, Fig. 21d). The ^{222}Rn-based model allows then to represent accurately the evolution of the measured electrical conductivity along the corridor.
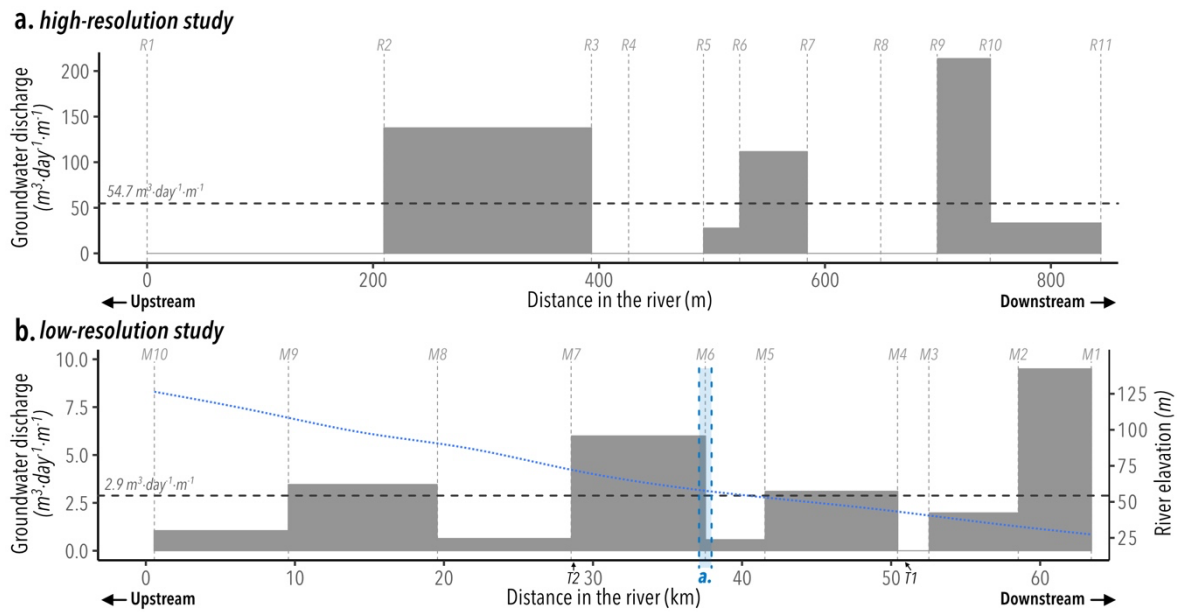
Figure 23. Metric groundwater discharge (in m^3·day^{-1}·m^{-1}) in the Matane River at the meander scale (a.) and at the corridor scale (b.) calculated by ^{222}Rn mass balance model following the equation 2. The dashed grey lines represent the mean discharge. The blue dotted line in panel b is the elevation (in m) along the river, calculated using the LiDAR data. The blue area shows the location of the high-resolution study site.

2.6.3 Coherence of the model for the two spatial configurations.

Whatever the spatial configuration, the ^{222}Rn mass balance was consistent with other more classical methods. These results support the different assumptions included in the model that considered i) a significant mixing of hyporheic water with shallow groundwater,

ii) a negligible impact of ^{226}Ra decay in rivers, and iii) a limited to no evaporation of ^{222}Rn into the atmosphere, at least at the studied scales. Even if the method is not easy to use due to logistic considerations, it is efficient to locate hotspots of groundwater discharges along a river reach, which indirect methods do not provide.

Sampling campaigns were carried out during summer baseflow for both spatial configurations with similar mean river discharges (6.3 and 6.8 $m^3 \cdot s^{-1}$ in July and August, respectively). Nonetheless, groundwater discharges were much higher at the meander scale than along the 64 km-long river corridor. At the specific meander location (from M5 to M7), the mean groundwater discharge was ~4 $m^3 \cdot day^{-1} \cdot m^{-1}$ in July, although it was ~55 $m^3 \cdot day^{-1} \cdot m^{-1}$ in August. This one-order difference could reflect short-term subsurface processes such as shallow aquifer recharge in the adjacent floodplain. A detailed examination of the piezometric levels in the flood plain revealed that mean piezometric levels slightly decrease during the July sampling campaign (Fig. 24a) and increased during the August sampling campaign (Fig. 24b). Because the river water level remains stable in summer, these changing piezometric conditions probably reflected the response of the regional aquifer to precipitations (i.e. 0.3 and 1.2 $mm \cdot day^{-1}$ over the weeks prior to the sampling periods in July and August respectively). Alone, this small gradient variation can't explain the differences of groundwater discharges between the two sampling periods. But a comparison between the total groundwater flux from the meander with the two river sections around it (57 290 and 46 200 $m^3 \cdot day^{-1}$, respectively) shows that the meander represent 81% of the total groundwater discharge in the M5 to M7 river section. Even if this contribution slightly varied with the piezometric level gradients, the one order difference is coherent between the spatial configurations, and the meander likely acted as a hotspot of groundwater discharge in this river section.
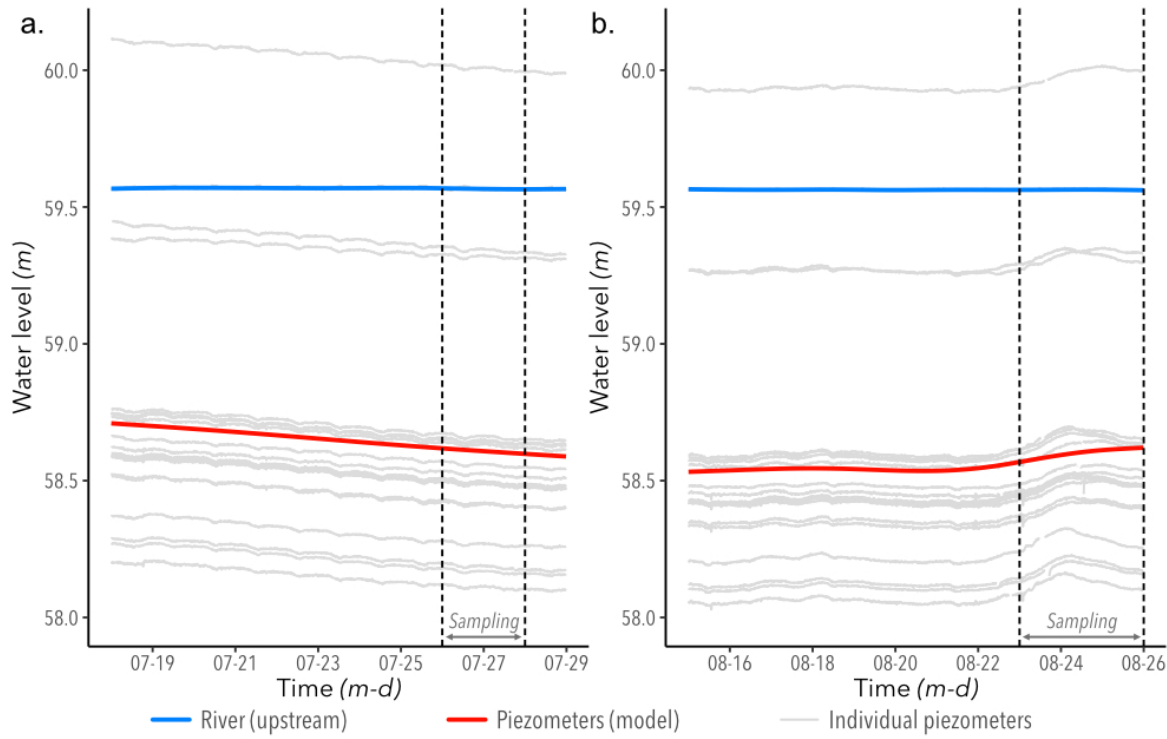
Figure 24. Temporal evolution of the piezometric levels at the meander scale during the July (a.) and August (b.) sampling campaigns. Blue lines represent the river water level upstream of the study site. Red lines represent the mean piezometric level in the adjacent aquifer. The time between the two dashed black lines indicated the sampling campaigns.

2.6.4 Groundwater-derived carbon fluxes

2.6.4.1 From groundwater to the river

Based on the mean groundwater discharges and on the median DIC concentrations in groundwater (i.e. 2.36 ± 0.63 and 2.56 ± 0.92 mmol·L^{-1}; Table 7), the groundwater-derived DIC fluxes were 6.8 and 140.3 mol·day^{-1}·m^{-1} at low-resolution and high-resolution scales, respectively. Because the DIC concentrations in groundwater between the two sampling campaigns were similar, the large difference observed between the DIC fluxes mainly reflects

the volumetric groundwater discharge rather than temporal differences in soil metabolism or soil leaching intensity.
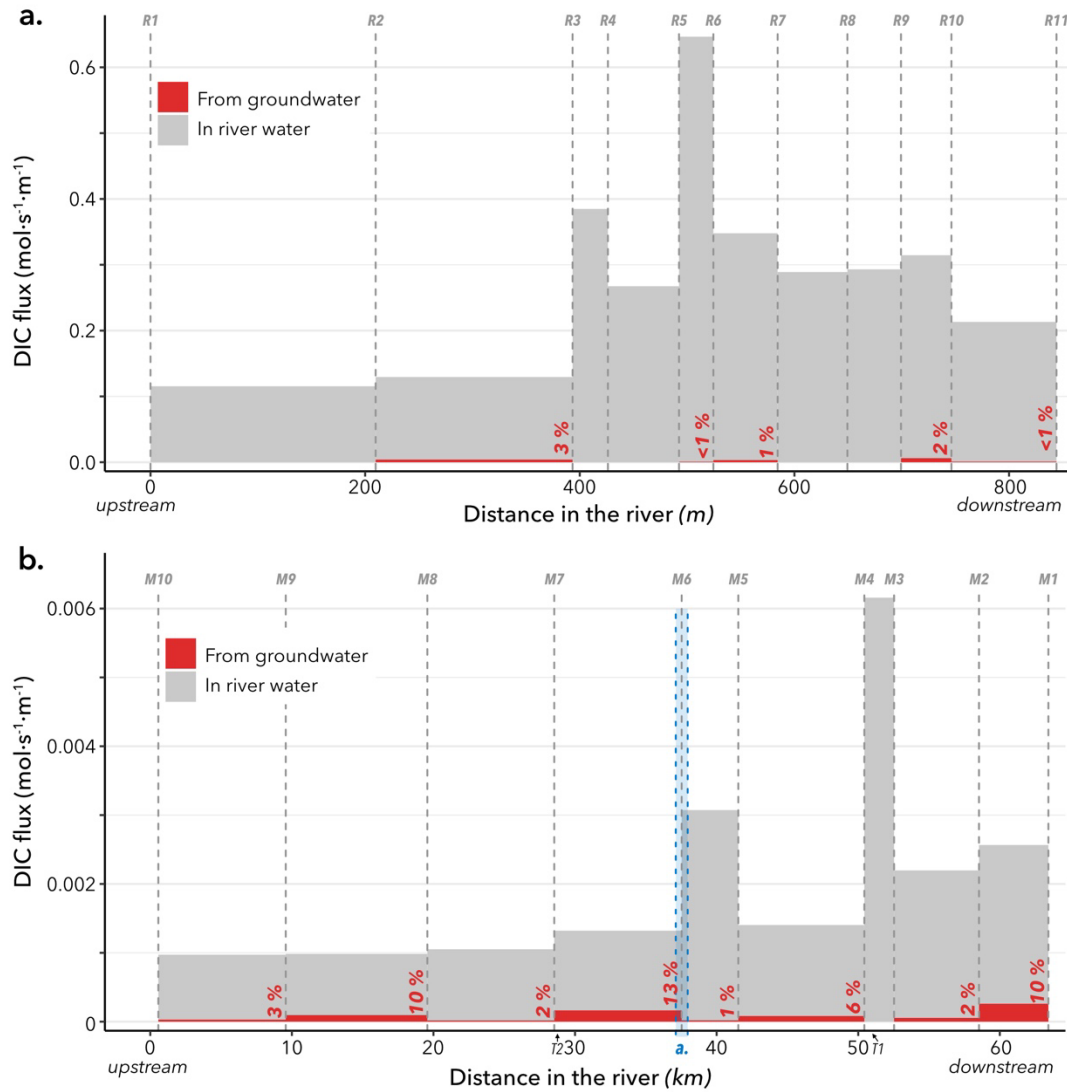
Figure 25. DIC fluxes in the river at the meander scale (a.) and at the corridor scale (b.). Groundwater-derived DIC fluxes (in red) were calculated from groundwater discharges estimated by the ^{222}Rn mass balance model and the groundwater median DIC concentrations. The flux of DIC in the river (in grey) was calculated by multiplying the DIC concentrations measured in the river by the river discharges. In the panel b, the blue area shows the location of the high-resolution study site.

For both resolutions, the DIC originating from the aquifer represented only a weak fraction of the total DIC transported by the river (Fig. 25). At the corridor scale, maximal contributions of ~13 % to ~10 % were observed in M9-M8, M7-M6 and M2-M1 and the mean contribution was 5 % (Fig. 25b). Similarly, at the meander scale, the mean contribution of groundwater to the DIC flux in the river was inferior to 1 % only with a maximal contribution of 3 % within the meander apex (Fig. 25a). Although groundwater supports the baseflow of Matane River during the summer period, the low contributions of groundwater-derived DIC to the riverine flux of DIC highlights the importance of other sources of DIC within the river, such as the aquatic metabolism (Hotchkiss et al., 2018). As observed by Hotchkiss et al. (2015), in small rivers and headstreams, groundwater acts as the primary source of CO_2, but their contribution is balanced with internal production as rivers grow larger. Here, with a Strahler order of 6, the Matane River is large enough to support metabolic DIC rather than external inputs.

2.6.4.2   From river to atmosphere

The prevalent forms of DIC in surface waters were examined through a detailed examination of the carbonate system with the "AquaEnv" package in R. It revealed that DIC is mostly under its HCO_3^- form in the river ($HCO_3^- = 98$ %, $CO_2 = 1$ %, $CO_3^{2-} = 1$ %, N = 36). In groundwater samples, the HCO_3^- form also dominated, but the contribution of CO_2 was slightly higher ($HCO_3^- = 95$ %, $CO_2 = 4$ %, N = 18), reaching up to 12 % in some samples. This change in DIC forms is mainly controlled by the pH. Considering that around 4 % of the calculated DIC fluxes from groundwater were under CO_2 form, groundwater-derived CO_2 fluxes were equal to 65 and 1596 mg C·day^{-1}·m^{-2} for the low-resolution and high-resolution scales, respectively. Those values were comparable to the CO_2 emissions obtained from equation 4 with outgassing fluxes of respectively 88 and 529 mg C·day^{-1}·m^{-2}. In the same way, the groundwater-derived CO_2 flux represented 73 % of the outgassing flux to the atmosphere at the corridor scale. The remaining contribution (~25%) likely occurred

as internal production. In contrast, groundwater-derived CO_2 was three times higher than the emission in the meander. Because both PCO2 and TA decreased in the downstream end of the meander (Fig. 20), this counter-intuitive result could not result from a buffering effect of river water as already described in Duvert et al. (2019) in the Howard and Daly rivers (Australia) where the authors noted that groundwater-derived CO_2 input was transformed into HCO_3^-. An active photosynthetic consumption as well as an instantaneous evasion of the CO_2 in excess as soon as groundwater enters the stream may contribute to the CO_2 loss. The lack of O_2 data prevents discussion about the photosynthetic aspect of this loss. Several studies have, however, already pointed out sampling artifacts and difficulties related to groundwater-derived CO_2 sampling (Deirmendjian and Abril, 2018; Venkiteswaran et al., 2014). The high CO_2 concentrations in groundwater and the macroscopic observations of seeps along the riverbed support the idea that the excess CO_2 evaded instantaneously to the atmosphere as soon as groundwater discharges. Generalizing this observation, if some of the groundwater-derived CO_2 cannot be collected by our sampling approach, all measured CO_2 fluxes to the atmosphere should also be underestimated, especially where groundwater discharges are high (as for example between M9 to M8, M6 to M5, and M2 to M1). Therefore, the calculated 75 % contribution of groundwater to the river – atmosphere CO_2 fluxes should be considered as a minimal contribution. Groundwater discharges, as an external carbon source to rivers, play a major role in the high concentrations of carbon in rivers and in the CO_2 exchanges between rivers and the atmosphere (Duvert et al., 2019; Ran et al., 2017).

During the sampling period, the Matane River globally acted as a source of CO_2 to the atmosphere and a large part of these emissions was due to the hydrological connectivity between the aquifer and the river. The estimated emissions are in the same order as the values reported for subarctic rivers located in the Canadian Shield. For example, Campeau et al. (2014) measured CO_2 emissions ranging from 20 to 5879 mg $C \cdot m^{-2} \cdot d^{-1}$ in Abitibi and James Bay rivers (Canada) and they determined a mean CO_2 flux of 449 mg $C \cdot m^{-2} \cdot d^{-1}$ (N=3) for large rivers with Strahler order of 6. In the Eastmain River basin, in James Bay region, Teodoru et al. (2009) reported a mean CO_2 emission of 391 mg $C \cdot m^{-2} \cdot d^{-1}$ from the Rivière à

l'Eau Claire, a river with dimensions similar to the Matane River. These outgassing fluxes are, however, low compared to more temperate and tropical systems. In the Ybbs river (a lower-alpine 5th order river in Austria), Schelker et al. (2016) measured emissions around $1210\ \text{mg C·m}^{-2}\text{·d}^{-1}$. In northern Australia, Duvert et al. (2019) calculated mean CO_2 emissions of 2300 and $8500\ \text{mg C·m}^{-2}\text{·d}^{-1}$ in the Howard River and Daly River, respectively. These CO_2 emission estimations are greatly controlled by seasons and hydroclimatic conditions, water temperature, river discharge, and CO_2 concentration (Halbedel and Koschorreck, 2013; Ran et al., 2017). Then, the groundwater discharges and associated DIC/CO_2 fluxes are transient, specifically in subarctic regions where hydroclimatic conditions changed drastically over the season. The values presented here represent snapshots of C fluxes in the Matane River during the summer season. Nevertheless, they shed light on the key role of groundwater in the riverine inorganic carbon cycle in a subarctic region, and specifically in the CO_2 outgassing fluxes from surface water. Such quantifications are particularly important in northern systems where significant changes in hydroclimatic conditions and terrestrial carbon storage are undergoing and are expected to continue to undergo.

2.7 CONCLUSION

Based on the measurements of groundwater discharges, this study aimed to quantify the contribution of the aquifer-river connectivity to stream DIC and CO_2. A ^{222}Rn mass balance model was tested at two different spatial configurations including measurements at high spatial resolution (m) in a well-known meander and measurements at low spatial resolution (km) along a 64 km long stream corridor. For both spatial configurations, the calculated groundwater discharges were heterogeneous ranging from 0 to $200\ \text{m}^3\text{·day}^{-1}\text{·m}^{-1}$ depending on the river sections. The meander scale study allowed, however, to precisely determine the groundwater discharge locations in the meander. The corridor scale study highlighted groundwater discharges all along the studied river sections but with lower

discharges compared to those of the meander scale study. The mean calculated groundwater discharges were in agreement with more classical approaches of external input estimation, as EC mass-balance models, hydrogeological budget and hydrological budget, highlighting the robustness of the Rn-based model.

Because the DIC concentrations were high in groundwater, those inputs increase DIC concentrations in the river. Although this increase seems low compared to instream DIC flux (< 10 %), the resulting groundwater-derived CO_2 flux to the river was significant and contributed between 75 and 300 % of the CO_2 evasion from the Matane River to the atmosphere. The CO_2 excess in groundwater probably instantaneously outgasses as soon as groundwater enters the stream, leading to an underestimation of the CO_2 fluxes from the river to the atmosphere. Despite this, our results revealed that the Matane River was a source of CO_2 to the atmosphere during the summer baseflow season, with PCO_2 in surface water reaching values as high as 2000 ppm in some river sections. Calculated CO_2 evasions using parametric relations were 88 and 529 mg $C \cdot day^{-1} \cdot m^{-2}$ depending on the scale of observation. These values are in the same magnitude of riverine emissions reported in other subarctic rivers. They are, however, in the lower range of emissions reported for rivers in tropical regions.

Our results highlight the key role of groundwater in the riverine inorganic carbon cycle in a subarctic region, and specifically in the CO_2 emissions. Radon in water is an effective proxy to quantifying groundwater discharge in rivers, at both site-specific and stream corridor scales. Further direct quantifications are needed to include groundwater as a source of CO_2 to the atmosphere in global carbon cycling, particularly in regions where important changes in hydroclimatic conditions are expected to undergo over the next decades.

2.8 CREDIT AUTHORSHIP CONTRIBUTION STATEMENT

2.9 DECLARATION OF COMPETING INTEREST

The authors declare that they have no known competing financial interests or personal relationships that could have appeared to influence the work reported in this paper.

2.10 FUNDING

2.11 ACKNOWLEDGMENTS

CHAPITRE 3
BASE DE DONNÉES HYDROGÉOLOGIQUES DANS L'ÉTUDE DE LA CONNECTIVITÉ EAU SOUTERRAINE – RIVIÈRE : LE PARTAGE OUVERT EST-IL BÉNÉFIQUE À L'AMELIORATION DE NOS CONNAISSANCES ?

3.1 RÉSUMÉ

La recherche scientifique publie annuellement de plus en plus d'études générant d'importantes bases de données. Ces dernières, coûteuses et chronophages à acquérir, sont souvent archivées une fois l'étude publiée, dans des ordinateurs ou des serveurs professionnels. Il devient ainsi difficile d'accéder à ces bases de données qui trop souvent finissent par être oubliées ou perdues. Pourtant de plus en plus de voix se lèvent pour demander que les bases de données scientifiques soient rendues publiques et accessibles afin qu'elles puissent être réutilisées dans le cadre de nouvelles études. Cet article cherche à évaluer si une base de données répond à plusieurs questions de recherche, et à vérifier à quel point il est possible de rendre disponibles et utilisables des bases de données dans le domaine de la connectivité entre les eaux souterraines et les rivières. Pour ce faire, une base de données hydrogéologique de suivi pluriannuel des niveaux piézométriques à haute résolution spatiale et temporelle dans un aquifère alluvial de la rivière Matane (Québec, Canada) entre 2011 et 2019 a été utilisée en tant qu'exemple de base de données à réutiliser. Des analyses successives de différentes problématiques considérant différentes dimensions de la base de données ont permis de renforcer et détailler certaines conclusions déjà proposées dans différentes études. Une modélisation de la surface piézométrique a permis la création de nouvelles données tertiaires sur le comportement général de l'aquifère. Ces analyses ont également permis de mettre en évidence des anomalies vis-à-vis du fonctionnement attendu de cette connectivité et ainsi d'apporter de nouvelles questions de recherche et pistes de

travail. La réutilisation de bases de données existantes avec un regard libre des questionnements originels est pertinente dans l'étude de la connectivité entre les eaux souterraines et les rivières. Ce partage se doit cependant d'être efficace et donc normalisé selon des principes clairs tels que les principes FAIR. Ceux-ci garantissent que les bases de données soient librement accessibles et exploitables avec une origine claire de la donnée et des métadonnées efficaces et utiles.

Ce chapitre fera l'objet d'un article scientifique qui sera soumis pour publication dans la revue *Progress in Physical Geography: Earth and Environment*. Cet article s'accompagnera de la publication de la base de données hydrogéologique traitée ici dans le répertoire Pangaea.de.

Contribution des auteurs :

Cet article a été corédigé par moi-même ainsi que les professeurs Gwénaëlle Chaillou, Thomas Buffin-Bélanger, et Paul Baudron. En tant que premier auteur, j'ai contribué à l'essentiel de la recherche de conceptualisation, de développement, de prélèvements sur le terrain, d'analyse des données, de leur interprétation, de productions de figures, et de rédaction de la première version de l'article. Ce travail de conceptualisation a été réalisé en collaboration avec l'ensemble des coauteurs qui ont tous contribué par leurs révisions et propositions à la version finale de l'article.

3.2 BASE DE DONNÉES HYDROGÉOLOGIQUES DANS L'ÉTUDE DE LA CONNECTIVITÉ EAU SOUTERRAINE – RIVIÈRE : LE PARTAGE OUVERT EST-IL BÉNÉFIQUE À L'AMÉLIORATION DE NOS CONNAISSANCES ?

Antoine Biehler[a], Thomas Buffin-Bélanger[a], Paul Baudron[b], Gwénaëlle Chaillou[c]

[a] *Université du Québec à Rimouski, 300 allée des Ursulines, Rimouski, Québec G5L 3A1, Canada*
[b] *Institut pour la Recherche et le Développement, UMR G-EAU, 34090 Montpellier, France ; Polytechnique Montréal, 2500 chemin de Polytechnique, Montréal (Québec), Canada, H3T 1J4*
[c] *Institut des Sciences de la Mer de Rimouski, Université du Québec à Rimouski, 310 allée des Ursulines, Rimouski, Québec G5L 3A1, Canada*

3.3 INTRODUCTION

La recherche scientifique génère annuellement de plus en plus d'articles publiés dans des revues à comité de lecture. Le nombre d'articles scientifiques publiés dans le domaine des sciences naturelles est ainsi passé d'environ 1.0 million de publications en 1996 à plus de 2.9 millions en 2020 (National Science Board National Science Foundation, 2021 - Fig. 26a). Pour beaucoup, ces travaux présentent des études de cas, s'appuient sur des sites spécifiques, ou synthétisent des analyses particulières pour répondre à une question de recherche. Ces réponses sont généralement obtenues après l'exploration et l'analyse des bases de données générées par les chercheurs puis sauvegardées sur des serveurs dans des laboratoires.

Dans le domaine de la connectivité entre les eaux souterraines et les rivières, le nombre d'articles scientifiques a progressivement augmenté au cours des deux dernières décennies. Ce domaine relativement récent ne générait qu'une vingtaine d'articles scientifiques par années entre 1997 et 2001. Cette fréquence de publication a ensuite rapidement augmenté pour arriver à environ 600 articles scientifiques en 2021 (Fig. 26b). Entre 1997 et 2021, 4 269 articles scientifiques répondant aux mots clés « groundwater AND river AND connectivity » sont ainsi recensés sur la plateforme ScienceDirect. Derrière chacune de ces études peuvent se cacher d'importantes bases de données, archivées après avoir répondu à leur objectif initial. Bien souvent, la mise en valeur des données acquises s'arrête après publication du

ou des articles scientifiques, et les bases de données sont par la suite oubliées ou perdues. Se pose alors la question de comment gérer ces bases de données pour les ouvrir à la communauté scientifique et optimiser leur utilisation. Des universités ou autres organismes de recherche s'organisent ainsi pour stocker ces bases sur des serveurs internes plus ou moins accessibles par le reste de la communauté scientifique (e.g. Système de Gestion des Données Environnementales de l'UQAR-ISMER ; CaltecDATA ; Wilfrid Laurier University Dataverse). À plus large échelle, d'autres plateformes en ligne à portée disciplinaire ou généraliste permettent le partage de bases de données à la communauté scientifique en général telles que Pangaea (*pangaea.de*), la Marine Geoscience Data System (*marine-geo.org*), ou encore EarthChem (*earthchem.org*). Mais là encore, la question des modalités d'usage et de réutilisation de ces données se pose.
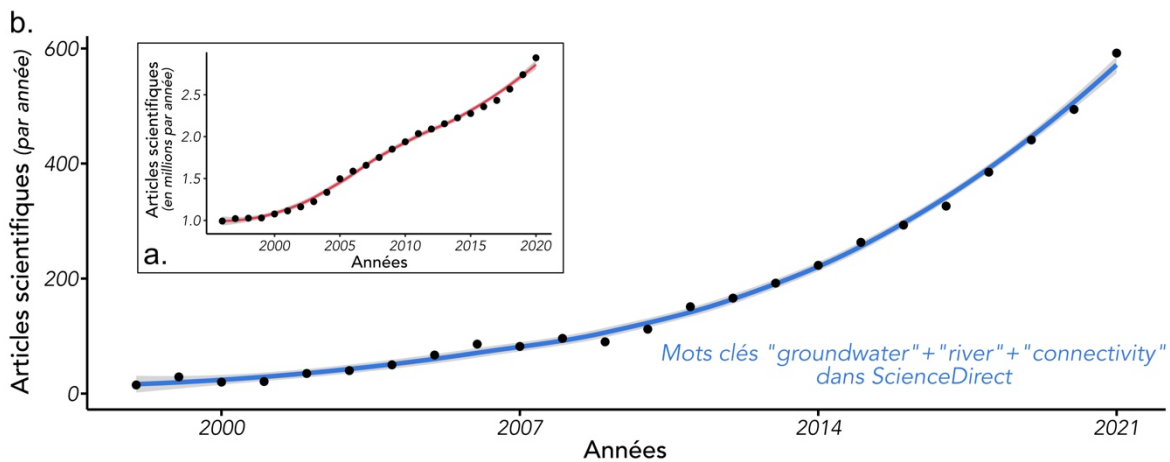
Figure 26. Nombre d'articles scientifiques publiés annuellement dans le monde (a.) et dans le domaine de la connectivité entre les eaux souterraines et les eaux de surface (b.). La fréquence spécifique correspond au nombre d'articles publiés par année comprenant les mots clés « groundwater », « river », et « connectivity » sur le site ScienceDirect en date du 30 juin 2022. La fréquence de publication totale est issue du National Science Foundation, *Science and Engineering Indicators* et correspond aux articles publiés dans les domaines de la physique, de la biologie, de la chimie, des mathématiques, de la médecine clinique, de la recherche biomédicale, de l'ingénierie, et des sciences spatiales.

De manière à cadrer ce partage de connaissances au travers de données brutes, les groupes de travail Jointly Designing a Data Fairport réuni aux Pays-Bas en 2014 et FORCE11

(Future Of Research Communication and E-scholarship) ont développé des principes généraux simples et indépendants du domaine d'étude pour le partage d'objets scientifiques tels que les bases de données, les algorithmes, les outils et les workflows (Wilkinson et al., 2016) : les principes FAIR. Ces principes d'optimisation du partage de la donnée scientifique impliquent que les données partagées puissent être découvertes (Findable), disponibles (Accessible), interopérables (Interoperable), et réutilisables (Reusable). Ainsi pour qu'un partage de base de données soit conforme aux principes FAIR, cette dernière doit disposer d'un numéro d'identification unique, tel un DOI (Digital Object Identifier), dont la gestion à long terme est assurée et qui permet de retrouver simplement une base de données et/ou ses métadonnées. Des métadonnées riches et qui utilisent des termes génériques, compréhensibles par la communauté scientifique, doivent accompagner les données publiées. Ces bases de données doivent pouvoir être téléchargées librement, ou sur autorisation, et leur licence d'utilisation doit être clairement spécifiée. Les données et métadonnées doivent pouvoir être lisibles à la fois par un opérateur humain et informatique afin de garantir sa disponibilité via les outils de recherche des serveurs de base de données.

Ce partage des bases de données est déjà bien implanté dans certains domaines tels que la génétique (e.g.: GenBank, Barcode of Life Data System, International Nucleotide Sequence Database Collaboration) ou en santé publique (e.g. National Addiction & HIV Data Archive Program). Cette mise en commun de l'information s'est ainsi par exemple implantée au cœur de certaines techniques analytiques telles de le *DNA barcoding* permettant d'identifier des espèces par comparaison de séquences d'ADN mesurées avec des séquences enregistrées dans des bases de données d'ADN (Ratnasingham et Hebert, 2007). En géosciences, le comité pour la publication de données dans les sciences de la Terre et dans les sciences spatiales (COPDESS) cherche à promouvoir le partage des données en accord avec les principes FAIR à travers son programme Enabling FAIR Data Project (COPDESS, 2018). Dans son engagement, le programme affirme que ce partage des données sur les plateformes appliquant les principes FAIR et approuvées par la communauté, aura le double

effet d'augmenter la qualité des données disponibles, mais aussi de faciliter les découvertes et la réutilisation des bases de données.

L'idée de faciliter de nouvelles découvertes par le partage et la réutilisation de bases de données déjà exploitées sous-entend que les réponses apportées par une base de données ne sont pas uniques. À son origine, une base de données est créée pour répondre à une question de recherche précise. Elle contient un certain nombre de dimensions sélectionnées dans l'intention de vérifier ou d'infirmer des hypothèses de recherches préétablies. On pourrait ainsi décrire une base de données nouvellement créée en spécifiant les paramètres qu'elle contient (quoi ?), le nombre de dimension exploitée (où ?, quand ?, comment ?), le destinataire des données (pour qui ?), et l'intention sous-jacente à la collecte des données (pourquoi ?). Cette description est en accord avec la définition donnée d'une base de données fournie par Chapman *et al.* et modifiée par Löffler *et al.* :

« Une base de données est une collection de données scientifiques incluant des résultats primaires et des métadonnées organisées et formatées dans un objectif particulier. » (Chapman et al., 2020 ; Löffler et al., 2021)

La réutilisation ou le partage de la base de données reviendrait selon cette définition à mettre en valeur les paramètres et les dimensions qui la définissent tout en universalisant son destinataire. L'intention derrière la prise de données serait alors relayée en tant que métadonnée permettant de comprendre la construction du jeu de données.

Ainsi, sur les 4 767 articles scientifiques recensés précédemment entre 1997 et 2021 avec les mots-clés « groundwater », « river », et « connectivity », si on met de côté les articles de synthèse (11 % du total des articles) la plupart de ces études ont généré des bases de données pour approfondir les connaissances dans le domaine de la connectivité entre les eaux souterraines et les rivières composées de données de plusieurs niveaux : primaire (données directement issues des appareils de mesures) ; secondaire (données traitées) ; ou tertiaire (données issues de modèles). Ces bases de données internes aux laboratoires ou aux universités ont pu ou pourraient être utilisées pour répondre à de nouvelles questions de

recherche. Par exemple, sur la rivière Matane (Québec, Canada), une plaine d'inondation a été instrumentée entre 2011 et 2019 sur le site de Saint-René-de-Matane, de manière à effectuer un suivi des niveaux piézométriques et de la température des eaux souterraines à haute résolution spatiale (21 piézomètres sur une surface de 17.8 ha) et temporelle (une mesure toutes les 15 minutes). Cette volumineuse base de données a été déjà été utilisée dans le cadre de cinq études successives. Cloutier et al. (2014) et Buffin-Bélanger et al. (2015) ont utilisé les données collectées lors d'épisodes de crue pour analyser la réponse de l'aquifère alluvial aux variations de débit d'eau dans la rivière dans le cadre de la propagation d'onde de crue dans l'aquifère. Larocque et al. (2016) ont utilisé les niveaux d'eau et les températures de l'aquifère, suite à différents épisodes de précipitation, pour analyser la capacité de l'aquifère à stocker de l'eau de la rivière. En 2020 et 2022 (articles en révision), Biehler et al. ont utilisé cette base de données pour quantifier les échanges entre l'aquifère alluvial et la rivière, en la combinant avec des données géochimiques et isotopiques.

La présente étude se fonde sur cette dernière base de données en tant que modèle théorique, et se questionne sur les possibles avancées de la recherche sur la connectivité eau souterraine – eau de surface dans le cadre d'une publication à large échelle des bases de données hydrogéologiques. Plus spécifiquement, cette étude regarde au travers d'exemples particuliers si une telle base de données peut répondre à plusieurs questions de recherche, et à quel point il est possible de rendre disponible et utilisable des bases de données dans le domaine de la connectivité entre les eaux souterraines et les rivières. Les avantages et inconvénients d'une généralisation de ces partages sont aussi discutés.

3.4   ANALYSE DE LA BASE DE DONNÉES MODÈLE

3.4.1   Description de la rivière Matane

La rivière Matane est une rivière à saumon située au Québec (Canada). Elle est connue pour ses épisodes récurrents d'inondations (Biron et al., 2013). Ces dernières sont causées pour certaines par des débordements de la rivière lors des crues importantes accompagnant

la fonte des neiges. D'autres épisodes d'inondations sont par ailleurs observés plus éloignés de la rivière, causés par exfiltration de la nappe d'eau souterraine. La rivière s'écoule au sein d'un bassin versant semi-alluvial de 1 678 km^2 formé par des phases d'érosion glaciaire qui s'achèvent il y a 15 800 ans avec la déglaciation et l'invasion progressive de la vallée par la mer de Goldthwait (jusqu'à 15 km dans la vallée), puis il y a 13 ka la baisse du niveau de la mer relatif (Dionne et Coll, 1995; Marchand et al., 2014). Son socle rocheux se compose de roches sédimentaires déformées de la période cambro-ordoviciennes (schistes ardoisiers, grès fins, calcaires, et conglomérats), associées à l'orogène appalachienne (Dionne et Coll, 1995; Ollerenshaw, 1967). Ces roches sont surmontées de dépôts glaciofluviaux non consolidés comprenant sables grossiers, graviers, et galets sur une épaisseur moyenne de 49 m (Buffin-Bélanger et al., 2015c; Marchand et al., 2014). La rivière, d'une longueur de 70 km, prend sa source dans les monts Chic-Chocs, s'écoule dans un bassin versant principalement forestier (87 % de sa surface - P. M. Biron et al., 2014), et se déverse dans l'estuaire du Saint-Laurent au niveau de la municipalité de Matane. La largeur moyenne de la vallée est de ~475 m pour une largeur moyenne de rivière de ~55 m. La migration latérale des chenaux de la rivière est semi-confinée avec localement des affleurements limitant l'amplitude des méandres. L'écoulement de la rivière est de type nivo-pluvial avec, en aval, un débit de plein bord de 350 m$^3 \cdot$s^{-1} (Cloutier et al., 2014), un débit d'étiage de 5 m$^3 \cdot$s^{-1}, et un débit moyen de 39 m$^3 \cdot$s^{-1} (période 1926 à 2021 ; station 021601 du Centre d'expertise hydrique du Québec, (2022)). La rivière est située en zone subarctique avec un contraste saisonnier important. Deux périodes d'étiages sont observées pendant l'année : l'une en hiver avec des températures moyennes mensuelles négatives de décembre à avril où la rivière est recouverte d'un couvert de glace, et l'autre en été.

3.4.2 La base de données hydrogéologiques sur la rivière Matane

En juin 2011, une plaine d'inondation de la rivière Matane de 17.8 ha a été instrumentée avec 15 piézomètres et une station de jaugeage installée en amont du méandre.

Six autres piézomètres ont été implantés en 2014 pour augmenter la résolution spatiale et mettre en place un transect partant de la rive à l'apex du méandre (Fig. 27a). Chaque piézomètre a été réalisé à partir de tube de PVC de 38 mm équipé à sa base d'une crépine à fentes de 0.3 mm d'ouverture. Ces piézomètres sont implantés de manière à ce que le bas de leur crépine atteigne une profondeur d'environ 3 m sous le niveau du sol et que leur niveau soit inférieur à celui de l'eau dans la rivière (Fig. 27b). Chacun des piézomètres est équipé d'un capteur Hobo U20-001 immergé et réglé pour effectuer une mesure de la pression et de température toutes les 15 minutes. Cette pression comparée à la pression atmosphérique (mesurée sur le site d'étude à l'aide d'un capteur similaire), à l'altitude évaluée à l'aide d'un DGPS (Differential Global Positioning System) de chaque piézomètre et à la profondeur de chaque capteur permet d'obtenir les niveaux piézométriques au niveau de chaque point de mesure. De la même manière, la station de jaugeage est composée d'un tube PVC coudé accessible depuis la berge dont la partie crépinée (fentes de 0.3mm d'ouverture) est située dans le lit de la rivière sous quelques centimètres de sédiments de fond.

Ainsi dans la base de données, à chacune des deux dimensions correspondant aux deux paramètres mesurés (niveau piézométrique et de température de l'eau souterraine) s'ajoutent trois autres dimensions : une longitude, une latitude, et une date allant du 23 juin 2011 à 11h45 au 5 juin 2019 à 13h45. Ces dimensions sont fournies pour 16 entités d'eaux souterraines (i.e. piézomètres) entre le 23/06/2011 et le 26/07/2014, puis 22 entités à partir du 26/07/2104 et une entité d'eau de surface (station de jaugeage). La base de données inclut ainsi 278 771 mesures par piézomètre (ou 170 409 pour les piézomètres installés en 2014) et par paramètre analysé, soit un total de 5 482 790 mesures potentielles par paramètre. Considérant sur cette période des absences de données dues au temps de chargement de données, aux vols et aux problèmes de bris de matériel, la base de données contient de manière effective 4 001 025 mesures pour chaque paramètre. L'analyse de cette base de données peut ainsi être faite en confrontant les dimensions et les paramètres les uns avec les autres. Le choix de ces confrontations est lié à la question de recherche ciblée.
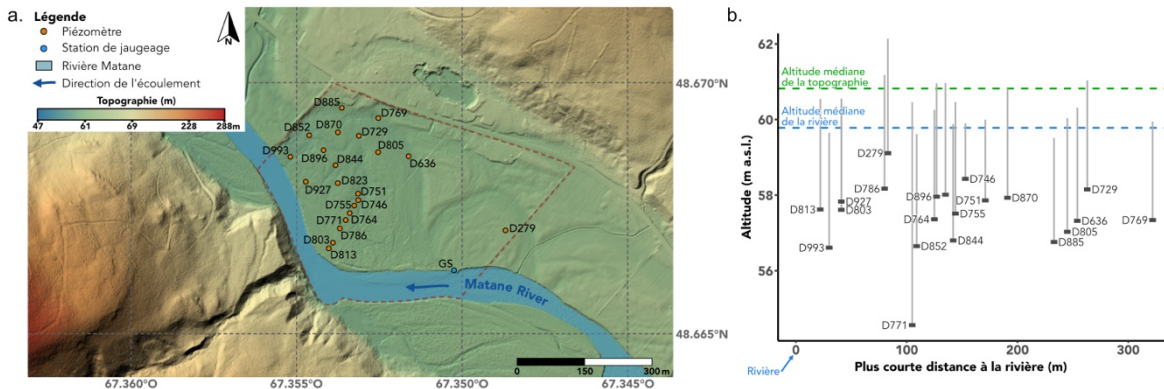
Figure 27. Implantation des piézomètres (a.) dans la plaine d'inondation de la rivière Matane et (b.) en profondeur. Chaque piézomètre est d'une longueur d'environ 3 m à l'exception de D771 qui a été implanté jusqu'à 6 m de profondeur. Dans (b.) la partie supérieure de la ligne gris clair correspond à l'altitude topographique au niveau de chaque piézomètre, mesuré à l'aide d'un GPS différentiel (DGPS). La base gris foncé correspond à l'altitude du bas de la crépine.

3.4.3 Analyse à deux dimensions : Existe-t-il un lien entre les niveaux piézométriques mesurés et la variation du niveau de l'eau dans la rivière ?

Une première version de ces confrontations, la plus classique, consiste à simplement analyser une dimension en fonction d'une autre dans un graphique. Cette représentation permet de mettre en évidence des relations fonctionnelles ou de causalité entre les dimensions. Ici, par exemple, nous allons chercher à vérifier si, et de quelle manière, les niveaux piézométriques mesurés dans l'aquifère alluvial varient avec l'évolution du débit dans la rivière au cours de la période de mesure. Cette question a déjà été abordée par Cloutier et al. (2014) mais basée sur seulement 6 % (sept épisodes de crues) de la période couverte par la base de données actuelle. La base de données prise dans son entièreté permettrait-elle d'avoir un nouvel éclairage sur cette question spécifique ?

Les niveaux piézométriques mesurés dans chaque piézomètre ont ainsi été confrontés au niveau mesuré dans la station de jaugeage (Fig. 28). Les niveaux piézométriques augmentent lorsque le débit de la rivière augmente. Cette observation est confortée par le

calcul des coefficients de corrélation de Spearman. À l'exception des piézomètres D769 et D813 (voir la Fig. 27 pour leur localisation), situés aux deux extrémités de la plaine d'inondation, tous les coefficients sont supérieurs à 0.6 indiquant une relation de dépendance significative entre les variations de niveau des eaux souterraines de la plaine alluviale et les variations de débit à l'amont de la rivière. Sur les 10 ans d'observation, les niveaux piézométriques augmentent avec le niveau de l'eau dans la rivière.

Cependant, un examen détaillé révèle que cette relation est significative tant que les altitudes de l'eau dans la rivière sont supérieures à 61.3 m, c.-à-d. l'altitude maximale du débit de plein bord dans la rivière (i.e. 350 $m^3 \cdot s^{-1}$). Lors de l'épisode de crue du début de l'année 2018 (du 20 au 27 janvier), par exemple, le niveau de la rivière est rapidement passé de 59.9 à 65.7 m avant de redescendre brutalement à son niveau initial. Cette augmentation brutale et ponctuelle ne s'est pas accompagnée d'une élévation du niveau piézométrique dans l'aquifère alluvial. Sur les 10 ans d'enregistrement, un épisode d'une telle ampleur ne s'est produit qu'une fois. Cette différence de comportement pourrait traduire une déconnexion ou une connexion ralentie entre la rivière et l'aquifère pour certains épisodes de crue « éclaire ». Les conditions hivernales et le gel du sol à cette période de l'année pourraient avoir induit une baisse de la conductivité hydraulique du sol et ralentir ainsi les infiltrations (Daniel et Staricka, 2000; Williams et Burt, 1974).
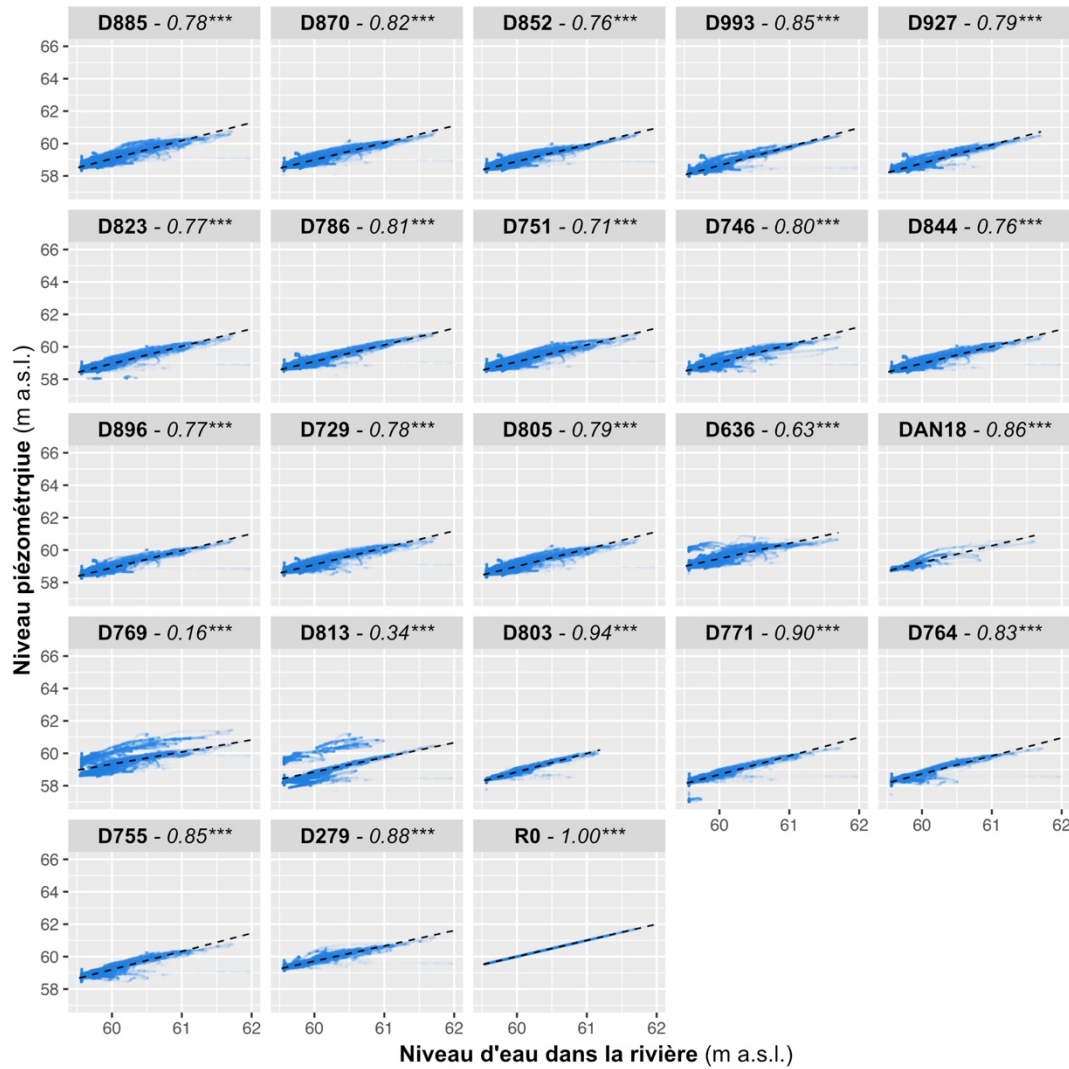
Figure 28. Niveaux piézométriques mesurés dans les différents piézomètres sur le méandre de la rivière Matane en fonction du niveau de la rivière en amont du méandre pour les données inférieures au débit de plein bord (61.3 m). Chaque observation est représentée par un point bleu avec une opacité de 3 % de telle sorte que l'intensité de la couleur soit représentative de la fréquence de l'observation dans le graphique. Le coefficient ρ de Spearman calculé pour chaque graphique est indiqué à la suite du nom du point d'observation (voir Fig. 27). Tous les tests de corrélation se sont révélés significatifs avec des p-values inférieures à 0,001.

Mis à part cet évènement de crue « éclair », l'évolution conjointe des niveaux piézométriques avec le niveau de l'eau dans la rivière est robuste. Cette étude en deux dimensions permet d'établir une relation fonctionnelle, mais ne permet cependant pas d'avoir

d'indications de causalité : les deux milieux peuvent réagir ensemble sous la pression d'un processus tiers, mais la variation d'un des milieux pourrait également contrôler les variations observées dans l'autre. Pour aller plus loin, d'autres paramètres peuvent être comparés en ajoutant par exemple une dimension temporelle pour analyser le décalage dans les variations (Cloutier et al., 2014) ou en ajoutant une dimension spatiale pour déterminer un sens d'écoulement (Biehler *et al.*, en révision).

3.4.4 Analyse à trois dimensions : Quelles sont les directions d'écoulement des eaux souterraines dans la plaine d'inondation à un débit de rivière donné ?

L'ajout d'une dimension spatiale dans l'analyse de la connectivité entre les eaux souterraines et les eaux de surface permet la production de cartes de niveau piézométrique. Ainsi, en plus de lier les niveaux d'eau dans la rivière à ceux dans l'aquifère, la position de chaque observation à un temps donné permet de déterminer le sens d'écoulement de la masse d'eau dans un continuum. Ici, par exemple, nous allons chercher à qualifier l'évolution temporelle de la direction des écoulements et établir des débits seuil d'apparition d'inondation par exfiltration. Cette question a déjà été abordée par Cloutier *et al.* (2014) et Buffin-Bélanger *et al.* (2015), mais en se basant respectivement sur 7 et 54 épisodes de crue entre juin et décembre 2011 et entre juin 2011 et septembre 2014. L'utilisation de la base de données complète donne accès à de nombreux exemples de crues d'intensités différentes. Ainsi, pour l'exercice, cinq cartes ont ici été produites correspondant à cinq états hydrologiques de la rivière observés entre 2013 et 2018 : depuis un état d'étiage ($14\ m^3 \cdot s^{-1}$ – Fig. 29a, mars 2013) jusqu'à un état de crue proche du débit de plein bord ($338\ m^3 \cdot s^{-1}$ - Fig. 29e, mai 2018). Pour contraindre la partie Sud de l'interpolation, des niveaux d'eau prédits dans la rivière ont été calculés à partir des niveaux mesurés dans la station de jaugeage en les corrigeant pour se conformer à la topographie de la rivière.

Les mesures de niveau d'eau dans la plaine sont interpolées de manière à obtenir un aperçu de la surface piézométrique en tout point de la plaine d'inondation. La grande densité

de points d'observation dans le méandre nous permet d'utiliser de manière relativement fiable la méthode d'interpolation par l'inverse de la distance pondérée. À la différence du krigeage qui implique la création d'un modèle statistique, cette méthode permet de représenter simplement des valeurs prédites entre les points d'observation en fonction de la proximité avec ces derniers.
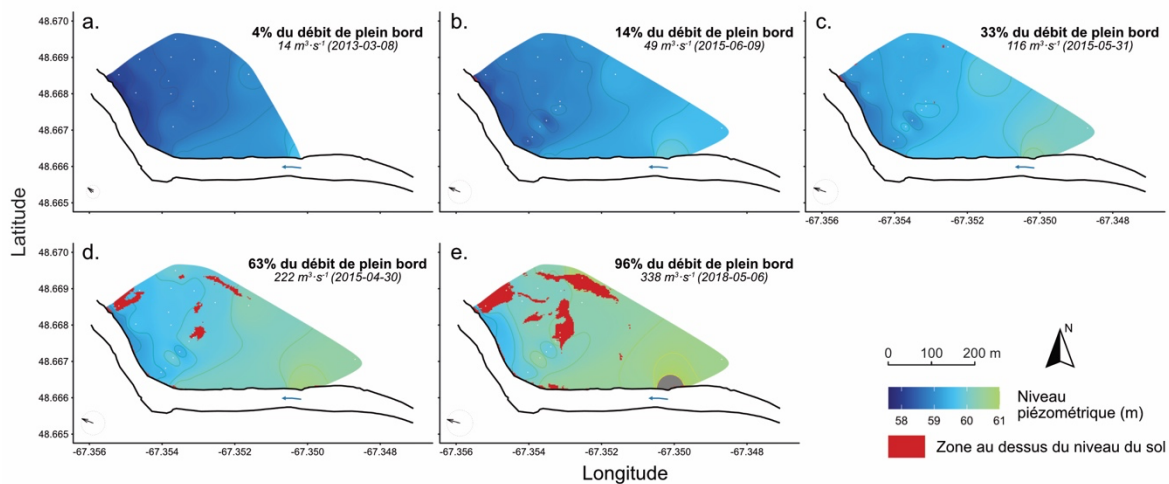
Figure 29. Cartes piézométriques réalisées par interpolations (inverse à la distance) des niveaux piézométriques dans les piézomètres (points blancs) pour différentes dates : a) mars 2013, b) avril 2015, c) mai 2015, d) juin 2015 et e) mai 2018). Les isohypses sont espacées de 0,25 m. Les zones en rouge sont les zones où le niveau piézométrique est supérieur à celui du sol (obtenu par relevé LiDAR) et où des inondations par exfiltration de la nappe d'eau souterraine sont probables. La zone grise en e. correspond au dépassement du débit de plein bord. La flèche incluse dans le cercle pointillé représente la direction et l'intensité relative du gradient d'écoulement au sein de l'aquifère alluvial.

Comme reporté précédemment, le niveau global de la nappe souterraine augmente avec le niveau de l'eau dans la rivière (Fig. 28). On observe cependant que cette augmentation n'est pas homogène dans la plaine. Quel que soit le débit, les niveaux piézométriques les plus faibles sont systématiquement proches de la rive, en aval de la zone d'étude, avec un gradient hydraulique qui va de la plaine vers la rivière. Deux grandes orientations semblent guider les gradients piézométriques. Un premier gradient, de l'Est vers Ouest, se met en place dans la moitié amont jusqu'à l'apex du méandre, surtout supporté par le piézomètre D279 et GS, qui indique une recharge de l'aquifère via l'infiltration d'eau de surface dans l'aquifère, mais

aussi via la propagation d'onde de crue comme déjà observée par Cloutier et al. (2014) et Buffin-Bélanger et al. (2015). Ce gradient est combiné à un second de direction Nord-Est vers Sud-Ouest conforme à la direction d'écoulement régional de la nappe d'eau souterraine. La résultante de ces deux composantes se traduit par un gradient de relativement faible intensité à l'étiage (~3 ‰ ; Fig. 29a) qui, dans les exemples présentés, augmente à mesure que le débit de la rivière augmente (~5 ‰ ; Fig. 29b à 29e.). Cette variabilité spatiotemporelle du gradient piézométrique met de l'avant une relation de co-influence : le niveau piézométrique dans l'aquifère alluvial est influencé par les différences de débit dans la rivière et une recharge provenant de l'écoulement souterrain dans le bassin versant. La topographie de la surface piézométrique résultante indique par ailleurs une décharge continue de l'eau souterraine dans la rivière dans la moitié aval du méandre depuis l'apex du méandre quel que soit le débit.

Ce système de représentation en trois dimensions permet de visualiser la topographie de la surface piézométrique au sein de la plaine alluviale et d'en déduire les caractéristiques de l'écoulement à un temps donné. Cependant, la figure 29 montre que cette piézométrie n'est pas stable dans le temps tant en matière d'altitude moyenne, de morphologie, ou de direction et d'intensité du gradient d'écoulement moyen. Sur les exemples, cette variabilité des caractéristiques de la surface piézométrique présente des impacts concrets au travers d'inondations par exfiltration de la nappe qui apparaissent déjà de manière ponctuelle pour un débit équivalent à 33 % du débit de plein bord soit 116 $m^3 \cdot s^{-1}$ (Fig. 29c). Les zones d'inondation s'étendent ensuite pour des débits plus élevés (Fig. 29d et 29e). Le débit à partir duquel ces inondations sont visualisées ici est très inférieur à celui déterminé par Cloutier *et al.* (2014) qui l'établissaient à 238 $m^3 \cdot s^{-1}$ basé sur un évènement particulier de crue (5 au 7 septembre 2011). Ce seuil est en revanche supérieur à celui observé par Buffin-Bélanger *et al.* (2015) qui établissaient la première inondation par exfiltration de nappe à partir de 40 $m^3 \cdot s^{-1}$. Ces inondations sont contrôlées à la fois par les variations de l'état hydrique de la rivière et par l'altitude initiale du niveau piézométrique (Buffin-Bélanger et al., 2015c). Ces deux forçages sont eux-mêmes liés aux quantités de précipitations reçues par le bassin versant

ainsi qu'à la vitesse de la fonte du couvert neigeux. Une telle représentation de la surface piézométrique est donc dépendante d'un évènement et d'un état particulier de l'aquifère et ne représente donc pas forcément une généralisation des variations du niveau piézométrique pour une saison donnée. Les différences de valeurs seuils de débits liés à une inondation par exfiltration de la nappe sont tributaires du choix des crues étudiées. Ainsi, une base de données sur une période de 10 ans permet d'avoir accès à plus de situations différentes, mais rend longue et fastidieuse une analyse systématique de chacune des crues. Les résultats d'une telle étude sont donc dépendants des critères de sélection des crues choisis par l'analyseur et ne représentent pas forcément la réalité de la variabilité de la surface piézométrique.

3.4.5 Analyse à quatre dimensions : Quelle est la variabilité temporelle saisonnière de la surface piézométrique au sein de la plaine d'inondation ?

La variabilité de la connectivité hydrologique entre la rivière et l'aquifère alluvial a déjà été abordée par Biehler et al. (2020) en combinant une base de données géochimique (eau souterraine et d'eau de surface, 9 campagnes d'échantillonnage) à une base de données piézométrique. Ici nous cherchons à déterminer grâce à la base de données complète si une variabilité saisonnière ou annuelle peut être observée dans la surface piézométrique. Une manière d'ajouter la dimension temporelle dans la représentation de la base de données consiste à analyser une variabilité au cours du temps. Ainsi, la figure 30 ne présente plus l'altitude des niveaux piézométriques dans la plaine, mais l'amplitude de variation de cette altitude (représentée par son écart interquartile) sur une période donnée. La dimension temporelle et la dimension d'altitude sont donc combinées au sein d'une nouvelle dimension utilisée pour représenter la base de données. La figure 30 présente cette variation au sein de l'aquifère alluvial en hiver (21 décembre au 20 mars, Fig. 30a), au printemps (21 mars au 20 juin, Fig. 30b), en été (21 juin au 20 septembre, Fig. 30c), en automne (21 septembre au 20 décembre, Fig. 30d), et sur une période annuelle (intégralité de la base de données 2011-2019, Fig. 30e). Un écart interquartile fort indique une forte dispersion des données du

piézomètre au cours du temps et donc beaucoup de variabilité. À l'inverse, un écart interquartile faible traduit des données d'altitude piézométrique relativement stables.

Globalement au cours des saisons, l'hiver, l'été, et l'automne apparaissent comme les périodes où les niveaux piézométriques restent les plus stables dans l'aquifère alluvial. Des zones de plus forte variabilité sont cependant observées proche de l'apex du méandre en hiver et, à moindre échelle, en automne. Une forte variabilité est également observée à toutes les périodes dans le piézomètre D769 qui se trouve dans une dépression topographique dans un paléochenal (Fig. 27a et 27b). À l'automne une zone de plus forte variabilité est aussi observée dans le fond de la plaine. En été (Fig. 30c), l'altitude du niveau piézométrique dans la plaine est stable avec un écart interquartile médian de 0.16 m contre 0.26 et 0.23 m en automne et en hiver respectivement. Le printemps est la saison où le plus de variabilité de niveau piézométrique est observée avec un écart interquartile médian de 0.77 m. Cette variabilité est plus importante proche de la rivière avec un maximum de variation de 1.16 m à l'apex du méandre (piézomètre D813). À l'échelle annuelle (Fig. 30e), on retrouve les mêmes zones de variabilité à l'apex et en fond de plaine, avec une variabilité globale plus élevée qu'en été, en automne, et en hiver (écart interquartile médian de 0.35 m). Les variations de niveaux piézométriques semblent ainsi suivre un patron saisonnier probablement contrôlé par des forçages hydroclimatiques locaux (débit de la rivière) et régionaux (recharge de l'aquifère régional). En hiver et au printemps, l'influence de la rivière semble dominer les variations de niveau piézométrique dans l'aquifère alluvial tandis qu'à l'été et à l'automne l'influence de la rivière semble être de moindre importance relativement à l'influence de l'écoulement régional des eaux souterraines du bassin versant.

Cette représentation, bien qu'occultant le niveau absolu d'élévation de la nappe d'eau souterraine, permet d'obtenir des informations sur la dynamique temporelle et spatiale des niveaux piézométriques. Elle met de l'avant les deux principaux forçages contrôlant l'élévation de la nappe et surtout la variabilité de leur influence respective au cours du temps (ici des saisons). Le forçage local par les niveaux d'eau dans la rivière en hiver et au printemps joue un rôle crucial dans l'élévation des niveaux piézométriques. L'importance de

ce forçage se matérialise sur le terrain par les variations de débit de la rivière qui peuvent être très rapides. Cependant, ce mode de représentation écrase la dimension temporelle sur une période donnée. Selon l'intervalle de temps choisi, il ne permet donc pas d'apprécier la réactivité de la variation de la surface piézométrique vis-à-vis des variations brutales de débit en rivière.
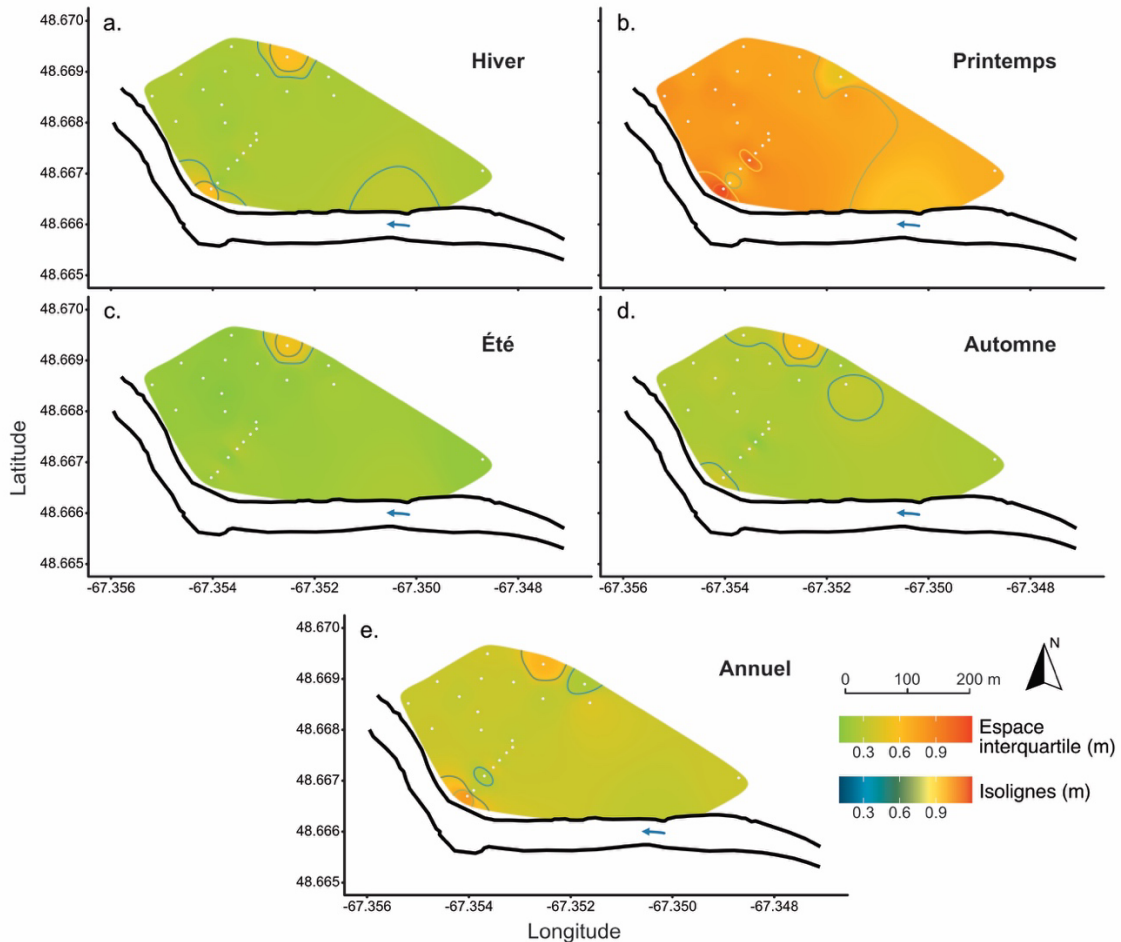
Figure 30. Variabilité des niveaux piézométriques au sein de la plaine d'inondation sur la rivière Matane sur la période 2011 - 2019. La variabilité est représentée par les espaces interquartiles calculés pour chaque piézomètre (a.) en hiver, (b.) au printemps, (c.) en été, (d.) à l'automne, et (e.) pour l'année entière. Ces données sont interpolées par la méthode inverse à la distance de manière à estimer la variabilité sur la surface totale de la nappe dans le méandre.

3.4.6 Analyse à cinq dimensions : Quelle est la réactivité de la surface piézométrique vis-à-vis des variations pluriannuelles de débits dans un contexte d'inondations par exfiltration de nappe ?

Une analyse de la vitesse de réaction de la surface piézométrique vis-à-vis d'une perturbation plus ou moins rapide du débit de la rivière nécessite un suivi à haute fréquence temporelle des niveaux piézométriques dans tous les piézomètres. Ainsi par exemple, il serait possible de représenter la crue de mai 2015 au travers de 3 cartes successives montrant l'état initial de la nappe, son état au pic de la crue et enfin son état après la crue (Fig. 31a). On voit alors simplement une augmentation du niveau piézométrique global causant des inondations par exfiltrations avec une réorientation de la direction d'écoulement vers le Nord suivi d'un retour vers la direction initiale. Cependant, cette analyse à 3 dimensions lisse l'épisode de crue (Fig. 31b). Les passages des niveaux d'eau dans la rivière de a.1 à a.2 puis à a.3 comportent de nombreux pulses successifs auxquels l'aquifère devrait répondre, mais l'intervalle de temps choisi entre les cartes ne permet pas d'apprécier ces réponses. Ainsi, à la différence d'une analyse en deux dimensions où on comparerait l'évolution de chaque niveau piézométrique pour déterminer un délai de transfert du pic de crue aux piézomètres comme présenté par Cloutier et al. (2014) sur 7 évènements de crues, l'objectif de cette section est de quantifier la vitesse de variation de l'intensité et du gradient de l'écoulement de la nappe. Il s'agit de générer des cartes piézométriques de l'état de la surface à des moments rapprochés et de les comparer au sein d'une série temporelle (time lapse). Le script d'interpolation par l'inverse à la distance pondéré utilisé pour générer les cartes piézométriques (e.g. Fig. 29) a été inclus au sein d'une structure itérative automatisant la génération de cartes avec un intervalle temporel de 4h (i.e. 6 cartes par jour). Ces 17 423 cartes piézométriques mises à la suite les unes des autres à une fréquence de 24 images par seconde permettent la création d'une vidéo (Fig. 31c) reflétant l'état de la surface piézométrique au cours du temps à une vitesse de 4 jours par secondes. En parallèle de l'interprétation visuelle, une approximation linéaire de la surface piézométrique est calculée de manière à déterminer, pour chaque itération, la direction générale d'écoulement de cette

surface piézométrique simplifiée ainsi que son gradient maximum selon la ligne de plus grande pente. Ce gradient est utilisé en tant qu'approximation de l'intensité du gradient d'écoulement simplifié.
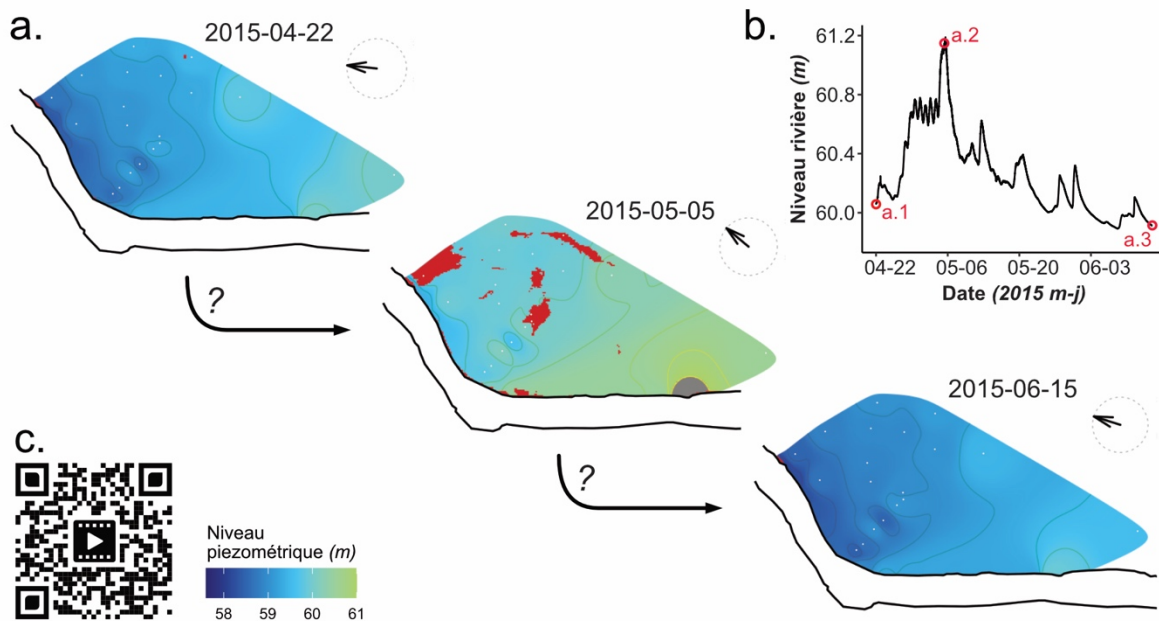
Figure 31. Évolution de la surface piézométrique au cours du temps (a.) pour la crue du 22 avril au 15 juin 2015 associée (b.) au niveau d'eau mesuré à la station de jaugeage (GS, Fig. 27) ; et (c.) pour l'ensemble de la période couverte par la base de données. Les zones rouges correspondent aux zones potentiellement inondées par exfiltration de la nappe d'eau souterraine. Le QRcode à scanner avec un téléphone intelligent ou une tablette informatique renvoie à la vidéo sur le site : https://youtu.be/8XREsxBwmfs

La visualisation de la base de données sous format vidéo permet dans un premier temps d'observer globalement le comportement de la nappe d'eau souterraine par rapport au niveau d'eau dans la rivière au sein de la plaine alluviale. Les zones où l'altitude est la plus basse et où convergent les eaux souterraines restent localisées dans la zone aval du méandre près de la rivière. Les zones de résurgence probable d'eau souterraine vers la rivière sont ainsi directement visibles et on peut s'attendre à une décharge maximale après l'apex du méandre (Fig. 31c). De la même manière, on visualise le lien étroit entre les variations de niveau d'eau dans la rivière et le comportement de la nappe sur l'ensemble du méandre. Ainsi en reprenant

l'exemple de la crue de mai 2015 (Fig. 31c : 5min36 à 5min49), la représentation vidéo montre bien les oscillations d'altitudes successives dans l'aquifère alluvial. La nappe souterraine atteint la limite de la topographie dès le 28 avril. Des inondations potentielles par exfiltration de la nappe sont observées dès le lendemain et se maintiennent jusqu'au 4 mai. Les zones submergées s'étendent ensuite ponctuellement lors du pic de la crue le 5 mai avant de progressivement décroitre les quatre jours suivants. S'ensuit une période d'oscillation où ces inondations réapparaissent partiellement en fonction des variations de niveau d'eau dans la rivière avant de totalement disparaitre dix jours après le pic de la crue. La réorientation de la direction de l'écoulement général réagit, elle aussi, par pulses successifs, traduisant une réactivité très importante de l'aquifère face aux variations de débit dans la rivière.

Par ailleurs, au-delà de la simple observation du comportement de la nappe d'eau souterraine, cette méthode permet de générer un nouvel objet d'étude, à savoir l'évolution au cours du temps de cette surface et de ses caractéristiques. La figure 32 représente ainsi, avec une résolution au 15 minutes et pour l'exemple de la crue de mars 2012, l'évolution de l'intensité de l'écoulement simplifié, sa direction, la proportion de surface potentiellement inondée par des exfiltrations dans la plaine alluviale et le niveau de la rivière. Au cours de la crue, les variations de l'intensité de l'écoulement semblent fortement liées à l'évolution de la direction du gradient général. Des variations d'intensité et de directions d'écoulement se produisent dès les premières augmentations dans le niveau de la rivière le 19 mars. Alors que l'augmentation du débit est relativement lisse, la surface piézométrique réagit par des pulses positifs d'intensité et de réorientation vers le Nord de la direction d'écoulement de la nappe jusqu'au pic de la crue entre le 22 et le 23 mars. Cette augmentation du débit se matérialise en surface par des inondations potentielles à partir du 21 mars pour une altitude de l'eau à la station de jaugeage d'environ 60,3 m. À partir de ce moment, la surface inondée augmente jusqu'au pic de crue. Une fois l'inondation passée, on observe un rééquilibrage de l'aquifère vis-à-vis de la rivière avec une modification rapide de la direction de l'écoulement vers le Sud-Ouest. Cette réorientation est accompagnée d'une diminution de l'intensité du gradient d'écoulement dans la première moitié de la réorientation, suivi d'une augmentation de

l'intensité dans sa seconde partie. Les deux paramètres de la surface piézométrique tendent ensuite progressivement à retrouver leurs valeurs d'origine. Cette dynamique semble traduire un phénomène de rebond post-crue de rééquilibrage des niveaux d'eau. Le niveau piézométrique dans la plaine augmente du fait de l'élévation du niveau de l'eau dans la rivière. Lors de la décrue, la composante « rivière » du gradient piézométrique diminue et l'eau accumulée dans la plaine se décharge vers la rivière selon le gradient d'écoulement régional. La dynamique asymétrique de l'évolution des surfaces potentiellement inondées dans le méandre (Fig. 32c) semble indiquer que contrairement à l'augmentation rapide des niveaux dans la plaine lors de la crue, le retour à des élévations « normales » et donc le rééquilibrage des niveaux piézométrique dans la plaine est plus progressif.
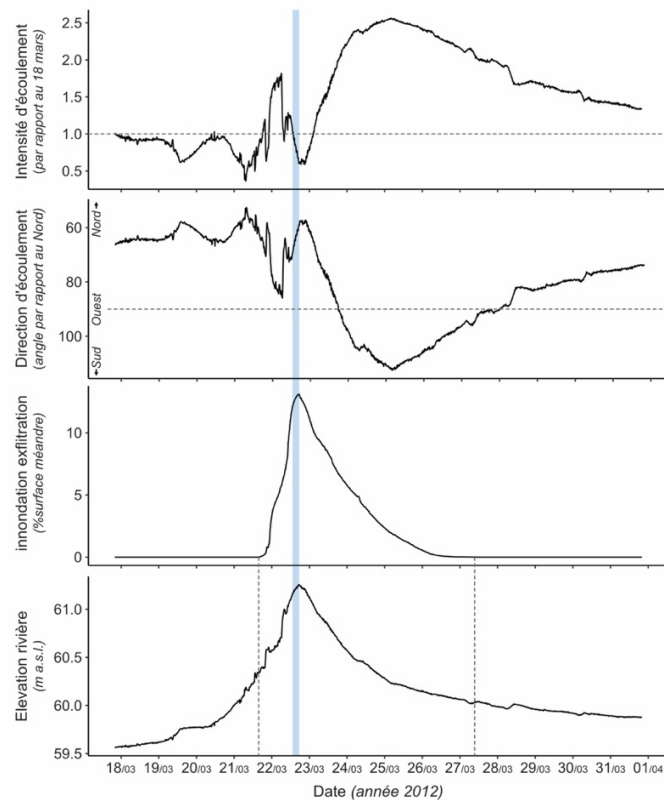
Figure 32. Évolution aux quinze minutes de a. l'intensité relative de l'écoulement souterrain (définie en 2.6) par rapport au début de la crue, b. la direction de l'écoulement, c. la surface potentiellement inondée par exfiltration de la nappe d'eau souterraine et de d. l'élévation de la rivière au cours de la crue du 18 mars au 1er avril 2012. La zone bleue correspond au pic de la crue.

Cette analyse en cinq dimensions de la base de données ne se focalise donc pas uniquement sur les données collectées. Elle utilise les données pour générer un nouvel objet d'étude qui lui-même peut être analysé de manière à poser de nouvelles questions et à y apporter de nouvelles réponses.

3.4.7 Bilan sur l'exploitation de la base de données

Les exemples précédents montrent qu'une réutilisation d'une base de données établie sur du long terme peut permettre de confirmer, d'infirmer, ou voire de peaufiner, des interprétations déjà obtenues mais aussi d'en évaluer la portée. Ainsi, la connectivité entre l'eau de surface et l'eau de la rivière a été clairement établie ici. Cependant certains évènements tels que la crue du 20 au 27 janvier 2018, ou encore certaines zones du méandre telles qu'au niveau du piézomètre D769, semblent faire exception aux règles générales. Une focalisation de l'étude sur ces seules exceptions aurait pu conduire à des résultats totalement différents et, peut-être, à une généralisation abusive des dynamiques proposées. La mise en évidence de ces « anomalies » permet de poser de nouvelles questions. On pourra ainsi s'interroger sur la dynamique d'une plaine alluviale dont la partie supérieure du sol gelé est recouverte d'un important couvert neigeux lors d'une crue hivernale de forte intensité ; ou encore sur l'importance d'un paléoméandre sur la recharge d'un aquifère alluvial. La réutilisation de la base de données a également permis de traiter de problèmes similaires en mobilisant d'autres méthodes d'analyse plus adaptées à une étude de longues périodes de temps telles que les cartes de variabilité, la visualisation par vidéo, ou encore la modélisation à haute fréquence de l'approximation des caractéristiques de la surface piézométrique. Ces techniques complémentaires permettent d'approfondir les connaissances déjà acquises et parfois de mettre en évidence des processus non visibles dans les analyses précédentes.

Cette possibilité de mobilisation de techniques complémentaires et de visualisation de problématiques connexes aux questions déjà étudiées est au centre de la philosophie d'un

partage de données. L'apport d'un regard extérieur, libre des questionnements originels et s'appuyant sur les travaux déjà effectués, peut permettre d'approfondir les réponses apportées à une question de recherche donnée et d'élargir le champ d'action de la base de données via de possibles intégrations inter- et trans- disciplinaires.

3.5 POSSIBILITÉS DE PUBLICATION DE BASES DE DONNÉES DANS LA RECHERCHE SCIENTIFIQUE ET DANS LE DOMAINE DE LA CONNECTIVITÉ EAU SOUTERRAINE – RIVIÈRE

3.5.1 Disponibilité et utilisation des bases de données dans la connectivité eau souterraine – rivière

3.5.1.1 Répertoire de base de données et certifications

Un partage efficace des bases de données nécessite des infrastructures spécifiques, durables, et fiables permettant à la fois de naviguer simplement entre les publications, et une soumission facilitée des données (Pampel et al., 2013). De nombreux répertoires de bases de données spécialisées ou généralistes sont déjà disponibles. Ainsi depuis sa mise en ligne en 2012, le registre re3data.org recense en mai 2022 2 872 répertoires de bases de données, tous domaines confondus, dont 805 dans les domaines des géosciences. Sur ces 805 répertoires, 687 se présentent comme permettant un libre accès aux données. Devant cette diversité, le choix d'un répertoire de bases de données doit alors se fonder sur les objectifs de publication qui seront retenus. Un répertoire généraliste permet la publication de tout type de base de données, quel que soit le champ de discipline. Il permet ainsi la publication de données issues d'études pour lesquelles des répertoires spécifiques n'existent pas encore (Xafis et Labude, 2019). En s'affranchissant des arrangements disciplinaires (Assante et al., 2016), un répertoire généraliste peut présenter moins de contraintes de renseignements et s'adapte donc relativement facilement à toute forme de base de données. Pour les utilisateurs, le vaste assemblage de bases de données répertoriées dans différents domaines pourrait favoriser les

études trans- ou multidisciplinaires. Cependant, l'absence de spécialisation dans les métadonnées peut à l'inverse « noyer » une base de données au milieu des autres et compliquer la recherche de bases sur un sujet ou un lieu précis (National Academies of Sciences Engineering and Medicine et al., 2020). Un répertoire disciplinaire pour sa part permet des recherches plus ciblées sur un sujet. Souvent, ces répertoires, parfois mieux implantés dans une communauté scientifique particulière, peuvent être plus consultés au sein de disciplines spécifiques du fait d'habitudes ou par simplicité. En s'adressant à un répertoire qui comprend et a l'habitude d'un certain type de données, le processus de révision est plus robuste et les métadonnées demandées plus pertinentes que dans un répertoire généraliste (Lyle, 2017). Au-delà de la portée donnée aux jeux de données, l'assurance d'un partage respectant les principes FAIR joue également un rôle important dans le choix du répertoire. Dans ce cadre, différentes certifications permettent de faire un tri dans les répertoires disponibles. La plus commune est la certification CoreTrustSeal. Cette certification créée en 2017 reprend les critères de l'association World Data System et de la certification Data Seal of Approval associant les principes FAIR à une volonté d'identifier les répertoires de bases de données dignes de confiance (L'Hours et al., 2019). Afin d'être certifié, le répertoire de bases de données doit prouver à des évaluateurs indépendants qu'il répond à 16 critères portant sur l'organisation en elle-même, la gestion des objets numériques entreposés, et la technologie utilisée (Table 8). Ainsi, sur les 805 répertoires de bases de données en géosciences recensés par re3data.org, seulement 75 répondent aux exigences de la certification CoreTrustSeal.

Tableau 8. Critères à respecter pour qu'un répertoire de bases de données obtiennent la certification CoreTrustSeal garantissant une gestion selon les principes FAIR de partage de bases de données. (CoreTrustSeal Standards and Certification Board, 2019).

Secteur	Objet	Description
Infrastructure de l'organisation	Mission / objectif	Le répertoire a pour mission explicite de fournir un accès et de préserver les données dans son domaine
	Licences	Le répertoire maintient toutes les licences applicables couvrant l'accès et l'utilisation des données et en assure la conformité
	Continuité d'accès	Le répertoire dispose d'un plan de continuité de manière à assurer l'accès continu et la préservation de son contenu
	Confidentialité / éthique	Dans la mesure du possible, le répertoire s'assure que les données sont générées, sélectionnées, mis à disposition et utilisés en accord avec les normes disciplinaires et éthiques
	Infrastructure organisationnelle	Le répertoire dispose des fonds adéquats et d'un nombre suffisant de personnel géré par un système de gouvernance clair pour efficacement mener à bien la mission
	Conseil spécialisé	Le répertoire adopte des mécanismes pour sécuriser un conseil et un feedback continu (soit interne, soit externe, incluant, si pertinent, un conseil scientifique)
Gestion de l'objet numérique	Intégrité et authenticité des données	Le répertoire garantit l'intégrité et l'authenticité des données
	Évaluation	Le répertoire accepte des données et des métadonnées basées sur des critères définis assurant leur pertinence et leur intelligibilité pour l'utilisateur des données
	Procédure de stockage des documents	Le répertoire applique des modalités et procédures documentées dans la gestion de l'archivage des données
	Plan de préservation	Le répertoire assume la responsabilité de la préservation sur le long terme et gère cette fonction de manière planifiée et documentée
	Qualité des données	Le répertoire dispose de l'expertise appropriée pour évaluer la qualité des données techniques et des métadonnées et s'assure qu'une information suffisante est disponible pour que l'utilisateur final puisse évaluer la qualité des données
	Workflow	L'archivage est réalisé en accord avec un workflow défini depuis le dépôt jusqu'à la dissémination des données
	Découverte et identification des données	Le répertoire permet aux utilisateurs de découvrir les données et se réfère à celle-ci à travers une citation appropriée et permanente
	Réutilisation des données	Le répertoire permet la réutilisation des données au cours du temps, en s'assurant que des métadonnées appropriées sont disponible pour supporter l'intelligibilité et l'utilisation des données
Technologie	Infrastructure technique	Le répertoire fonctionne sur des systèmes opérationnels pertinents et sur d'autres logiciels d'infrastructure interne et utilise des technologies informatiques matériel et logiciel approprié aux services qu'il fournit à sa communauté cible
	Sécurité	L'infrastructure technique du répertoire assure la protection de l'installation et de ces données, produits et utilisateurs

3.5.1.2   Importance des métadonnées

Au sein de ces répertoires, les principes FAIR et particulièrement la notion de découverte (Findable) de bases de données nécessitent que l'utilisateur soit capable de trouver simplement des données (Garnett et al., 2017). Le simple jeu de données ne laisse dans ce cadre que peu de possibilité de résultats au sein d'une recherche par mots-clés ou par domaines. Des informations complémentaires expliquant la base de données sont ainsi nécessaires : des métadonnées explicitant ce que sont les mesures ou analyses, où et quand elles ont été prises, comment elles ont été prises, et qui les a prises. En fournissant ces informations lors de la soumission au répertoire ainsi que différents mots-clés associés au jeu de données, une simple recherche dans le répertoire permet de renvoyer vers une sélection de bases de données liées au domaine ou au lieu de recherche. Les métadonnées sont donc un outil important de visibilité dans le cadre d'un partage des bases de données.

Au-delà de cette fonction de visibilité, la présence de métadonnées détaillées permet également aux utilisateurs de comprendre d'où proviennent les données qui leur sont fournies (Van Noorden, 2013). Une description de la base de données de bonne qualité et des métadonnées bien définies apparaissent comme les attributs les plus importants dans le cadre d'une stratégie d'ouverture des bases de données (Schmidt et al., 2016). Avec des informations claires sur les méthodes de prélèvement et d'analyse, les utilisateurs pourront ainsi méthodologiquement les inclure de manière fiable et raisonnée dans leurs propres études et ainsi adéquatement réutiliser une base de données sans risquer par exemple des comparaisons abusives. La richesse des métadonnées fournies influe ainsi directement sur le respect du quatrième principe FAIR demandant l'optimisation des possibilités de réutilisation de la base de données.

3.5.2 Vers une généralisation de la publication des bases de données ?

Le partage de base de données est une étape de plus dans la transformation du monde scientifique vers une recherche ouverte, transparente et accessible. Récemment, cette aspiration au changement a été réaffirmée lors de la 40e session de la conférence générale de l'UNESCO (Organisation des Nations Unies pour l'éducation, la science et la culture) en 2019 avec l'adoption en 2021 de recommandations pour une science ouverte. Ces recommandations décrivent les connaissances scientifiques ouvertes comme désignant le libre accès, entre autres, aux publications scientifiques, aux données de recherche, et aux métadonnées de manière rapide, universelle, et gratuite (UNESCO, 2021). Pourtant, une comparaison sur *Dimension.ai*[3] du nombre d'articles scientifiques et du nombre de bases de données montre que les bases de données ne représentent que 17 % du total d'articles scientifiques publiés depuis 2010 avec 60 022 497 articles scientifiques pour 10 429 638 jeux de données recensés (en mai 2022). Ce pourcentage devient quasiment nul pour réponses aux mots clés « groundwater », « river » et « connectivity » avec 54 231 articles pour 15 bases de données publiées depuis 2010 (en mai 2022). La publication de bases de données reste donc une pratique limitée dans la communauté scientifique en hydrogéologie notamment. Cette volonté de normalisation du partage de données se confronte en effet à des barrières méthodologiques, légales et techniques (Assante et al., 2016), ou encore à des barrières culturelles (Digital Science et al., 2021) parfois profondément ancrées dans le monde de la recherche scientifique. Ainsi une enquête réalisée auprès de 4491 chercheurs dans 192 pays différents dans le cadre du rapport sur l'état de la donnée ouverte (Digital Science et al., 2021) indique que les principaux freins au partage de données scientifiques sont la crainte d'une mauvaise utilisation des données, la crainte de ne pas recevoir suffisamment de crédit pour les données partagées, et l'incertitude concernant les licences associées aux données. Par ailleurs, une autre enquête (Stuart et al., 2018) réalisée auprès de 365 chercheurs dans le

---

[3] Application internet portée par Digital Science recensant les objets numériques à portée scientifique doté d'un identifiant permanent (Hook et al., 2018).

domaine des Sciences de la Terre souligne que la difficulté d'organiser ses données de manière utile et présentable est un problème pour 49 % des répondants dans le cadre d'un partage des données. Face à ces difficultés, de nombreux journaux de publications scientifiques ont fait le choix d'inciter à plus de transparence dans la diffusion des données scientifiques (Candela et al., 2015). Des journaux comme Biogeochemistry, Soil, Biogeosciences, Geochimica et Cosmochimica Acta, ou encore Journal of Hydrology encouragent ou imposent ainsi soit la publication des données associées aux études qu'ils publient, soit la rédaction d'une *déclaration de disponibilité des données* permettant de définir où sont les données et sous quelles conditions il est possible d'y accéder. Cette stratégie d'obligation d'archivage et de mise à disposition des données de recherche augmente de près de 974 fois les chances qu'une personne extérieure obtienne un accès aux données de recherches en comparaison avec des publications scientifiques sans politique d'accès aux données (Vines et al., 2013). Il s'agit ainsi d'une stratégie efficace d'incitation du monde de la recherche scientifique au partage des bases de données de recherche (Thelwall et Kousha, 2017). Au niveau réglementaire, certaines agences gouvernementales aux États-Unis, au Royaume-Uni, ou encore à l'échelle de l'Union européenne ont également décidé de conditionner l'attribution de financements sous réserve d'un partage de données découlant des études (Lin et Strasser, 2014). Au Canada, les trois principales agences gouvernementales de financement de la recherche (IRSC, CRSNG, et CRSH) ont également décidé à partir de mars 2021 qu'un plan de gestion des données clair devrait être inclus dans les demandes de certains financements. Cet éclaircissement sur la gestion de données issues de financement public devrait être par la suite généralisé aux autres financements accordés par les trois agences (Interagency research funding, 2021).

Malgré les difficultés d'implantation, la communauté scientifique s'accorde à dire qu'un partage généralisé des données de recherche accélérerait la performance des Sciences (Candela et al., 2015; Van Noorden, 2013). À titre personnel pour le chercheur, un partage de ses données scientifiques selon les principes FAIR peut se traduire par plus de possibilités de citation de ses travaux et donc une plus grande visibilité pour ses recherches (Molloy,

2011; Piwowar et al., 2007). Au niveau plus large de la recherche scientifique, le partage des données peut représenter une opportunité pour d'autres équipes, de la même discipline ou non, de considérer différemment un phénomène ou une problématique en appliquant de nouvelles analyses au jeu de données, ou en l'associant à une base de données complémentaire (Downs, 2021). Comme illustré dans la section 3.4 de cet article, la base de données peut également être réutilisée par l'équipe de recherche d'origine ou par une nouvelle équipe, pour prolonger une étude en approfondissant la problématique de base. Ces possibilités de réutiliser une base de données optimisent ainsi l'investissement humain et financier d'origine pour en tirer le maximum de connaissances et d'avancées scientifiques.

3.6 CONCLUSION

L'objectif de cet article était de discuter des possibles avancés scientifiques dans le domaine de la connectivité entre les aquifères et les rivières dans le cadre d'une publication ouverte de données scientifiques. En considérant plusieurs problématiques confrontant les dimensions inclues dans la base de données, l'exemple présenté sur la rivière Matane a permis de montrer que malgré les cinq études déjà réalisées sur le méandre, de nouveaux éléments pouvaient encore être extraits des données. Ces éléments ont permis de réaffirmer la forte connectivité en place au niveau du méandre, mais aussi de mettre en évidence des particularités encore non prises en comptes telles que la déconnexion observée lors de la crue hivernale de janvier 2018 ou la forte variabilité des niveaux piézométriques dans le piézomètre D769 dans le fond de la plaine. Enfin, la réutilisation des données au sein d'un modèle comme celui permettant l'interpolation des cartes piézométriques a permis d'acquérir un tout nouveau jeu de données composé de 17 423 cartes piézométriques générées automatiquement et d'une base de données tertiaire décrivant les caractéristiques globales de la surface piézométrique (direction et intensité moyenne d'écoulement) et les taux théoriques de surfaces inondées par exfiltration de nappe avec une résolution de 4 h entre 2011 et 2019. La réexploitation de cette base de données hydrogéologique a ainsi permis d'approfondir les connaissances sur la connectivité hydrologique entre l'aquifère et la rivière au niveau du

méandre. Son partage en accord avec les principes FAIR pourrait se révéler être une opportunité plus grande encore, une fois laissée entre les mains de la communauté scientifique mondiale.

Ces résultats basés sur une base de données particulière, impliquent que des opportunités similaires peuvent être incluses dans beaucoup d'autres jeux de données assemblés dans le cadre de la recherche sur la connectivité entre les aquifères et les rivières ainsi que dans celui de la recherche scientifique en général. Pour qu'ils soient efficaces, ces partages doivent être supportés par une méthodologie exigeante de description de la donnée générée, ainsi que par une infrastructure de répertoires de données performante. Un travail de sensibilisation reste cependant à faire pour créer des incitatifs forts pour la communauté scientifique, afin qu'un partage généralisé des données de recherche avec tous les avantages qui en découlent, soit mis en place et accepté comme faisant partie intégrante du travail du chercheur.

CONCLUSION GÉNÉRALE

Compte tenu de l'évolution de nos sociétés dans le contexte actuel de changement climatique, la protection des ressources en eaux douces est aujourd'hui un thème central en recherche. Dans ce cadre, l'export de polluants vers les rivières est régulé par différentes techniques de gestion qui mettent à profit les processus physiques et géochimiques naturels des zones ripariennes (Anbumozhi et al., 2005; Fischer et al., 2000). Cependant, les processus de surface tels que la migration des chenaux ou les inondations des plaines alluviales, ont conduit à proposer des concepts de gestion intégrés beaucoup plus large dans le but de préserver des « espaces de liberté » autour des rivières (Biron et al., 2014). La dimension souterraine des échanges hydrologiques entre les rivières et leurs bassins versants reste cependant peu intégrée dans les pratiques de gestion. Les eaux souterraines interagissent pourtant avec les eaux de surface au travers de la zone hyporhéique. Cette zone de mélange est généralement délimitée par des considérations écologiques et géochimiques. La quantité et la qualité de l'eau transportée par les cours d'eau étant dépendantes de la connectivité des rivières avec les aquifères (Brunner et al., 2017; Meals et al., 2010), une bonne compréhension du fonctionnement de ces échanges est nécessaire. Diverses méthodes permettent d'étudier cette connectivité. Parmi elles, l'utilisation du radon (^{222}Rn), en tant que traceur d'un contact prolongé entre l'eau et la matrice aquifère, permet de qualifier et quantifier les mélanges entre les eaux souterraines et les eaux de surface (Burnett et al., 2010; Cook, 2015).

L'objectif de cette thèse était de **qualifier et de quantifier la connectivité entre les eaux souterraines et les rivières en combinant des approches géochimiques et hydrogéologiques**. Trois questionnements principaux ont été considérés pour répondre à cet objectif. Ce travail s'est intéressé d'une part à l'extension spatiale de la zone hyporhéique du point de vue de l'évolution temporelle de la géochimie des eaux souterraines, et aux

principaux facteurs qui contrôlent cette extension (Chapitre 1), et d'autre part à la quantité d'eau souterraine et de carbone inorganique dissous (DIC) arrivant dans la rivière et au flux associé de CO_2 vers l'atmosphère (Chapitre 2). Le volume très important de données géochimiques et hydrogéologiques assemblé au cours de cette étude a mené à une réflexion approfondie et illustrée sur un usage étendu et partagé des bases de données générées dans le but d'approfondir les connaissances sur la connectivité entre les eaux souterraines et les eaux de surface (Chapitre 3).

La rivière Matane (Québec, Canada) a servi de modèle d'étude afin de répondre à l'objectif principal de cette thèse. Les plaines alluviales de cette rivière localisée en région subarctique sont régulièrement inondées du fait d'exfiltrations de la nappe d'eau souterraine, traduisant une forte connectivité entre la rivière et l'aquifère. Déjà l'objet de précédentes études (Buffin-Bélanger et al., 2015c; Cloutier et al., 2014; Larocque et al., 2016b), un méandre de la rivière a ainsi été instrumenté de 2011 à 2019 et a fait l'objet d'un suivi à haute résolution spatiale et temporelle des niveaux piézométriques dans l'aquifère. Cette expérience sur le fonctionnement du méandre en termes de propagation des ondes de crues dans l'aquifère s'est révélée être un atout non négligeable dans l'analyse de la connectivité géochimique et d'échanges de masse d'eau dans le système. Ces connaissances préalables ont été couplées à l'utilisation du radon de manière à cibler spécifiquement les processus liés aux eaux souterraines. Le radon, en tant qu'outil géochimique, a servi de véritable colonne vertébrale méthodologique dans les deux premiers chapitres de cette thèse. Au travers de la combinaison innovante de ses fonctions d'indicateur de mélange dans l'aquifère, d'outil de quantification de la décharge et de base de calcul des temps de résidences de l'eau dans l'aquifère alluvial, **le radon s'est révélé être un outil extrêmement efficace et fiable. Il s'intègre parfaitement dans une approche globale géochimique et hydrogéologique appliquée à la recherche sur la connectivité entre les eaux souterraines et les eaux de surface.**

L'étude du premier sous-objectif a démontré l'importance du débit de la rivière et de la saisonnalité dans l'extension spatiale de la zone hyporhéique. La géochimie des eaux

souterraines de l'aquifère alluvial est dépendante des infiltrations d'eau de surface dans l'aquifère. **La zone géochimiquement impactée n'est pas limitée à quelques mètres de rivage, mais peut s'étendre jusqu'à plusieurs dizaines, voire centaines, de mètres de la rivière. Ce contrôle exercé par le débit des rivières s'accompagne de variations dans les transferts transversaux et verticaux d'eau souterraine dans l'aquifère alluvial.** Compte tenu de l'importance de l'utilisation de puits résidentiels d'eau potable en dehors des centres urbains, cette influence directe de la rivière sur la géochimie des eaux souterraines souligne la nécessité d'une approche hydraulique et géochimique combinée et étendue dans le temps afin d'assurer une protection efficace de la ressource en eau souterraine. Ces résultats supportent l'idée de *corridor hyporhéique* proposé par Stanford & Ward (1993) en pointant les échanges hydrologiques, mais aussi géochimiques entre les eaux souterraines et les eaux de la rivière sur des distances considérables au sein de l'aquifère alluvial.

Le second sous-objectif s'est ensuite intéressé au devenir de l'eau transitant dans l'aquifère alluvial. L'utilisation du radon au sein d'un modèle de type bilan de masse a permis de montrer que les quantités d'eau souterraine arrivant en surface dans la rivière sont hétérogènes le long du chenal. Cette hétérogénéité a été observée aux deux échelles spatiales étudiées à basse (infra-kilométrique) et haute (supra-kilométrique) résolutions. Un échantillonnage d'eau à haute résolution spatiale dans la rivière permet de localiser avec précision des zones de décharge d'eau souterraine dans les eaux de surface. Ces apports externes d'eaux concentrés en DIC contribuent au transport horizontal de carbone le long du chenal, mais ne représente qu'une part limitée (inférieur à 13 % dans cette étude) du flux de DIC total transporté par la rivière. **Le DIC apporté par les eaux souterraines contribue cependant fortement au flux vertical de carbone dans la rivière. Dès son arrivée en surface, un flux très important de CO_2 issu des eaux souterraines dégaze quasi instantanément vers l'atmosphère. Les résultats soulignent l'importance des décharges d'eau souterraine en rivière dans la géochimie des eaux de surface et dans le cycle du carbone inorganique.** Dans le contexte de changement climatique global, les flux d'eaux et de carbones inorganiques actuellement observés en région subarctique pourraient être

modifiés à la faveur d'une augmentation des flux de CO_2 dégazé depuis les rivières vers l'atmosphère (Campeau et del Giorgio, 2014).

Afin d'étudier et de documenter les évolutions de ces processus d'échange au sein du corridor hyporhéique et de manière à assurer une conservation des données scientifiques générées, le troisième sous-objectif s'intéresse au potentiel de réutilisation de bases de données hydrogéologiques dans une optique d'optimisation de la recherche sur la connectivité eaux souterraines – rivière. L'étude systématique de la base de données hydrogéologique acquise entre 2011 et 2019 sur la plaine alluviale de la rivière Matane a montré que malgré les précédents projets déjà réalisés sur ces données, des informations supplémentaires pouvaient encore en être extraites. En plus de réaffirmer et d'approfondir les connaissances sur la connectivité existante au niveau du méandre, une nouvelle approche utilisant les caractéristiques modélisées de la surface piézométrique au cours du temps a permis la création d'un nouveau jeu de données tertiaires. Cet exemple montre que **la publication ouverte de bases de données constitue une opportunité exceptionnelle pour la recherche scientifique. Des bases de données acquises dans le cadre d'études particulières peuvent être soumises à de nouvelles expertises ou être intégrées à des études plus larges.** Un jeu de données assemblé en région subarctique à un temps précis peut ainsi être comparé sans frais supplémentaires à d'autres données collectées dans des régions différentes ou similaires. Un partage efficace respectant les principes de publication tels que les principes FAIR (*Findability*, *Accessibility*, *Interoperability*, and *Reuse*) assure le stockage et les capacités de réutilisation des bases de données partagés sur le long terme. Ce partage, s'il pouvait être généralisé, permettrait une optimisation de la recherche sur la connectivité entre les eaux souterraines et les rivières.

Ensemble, ces sous-objectifs montrent que la connectivité entre les aquifères et les rivières se traduit par des processus d'échanges hydrologiques et géochimiques importants. **Loin d'être une zone interface figée, l'extension spatiale du corridor hyporhéique évolue le long de la rivière au cours du temps. Cette évolution est principalement dépendante des débits dans la rivière. L'eau de surface s'infiltre et se mélange à l'eau**

de l'aquifère alluvial dans le corridor hyporhéique. L'eau du corridor hyporhéique se décharge en surface et influence donc la géochimie de l'eau dans la rivière. Du point de vue de la géochimie, la connectivité entre les eaux souterraines et les eaux de surface doit ainsi être considérée comme faisant partie intégrante d'un continuum dont la partie visible est la rivière (Fig. 33).
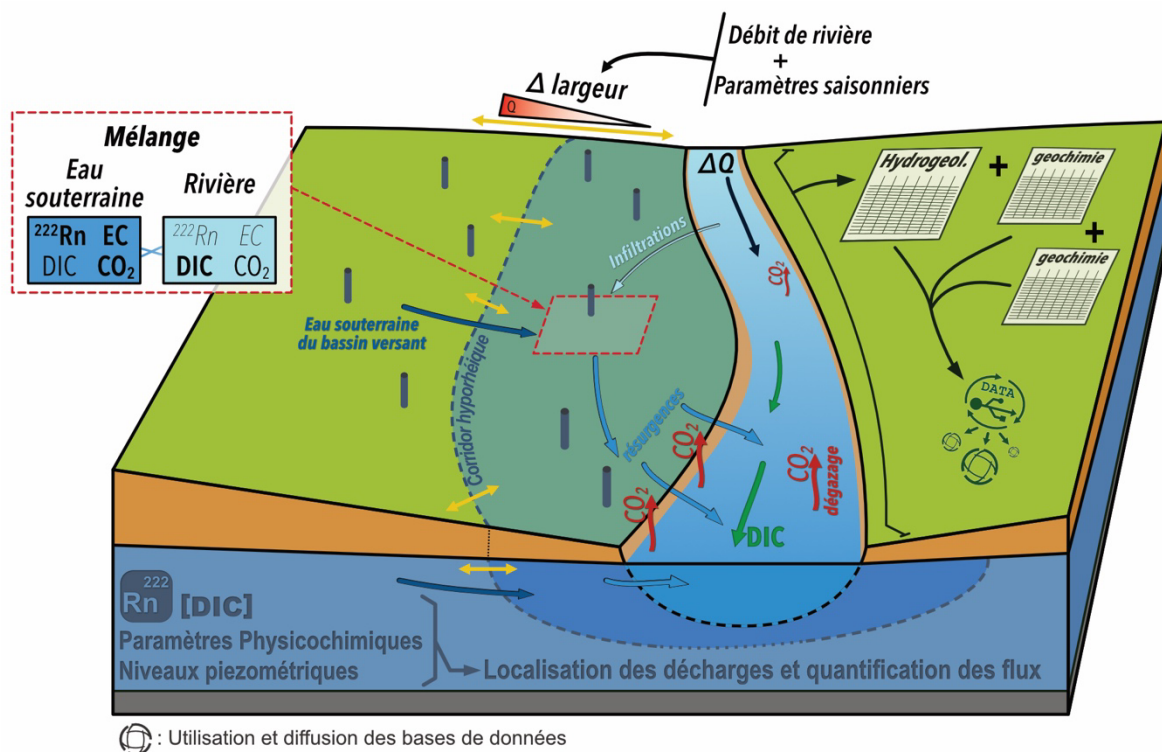
Figure 33. Schéma conceptuel des principaux flux d'échange hydrologiques et géochimiques dans le continuum aquifère-rivière présentés dans cette thèse. L'ensemble des bases de données générées au cours de l'étude des différents sous-objectifs sont publiées ou soumises pour publication dans le répertoire de base de données Pangaea.de.

LIMITATIONS DE L'ÉTUDE

Cette étude hydrogéologique et géochimique de la connectivité entre les eaux souterraines et les rivières a été réalisée sur une portion localisée de la rivière Matane. Bien qu'apportant des avantages certains du point de vue de l'instrumentation et des connaissances

particulières associées au site d'étude, ce choix a limité nos observations et interprétations à un milieu relativement peu urbanisé et à une section en aval de la rivière (ordre de Strahler de 6). Bien que n'ayant pas véritablement d'impact sur l'approche méthodologique au cœur de cette étude, l'imperméabilisation des sols, l'anthropisation des cours d'eau, les éventuels prélèvements d'eau dans l'aquifère, les types de sol, ou encore les différences d'activité biologique pourraient avoir un impact sur l'intensité des flux calculés et sur l'extension spatiale du corridor hyporhéique.

Certaines limites sont également à considérer dans la représentativité des flux calculés au cours de l'étude. Ainsi, les mesures nécessaires aux calculs des flux de CO_2 à l'atmosphère ont été réalisées en journée alors que l'activité photosynthétique de la végétation dans la rivière consomme du CO_2. Des mesures nocturnes de la pression partielle de CO_2 en rivière auraient ainsi pu donner des concentrations en CO_2 plus élevées que les mesures réalisées en journée. Les flux calculés au cours de cette étude, bien qu'importants, reflètent ainsi une réalité diurne des émissions de CO_2 vers l'atmosphère qui pourraient sous-estimer le flux réel intégrant une période jour-nuit de 24 h (Gómez-Gener et al., 2021). Par ailleurs, les estimations des flux d'eau souterraine vers la rivière et des flux de CO_2 vers l'atmosphère n'ont pas été répétées dans les mêmes conditions de résolution au cours de l'été. Les flux calculés reflètent donc l'état des échanges à un instant donné dans des conditions hydrologiques et géochimiques particulières au moment des analyses en juillet et en août. Ils sont donc représentatifs de ce qu'il peut se passer dans la rivière au cours de l'étiage d'été, mais ne peuvent pas être extrapolés à la période estivale dans son intégralité. Enfin, les contraintes hivernales (sol gelé, couvert de glace sur la rivière, et conditions climatiques hivernales) ont limité l'accès aux eaux souterraines et à la rivière. Bien que les niveaux piézométriques aient été suivis sur l'année entière, ce travail de thèse n'a pas considéré la géochimie des eaux au cours de l'étiage d'hiver. Cet étiage particulier implique une alimentation de la rivière par des eaux souterraines dans un contexte d'activité biologique faible, mais avec un couvert de glace pouvant limiter les processus de dégazage vers l'atmosphère. Ce couvert de glace peut potentiellement favoriser les exports horizontaux de

carbone, et engendrer un flux ponctuel très important de CO_2 à l'atmosphère lors de la rupture du couvert de glace et de la réouverture du système.

Du point de vue de la méthodologie, le choix de l'usage du k_{600} pour calculer les flux de CO_2 vers l'atmosphère était justifié dans cette étude par des contraintes temporelles et matérielles. Ce coefficient est utilisé dans un grand nombre d'études et sa méthode de calcul s'appuie sur de nombreuses mesures de terrain, mais n'en reste pas moins une valeur calculée empiriquement en fonction de la morphologie du chenal (Raymond et al., 2012). Une estimation plus directe de la vitesse de transfert aurait pu être réalisée par des mesures de PCO$_2$ dans des chambres flottantes placées sur la rivière (Marx et al., 2017). Afin de minimiser cette incertitude liée à l'utilisation d'une donnée empirique par rapport à une donnée mesurée, la méthode de calcul du k_{600} utilisée ici (équation 7 proposée par Raymond et al. 2012) a été choisie de manière à optimiser le caractère prédictif de l'équation tout en considérant un maximum de caractéristiques de la rivière (vitesse de l'écoulement, pente du chenal, débit, et profondeur de la colonne d'eau).

Perspectives générales

Malgré ces contraintes, cette étude a permis de faire un état des lieux de la connectivité entre la rivière Matane et son aquifère en région subarctique. L'application sur cette rivière d'une approche centrée autour du radon a mis en valeur ce traceur en tant qu'outil de recherche performant et précis à la fois dans l'étude des résurgences d'eau souterraine, mais aussi dans l'étude des interactions hydrologiques et géochimiques au sein des aquifères alluviaux. La multiplication des études hydrologiques et géochimiques dans des milieux différents et un partage optimisé des bases de données peut permettre d'approfondir encore les connaissances sur ce continuum et ainsi d'assurer une protection efficace de la ressource en eau douce potable.

Étant donné le contexte actuel de changement climatique global et de l'évolution des sociétés vers une urbanisation de plus en plus étendue (United Nations, 2015), des études de ce type sont aujourd'hui extrêmement importantes pour tenter de prédire comment la qualité de la ressource en eau va être impactée dans le futur. Dans ce contexte, le débit des rivières et les facteurs saisonniers qui influencent la connectivité entre les eaux souterraines et les rivières vont être modifiés. Cette étude sur la rivière Matane est localisée en région subarctique où la neige accumulée au cours des hivers longs et froids joue un rôle important sur la recharge des aquifères. Un climat plus chaud pourrait réduire les capacités de recharge printanière des aquifères souterrains et modifier l'équilibre des échanges hydrologique en place. Les flux de CO_2 vers l'atmosphère obtenue dans le chapitre 2 sont par ailleurs inférieurs à ceux obtenus dans le cadre d'autres études dans des climats plus chauds. Dans un contexte de changement climatique, les milieux nordiques sont particulièrement et rapidement affectés par le réchauffement des températures (IPCC, 2022). Le suivi de la connectivité entre les eaux souterraines et les rivières dans ces zones est donc particulièrement important pour suivre ces modifications. La comparaison de ces données avec d'autres études similaires dans des climats et des environnements différents peut permettre de prédire l'évolution du continuum aquifère - rivière et donc potentiellement d'actualiser efficacement les modes de gestion de la ressource en eau. Un partage global, optimisé et généralisé des bases de données est, dans ce cadre, particulièrement important. Cette réutilisation des données scientifiques à des fins de comparaison contribue à justifier l'énergie investie dans le fonctionnement des serveurs. Ces « data centers » nécessitent en effet d'importantes quantités d'énergie pour assurer le fonctionnement des serveurs et leur refroidissement. À l'échelle de l'Union européenne par exemple, le fonctionnement de ces centres (tous domaines et fonctions confondus) représentait en 2018 2,7 % de la demande en électricité (Montevecchi et al., 2020). Cette contrepartie à la stratégie d'un partage généralisé des bases de données scientifiques ne remet pas en cause les bénéfices qu'elle apporte dans le cadre de la recherche, notamment sur la connectivité entre les eaux souterraines et les rivières, et qui ont été discutés dans le troisième chapitre de cette thèse. Dans le cadre de la lutte contre les changements climatiques, il convient cependant de ne pas occulter cette

problématique afin de pouvoir optimiser le fonctionnement de ces centres à porter scientifique.

L'existence d'un continuum aquifère-rivière ajoutée à ces perspectives de recherches soulève ainsi de nouvelles questions dans le domaine de la connectivité entre les eaux souterraines et les eaux de surface. En premier lieu, des recherches sont encore nécessaires quant à l'importance de l'hiver dans la dynamique d'échanges entre les aquifères, les rivières et l'atmosphère. Pour des raisons techniques liées à l'utilisation des piézomètres, l'***impact de l'étiage d'hiver sur le continuum aquifère-rivière en région subarctique*** n'a pas pu être abordé au cours de cette étude. Les précipitations étant sous forme solide et les températures étant extrêmement froides, il s'agit d'une période de l'année au cours de laquelle l'alimentation en eau des rivières est assurée quasi exclusivement par les résurgences d'eaux souterraines. Ces eaux drainent des sols dont la végétation est en dormance avant d'atteindre la surface au niveau d'un chenal recouvert d'une couche de glace. Cette problématique implique des sous-questions à la fois sur les techniques d'échantillonnage compatibles avec les conditions hivernales, mais aussi sur les processus d'échanges en place au niveau des résurgences d'eau souterraine. L'imperméabilité de la glace de rivière aux passages des gaz est dans ce cadre particulièrement importante. Au niveau de la méthodologie de quantification des décharges d'eau souterraine grâce au radon, cette limitation du flux de dégazage vers l'atmosphère peut fortement encourager un maintien d'une activité élevée en radon dans les eaux de surface sous la glace donnant un rôle plus important au flux de désintégration et d'export de radon dans le système. De la même manière, le CO_2 apporté par les eaux souterraines pourrait se retrouver bloqué dans ou sous la glace de rivière (Öquist et al., 2009) ou encore être exporté sur de plus grandes distances vers l'océan. Dans le cas d'un stockage dans les glaces, le flux de CO_2 émis vers l'atmosphère lors du dégel devrait aussi être étudié pour pouvoir construire un aperçu complet de l'impact de la connectivité entre les eaux souterraines et les eaux de surface sur les flux annuels de CO_2 vers l'atmosphère en région subarctique. Par ailleurs dans le troisième chapitre de cette thèse, un évènement important et exceptionnel de crue a été observé en janvier 2018. Celui-ci n'ayant pas impacté

les niveaux piézométriques dans l'aquifère, il convient de s'interroger sur l'impact des conditions hivernal sur la connectivité hydrologique et géochimique entre les eaux souterraines et les rivières au sein des corridors hyporhéiques. Une fois cette dynamique hivernale des échanges hydrologiques et géochimiques établie, il sera possible de suivre son évolution dans le cadre d'un réchauffement du climat.

Ensuite, dans le but d'obtenir une vision exhaustive de la connectivité hydrologique et géochimique, il conviendrait de réaliser de telles évaluations dans divers environnements en s'interrogeant sur l'**impact de différents usages du sol à proximité de la rivière sur le continuum aquifère-rivière**. L'artificialisation des sols du corridor hyporhéique par l'urbanisation, par l'agriculture, ou par l'aménagement d'aires récréatives modifie la structure et/ou le revêtement des sols. Ces modifications entrainent une variation de conductivité hydraulique plus ou moins marquée des premiers centimètres des sols pouvant affecter les capacités d'infiltration de l'eau de précipitation dans les aquifères alluviaux (Jarvis et al., 2013). Ces changements pourraient ainsi avoir un impact sur l'équilibre au sein du continuum aquifère-rivière et altérer les échanges hydrologiques. Par ailleurs, ces modifications d'usages modifient également l'activité biologique des sols et peuvent donc influencer les flux de carbones arrivant au niveau des rivières, et des flux de CO_2 dégazé vers l'atmosphère. La multiplication de ces études et donc des bases de données disponibles dans le cadre d'environnements variés pourra permettre de mieux évaluer les potentiels impacts d'une urbanisation plus ou moins intense des zones riveraines sur le fonctionnement des rivières.

Au-delà du seul fonctionnement hydrologique et géochimique du continuum aquifère-rivière, l'objectif international de préservation des masses d'eau douce implique de s'interroger sur les autres éléments chimiques contrôlant la qualité des eaux de surface. L'existence d'un corridor hyporhéique dépassant le cadre spatial restreint de la rive conduit à s'interroger sur **comment cette connectivité hydraulique et géochimique entre les eaux souterraines et les eaux de surface s'intègre dans les processus connus de migrations des polluants d'origine agricole, industrielle, et urbaine ?** Au travers de l'analyse des

paramètres physico-chimiques de l'eau (conductivité électrique, pH, température, isotopes stables de l'eau, activité en radon, concentration en DIC), cette étude a montré une influence géochimique mutuelle entre les eaux souterraines alluviales et les rivières. Les transferts d'intrants anthropiques et de leurs métabolites dans les sols du corridor hyporhéique devraient être considérés sur une large amplitude spatiale autour des rives de manière à évaluer la vulnérabilité des aquifères et des rivières face à un aléa de déversement ponctuel ou chronique de polluants. Les conclusions apportées à cette dernière problématique devraient amener à une étude coût-bénéfice allant au-delà du domaine de l'hydrologie et de la biogéochimie portant sur **la faisabilité et l'acceptabilité d'une extension législative de l'étendue des bandes riveraines** en tant que zone tampon de protection entre les activités humaines et les rivières ? Au Québec la largeur de ces bandes riveraines est fixée de 10 à 15 mètres autour de la rivière en tout temps, mais est réduite à trois mètres dans le cas d'activités agricoles (MELCC - Ministère de l'Environnement et de la Lutte contre les changements climatiques, 2018). L'étendue de ces zones de protection des rivières est très inférieure à l'extension spatiale que peuvent atteindre les corridors hyporhéiques. Cette législation devrait donc être adaptée pour mieux se conformer à cette réalité.

Conclusion

L'utilisation d'outils géochimiques et hydrogéologiques a permis de faire un suivi des interactions entre les masses d'eau souterraine et de surface et ainsi de mettre en évidence le continuum aquifère-rivière en précisant son potentiel d'extension spatial. Celui-ci est variable le long du chenal et est dépendant des débits d'écoulement dans les rivières. Il intègre des flux d'eau de surface qui s'infiltre vers l'aquifère alluvial et des flux qui retournent vers la rivière. Une quantification de ces flux à l'aide des outils géochimiques, notamment grâce au radon et à la conductivité électrique, a permis d'évaluer leur importance relative au cours de l'année dans le cas des infiltrations et au cours de l'étiage dans le cas des résurgences d'eaux souterraines. La collection de données issues de cette thèse sur un modèle

d'étude en milieu subarctique est une contribution unique aux bases de données publiées dans le domaine de la recherche sur la connectivité entre les eaux souterraines et les rivières. L'objectif principal de cette thèse consistant à qualifier et à quantifier la connectivité hydrogéochimique aquifère-rivière en combinant des approches géochimiques et hydrogéologiques a donc été atteint. Certaines contraintes dans cette étude ont été identifiées et nous permettent de nous interroger sur de nouvelles problématiques qui devront donner lieu à des études complémentaires.

ANNEXES

ANNEXE I

FLOW AND DISCHARGE OF GROUNDWATER FROM A SNOWMELT-AFFECTED
SANDY BEACH

(Chaillou et al., 2018)

Research papers

Flow and discharge of groundwater from a snowmelt–affected sandy beach

G. Chaillou [a,⹋], F. Lemay-Borduas [a], M. Larocque [b], M. Couturier [a], A. Biehler [a], G. Tommi-Morin [a]

[a] Canada Research Chair in Geochemistry of Coastal Hydrogeosystems, Québec–Océan, Boreas Group on the North Systems, Université du Québec à Rimouski, 300 Allée des Ursulines, Rimouski, QC G5L 3A1, Canada
[b] GEOTOP and Département des sciences de la Terre et de l'atmosphère, Université du Québec à Montréal, 9 C.P. 8888, Succ. Centre-Ville, Montréal, QC H3C 3P8, Canada

a b s t r a c t

The study is based on a complex and unique data set of water stable isotopes (i.e., d^{18}O and d^2H), radon–222 activities (i.e., ^{222}Rn) and groundwater levels to better understand the interaction of fresh groundwater and recirculated seawater in a snowmelt–affected subterranean estuary (STE) in a boreal region (Îles-de-la-Madeleine, Qc, Canada). By using a combination of hydrogeological and marine geochemical approaches, the objective was to analyze and quantify submarine groundwater discharge processes through a boreal beach after the snow melt period, in early June. The distribution of d^{18}O and d^2H in beach groundwater showed that inland fresh groundwater contributed between 97 and 30% of water masses presented within the STE. A time series of water table levels during the 16 days of the study indicated that tides propagated as a dynamic wave limiting the mass displacement of seawater within the STE. This up-and-down movement of the water table (10–30 cm) induced the vertical infiltration of seawater at the falling tide. At the front of the beach, a radon–based mass balance calculated with high-resolution ^{222}Rn survey estimated total SGD of 3.1 m^3/m/d at the discharge zone and a mean flow to 1.5 m^3/m/d in the bay. The nearshore discharge agreed relatively well with Darcy fluxes calculated at the beach face. Fresh groundwater makes up more than 50% of the total discharge during the measuring campaign. These results indicate that beaches in boreal and cold regions could be important sources of freshwater originate and groundwater–borne solutes and contaminants to the marine environment after the snowmelt.

2017 Elsevier B.V. All rights reserved.

1. Introduction

Submarine groundwater discharge (SGD) is widely recognized as a significant transport pathway for chemicals entering the coastal ocean (Li et al., 1999; Moore, 2010; Robinson et al., 2007). This is particularly important where rapidly growing coastal populations induce complex changes in landscapes and ecosystems as well as increased pressure on coastal water resources. In locations around the world, deterioration in coastal water quality (e.g., bacterial proliferation, harmful algal blooms, hypoxia, acidification, fish and shellfish mortality) have been attributed to changes in the quality and volume of groundwater discharged to the ocean (Hwang et al., 2010; Valiela et al., 1990).

The intertidal and nearshore zones of sandy beaches play key roles in the connection across the coastal continuum, from water-

shed to coast (Heiss and Michael, 2014; Robinson et al., 2007). Moore (1999) coined the term "subterranean estuary (STE)" for the beach aquifer to emphasize the importance of freshwater and seawater mixing and water-rock interactions as fresh groundwater transits toward the sea. Similarly to surficial estuaries, solute concentrations change greatly in the dispersion zone of the subterranean estuary (Beck et al., 2015). Their chemical behaviors within the STE are complex and closely tied to the subsurface salinity distribution. Multiple physical forces drive subsurface flow and residence times, and thus control the reaction rates and transformations in this biogeochemically active zone (Cable and Martin, 2008; Michael et al., 2005; Robinson et al., 2007). Santos et al. (2012) identified at least 12 independent drivers that include both terrestrial (e.g., hydraulic gradient, seasonal oscillation of the water table) and marine (e.g., wave and tidal pumping, ripple and bed form migration, bioirrigation) processes that interact in complex ways. These processes force flow across the water-sediment interface, albeit under different spatial and temporal scales, and consequently influence the export of groundwater-borne,

⹋ Corresponding author at: Département Biologie, Chimie, Géographie, 300 Allée des Ursulines, Rimouski, Qc G5L 3A1, Canada.
E-mail address: gwenaelle_chaillou@uqar.ca (G. Chaillou).

recirculated, and newly formed compounds to the sea. Thus, an in-depth understanding of the hydrological SGD processes is necessary to accurately predict chemical fluxes to coastal environments.

The nearshore area of the beach aquifer is a dynamic zone where fresh groundwater exits the subterranean system through a narrow discharge zone often bounded by two saline zones. At the seaward boundary below the discharge zone, the saltwater wedge is a fresh groundwater-seawater interface induced by a density gradient where dispersion dominates the exchanges. The nearshore location of this interface moves on a seasonal scale (Michael et al., 2005) in relation to the hydraulic pressure and density difference between fresh and seawater. At the landward boundary, above the discharge zone of fresh groundwater, tides and waves drive seawater into the beach aquifer, forming an upper surficial recirculation cell where advection is the primary process by which solutes move across the sediment-water interface. The resulting hydraulic gradient generates downward and seaward circulations of seawater to the nearshore aquifer, which forms a seawater-freshwater mixing zone where dispersion dominates the chemical processes (Abarca et al., 2013; Heiss and Michael, 2014; Ullman et al., 2003; Xin et al., 2010). Many recent studies on groundwater dynamics in beaches employed groundwater models based on salinity and sometimes on water level measurements (Abarca et al., 2013; Evans and Wilson, 2017; Heiss and Michael, 2014; Heiss et al., 2014; Robinson et al., 2007; Xin et al., 2010). These investigations have all highlighted the necessity to obtain integrated in situ measurements of SGD in specific-sites to characterize the nearshore groundwater dynamics.

In boreal and cold regions, the water table elevation is high after snow melt (i.e., in early June), inducing in the inland aquifer a strong horizontal head gradient perpendicular to the shore and high Darcy flows to the coastal embayment (Chaillou et al., 2016). However, these cold regions are still rarely considered as SGD sources. A more detailed knowledge of groundwater discharge, and particularly of fresh groundwater, is critical to the determination of regional and global mass fluxes to coastal zones. Such quantification is particularly crucial in the North where the hydrology is changing rapidly, and is expected to continuously change, in response to climate warming (Adam et al., 2009). The aim of this study was to combine hydrogeological and geochemical in situ measurements to analyze SGD processes in a snowmelt-affected STE settled in the Îles-de-la-Madeleine, an archipelago located in the southeastern of the Gulf of St. Lawrence. The study relied on a time series analysis of hydraulic heads measured along a shore-perpendicular transect of multilevel sampling wells to examine the effect of tidal oscillation on the mixing zone. The spatial and temporal distribution of radon-222 (^{222}Rn; an effective proxy of short-term processes ($t_{1/2}$ =3.8 d) at the groundwater-surface water interface Burnett et al., 2001) and stable isotopes of water (d^{18}O and d^{2}H) were also examined to characterize the fresh groundwater dynamics and to estimate the magnitude of fresh groundwater discharge to the bay after the snowmelt in early June. According to our knowledge, this study presents the first in-depth analyses of nearshore groundwater dynamics influenced by the snowmelt in a boreal sandy beach.

2. Materials and methods

2.1. Hydrological context of the study area

This study was conducted in the subterranean estuary at Martinique Beach on Îles-de-la-Madeleine in the province of Québec (Canada) (Fig. 1). The hydrogeological context of the Îles-de-la-Madeleine has been presented by Comte and Banton (2007). The main aquifer of the Archipelago is composed of sandstones from

the Permian Inferior period (the Cap-aux-Meules formation; Brisebois, 1981) with a mean transmissivity of 1.5-4 10^3 m^2/s and a mean recharge of 230 mm/y (i.e., 25-30% of the annual precipitation; Madelin'Eau, 2004). Groundwater flows through the unconfined Permian sandstone aquifer and discharges to the sea, both directly and through the overlying Quaternary deposits. Martinique Beach originates from a recent transgression sequence. The rapid rates of sea-level rise along the Atlantic coasts of Canada over the middle to late Holocene buried the unconfined Permian sandstone aquifer that is now covered by tidal sediments. These buried environments are geological evidence of local and regional submergences over the last millennia (Scott et al., 1995). Sediment cores collected on Martinique Beach were analyzed using scanning electron microscopy (SEM) coupled to an energy dispersive X-ray spectrometer and revealed that the Quaternary sediment of the beach are 300 Im and mainly composed of silicate mixed with small amount of silt (>5%). The underlying sandstone aquifer is composed of fine red-orange sands (100 Im) composed of silicate and aluminosilicate (Chaillou et al., 2014). Its localization in the beach and its offshore extent is unknown. The site experiences little wave action except during storm events. Tides are semi-diurnal with a spring tide range 1m.

Previous studies on groundwater discharge and biogeochemistry of the superficial STE have been conducted at this site (Chaillou et al., 2016; Chaillou et al., 2014; Couturier et al., 2016). The shallow superficial unconfined beach aquifer releases both fresh groundwater and recirculated seawater to the coastal embayment. Within the beach, fresh groundwater flows towards the seaward discharge region below a narrow intruding saline circulation cell located near the top of intertidal sediments. In spring 2013, Chaillou et al. (2016) used mean regional and local water table levels to estimate groundwater flows ranging from 0.02 m/d in the sandstone Permian aquifer to 0.30 m/d at the beach face.

2.2. Field measurements

2.2.1. Water table levels and hydrogeological properties

Three piezometers equipped with pressure sensors were installed in a 45 m transect of the study site perpendicular to the beach front (Figs. 1c and 2). The first piezometer was located at the mean low tide mark (P$_3$); the second one was located in the intertidal area, 10 m further inland (P$_{13}$); and the third was located on the beach terrace, 43 m from P$_3$ (P$_{44}$; Fig. 2). The piezometers were made from 38 mm ID PVC pipes sealed at the base and equipped with 0.4 m long screens at the bottom end. At every location, piezometers extended 1.50 m below the beach surface so that the bottom end would always be below the water table. Automated level loggers (Hobo U20-001) recorded groundwater levels every 10 mins from 20 May 2013 to 7 June 2013 (16 days). Time series were corrected for barometric pressure from a barologger located at the study site. A permanent Government of Canada sea-level station (Cap-aux-Meules CAM Station #1970; http://tides.gc.ca/) was used as a reference. The station is located at 5 km from the study site (Fig. 1b). This station recorded water levels every three minutes during the sampling period. Guelph permeameter measurements (N =15) provided a mean hydraulic conductivity of 11.4 ±4.4 m/d in the unsaturated surficial sands.

2.2.2. Stable isotopes of water and physicochemical parameters of groundwater

Groundwater was sampled for salinity, ^{222}Rn and stable isotopes of water at high (27-31 May 2013) and low (3 June 2013) tides. A 20 m cross-shore transect of multi-level samplers (M$_{1-7}$; Fig. 2) was set up in the intertidal zone, where beach groundwater and recirculating seawater most likely discharge. The multi-level samplers consisted of 2.5 m PVC pipes with eight
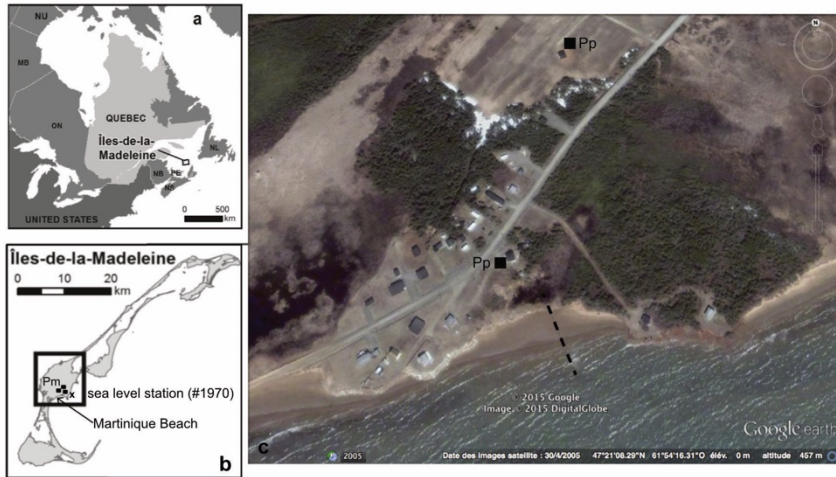
Fig. 1. Location of the study area (a, b) in the central Cap–aux–MeulesIsland on the Îles–de–la–Madeleine. The sampling transect (dotted line) is located in Martinique Beach (c). Pm (in panel b) and Pp (in panel c) indicate the municipal and private wells used to collect fresh inland groundwater end–member samples. The location of the Government of Canada's sea–level station number 1970 is also shown.
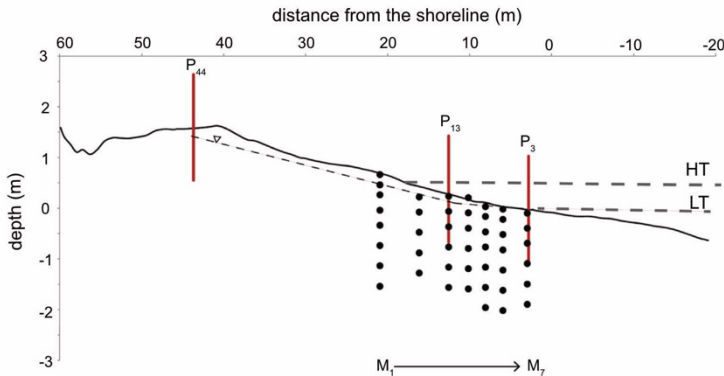
Fig. 2. Conceptual diagram of the cross–shoretransect in Martinique Beach. Beach morphology was measured using a differential global positioning system (DGPS). Depth is referenced to mean sea level (0 m). High and low tide marks (HTL and LTL) are reported. Black dots indicate the sampling port positions of the different multi–level samplers inserted into the beach (M_1–M_7). The fine dashed line is the mean position of the water table level as measured by piezometers P_3, P_{13}, and P_{44} (vertical red lines). (For interpretation of the references to colour in this figure legend, the reader is referred to the web version of this article.)

ports connected to flexible Tygon tubing, as described in Martin et al. (2003). Multi–level samplers were designed to collect water at 10, 30, 50, 80, 110, 150, 190, and 230 cm below the beach surface. Beach groundwater was pumped with a peristaltic pump into an in–line flow cell where specific conductivity (SpCond), dissolved oxygen saturation (DO), temperature, and pH were monitored using a calibrated multiparametric probe (600QS, YSI Inc.). After stabilization of physicochemical parameters, groundwater was collected in 30 ml scintillation vials for water isotope analysis. The radon–approach is described in the next section.

Groundwater end–member samples were collected in the manner described above from private and municipal water wells (Pp and Pm, respectively) located 50 and 2000 m inshore of the cross–shoretransect (Fig. 1b, c). Private wells were purged before the sampling. Seawater end–member samples were collected approximately 50 cm below the seawater surface using a submersible pump about 900 m offshore in Martinique Bay. Stable isotopes of water ($d^{18}O$, d^2H) are used as conservative tracers of mixing processes to investigate and quantify meteoric groundwater–seawater interaction since seawater and meteoric groundwater have unique and distinct end–member signatures (Povinec et al., 2012; Schiavo et al., 2009).

Stable isotopes of water ($d^{18}O$ and d^2H) were analyzed by EA-IRMS at the GEOTOP–UQAM Laboratory. Accuracies are ±0.05‰ (at the $1r$ level) and ±1‰ (at the $1r$ level) for $d^{18}O$ and d^2H, respectively. Isotopic analyses are reported compared to the inter-

national Vienna Standard Mean Ocean Water (VSMOW) as defined by Gonfiantini (1978). Reference materials were used throughout the isotopic water analyses to ensure high quality data.

2.2.3. ^{222}Rn measurements

2.2.3.1. High resolution ^{222}Rn survey in the bay. Radon was used as a geochemical tracer to estimate total submarine groundwater discharge into the bay. ^{222}Rn is an effective qualitative and quantitative tracer because groundwater concentrations are typically higher than those in coastal seawater, regardless of fluid origin or composition. It mixes conservatively once introduced to seawater. A high-resolution spatial survey of ^{222}Rn was performed on 29 May 2013 over 12 h to identify the general distribution of Rn in the bay (surface area = 0.6 km 0.3 km = 0.180 km^2) and to quantify total SGD after the snow melt. ^{222}Rn activity was measured according to Dulaiova et al. (2005) by a radon-in-air detector connected to an air–water exchanger (showerhead–type exchanger; RAD-AQUA, Durridge). From a small boat, water was continuously collected from a submersible pump at 50 cm below the boat and injected into the spray chamber at a rate of 3 L min^1. The water depth was continuously recorded by a DualBeam sonar (200 kHz and 83 kHz) with and GPS Chartplotting. After 20 min of preliminary air–water equilibration in the middle of the bay (0.7 km from the shoreline), the equilibrated air was continuously pumped through Drierite desiccant to the RAD7 radon detector. The RAD7 estimates ^{222}Rn activity by measuring the decay of the radioactive daughters ^{218}Po and ^{214}Po, as described by Burnett et al. (2010). Here, the ^{222}Rn activity was measured over 10 min of count integration. As the boat moved slowly (1.2 km/h), the radon activity of each run was associated with a GPS trace, mean water depth, and mean physicochemical parameters (SpCond, T, DO) continuously recorded (sampling period = 1 min) by a calibrated automatic multiparametric probe fixed near the submersible pump. This produced 28 segments in the 0.180 km^2 studied area that are represented by 28 points positioned at the middle of the GPS segments. Temperature and humidity were monitored continuously during experiments and served to automatically correct radon-in-water activities using the Capture software from Durridge. Analytical uncertainties based on counting statistics are approximately 48% (2r).

2.2.3.2. ^{222}Rn measurements in inland and beach groundwater. Fresh groundwater end–members were also analyzed using an in situ radon-in-water approach similar to that described above. A submersible pump was lowered into municipal and private wells and water was continuously injected into the spray chamber. After 20 min of air–water equilibration, the ^{222}Rn activities were analyzed over four 10 min runs. Radon-in-water measures were automatically corrected using temperature and humidity. The analytical uncertainty was approximately 15% (2r). Each ^{222}Rn activity was associated with measurements of SpCond, T, DO, and pH measured by a mutliparametric probe fixed on the pump. A second survey of ^{222}Rn activities in the fresh groundwater end–members was also performed in June 2015. At that time, discrete water samples were collected in 2 L plastic bottles that were tightly sealed. The water was bubbled to allow ^{222}Rn degassing in the bottle's 30 ml head–space (RAD–H$_2$O, Durridge). As with the RAD–Aqua technique, the equilibrated air flows through Drierite desiccant to the radon-in-air detector (RAD7, Durridge) and is then re-injected into the bottle's head-space to close the loop. The air volume of the closed-loop and water volume of the bottle are known and constant over the measurement, and they are independent of flow rate. The air recirculates through the water and continuously extracts the radon until a state of equilibrium develops. Radon-in-water activities were corrected using temperature and humidity measurements. Finally, ^{222}Rn activity was corrected

for the initial radon decay that took place between sampling and analysis. Analytical uncertainties were less than 12% (2r).

Efforts were also made to measure ^{222}Rn activities in beach groundwater to obtain an accurate estimate of radon groundwater end–member. Additional ^{222}Rn measurements were performed in June 2015 at the M$_3$ and M$_7$ multi-level samplers. At this period, water was collected in 2 L sample bottles that were tightly sealed and analyses were performed as described above. Table 1 gives a summary of the different measurements of Rn performed for the study.

2.3. Mineral–bound ^{226}Ra activity

The ^{226}Ra activity of sediments was determined using samples collected from surficial Holocene inshore and offshore sediment and in the underlying Permian sandstone aquifer using a hand auger.

Thirteen sediment samples were collected from the surface to 1.5 m depth. These measurements were done as a first attempt of the activity of ^{226}Ra–supported ^{222}Rn in beach groundwater. Sediment samples were dried, crushed and sealed in vials fitted for a high–purity Germanium gamma–ray spectrometer (ORTEC DSPEC jr. 2.0). They were left in sealed vials for at least 23 days to ensure radioactive re-equilibration between the ^{226}Ra and the short–lived daughters of the ^{238}U series (Zielinski et al., 2001). Counting time was fixed at 3–4 days to provide adequate counts for the peaks of interest. ^{226}Ra counts were based on the measurement of ^{214}Pb (using the 295.2 and 352 keV) and ^{214}Bi (609 keV) peaks. The counting error is <10%. Disintegrations per minutes (dpm)/g were converted in Bq/m^3 of wet sediment. The diffusive production of ^{222}Rn from the sediments underlying the bay were calculated using the relation proposed by Burnett and Dulaiova (2003) as follow (1)

$$J_{diff} = 0.495 \ ^{226}Ra + 0.303 \qquad (1)$$

where ^{226}Ra is the activity of the sediment (Bq/kg).

2.4. Analyses of water table levels: cross correlation, time lag, and tidal harmonic analysis

Tidal propagation in STE has often been studied by combining Darcy's Law either with analytical solutions (Elgar, 1999; Li et al., 1999), using cross-correlation analysis (Rotzoll and El–Kadi, 2008), or using numerical models (Abarca et al., 2013; Robinson et al., 2007)). Here, the intensity of the relationship and the time lag of the whole time series were determined by cross-correlating water levels from the ocean and unconfined beach aquifer. In addition, each time series was analyzed by a time-frequency analysis and compared to a theoretical tide signal using a classical tidal harmonic analysis. The tidal signal may be decomposed into 17 constituents including five major ones that contribute to approximately 95% of the signal. The diurnal harmonic components and their frequencies (h^1) are O1 (0.03873) and K1 (0.04178), while the semidiurnal components are M2 (0.08051), S2 (0.08333), and M3 (0.12076). Correlations between time series and purely tide-induced oscillations as well as the amplitude of each tidal constituent were estimated to better understand the tidal propagation throughout the beach. Time series analyses were performed with Rstudio using the Applied Statistical Time Series Analysis (stata) package (Baum, 2004) and tidal harmonic analyses were performed with Matlab.

143

Table 1
Summary of Rn measurements.

Location	Date	Analytical equipment	Equilibration time (min)	Run series (min)	A_{Rn} range (Bq/m^3)	% Uncertainties (2r)
Martinique Bay	05-29-2013	Rad-Aqua	20	10[*]	6–66	48
Pm and Pp wells	05-26/31-2013	Rad-Aqua	20	10 (4)[**]	12,300-16,200	12
Pm and Pp wells	06-10/12-2015	Rad-H$_2$O	40	5(8)[**]	12,000-17,100	12
Beach groundwater	06-10/12-2015	Rad-H$_2$O	40	5(8)[**]	0–21,000	11

[*] Over the survey period.
[**] number of runs after air-water equilibration.

2.5. Quantification of SGD

2.5.1. ^{222}Rn water column mass balance

SGD estimations in Martinique Bay were based on a steady–state ^{222}Rn–derived mass balance model proposed by Burnett et al. (2008). Assuming a steady–state for the 12 h integration period (i.e., one complete tidal cycle), the mass balance model incorporates sources of ^{222}Rn (input flux, RF$_{in}$) balanced by losses (output flux, RF$_{out}$). The excess of ^{222}Rn is attributed to the total groundwater input (F$_{GW}$) as follows:

$$F_{GW} = RF_{in} - RF_{out} \qquad (2)$$

where

$$RF_{in} = F_{in} + F_{riv} + F_{diff} + F_{resup} + F_{prod} \qquad (3)$$

$$RF_{out} = F_{out} + F_{decay} + F_{atm} \qquad (4)$$

The excess input flux of ^{222}Rn is the sum of Martinique Bay input (F$_{in}$) due to local circulation (i.e., currents and tides), river input (F$_{riv}$), chemical diffusion from underlying sediment (F$_{diff}$) due to (1), production of resuspended sediment (F$_{resup}$), and internal production in the water column (F$_{prod}$). Output flux integrates the loss of excess ^{222}Rn by natural radioactive decay in the water column (F$_{decay}$), the loss to the atmosphere (F$_{atm}$), and the flux that leaves the box (F$_{out}$) due to local water circulation (i.e., currents and tides). Here, surficial input from rivers (F$_{riv}$) is not relevant in the calculations since there is no surficial water flow in the study area. In addition, ^{222}Rn growth from ^{226}Ra decay in the water column (F$_{prod}$) is not considered because it is often assumed to be limited or null in tidal environments (see Peterson et al. (2010)).

Based on the continuous measurements of T, SpCond, and ^{222}Rn in the bay, a multivariate statistical approach was applied to determine sample clusters where radon and physicochemical parameters could be assumed as homogeneous, regardless the tide cycle and the location. This method, often used in hydrogeochemistry studies, is a quantitative and independent approach for classifying and grouping water samples. In this study, a hierarchical cluster analysis (HCA) was applied. A K–means clustering determined the exact number of clusters to extract from the database. A plot of the within–group sum of squares by the number of clusters extracted revealed that only two clusters accurately classified the dataset. The subsequent HCA analysis revealed that each of the clusters was also composed of two subgroups of samples, which corresponded to the samples collected at falling and rising tide, respectively. Steady–state water–column mass balance of excess ^{222}Rn was then applied for each cluster assuming that for a given water column depth, and surface area, the ^{222}Rn inventory is in steady state. SGD were quantified in each cluster, calculating the different input and output fluxes (i.e., Eqs. (2)(4)) as described in details in Baudron et al. (2015) and modified from Dulaiova et al. (2010) and Smith and Swarzenski (2012).

Tidal currents induce tracer exchanges between the different cluster (F$_{in}$ in Eq. (3) and F$_{out}$ in Eq. (4)) and offshore seawater. Tide acts as both a source and a loss of ^{222}Rn in the water–column mass balance. No data are available on long–shore and tidal currents in the Martinique Bay. As a first approximation, long–shore current is assumed to be limited in this small study area, and only tides are included in the model. The input/output volume of water induced by tide is assumed to be equal. This volume is estimated based on a tidal range of 0.8 m during the sampling period, the mean distance between the high and low tide marks of 30 m, and the width of the studied zone of 300 m. This represented a water volume of 56,700 m^3 that transits in the seaward direction during ebb tide, exporting ^{222}Rn–enriched water, and an equal volume of seawater that flows landward at flood tide, with ^{222}Rn–poor seawater. Therefore, the net flux was a combination of these exchanges.

3. Results and discussion

3.1. Fresh inland groundwater distribution along the STE

The isotopic composition of the groundwater and seawater end–member samples showed contrasted compositions (Fig. 3). The mean inland groundwater d^{2}H was 64.1 ±4.1‰ and d^{18}O was 9.8 ±0.6‰. These depleted values were comparable with data obtained in an eastern region of Québec (Chaillou et al., 2017), and reflected the role of snow melt on aquifer recharge in these
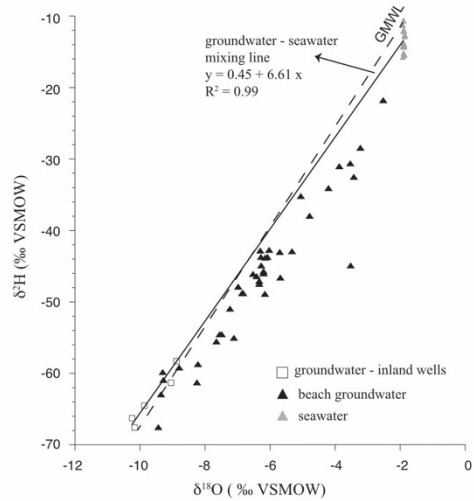
Fig. 3. Isotopic composition of groundwater samples showing the meteoric groundwater–seawater mixing line and the linear relation between samples from the beach system with their respective equations. The global meteoric water line (GMWL) is also reported.

regions. Seawater d^2H was 12.7 ±1.6‰ and $d^{18}O$ was 2.0 ± 0.1‰. The isotope signature of beach groundwater was slightly below the groundwater–seawater mixing line probably due to evaporating processes during the groundwater transit from the aquifer to the coastal zone through the shallow surficial beach aquifer. However, both the absence of distinct isotopic signatures along the STE and similarity between fresh beach and inland groundwater suggest a common origin and the absence of additional fresh-endmember groundwater to the nearshore zone.

Using these stable isotope signatures, it was possible to calculate the contribution of fresh inland groundwater to the beach samples using a simple two end-member mixing model. Based on mean fresh groundwater (64.1‰ d^2H; 9.8‰ $d^{18}O$) and seawater (12.7‰ d^2H; 2.0‰ $d^{18}O$) values, the proportion of fresh groundwater was between 30% in the intertidal zone and 97% in the deepest part of STE (Fig. 4a). Thus, the contribution of the marine end-member was limited to the upper recirculation cell. These results agree with the recent modeling work of Heiss and

Michael (2014) who showed that the beach groundwater is mostly fresh when water table is maximum. The size of the circulation cell and area of the mixing zone were mostly affected by seasonal water table oscillations, and the intertidal circulation cell limited horizontally and vertically as the inland water table increased (Heiss and Michael, 2014). The snowmelt, which is the major period of aquifer recharge in this cold region, induced the landward displacement of the fresh discharge zone and probably support a high fresh SGD flux to the coastal zone.

The spatial limitation of the upper recirculation cell was also supported by the vertical ^{222}Rn distribution (Fig. 4b and c), which showed a downward gradient starting at 0.3 m (in M_3) and 0.8 m (in M_7) below the surface. Deeper, ^{222}Rn values rapidly increased and reached values higher than 12,000 Bq/m^3, which was in the range of values measured in inland wells (Table 2) supporting the idea of a similar production source of ^{222}Rn both in inland and beach groundwater. ^{222}Rn activity in beach groundwater was not simply reflected in the transport of ^{222}Rn-enriched fresh
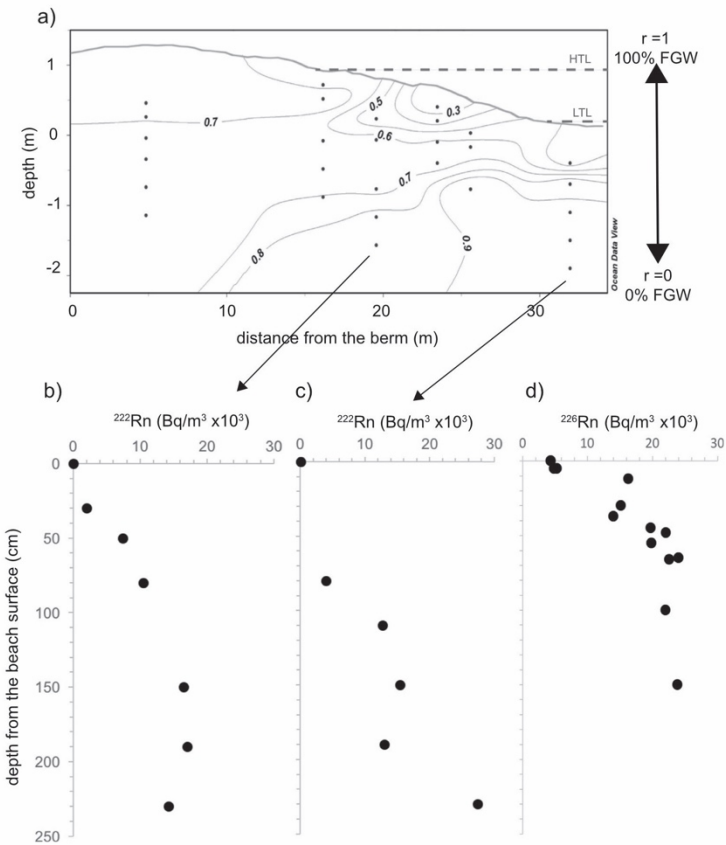
Fig. 4. Distribution of fresh groundwater within the beach based on the isotopic approach. a) Contribution of fresh groundwater at high tide calculated using a two end-member mixing model; when the ratio r =1, the fresh groundwater (FGW) contribution is 100%. Depth is relative to mean sea level (0 m) and the contour lines were derived by the gridding DIVA method included in Ocean Data View Software (Schlitzer, 2016). The black dots are the positions of the sampling ports (M_2–M_7; Fig. 2), and HTL and LTL refer to the high and low tide marks. b) and c) Vertical distribution of ^{222}Rn (Bq/m^3) activities measured at M_3 and M_7, respectively, and d) mineral-bound ^{226}Ra activity (Bq/m^3). In panel b, c, and d, the depth is from the beach surface (cm).

Table 2
Amplitude (in cm) of the five major tide constituents in the different water-level time series recorded by three piezometers (P_{44}, P_{13}, and P_3) over the study period.

Tidal constituent	Amplitude (cm)		
	P_{44}	P_{13}	P_3
O1	0.49	1.32	5.93
K1	0.26	3.71	8.74
M2	0.27	5.57	16.43
S2	0.27	0.98	2.78
M3	0.19	1.34	2.89
Rtotal tide	1.50	11.58	33.88

groundwater: ^{222}Rn is produced locally and hydraulic conductivity does not control its activity. In addition to the transport of inland groundwater, the in situ production from mineral–bound ^{226}Ra controlled the distribution of ^{222}Rn. Fully understanding the role of mineral–bound ^{226}Ra as source of ^{222}Rn in these groundwater samples would require specific emanation experiments which are beyond the scope of this paper. Nevertheless, the vertical distribution of ^{226}Ra allowed to estimate maximal activities distribution of groundwater ^{222}Rn, assuming secular equilibrium. The high activity of mineral–bound ^{226}Ra at depths below 0.5 m (Fig. 4c) probably reflected the lithologic difference between the deep Permian sandstone aquifer and the Holocene sediment associated with changes in porosity and hydraulic conductivity. The ^{222}Rn activities measured below 0.5 m depth in 2013 and 2015 and by two different approaches (Table 1) were slightly lower than ^{226}Ra activity in mineral matrix suggesting that ^{222}Rn in groundwater was near secular equilibrium with ^{226}Ra. Chaillou et al. (2016) proposed a transit time of 32 days though the 35 m beach transect (from M1 to M7; Fig. 2), beyond the mean–life of radon (5.5 d), indicating the importance of in situ production from mineral–bound ^{226}Ra as in inland groundwater. The well–defined concave upward profile of ^{222}Rn was attributed to the advective transport of ^{222}Rn–rich water and its mixing with the ^{222}Rn–poor overlying seawater. The lowest activities at the surface indicated that the residence time was not sufficient to reach secular equilibrium. This zone of deficiency is consistent with the position of the surficial recirculation cell.

3.2. Tidal flow dynamics at the nearshore aquifer

3.2.1. Tide as a dynamic wave

Time series of water levels and tidal oscillation indicated a strong synchronicity between tides and beach groundwater levels in the tidal zone of the bay (Fig. 5a, piezometers P_3 and P_{13}). A cross–correlation analysis between tidal oscillation using the CAM station as the input function and beach groundwater levels at P_3 and P_{13} as the output functions showed a strong relationship, with $r_{xy}(k)$ values of 0.89 (P_3) and 0.67 (P_{13}) at maximum correlation. This relation was not significant with the P_{44} time series, which was too far from the nearshore zone to record tidal oscillation. A frequency analysis of these time series shows the effect of tidal constituents (Fig. 5b). The five major constituents, O1, K1, M2, S2, and M3, clearly controlled the water level in the tidal zone, and particularly at the low–tide mark, explaining more than 30 cm of the fluctuation at P_3, 11 cm at P_{13} and less than 2 cm at P_{44} (Table 2). The damped tidal signal at P_{44} shows that the tide had limited impact outside the intertidal zone.

The tidal propagation velocity in the intertidal zone can be estimated from time lags between P_3 and P_{13} derived from the cross–correlation analysis. The groundwater crest reached P_{13} only 10 min later than P_3, indicating that the pressure wave moved through STE at approximately 60 m/h. This value is 4–5 orders of magnitude higher than the maximum horizontal flow velocity of 30 cm/d previously estimated by assuming an isotropic aquifer

with a permeability K = 11.4 10^3 cm/d. The non–conservation of the fluctuation across the transect (Table 2), the delayed and dampened signal through the STE, and the high propagation velocity of the wave support the idea that the tide propagated as a dynamic wave within the STE. Without mass displacement of seawater into the STE, the formation of a recirculation cell and of its associated mixing zone only resulted from the vertical infiltration of seawater during the falling tide within the unsaturated zone between the water table and the beach surface.

3.2.2. Groundwater discharge dynamics at the beach face

Hydraulic heads were used to compute hydraulic gradients in the beach and calculate Darcy flows at the discharge zone. Chaillou et al. (2016) previously used a mean head gradient at 0.025, a value integrated over the study period of 16 days, to calculate an average groundwater flux without considering temporal variations induced by tidal oscillations. A horizontal hydraulic gradient was calculated between piezometer pairs, from the inland to the sea (P_{44}–P_{13}, P_{13}–P_3, and P_{44}–P_3) to produce a continuous head gradient time series. In Fig. 6, we observe the changing nature of exchanges between seawater and groundwater through tidal cycles, regardless of the position in the STE. The rising water table induced by tidal wave propagation contributed to dynamic horizontal gradients. These horizontal head gradients rapidly changed and were negatively correlated with the tidal oscillations recorded in the bay: the head gradient was maximal at low tide and fell to minimum values at high tide. Although the gradient changed rapidly during the transition from rising to falling tide, it showed a plateau with almost constant values during the transition from falling to rising tide. Hydraulic gradients induced in the intertidal zone remained constant over four to six hours around low tide. This pattern reflected the infiltration of seawater in the unsaturated zone during the downward migration of the water table. At that point, the horizontal gradient was positive most of the time, except during a few sporadic periods when the tide range was the highest (28–29 May). Hence, since the time–averaged beach hydraulic gradient was higher than sea level, it drove beach groundwater towards the discharge zone of the beach. Thus, seawater that entered the STE via vertical infiltration filled the empty space only when the water table dropped during the falling tide. The inland head gradient was sufficiently high at snow melt period to limit the infiltration of seawater within the STE, confirming the importance of fresh nature of the STE at the period.

Based on Darcy's Law and assuming that the hydraulic gradient component parallel to the coastline was null, groundwater fluxes in the beach aquifer (q; cm/d) were calculated as (5)

$$ q = K \cdot grad(h) \qquad (5) $$

where K is the mean hydraulic conductivity. A continuous time series of q was calculated (Fig. 6c). Using the average hydraulic conductivity and the average head gradient along the beach transect, qmean values ranged from 19 to 43 cm/d. The pattern of qmean values parallels that of grad(h), with the highest fluxes during low tide and the lowest at high tide. This tidal pumping effect is generally seen as an asymmetric seawater recirculation process (see Santos et al., 2009a) in which infiltration of seawater is large during rising tide and infiltration discharge is smaller during falling tides. Here, a detailed examination of the beach groundwater fluxes shows a different pattern. Infiltration and discharge were symmetrical. The high and constant fluxes measured during the transition period between falling and rising tide are expected to reflect the outflow of the seawater infiltrated within the unsaturated zone (Li et al., 1999). This maximal flux was relatively constant over the study period and close to 38–40 cm/d. To convert these results to volumetric flux, which is the discharge per unit width of the aquifer (in m^3/s), the cross–sectional flow area was determined using global posi-

146
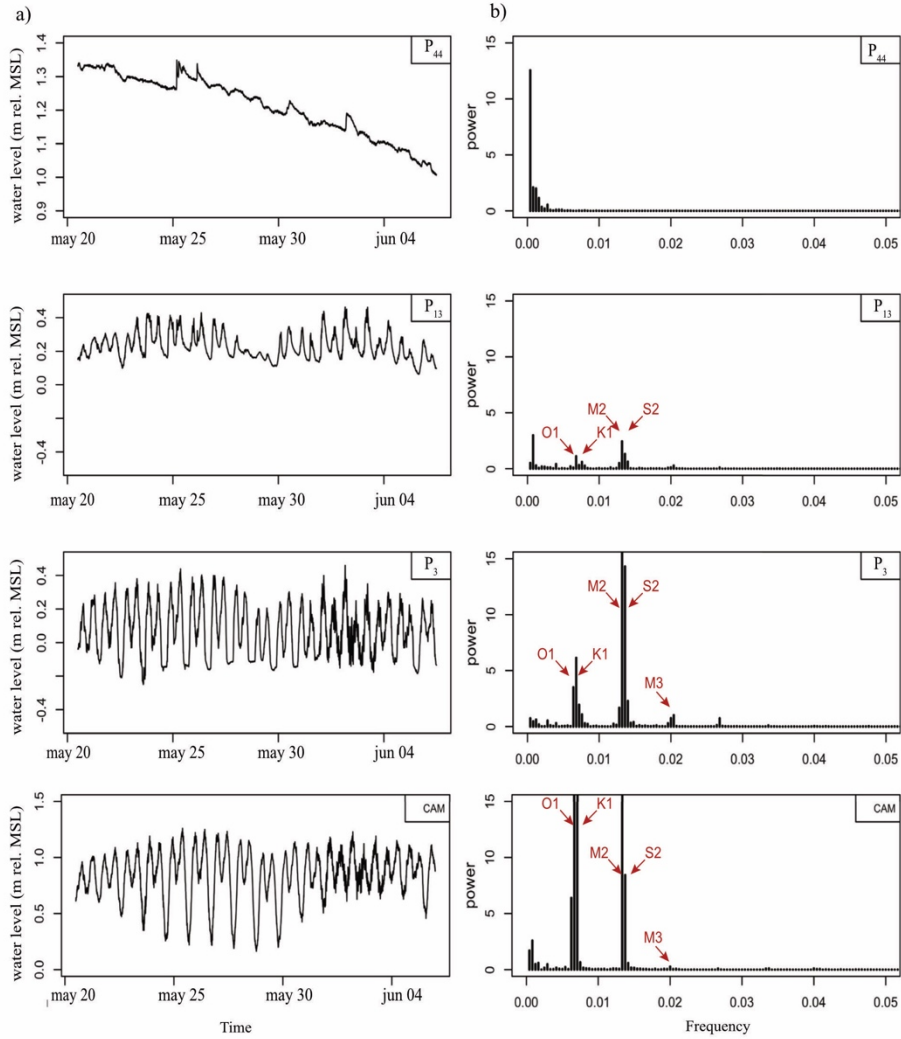
Fig. 5. a) Time series of water levels recorded every 10 min at the three piezometers (P$_3$,P$_{13}$, and P$_{44}$) and tidal oscillation at the CAM station during the 16 days of the study. Water levels are reported relative to mean sea level (0 m depth). b) Frequency analysis (10 min intervals) of the time series. The major tidal constituents (O1, K1, M2, S2, and M3; Table 3) are reported.

tioning system (GPS) measurements of 1200 m of shoreline (Chaillou et al., 2016). Based on the Ghyben–Herzberg and Glover relationship (Cooper et al., 1964), the top 7.7 m of the aquifer at the discharge zone (P$_3$) is fresh (except for the narrow surficial recirculation cell). Hence, using a depth of 7.7 m the maximal volumetric groundwater flux through the discharge zone was 0.040–0.043 m^3/s, assuming a uniform hydraulic conductivity (K) and an isotropic shallow aquifer all along the 1200 m of shoreline. These fluxes were 30% higher than those previously reported by

Chaillou et al. (2016) who neglected the effect of tidal oscillations in the intertidal zone (i.e. an average of 0.029 m^3/s). The outflow of the seawater infiltrated within the unsaturated part of the intertidal zone explains the difference in the calculation. This outflow contributed to only around 30% of the total discharge at the nearshore and is relatively small compared to the contribution of seawater reported that usually represented more than 90% of the total SGD, whatever the season (Martin et al., 2007; Mulligan and Charette, 2006; Taniguchi et al., 2002).
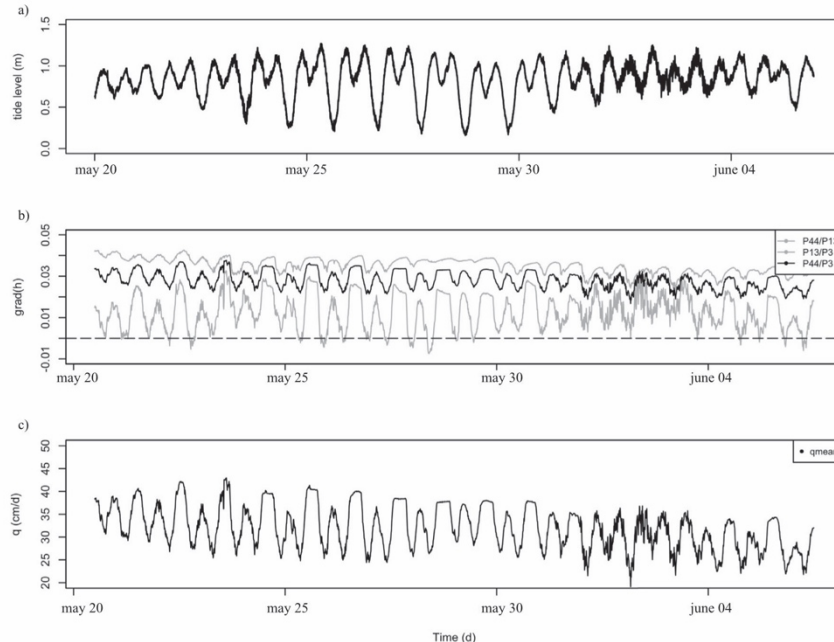
Fig. 6. a) Time series of tidal oscillation in Martinique Bay recorded at the Government of Canada Cap–aux–Meulestidal station (CAM station). b) Times series of horizontal head gradients measured between P_{44} and P_{13}, P_{13} and P_3, and P_{44} and P_3. The dashed line is the null gradient. Positive gradients correspond to seaward flow and negative gradients to landward flow. c) Time series of Darcy fluxes (cm/d) measured based on head gradients and hydraulic conductivities. The mean q value (qmean) was calculated based on the horizontal head gradient between P_{44} and P_3 with a mean hydraulic conductivity of $11.4 \ 10^3$ cm/d.

3.3. SGD estimation in front of the discharge zone

The high–resolution radon survey was done on 29 May 2013 (Table 1), when nearshore flow is supposed to be comprise between 30 and 40 cm/d (i.e., $0.04 \ m^3/s$) whatever the tide level (Fig. 6c). Fig. 7 presents the spatial distribution of the dataset. ^{222}Rn activities in the bay ranged from 6 to 66 Bq/m^3 and were three orders of magnitude lower than in inland and beach groundwater (12,000–17,000 Bq/m^3). The water depth in the studied area is 3.5 m, and the water is assumed to be vertically well mixed. Even though the studied area is small (0.180 km^2), the radon and physicochemical measurements showed spatial heterogeneity in front of the beach. This distribution resulted from the spatial patchiness of SGD at the discharge zone (Blanco et al., 2008; Welti et al., 2015) as well as the tidal effect that change the hydraulic gradient in the coastal aquifer and dilute the tracer concentrations in the water column (Burnett and Dulaiova, 2003; Dulaiova et al., 2010). The continuous radon measurements indicated high activities (up to 50 Bq/m^3) at the nearshore and a decrease with distance from the shore. These high activities were associated with lower electrical conductivities. Temperature data also showed a gradient from the beach to the bay that was probably linked to water depth (from 0.5 to 3.5 m) and tide level. The two clusters revealed by HCA analysis indicated that the data set is distributed in function of the distance from the shore whatever the tide level (Fig. 7d). The cluster 2 (N =16; Table 3), in the front of the beach, showed the highest ^{222}Rn activities and the lowest conductivities. In the cluster 1 (N =11; Table 3), ^{222}Rn activities were lower and conductivity was higher. The STE

was a diffuse source of ^{222}Rn–enriched groundwater to the bay. Assuming a well–vertical mixing in these shallow coastal waters, the radon in each cluster was assumed to be at steady state and the radon–derived mass balance was estimated in each box. The values used to determine total SGD fluxes are reported in Table 4. The calculated excess flux of ^{222}Rn was two times higher in the nearshore compared to the offshore box, with F_{GW} decreasing from 5.35 to $2.65 \ 10^7$ Bq/d.

A well–defined groundwater end–member is needed to convert these ^{222}Rn fluxes to volumetric SGD fluxes (Atkins et al., 2013; Baudron et al., 2015; Smith and Swarzenski, 2012). The approach consisted in choosing a regional groundwater end–member that represented the ^{222}Rn activity of the advected fluid, whatever its salinity. Radon activities measured in inland groundwater ranged from 12,000 to 17,000 Bq/m^3. The Archipelago's Permian aquifer is often considered as having homogeneous geochemical and hydrogeological characteristics (Comte and Banton, 2007). Its residence time has been estimated to range between one and four years (Madelin'Eau, 2004), well beyond the time of production from mineral–bound ^{226}Ra. The range of radon activities was larger in beach groundwater, ranging from a few Bq/m^3 at the surface to 21,000 Bq/m^3 in the deep part of the STE, and was not dependent of the salinity (Fig. 8). Excluding the radon activities from the surficial saline samples, the mean radon activity of local groundwater that included both fresh inland and beach groundwater were 14,067 Bq/m^3. This value represented a realistic end–member for radon activity in advected fluid and led to volumetric discharges of SGD (δQ_{GW}) to the bay ranging from 0.021 to 0.044 m^3/s (Table 4).
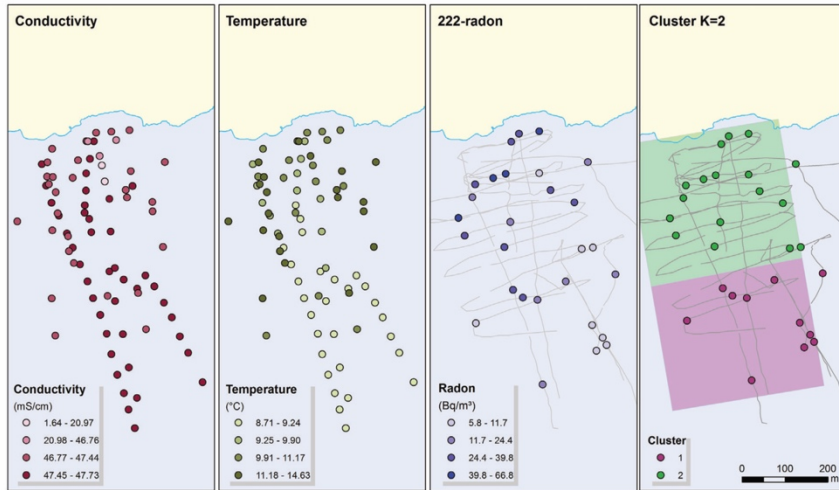
Fig. 7. Spatial distribution of specific conductivity (mS/cm) a), temperature (°C)b), and ^{222}Rn (Bq/m^3) c) in Martinique Bay offshore from the studied beach (29 May 2013). The GPS traces have been reported in grey lines in panel c. Panel d) shows the distribution of the two clusters as defined by a K–means analysis (see text for details) and their respective surface used for the calculations. The average values of physicochemical parameters, radon, and distance between clusters are reported in Table 3.

Table 3

Mean geochemical and physical characteristics of each cluster. N is the number of samples in each cluster. Depth (m) was from bathymetric data and distance (m) corresponds to the mean distance from the cluster to the shoreline estimating using a geographical information system. Surface area (m^2) was determined assuming a mean width of 300 m.

Cluster	N	Temperature (°C)	Specific conductivity (mS/cm)	^{222}Rn (Bq/m^3)	Distance (m)	Depth (m)	Surface area (km^2)
1	11	9.91	47.45	16.35	518	2.9	0.9
2	16	11.39	47.10	32.19	155	1.5	0.9

Table 4

Parameters and values used to determine submarine groundwater fluxes in each defined box. Clusters refer to groups of samples presented in Table 3. It is important to note the integration of tide current in the equation because it is the most important in-out flux of radon in the model.

Parameter	Units	Cluster 1	Cluster 2
A_{bay}	Bq/m^3	16.35	32.9
A_{GW}	Bq/m^3	$1.40\,10^4$	$1.40\,10^4$
F_{in} tide	Bq/d	$2.23\,10^6$	$2.23\,10^6$
F_{diff}	Bq/d	$1.44\,10^5$	$1.44\,10^5$
RF_{in}	Bq/d	$2.37\,10^6$	$2.37\,10^6$
F_{out} tide	Bq/d	$2.33\,10^6$	$4.60\,10^5$
F_{decay}	Bq/d	$5.53\,10^5$	$9.91\,10^5$
F_{atm}	Bq/d	$7.82\,10^1$	$1.54\,10^1$
RF_{out}	Bq/d	$2.89\,10^7$	$5.59\,10^7$
F_{GW}	Bq/d	$2.65\,10^7$	$5.35\,10^7$
Q_{GW}	m^3/s	$2.18\,10^2$	$4.40\,10^2$

Fig. 8. ^{222}Rn activities measured in fresh inland (grey dots) and beach groundwater (black dots) relative to groundwater conductivity. The dotted line is the mean value of ^{222}Rn excluding the samples located in the saline recirculation cell.

The main fluxes influencing the mass balance were the tidal fluxes in both directions whereas wind speed and ^{222}Rn evasion to the atmosphere had a low impact on the budget (Table 4). This tide–driven flux estimate was based on a simple model, where tide propagated as a constant volume of water, in and out of the two clusters with no loss to the adjacent area due to longshore currents, as in streams or estuaries (Atkins et al., 2013). Even though uncertainties were high with this approach, ^{222}Rn–derived SGD equal to the Darcy flow (i.e., from 0.034 to 0.041 m^3/s the day of

the survey). Comparing SGD estimation techniques in relation to scaling is still a challenge. Here, the excellent agreement between both radon and hydrological–based estimates of SGD is explained by the high spatial resolution of radon measurements, the integration of tidal oscillation in the Darcy flow estimation and an accurate Rn end–member value. Because it uses many point measurements over the area of interest, the Rn–based approach integrates both the spatial and tidal variabilities of the groundwater discharge and allow an accurate STE–integrated estimating of

SGD to the bay. To compare the volumetric estimates from this study with those of the literature, the volumetric fluxes were divided by the length of shoreline (1200 m). The shore–normal estimates ranged from 3.1 m^3/m/d and 1.5 m^3/m/d from the near-shore to the bay, respectively. This shoreline flux shows magnitudes equal to other microtidal STE, such as Waquoit Bay (Cape Cod, Massachusetts; 4–5.6 m^3/m/d; Mulligan and Charette, 2006), the Gulf of Thailand (3.7–7.8 m^3/m/d; Burnett et al., 2007), western Australia (2.5–8 m^3/m/d; Smith and Nield, 2003), Shelter Island (Long Island, New York; 0.4–17 m^3/m/d; Burnett et al., 2006), and Turkey Point (Florida; 0.7–22 m^3/m/d; Santos et al., 2009b).

Estimate the fresh SGD contribution to these total fluxes is not straightforward. Two approaches were implemented to choose an appropriate fresh SGD fluxes: a first one based on a regional and multi–annual hydrological mass balance of the Permian aquifer, and a second one based on Darcy flow estimated in the beach over the sampling period. Using the hydrological model proposed by Madelin'Eau (2004), the average fresh inland groundwater discharge is about 1.6 m^3/m/d, based on a decade of water level and on an average recharge rate of 230 mm/y (i.e., 25–30% of the annual snow and rain precipitation). This average flux represented 50% of the total SGD we measured near shore. This approach provided a conservative contribution despite it being based on an annual dynamic of recharge/discharge of the main island aquifer. The alternative approach provides an estimate of fresh groundwater flow of 2.1 m^3/m/d (i.e., 0.029 m^3/s, Chaillou et al., 2016) during the sampling period leading to a fresh contribution of 67% at the near shore. In both cases, fresh groundwater is then an important source of water to Martinique Bay compared to other studied sites, where the fresh inland groundwater contribution was often less than few percent. This high fresh groundwater fluxes were in agreement with isotopic and hydrologic results obtained within the STE. The snowmelt and absence of river in the archipelago contributed to the marked enhancement of fresh inland groundwater input to the bay during the snow melt period. Despite the fact that these results need further improvement notably with more radon surveys at different seasons, this first SGD–derived ^{222}Rn estimation already provided reliable SGD discharge through a snowmelt–affected STE during the spring season, when the water table is high. These findings also point out the crucial spring period, when snow melts and fresh inland groundwater acts as a path of anthropogenic solutes to marine environments.

4. Conclusions

This paper presented further evidence on the importance of boreal sandy beaches as a source of fresh groundwater to adjacent marine environments, particularly after the snow melt. The unique multi–parametric approach used in this study provided improved estimates of groundwater flow and solute transport through the discharge zone. The distribution of d^{18}O and d^{2}H in beach groundwater showed that fresh inland groundwater issue from snowmelt contributed from 30% to 97% of the water mass in the STE. In the deep part, the residence time of groundwater was sufficiently long that ^{222}Rn in groundwater was near secular equilibrium with mineral–bound ^{226}Ra. At the surface, however, the advective upward transport of ^{222}Rn–rich water and mixing with ^{222}Rn-poor overlying seawater induced a loss in ^{222}Rn. A time series of water table levels along the STE transect revealed that the tide propagated as a dynamic wave limiting the displacement of seawater within the STE. This up–and–down movement of the water table induced the vertical infiltration of seawater into the unsaturated part of the sediment which is very limited due to the high water table. In the bay, a radon–based mass balance model based on a high-resolution ^{222}Rn survey revealed shore–normal discharges

ranging from 3.1 m^3/m/d at the shore to 1.5 m^3/m/d. These near–shore discharges agreed quite well with Darcy fluxes calculated in the STE. Fresh inland groundwater makes up more than 50% of the total discharge, suggesting that boreal sandy beaches are important sources of freshwater and potential paths of groundwater–borne solutes to marine environments, particularly in the snowmelt season. This study demonstrated that it is crucial to quantified groundwater flow in site–specific scale in cold regions to refine estimates of global fresh and total groundwater discharge to coastal ocean.

References

Abarca, E., Karam, H., Hemond, H.F., Harvey, C.F., 2013. Transient groundwater dynamics in a coastal aquifer: the effects of tides, the lunar cycle, and the beach profile. Water Resour. Res. 49, 2473–2488. https://doi.org/10.1002/wrcr.20075.

Adam, J.C., Hamlet, A.F., Lettenmaier, D.P., 2009. Implications of global climate change for snowmelt hydrology in the twenty–first century. Hydrol. Process. 23, 962–972. https://doi.org/10.1002/hyp.7201.

Atkins, M.L., Santos, I.R., Ruiz–Halpern, S., Maher, D.T., 2013. Carbon dioxide dynamics driven by groundwater discharge in a coastal floodplain creek. J. Hydrol. 493, 30–42. https://doi.org/10.1016/j.jhydrol.2013.04.008.

Baudron, P., Cockenpot, S., Lopez–Castejon, F., Radakovitch, O., Gilabert, J., Mayer, A., Garcia–Arostegui, J.L., Martinez–Vicente, D., Leduc, C., Claude, C., 2015. Combining radon, short–lived radium isotopes and hydrodynamic modeling to assess submarine groundwater discharge from an anthropized semiarid watershed to a Mediterranean lagoon (Mar Menor, SE Spain). J. Hydrol. 525, 55–71. https://doi.org/10.1016/j.jhydrol.2015.03.015.

Baum, C.F., 2004. A review of Stata 8.1 and its time series capabilities. Int. J. Forecasting 20, 151–161. Available as Boston College Economics Working Paper No. 581, http://fmwww.bc.edu/ec–p/wp581.pdf.

Beck, A.J., Kellum, A.A., Luek, J.L., Cochran, M.A., 2015. Chemical flux associated with spatially and temporally variable submarine groundwater discharge, and chemical modification in the subterranean estuary at Gloucester point, VA (USA). Estuaries Coasts 1–12. https://doi.org/10.1007/s12237–015–9972–0.

Blanco, A.C., Nadaoka, K., Yamamoto, T., 2008. Planktonic and benthic microalgal community composition as indicators of terrestrial influence on a fringing reef in Ishigaki Island, Southwest Japan. Marine Environ. Res. 66, 520–535. https://doi.org/10.1016/j.marenvres.2008.08.005.

Brisebois, D., 1981. Lithostratigraphie des strates permo–carbonifères, de l'archipel des Îles–de–la–Madeleine. Ministère de l'Énergie et des Ressources du Québec. DPV–796.

Burnett, W.C., Dulaiova, H., 2003. Estimating the dynamics of groundwater input into the coastal zone via continuous radon–222 measurements. J. Environ. Radioact. 69, 21–35. https://doi.org/10.1016/S0265–931X(03)00084–5.

Burnett, W.C., Peterson, R., Moore, W.S., 2008. Radon and radium isotopes as tracers of submarine groundwater discharge – Results from the Ubatuba, Brazil SGD assessment intercomparison. Estuarine Coastal Shelf Sci. 76, 501–511. https://doi.org/10.1016/j.ecss.2007.07.027.

Burnett, W.C., Peterson, R.N., Santos, I.R., Hicks, R.W., 2010. Use of automated radon measurements for rapid assessment of groundwater flow into Florida streams. J. Hydrol. 380, 298–304. https://doi.org/10.1016/j.jhydrol.2009.11.005.

Burnett, W.C., Taniguchi, M., Oberdorfer, J., 2001. Measurement and significance of the direct discharge of groundwater into the coastal zone. J. Sea Res. 46, 109–116.

Burnett, W.C., Wattayakorn, G., Taniguchi, M., Dulaiova, H., Sojisuporn, P., Rungsupa, S., Ishitobi, T., 2007. Groundwater–derived nutrient inputs to the Upper Gulf of Thailand. Cont. Shelf Res. 27, 176–190. https://doi.org/10.1016/j.csr.2006.09.006.

Cable, J.E., Martin, J.B., 2008. In situ evaluation of nearshore marine and fresh pore water transport into Flamengo Bay, Brazil. Estuarine Coastal Shelf Sci. 76, 473–483. https://doi.org/10.1016/j.ecss.2007.07.045.

Chaillou, G., Couturier, M., Tommi-Morin, G., Rao, A.M.F., 2014. Total alkalinity and dissolved inorganic carbon production in groundwaters discharging through a Sandy Beach. Procedia Earth Planet. Sci. 10, 88–99. https://doi.org/10.1016/j.proeps.2014.08.017.

Chaillou, G., Lemay-Borduas, F., Couturier, M., 2016. Transport and transformations of groundwater–borne carbon discharging through a sandy beach to a coastal ocean. Can. Water Res. J./Revue canadienne des ressources hydriques 1–14. https://doi.org/10.1080/07011784.2015.1111775.

Chaillou, G., Touchette, M., Buffin-Bélanger, T., Cloutier, C.-A., Hétu, B., Roy, M.-A., 2017. Hydrogeochemical evolution and groundwater mineralization of shallow aquifers in the Bas–Saint–Laurent region, Québec, Canada. Canadian Water Res. J./Revue canadienne des ressources hydriques. https://doi.org/10.1080/07011784.2017.1387817. 1918–1817 (online).

Comte, J.C., Banton, O., 2007. Cross-validation of geo-electrical and hydrogeological models to evaluate seawater intrusion in coastal aquifers. Geophys. Res. Lett. 34, L10402. https://doi.org/10.1029/2007GL029981.

Cooper, H.H., Kohout, F.A., Henry, H.R., Glover, R.E., 1964. Sea Water in Coastal Aquifers, Water Supply Paper, serie 1613. U.S. Departement of the Interior, Washington.

Couturier, M., Nozais, C., Chaillou, G., 2016. Microtidal subterranean estuaries as a source of fresh terrestrial dissolved organic matter to the coastal ocean. Mar. Chem. 186, 46–57. https://doi.org/10.1016/j.marchem.2016.08.001.

Dulaiova, H., Camilli, R., Henderson, P.B., Charette, M.A., 2010. Coupled radon, methane and nitrate sensors for large-scale assessment of groundwater discharge and non–point source pollution to coastal waters. J. Environ. Radioact. 101, 553–563. https://doi.org/10.1016/j.jenvrad.2009.12.004.

Dulaiova, H., Peterson, R., Burnett, W.C., Lane–Smith, D., 2005. A multi–detector continuous monitor for assessment of 222Rn in the coastal ocean. J. Radioanal. Nucl. Chem. https://doi.org/10.1007/s10967–005–0595–.

Elgar, S., 1999. Tidal water table fluctuations in a sandy ocean beach. Water Resour. Res. 35 (8), 2313–2320.

Evans, T.B., Wilson, A.M., 2017. Submarine groundwater discharge and solute transport under a transgressive barrier island. J. Hydrol. 547, 97–110. https://doi.org/10.1016/j.jhydrol.2017.01.028.

Gonfiantini, R., 1978. Standards for stable isotope measurements in natural compounds. Nature 271, 534–536.

Heiss, J.W., Michael, H.A., 2014. Saltwater–freshwater mixing dynamics in a sandy beach aquifer over tidal, spring–neap, and seasonal cycles. Water Resour. Res. 50, 6747–6766. https://doi.org/10.1002/2014WR015574.

Heiss, J.W., Ullman, W.J., Michael, H.A., 2014. Swash zone moisture dynamics and unsaturated infiltration in two sandy beach aquifers. Estuarine Coastal Shelf Sci. 143, 20–31. https://doi.org/10.1016/j.ecss.2014.03.015.

Hwang, D.–W., Kim, G., Lee, W.–C., Oh, H.–T., 2010. The role of submarine groundwater discharge (SGD) in nutrient budgets of Gamak Bay, a shellfish farming bay, in Korea. J. Sea Res. 64, 224–230. https://doi.org/10.1016/j.seares.2010.02.006.

Li, L., Barry, D.A., Stagnitti, F., 1999. Submarine groundwater discharge and associated chemical input to a coastal sea. Water Resour. Res. 35, 3253–3259.

Madelin'Eau, 2004. Gestion des eaux souterraines aux Îles–de–la–Madeleine un défi de développement durable Final Report. MDDEFP, Rimouski, Qc, Ca, p. 58.

Martin, J.B., Hartl, K., Corbett, D., Swarzenski, P., Cable, J., 2003. A multi–level pore–water sampler for permeable sediments. J. Sediment. Res. 73, 128–132.

Martin, J.B., Cable, J.E., Smith, C., Roy, M., Cherrier, J., 2007. Magnitudes of submarine groundwater discharge from marine and terrestrial sources: Indian River Lagoon, Florida. Water Resour. Res. 43. https://doi.org/10.1029/2006WR005266.

Michael, H.A., Mulligan, A.E., Harvey, C.F., 2005. Seasonal oscillations in water exchange between aquifers and the coastal ocean. Nature 436, 1145–1148. https://doi.org/10.1038/nature03935.

Moore, W.S., 1999. The subterranean estuary: a reaction zone of ground water and sea water. Mar. Chem. 65, 111–125.

Moore, W.S., 2010. A Reevaluation of Submarine Groundwater Discharge Along the Southeastern Coast of North America. Global Biogeochemical Cycles 24, GB4005. doi: 10.1029/2009GB003747.

Mulligan, A.E., Charette, M.A., 2006. Intercomparison of submarine groundwater discharge estimates from a sandy unconfined aquifer. J. Hydrol. 327, 411–425. https://doi.org/10.1016/j.jhydrol.2005.11.056.

Peterson, R.N., Santos, I.R., Burnett, W.C., 2010. Evaluating groundwater discharge to tidal rivers based on a Rn–222 time–series approach. Estuarine Coastal Shelf Sci. 86, 165–178. https://doi.org/10.1016/j.ecss.2009.10.022.

Povinec, P.P., Burnett, W., Beck, A., Bokuniewicz, H., Charette, M., Gonneea, M.E., Groening, M., Ishitobi, T., Kontar, E., Liong Wee Kwong, L., Marie, D.E.P., Moore, W.S., Oberdorfer, J.A., Peterson, R., Ramessur, R., Rapaglia, J., Stieglitz, T., Top, Z., 2012. Isotopic, geophysical and biogeochemical investigation of submarine groundwater discharge: IAEA–UNESCO intercomparison exercise at Mauritius Island. J. Environ. Radioact. 104, 24–45. https://doi.org/10.1016/j.jenvrad.2011.09.009.

Robinson, C., Li, L., Barry, D., 2007. Effect of tidal forcing on a subterranean estuary. Adv. Water Res. 30, 851–865.

Rotzoll, K., El–Kadi, A.I., 2008. Estimating hydraulic properties of coastal aquifers using wave setup. J. Hydrol. 353, 201–213. https://doi.org/10.1016/j.jhydrol.2008.02.005.

Santos, I.R., Eyre, B.D., Huettel, M., 2012. The driving forces of porewater and groundwater flow in permeable coastal sediments: a review. Estuarine Coastal Shelf Sci. 98, 1–15.

Santos, I.R., Burnett, W.C., Dittmar, T., Suryaputra, I.G.N.A., Chanton, J., 2009a. Tidal pumping drives nutrient and dissolved organic matter dynamics in a Gulf of Mexico subterranean estuary. Geochim. Cosmochim. Acta 73, 1325–1339. https://doi.org/10.1016/j.gca.2008.11.029.

Santos, I.R., Dimova, N., Peterson, R.N., Mwashote, B., Chanton, J., Burnett, W.C., 2009b. Extended time series measurements of submarine groundwater discharge tracers (222Rn and CH4) at a coastal site in Florida. Mar. Chem. 113, 137–147. https://doi.org/10.1016/j.marchem.2009.01.009.

Schiavo, M.A., Hauser, S., Povinec, P.P., 2009. Stable isotopes of water as a tool to study groundwater–seawater interactions in coastal south–eastern Sicily. J. Hydrol. 364, 40–49. https://doi.org/10.1016/j.jhydrol.2008.10.005.

Schlitzer, R., 2016. Ocean Data View http://odv.awi.de.

Scott, D.B., Gayes, P.T., Collins, E.S., 1995. Mid–holocene precedent for a future rise in sea–level along the Atlantic coast of North America. Coast. Educ. Res. Found. Inc. 11 (3), 615–622.

Smith, A.J., Nield, S.P., 2003. Groundwater discharge from the superficial aquifer into Cockburn Sound Western Australia: estimation by inshore water balance. Biogeochemistry 66, 125–144. https://doi.org/10.1023/B:BIOG.0000006152.27470.a9.

Smith, C.G., Swarzenski, P.W., 2012. An investigation of submarine groundwater—borne nutrient fluxes to the west Florida shelf and recurrent harmful algal blooms. Limnol. Oceanogr. 57, 471–485. https://doi.org/10.4319/lo.2012.57.2.0471.

Taniguchi, M., Burnett, W.C., Cable, J.E., Turner, J.V., 2002. Investigation of submarine groundwater discharge. Hydrol. Process. 16, 2115–2129. https://doi.org/10.1002/hyp.1145.

Ullman, W., Chang, B., Miller, D., Madsen, J., 2003. Groundwater mixing, nutrient diagenesis, and discharges across a sandy beachface, Cape Henlopen, Delaware (USA). Estuarine Coastal Shelf Sci. 57, 539–552.

Valiela, I., Costa, J., Foreman, K., Teal, J.M., Teal, J., Howes, B., 1990. Transport of groundwater–borne nutrients from watersheds and their effects on coastal waters. Biogeochemistry 10, 177–197. https://doi.org/10.1007/BF00003143.

Welti, N., Gale, D., Hayes, M., Kumar, A., Gasparon, M., Gibbes, B., Lockington, D., 2015. Intertidal diatom communities reflect patchiness in groundwater discharge. Estuarine Coastal Shelf Sci. 163, 116–124. https://doi.org/10.1016/j.ecss.2015.06.006.

Xin, P., Robinson, C., Li, L., Barry, D.A., Bakhtyar, R., 2010. Effects of wave forcing on a subterranean estuary. Water Resour. Res. 46. https://doi.org/10.1029/2010WR009632. n/a–n/a.

Zielinski, R.A., Otton, J.K., Budahn, J.R., 2001. Use of radium isotopes to determine the age and origin of radioactive barite at oil–field production sites. Environ. Pollut. 113, 299–309.

ANNEXE II

CARBON DIOXIDE SOURCES AND SINKS IN THE DELTA OF THE PARAÍBA DO
SUL RIVER (SOUTHERN BRAZIL) MODULATED BY CARBONATE
THERMODYNAMICS, GAS EXCHANGE, AND ECOSYSTEM METABOLISM
DURING ESTUARINE MIXING

(Cotovicz et al., 2020)

Carbon dioxide sources and sinks in the delta of the Paraíba do Sul River (Southeastern Brazil) modulated by carbonate thermodynamics, gas exchange and ecosystem metabolism during estuarine mixing

Luiz C. Cotovicz Jr[a,b,*], Luciana O. Vidal[c], Carlos Eduardo de Rezende[c], Marcelo C. Bernardes[a], Bastiaan A. Knoppers[a], Rodrigo L. Sobrinho[a], Renan P. Cardoso[d], Marcelo Muniz[d], Roberto Meigikos dos Anjos[d], Antoine Biehler[e], Gwenaël Abril[a,f]

[a] Programa de Geoquímica, Universidade Federal Fluminense, Niterói, RJ, Brazil
[b] Instituto de Ciências do Mar (LABOMAR), Universidade Federal do Ceará, Fortaleza, CE, Brazil
[c] Laboratório de Ciências Ambientais, Centro de Biociências e Biotecnologia Universidade Estadual do Norte Fluminense, Campos dos Goytacazes, RJ, Brazil
[d] Laboratório de Radioecologia e Alterações Ambientais, Instituto de Física, Universidade Federal Fluminense, Niterói, RJ, Brazil
[e] Canada Research Chair in Geochemistry of Coastal Hydrogeosystems, Québec-Océan, Boreas Group on the North Systems, Université du Québec à Rimouski, Rimouski, Canada
[f] Biologie des Organismes et Ecosystèmes Aquatiques (BOREA), UMR 7208, Muséum National d'Histoire Naturelle, CNRS, IRD, SU, UCN, UA, Paris, France

A R T I C L E   I N F O

A B S T R A C T

Tropical estuarine deltas generally present poorly buffered waters in their freshwaters. Carbonate chemistry predicts that mixture of such warm freshwater with seawater will create rapid consumption of the freshwater carbon dioxide (CO_2) by the carbonate buffering capacity of the seawater. In this study, we used the Paraiba do Sul River as a laboratory to investigate how thermodynamics compare with biological processes, gas exchange, and tidal advection from mangrove. We conducted three spatial surveys covering the salinity gradient of the main channel and surrounding mangrove waters and one 24–h mooring in a mangrove creek. In the main channel, dissolved inorganic carbon (DIC) and total alkalinity (TA) showed closely conservative distribution along the salinity gradient, increasing seaward. The partial pressure of CO_2 (pCO_2) followed a bell–shaped curve predicted by carbonate chemistry for conservative mixing of river and ocean endmembers. During high river flow, pCO_2 sharply decreased between salinities 0 and 5 (1800 to 390 ppmv), a pCO_2 drawdown attributed to riverine outgassing and thermodynamics. Indeed, the mixing of TA–poor freshwater ($363 \pm 16\,\mu mol\,kg^{-1}$) with TA–rich seawater creates a deficit of dissolved CO_2 not related to biotic processes. During low river flow, the entire mixing zone was undersaturated in pCO_2 with an increasing trend seaward. However, observed pCO_2 values were slightly above those predicted by conservativity. Approximately half of this deviation was attributed to biological activity (net heterotrophy), and remaining deviation was assigned to the effects of gas exchange (18%) and water heating (36%). The effect of gas exchange was higher in fresh and low salinity waters, re-flecting the higher outgassing/ingassing of CO_2, and lower buffering capacity. Water heating was more im-portant in mid–to high–salinities as a result of diel patterns of solar irradiance. Heterotrophy was slight and not able to outcompete thermodynamics and generate outgassing during estuarine mixing. Consistently, stable isotopic signatures of DIC ($\delta^{13}C$–DIC) presented slight deviations below the conservative mixing, corroborating net heterotrophy in the main channel. Areas of CO_2 uptake due to phytoplankton activity were identified but restricted to the freshwater endmember during low river flow, with lowest pCO_2 (up to 41 ppmv) and the highest chlorophyll a (up to $21.3\,\mu g\,L^{-1}$). The estuary was a CO_2 sink during low river flow (-1.34 to $-5.26\,mmolC\,m^{-2}\,d^{-1}$) and a source during high river flow (5.71 to $19.37\,mmolC\,m^{-2}\,d^{-1}$). In the mangrove creek, the pCO_2, DIC, $\delta^{13}C$–DIC and TA presented deviations from the conservativity, with slopes between TA and DIC demon-strating organic carbon degradation mediated by aerobic respiration and sulphate reduction. Mangrove creek waters were a CO_2 source (average of $134.81\,mmolC\,m^{-2}\,d^{-1}$), exhibiting high values of pCO_2 (up to 21,720 ppmv). The results reveal that the low buffering capacity in the main channel of tropical estuarine deltas can be the predominant driver of pCO_2, generating CO_2 undersaturation along the mixing zone, a process overlooked in estuarine systems. Moreover, air–water CO_2 exchange, thermal variability, and biological activities contribute to

---

deviation of the carbonate system from conservative mixing in specific estuarine areas, also modulating pCO$_2$ variability.

1. Introduction

The concentration of carbon dioxide (CO$_2$) in Earth's atmosphere has been increasing at fast rates, and the current CO$_2$ level is unprecedented over the past 3 million years (Willeit et al., 2019), changing approximately from 277 ppmv in 1750 (Joos and Spahni, 2008) to 414 ppmv in April 2019 (NOAA, 2019), as a result of fossil fuel burning and land-use changes. According to recent estimates, the oceans and the land absorb approximately 23 and 32% of these total emissions, respectively, whereas the remaining 45% accumulate in the atmosphere (Le Quéré et al., 2018). This CO$_2$ accumulation in the atmosphere is causing global warming, with CO$_2$ as the most important anthropogenic-derived greenhouse gas (IPCC, 2013). In addition, penetration of CO$_2$ in the ocean is causing acidification, increasing the surface ocean partial pressure of carbon dioxide (pCO$_2$), with a net decline of pH (Gattuso et al., 2015). While carbon sink in the open ocean is currently estimated with a relative high degree of confidence (2.5 $\pm$ 0.5 GtC yr^{-1}; Le Quéré et al., 2018), the air-water CO$_2$ fluxes and controlling processes remain uncertain in the coastal ocean. Indeed, coastal oceans have not been satisfactory included in global carbon budget calculations, despite their importance in terms of global carbon cycling (Chen and Borges, 2009; Cai, 2011; Bauer et al., 2013).

Estuaries are aquatic ecosystems characterized by the mixing of fluvial and marine waters, hosting a large diversity of interfaces and gradients, with distinct physical, geomorphological and biological features (Cai, 2011; Borges and Abril, 2011). Studies have shown that CO$_2$ emissions by estuarine systems and near-shore coastal waters are globally significant (Chen and Borges, 2009). However, in 10 years of global data compilation, CO$_2$ emission estimates have decreased by a factor of 6. The first global estimate of estuarine CO$_2$ emissions calculated a degassing of 0.6 PgC yr^{-1} (Abril and Borges, 2004), whereas the two lasts estimates showed degassing of approximately 0.1 PgC yr^{-1} (Chen et al., 2013; Laruelle et al., 2013). This decline has been attributed to various factors, mainly the disproportional and insufficient global sampling (poor coverage in tropical regions and the Southern Hemisphere), few studies with direct and continuous measurements of pCO$_2$, and low temporal resolution (semi-diurnal, diurnal, seasonal, and annual) (Borges and Abril, 2011; Cai, 2011; Chen et al., 2013).

In general, the upper estuarine regions with low-salinity waters are important sources of CO$_2$ to the atmosphere. This is normally attributed their net heterotrophy and, to a lesser extent, to inputs of CO$_2$-enriched freshwater and lateral inputs from intertidal areas such as salt marshes and mangroves (Cai et al., 1999; Cai et al., 2011; Borges and Abril, 2011). However, in some estuaries, the riverine contributions of CO$_2$ (allochthonous sources) can be greater than contribution of estuarine heterotrophy (autochthonous sources) at certain times of the year (Jiang et al., 2008; Joesoef et al., 2015; Van Dam et al., 2018a). Climatological and hydrological characteristics may change seasonally according to river water discharge, temperature, and formation of vertical stratification, which modulate physical mixing and biological production (Frankignoulle et al., 1998; Salisbury et al., 2008; Borges and Abril, 2011; Dinauer and Mucci, 2017). Downstream in the seaward direction, estuarine mixing zones are considered as moderate CO$_2$ sources, whereas the marine domain from the river mouth to the shelf break generally behaves as a CO$_2$ sink (Frankignoulle et al., 1998; Borges and Abril, 2011; Chen et al., 2013). In general, the pCO$_2$ values and CO$_2$ emissions are much higher in river-dominated estuaries than in marine-dominated estuaries (Jiang et al., 2008; Cotovicz Jr. et al., 2015). In addition to the marked and complex natural variability, the coastal ocean hosts approximately 37% of the human population (Cohen et al., 1997), creating human-induced modifications in the metabolism of aquatic ecosystems associated with nutrient enrichment and eutrophication (Frankignoulle et al., 1998; Zhai et al., 2007; Cotovicz Jr. et al., 2015; Kubo et al., 2017).

Historically, studies addressing estuaries have identified biological processes as predominant drivers on pCO$_2$ distribution and CO$_2$ fluxes along salinity gradients (Frankignoulle et al., 1998; Cai et al., 1999; Borges and Abril, 2011). However, the theory of carbonate chemistry predicts drastic abiotic changes in proportions of dissolved CO$_2$, bicarbonate (HCO$_3^-$), and carbonate (CO$_3^{2-}$) during the mixing of freshwater with seawater. The influence of thermodynamics in the CO$_2$ system in estuarine waters was first described by the pioneer studies of Mook and Koene (1975) and Whitfield and Turner (1986). These authors showed that modification of the carbonate equilibria in estuarine waters during the mixing of freshwater with seawater results in changes in the pCO$_2$ and, in turn, in the CO$_2$ fluxes at the air-water interface (Whitfield and Turner, 1986; Hu and Cai, 2013; Cai et al., 2013). In particular, the displacement of acid-base equilibrium during the mixing of weakly buffered freshwater (low TA concentration) with well buffered seawater (high TA concentration) can generate pCO$_2$ values far below that of the atmosphere, with no need for biological uptake (Whitfield and Turner, 1986). In this regard, thermodynamic processes would be potentially significant compared with biological processes in oligotrophic/mesotrophic estuaries with short residence times as, for example, estuarine deltas. Thermodynamic changes as the main driver of carbonate chemistry changes along the salinity gradient in estuaries were have been demonstrated in theoretical studies (Hu and Cai, 2013; Salisbury, 2008; Cai et al., 2013), but rarely validated using field data. In the Amazon River plume, pCO$_2$ undersaturation has been attributed mainly to phytoplankton productivity (Ternon et al., 2000; Körtzinger, 2003); however, recent findings showed that, from a salinity value of approximately 10, surface water becomes undersaturated as a result of the mixing effect (Lefèvre et al., 2017).

The geographical position also exerts influence over CO$_2$ concentrations and emissions across different latitudes. Estuaries located at low and intermediate latitudes present the largest flux per unit area, whereas those located in regions north of 50° N and south of 50° S present the lowest flux per unit area (Chen et al., 2013). These differences are attributed to local/regional characteristics of the coastal zone, including the mixing of freshwaters (presenting variable levels of pCO$_2$) with low-pCO$_2$ shelf waters, water temperature, and biogeochemistry complexity (Chen et al., 2013). However, it should be highlighted that studies on carbon cycling conducted in tropical coastal regions are overlooked compared with those in temperate and boreal regions. In addition, tropical rivers present lower TA concentrations than temperate/boreal rivers (Cai et al., 2008), thus the impact of thermodynamic processes during river-ocean mixing can be especially important in tropical estuaries. Estuarine deltas can locally/regionally be the main estuarine type through which significant terrestrial carbon is transported to the ocean (Laruelle et al., 2013). Deltas are mostly located in tropical and sub-tropical regions (Laruelle et al., 2013).

The present study aims at investigating the carbonate chemistry and air-water CO$_2$ exchange in the Paraiba do Sul River estuary (PSRE), southeastern Brazil. This estuary is a tropical mesotrophic ecosystem that has been suffering with increasing eutrophication and construction of dams in its watershed. This ecosystem has a short residence time and low TA concentrations in freshwater, potentially generating pCO$_2$ undersaturation conditions during mixing with seawater as a result of thermodynamic changes –a fact that is still disregarded globally. Based on high resolution monitoring of carbonate chemistry parameters along

154
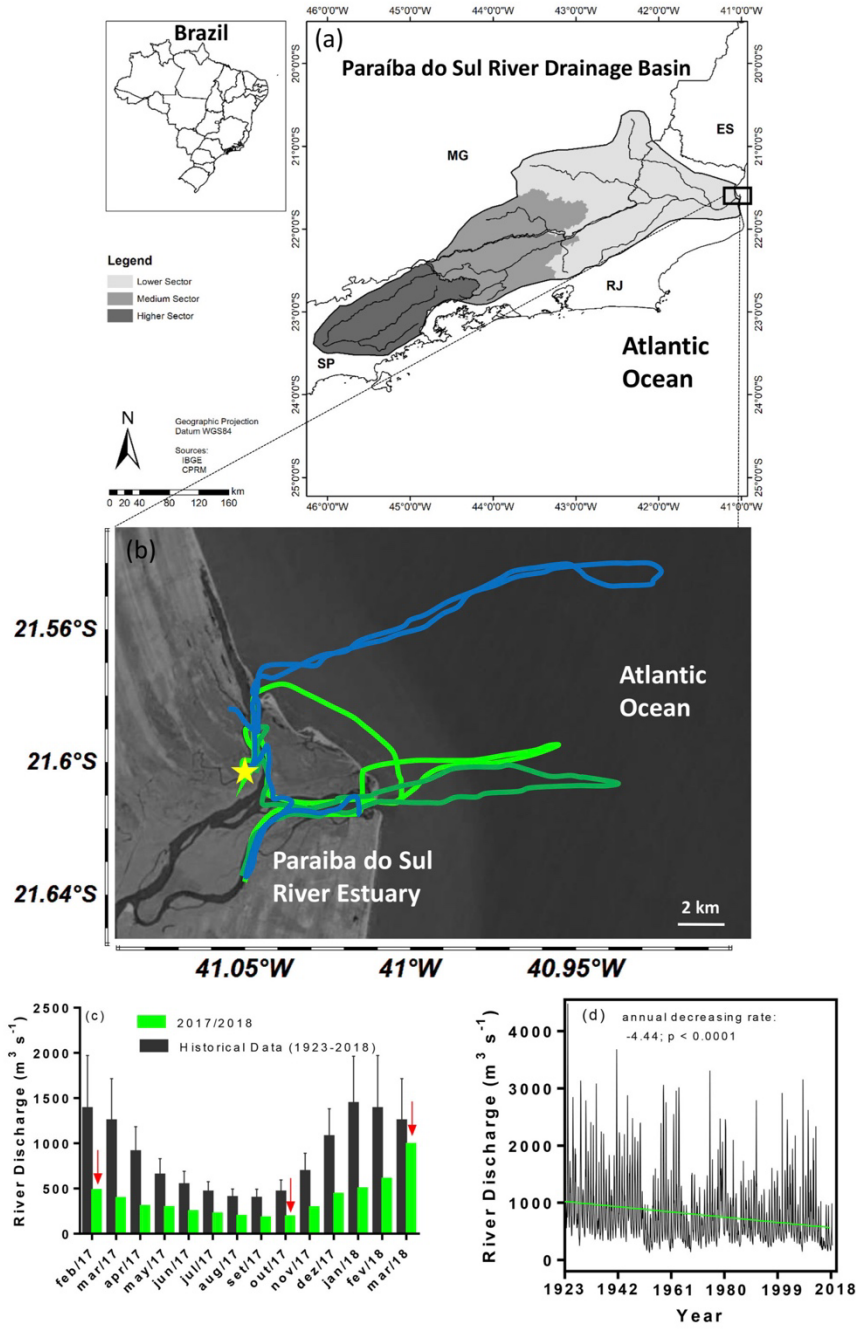
(caption on next page)

3

Fig. 1. Map 1a shows the localization of the state of Rio the Janeiro. The river basins are shown in shades of grey. Map 1b shows the localization of the PSRE and adjacent shelf waters. The colored lines represent the boat track with online and continuous measurements of pCO_2, DO, pH, temperature, and salinity. Note that the boat track varied in each sampling campaign: light green, dark green and blue represent Feb 17, Oct 17 and Mar–18, respectively. Along the boat track, discrete stations were sampled (the exact localization of the sampling stations exhibited variations between sampling campaigns according to the boat track and the salinity gradient). The yellow star represents the localization of the anchoring station (Eulerian time-series data). Graph c shows a comparison between the river water discharge for the year of sampling (2017/2018) and the historical average. The red arrows are the sampling months. Graph d shows a historical tendency of decreasing river flow (average monthly values). (For interpretation of the references to colour in this figure legend, the reader is referred to the web version of this article.)

the entire salinity gradient, we could differentiate between the biotic and abiotic contributions to water pCO_2 distributions and CO_2 fluxes at the air–water interface; we also analyzed the metabolism of the main channel using pCO_2 distributions and stable isotope data.

2. Material and methods

2.1. Study area

The Paraiba do Sul River is an important water resource located in the southeast region of Brazil. The river watershed has an area of approximately 54,400 km^2, with a length of 1145 Km, traversing the most industrialized and urbanized region of Brazil (the states of São Paulo, Minas Gerais and Rio de Janeiro). According to previous studies, the river basin is divided into three regions (Ovalle et al., 2013): 1. the upper basin (7300 km^2), with water sources at 1800 m of altitude until 600 m in a valley of crystalline rocks; 2. the medium basin (27,500 Km^2), with average elevation of 500 m; 3. the lower basin (22,500 km^2), comprising coastal plains, with extensive meanders and islands until the river mouth into the Atlantic Ocean (Fig. 1).

The PSRE, located at the north region of the state of Rio de Janeiro (21°37′ S; 41°01′ W), is composed of a main river channel and a minor secondary channel (Fig. 1). The secondary channel harbors a mangrove forest of approximately 8 km^2 (Sterza and Fernandes, 2006). The coast is microtidal with high energy of waves, forming an estuarine delta. According to the Köppen's classification, climate in the region is Aw, with wet summers (November to January) and dry winters (July to September) (Cotovicz Jr. et al., 2013). The river discharge in the estuary follows a seasonal cycle, with high water flow in summer and early spring and low water flow in winter and early autumn, with discharges averages of 1158 and 444 $m^3\ s^{-1}$, respectively. The river discharge modulates the residence time of waters in the mixing zone (Souza et al., 2010) and the extension of the river plume in the adjacent coastal ocean (Rudorff et al., 2011). During low water flow, the plume is reduced and it takes approximately 10 days for the water to reach open ocean (salinity 35), whereas during high water flow, the plume is extended along the shelf and the residence time decreases to 6 days (Souza et al., 2010).

The river has undergone increasing anthropogenic influences. The total human population on its watershed is estimated at 5 million inhabitants. Considering only the estuarine region, the surrounding population is estimated at approximately 600,000 inhabitants (IBGE, 2018). In addition, the lower basin presents extensive farming, particularly sugar cane production (Ovalle et al., 2013). The coverage of wastewater treatment plans is still very small in the region, less than 50% of the total households. Therefore, the estuary receives a large amount of industrial, agricultural and domestic effluents, with large inputs of nutrients to the waters, thus presenting mesotrophic characteristics (Cotovicz et al., 2013). Reservoirs and hydroelectric dams have been constructed along the drainage basin (forty–seven different hydroelectric power plants; Ovalle et al., 2013), which have changed hydrological patterns and potentially altered carbon cycling in the estuary.

2.2. Sampling strategy

Three extensive spatial surveys were conducted in the estuary on February 17, October 17 and March 18. The Feb 17 sampling, historically considered as the rain season, presented an accumulated monthly precipitation of 40 mm, which is 60 mm lower than the historical average, with a 7–day accumulated precipitation before sampling of only 1 mm. The Oct 17 sampling presented an accumulated monthly precipitation of 13 mm (80 mm lower than the historical average), with a 7–day accumulated precipitation before sampling of 4 mm. The Mar 18 sampling presented an accumulated monthly precipitation of 376 mm, which is 267 mm higher than the historical data. Thus, the Feb 17 and Oct 17 samplings were considered dry conditions and the Mar 18 sampling was considered wet condition. These climatological characteristics influenced the hydrological pattern. The Feb 17 and Oct 17 samplings were conducted during low river flow, with average discharges of 288 and 178 $m^3\ s^{-1}$, respectively (Fig. 1c,d), whereas the Mar 18 collection was performed during high river flow, with average discharge of 1240 $m^3\ s^{-1}$. The mean historical river water discharge (reference period of 95 years, 1923–2018) presented higher values than the discharge verified on the sampling days (Fig. 1c,d). The regression line of the historical data shows that the river discharge has been decreasing at a rate of ~5 $m^3\ s^{-1}$ per year, which means that the mean discharge has already decreased by 475 $m^3\ s^{-1}$.

In each sampling campaign, continuous and discrete aquatic measurements were performed. Continuous and online measurements were conducted for pCO_2, dissolved oxygen (DO), pH, salinity, and temperature. Surface water was sampled in the mangrove creeks and in the main channel in discrete points distributed regularly along the whole salinity gradient (0 to 35) with approximately three salinity unit increments. Discrete samples were used to analyze TA, Chl a, and δ^{13}C-DIC. The spatial surveys covered the freshwater domain (upper estuary), the mixing zone (complete salinity gradient), and the external estuary (river plume adjacent to the coastal ocean). The spatial surveys started in the morning, at around 8:30 am, and finished in the early–afternoon, at around 4:00 pm. In addition to the spatial survey screening, an Eulerian time series (24 h of sampling) was conducted in the mangrove tidal creek located in the secondary channel on March 2018 (Fig. 1), combining continuous measurements and discrete water sampling within 2 h of interval for the same water parameters previously described.

2.3. Continuous measurements

Continuous samplings were performed from a boat, with real–time measurements of position, pCO_2, DO, pH, salinity, and temperature, at a frequency of 1 min (Frankignoulle et al., 2001; Abril et al., 2014; Cotovicz Jr. et al., 2016). Briefly, a water pump placed at a depth of ~0.5 m provided continuous 6 L min^{-1} water flux to the boat. A part of this flux (~3 L min^{-1}) was directed to an equilibrator to measure the pCO_2. The marble equilibrator consisted of an acrylic tube (60 cm in length; 8 cm in diameter) filled with glass marbles where the water flows from top to bottom and a closed air circuit with a flow of ~1 L min^{-1} in the opposite direction, from bottom to top. The air is dried using a desiccant (Drierite™) and pumped into a non–dispersive infrared gas analyzer (Li–820 NDIR, LI–COR). Before and after each

4

156

sampling campaign, the NDIR was calibrated using gas standards with air pCO_2 values of 410, 1007 and 5035 ppmv (White Martins Certified Material, RJ, Brazil). Fresh soda lime was used to set the zero and the standard at 1007 ppmv was used to set the span. The air standards of 1007 and 5035 ppmv were used to verify the system stability. The boat speed was 8-10 km h^{-1} during the spatial surveys. The equilibration time of the pCO_2 measurement system is 2-3 min (Cotovicz Jr. et al., 2016). This gas equilibration device is ideal for pCO_2 analysis in estuarine waters due to its fast response time (Frankignoulle et al., 2001, Abril et al., 2014; Cotovicz Jr. et al., 2016). This time is sufficient to guarantee the equilibration along the estuarine mixing. In the steepest part of the salinity gradient, between salinities 10 and 20, the velocity of the vessel was reduced to less than 2 km h^{-1} before all discrete sampling, this allowed a complete gas equilibration for pCO_2 measurements. Accuracy of the pCO_2 measurements was estimated at $\pm$ 5 ppmv. Temperature, salinity, and DO were measured using a calibrated YSI Professional Plus multiparameter meter, and pH was measured using a WTW 3310 pH meter equipped with a Sentix 41 electrode, calibrated with a three-point standard (pH 4.01, pH 7.00 and pH 10.01) according to the National Institute of Standards and Technology (NIST), before and after each sampling campaign. The precision of the pH measurements estimated after seven verifications against standards before and after each sampling campaign was approximately 0.01 NBS units. For the anchored continuous sampling (Eulerian approach), the total duration of sampling was 20 h, encompassing one complete tidal cycle plus one ebb tide period. Two tidal cycles of measurements were not completed due to logistic problems.

2.4. Discrete measurements and laboratory analysis

Discrete samples were collected at a depth of ~0.5 m using a Niskin bottle and then stored for further laboratory chemical analysis (i.e., fixed and/or kept on ice in the dark). The water was filtered with Whatman®grade GF/F glass microfiber filters (pre-combusted at 500 °C for 6 h), followed by determination of TA and Chl a. The filters used to analyzed Chl a were kept at −18 °C prior to analysis. TA measurements were performed according to the classical Gran (1952) titration in an automated titration system (Metler Toledo model T50) in filtered water samples. The accuracy of this method was better than $\pm$ 5 µmol kg^{-1} (inferred from certified reference material – CRM; A. G. Dickson from Scripps Institution of Oceanography). Chl a was extracted from the filters with 90% acetone and quantified by spectrophotometry according to Strickland and Parsons (1972). For δ^{13}C–DIC measurement, water was sampled and transferred directly to 150 mL serum vials, which were poisoned by adding 0.2 mL of a $HgCl_2$ saturated solution, and then sealed. In the laboratory, δ^{13}C–DIC was determined following the protocol by Bouillon et al. (2007). A headspace of approximately 40 mL was created with Helium, and 0.2 mL of ultrapure concentrated H_3PO_4 was introduced to convert all inorganic carbon to CO_2. The samples were shaken and kept in the dark at controlled temperature of 25 °C for 12 h. The δ^{13}C of CO_2 in the headspace was determined by injecting 0.5-1 mL of headspace gas in an isotopic ratio mass spectrometer (IRMS) equipped with a manual gas injection port. δ^{13}C–DIC was calibrated using laboratory standards, which were prepared by adding 45 mg of Na_2CO_3 in a sealed vial flushed with helium and dissolved with 3 mL of 85% H_3PO_4, as described in Deirmendjian and Abril (2018). This standard was calibrated against a certified standard (NBS 19, −1.96‰) using a dual–inlet IRMS. The isotopic value of the Na_2CO_3 standard was −4.5 $\pm$ 0.2‰. The obtained δ^{13}C values were corrected for the partitioning of CO_2 between the gaseous (headspace) and water phases in each sample using the algorithm of Miyajima et al. (1995). Repeatability of the analysis was ~0.1‰. The δ^{13}C–DIC concentrations are reported in ‰ relative to the standard Vienna Pee Dee Belemnite (V–PDB) scale.

2.5. Calculations

2.5.1. Carbonate system

DIC was calculated from pCO_2, TA, temperature, and salinity using the CO2calc 1.2.9 program (Robbins et al., 2010). We used the dissociation constants for carbonic acid proposed by Mehrbach et al. (1973) refitted by Dickson and Millero (1987), the borate acidity constant from Lee et al. (2010), the dissociation constant for the HSO_4^- ions from Dickson (1990) and the CO_2 solubility coefficient of Weiss (1974). The estimated uncertainty was better than $\pm$ 6 µmol kg^{-1} for DIC (Orr et al., 2018).

2.5.2. Excess DIC (E–DIC) and apparent utilization of oxygen (AOU)

The excess of DIC (E-DIC, µmol kg^{-1}) was calculated according to Abril et al. (2003):

$$E\text{-}DIC = DIC_{sample} - DIC_{equilibrium} \tag{1}$$

where DIC_{sample} represents the measured concentration of DIC (µmol kg^{-1}) and $DIC_{equilibrium}$ is the theoretical DIC at atmospheric equilibrium (µmol kg^{-1}). $DIC_{equilibrium}$ was calculated from the observed TA and the measured atmospheric pCO_2 during the cruises.

The apparent oxygen utilization (AOU, µmol kg^{-1}) was calculated as proposed by Benson and Krause (1984):

$$AOU = DO_{equilibrium} - DO_{sample} \tag{2}$$

where DO_{sample} is the measured DO, and $DO_{equilibrium}$ is the DO saturation.

2.5.3. Diffusive air–water CO_2 fluxes

Diffusive fluxes of CO_2 at the air-water interface were calculated according to the following equation:

$$FCO_2 = k_{CO2,T} \cdot k_0 \cdot \Delta pCO_2 \tag{3}$$

where FCO_2 is the diffusive flux of CO_2, $k_{CO2,T}$ is the gas transfer velocity of CO_2 at a given temperature (T), k_0 is the solubility coefficient of CO_2 calculated from in situ temperature and salinity (Weiss, 1974), and the ΔpCO_2 is the difference between the measured water pCO_2 and the measured atmospheric pCO_2. The atmospheric pCO_2 was measured every sampling day at morning, noon and afternoon. The gas transfer velocity of CO_2 $k_{CO2,T}$ was computed as follows (Jähne et al., 1987):

$$k_{CO2,T} = k_{600} \cdot (600/Sc_{CO2,T})^n \tag{4}$$

where k_{600} is the gas transfer velocity normalized to a Schmidt number of 600 (Sc = 600 for CO_2 at 20 °C), $Sc_{CO2,T}$ is the Schmidt number of CO_2 at a given temperature (Wanninkhof, 1992), and n being equal to 2/3 for wind speed < 3.7 m s^{-1} and equal to 0.5 for higher wind speed (Jähne et al., 1987; Guérin et al., 2007).

To compute the k_{600} values, we used three different parameterizations proposed by Wanninkhof (1992), Raymond and Cole (2001) and Abril et al. (2009), according to respectively:

$$k_{600}(W92) = 0.31(U10^2) \tag{5}$$

$$k_{600}(RC01) = 1.91exp^{0.35U10} \tag{6}$$

$$k_{600}(A09) = 1.80exp^{0.0165v} + [1.23 + 1.00LOG(S)]U10 \tag{7}$$

where k_{600} is the gas transfer velocity normalized to a Schmidt number of 600 expressed in cm h^{-1}, v is the water current velocity in m s^{-1}, S is the surface area of the specific estuarine section considered in km^2, and U10 is the wind speed at 10 m height in m s^{-1}. Water-to-air CO_2 fluxes were calculated using the daily–average pCO_2 for each estuarine domain: low salinity domain (salinities 0-5), mixing domain (salinities 5-25), marine domain (salinities > 25), and mangrove domain. We also differentiated the gas transfer velocities at different moments (morning, afternoon and nighttime). We divided the gas transfer velocities for these periods because the region is strongly impacted by marine breezes, wind speed being stronger during midday/afternoon than

during the night/early morning (Amarante et al., 2002; Cotovicz Jr. et al., 2015). Wind speed wind velocity (U10), accumulated precipitation and atmospheric temperature were recorded in the meteorological station of Campos dos Goytacazes City and were provided by the National Institute for Space Research (INPE). The water current velocities were taken from Ovalle et al. (2013).

Rudorff et al. (2011) calculated the spatial coverage of the Paraiba do Sul River plume applying a spectral linear mixture analysis. The authors proposed a linear regression to estimate the surface area of the estuarine plume in the coast as a function of the historical river discharge. We applied this general linear regression to estimate the river plume spatial coverage for our sampling period of maximal river discharge (Mar–18), when the river discharge averaged 1240 m^3 s^{-1}, and the extension of river plume was calculated at about 90.75 km^2. Accounting for the salinity values along the boat's trajectories, we constructed maps of surface salinity applying the data–interpolating variational analysis (DIVA gridding) using the Ocean Data View Software. The spatial coverages of the salinity zones for each sampling campaign were used to calculate the area–averaged CO$_2$ flux (Fig. S1, Supplementary file).

2.5.4. Mixing models

Two types of mixing models were applied, one for TA, DIC and δ^{13}C-DIC in the discrete samples, and one for temperature, salinity and pCO$_2$, which were recorded continuously.

For DIC and TA, the model assumes conservative mixing according to.

$$C_{mix} = C_{freshwater} C_{freshwater} + C_{marine}(1 - C_{freshwater}) \qquad (8)$$

where C$_{mix}$ is the concentration of a given solute during conservative mixing (in our case TA and DIC), and the subscripts freshwater and marine indicate the endmember concentrations in the river and the ocean, respectively. The freshwater fraction (F$_{freshwater}$) is calculated as:

$$F_{freshwater} = 1 - sal_{sample}/sal_{marine} \qquad (9)$$

where sal refer to the salinity, and the subscript sample refers to the in situ values for each station.

Concerning stable isotope ratios, we calculated the conservative mixing of δ^{13}C-DIC(δ^{13}C-DIC$_{mix}$) according to Mook and Tan (1991), as follows:

$$\delta^{13}C = ===DIC_{mix}$$
$$= sal_{sample}(DIC_{freshwater} \quad \delta^{13}C_{freshwater} - DIC_{marine}\delta^{13}C_{marine}) + sal_{freshwater}$$
$$DIC_{marine}\delta^{13}C_{marine} - sal_{DIC} \qquad \delta^{13}C_{freshwater}$$
$$/sal_{sample}(DIC_{freshwater} - DIC_{marine}) - sal_{DIC} = marine$$
$$- sal_{DIC} = freshwater \qquad (10)$$

where δ^{13}C is the isotopic signature of DIC, the subscripts freshwater and marine indicate the endmember concentrations in the river and the ocean, respectively, and the subscript sample indicate the in situ values at each station.

The TA and DIC concentrations measured in the discrete samples (see result section) were close to the conservative mixing line. Thus we could compute these two parameters for each salinity obtained with the continuous measurements. The theoretical pCO$_2$ conservative mixing curve (pCO$_{2mixing}$) was obtained by solving the carbonate system using the in situ temperature and salinity, and the computed conservative TA and DIC for each salinity value obtained with the continuous measurements from the estuary (Jiang et al., 2008; Joesoef et al., 2015). Because the pCO$_2$ was variable in the freshwater endmember, we calculate the average and standard deviations for each sampling campaign.

In order to allow a full comparison with the observed pCO$_2$ distribution, two corrections of the conservative mixing pCO$_2$ model are necessary: a correction for gas exchange (refer as pCO$_{2gas\ exchange}$) and another for the effect of heating or cooling (refer as pCO$_{2cooling/heating}$) in the estuary. In order to correct the mixing pCO$_2$ curve for gas exchange, an iterative calculation was applied for each salinity increment. The loss or gain of DIC as CO$_2$ evasion or invasion between each salinity increment "sal" was calculated as:

Table 1

Mean (± standard deviation), minimum and maximum values of the principal physicochemical properties on the waters of the PSRE, separated by sampling campaigns and estuarine zones.

Salinity interval / estuarine region	Sal.	Temp. (°C)	pCO$_2$ (ppmv)	DIC (µmol kg-1)	pH (NBS)	TA (µmol kg-1)	δ^{13}C–DIC(‰)	Chl a (µg L-1)	DO (%sat)
Feb. – 17									
0–5	0.8 ± 1.0	30.8 ± 0.4	157 ± 47	428 ± 72	8.40 ± 0.36	441 ± 91	−3.64 ± 0.56	15.3 ± 4.7	110 ± 6
	(0.0 / 4.9)	(28.1 / 31.8)	(41 / 321)	(357 / 655)	(7.29 / 9.36)	(347 / 670)	(−4.81 / −2.30)	(8.0 / 21.3)	(91 / 122)
5–30	19.0 ± 6.9	29.1 ± 0.5	306 ± 83	1982 ± 79	8.12 0.08	1234 ± 362	0.27 ± 1.07	7.0 ± 1.4	92 ± 4
	(5.3 / 29.8)	(27.3 / 30.7)	(121 / 446)	(1902 / 2061)	(7.61 / 8.61)	(747 / 1882)	(−2.12 / 1.93)	(4.3 / 9.2)	(86 / 102)
> 30	31.8 ± 1.6	27.9 ± 1.0	459 ± 8	1884 ± 130	8.04 ± 0.01	2239 ± 96	2.46 ± 0.11	1.14 ± 0.88	88.4 ± 0.9
	(30.3 / 33.5)	(26.2 / 28.2)	(402 / 472)	(1689 / 2061)	(8.00 / 8.06)	(2143 / 2336)	(2.34 ± 2.57)	(0.26 /2.02)	(84.1 / 89.5)
Mangrove creek	1.2 ± 0.3	30.7 ± 0.2	1479 ± 606	784 ± 137	7.49 ± 0.11	719 ± 120	−7.47 ± 0.64	12.8 ± 1.1	99.1 ± 0.7
	(0.5 / 1.7)	(30.3 / 31.3)	(456 / 2840)	(647 / 922)	(7.29 / 7.88)	(599 / 839)	(−8.11 / −6.82)	(10.5 / 14.6)	(98.4 / 100.1)
Oct. – 17									
0–5	1.1 ± 1.2	25.4 ± 0.3	192 ± 52	440 ± 81	8.40 ± 0.15	458 ± 86	−3.47 ± 0.36	6.04 ± 1.38	107 ± 9
	(0.0 / 4.9)	(24.6 / 26.2)	(91 / 300)	(347 / 558)	(8.06 / 8.77)	(352 / 573)	(−4.23 / −2.89)	(3.86 / 11.86)	(82 / 119)
5–30	19.4 ± 6.0	25.6 ± 0.3	275 ± 62	1158 ± 228	8.47 ± 0.05	1306 ± 266	0.46 ± 0.80	2.49 ± 0.31	89 ± 7
	(5.1 / 29.9)	(24.4 / 26.2)	(102 / 414)	(713 / 1629)	(8.05 / 8.66)	(777 / 1874)	(−1.51 / 1.71)	(1.54 / 3.14)	(79 / 116)
> 30	32.0 ± 0.9	24.0 ± 0.5	390 ± 14	1895 ± 38	8.40 ± 0.01	2211 ± 47	2.19 ± 0.23	1.64 ± 1.30	92 ± 5
	(30.1 / 33.0)	(23.4 / 25.0)	(356 / 429)	(1818 / 1941)	(8.37 / 8.44)	(2120 / 2274)	(1.91 / 2.50)	(0.31 / 4.24)	(86 / 111)
Mangrove creek	5.1 ± 1.1	24.5 ± 0.1	4016 ± 2643	1755 ± 1172	7.44 ± 0.15	1019 ± 211	−8.96 ± 1.53	6.05 ± 1.63	80 ± 14
	(0.1 / 7.2)	(24.0 / 25.2)	(525 / 11,514)	(753 / 4687)	(7.13 7.98)	(700 / 1467)	(−11.82−7.00)	(3.83 / 9.65)	(48 / 112)
Mar. – 18									
0–5	0.1 ± 0.13	29.0 ± 0.4	1946 ± 252	469 ± 86	7.10 ± 0.13	428 ± 101	−7.38 ± 1.49	1.81 ± 0.37	58 ± 3
	(0.0 / 4.4)	(28.1 / 31.1)	(1187 / 2411)	(381 / 667)	(6.43 / 8.20)	(337 / 663)	(−9.07 / −4.64)	(0.85 / 2.72)	(58 / 80)
5–30	17.4 ± 6.6	29.5 ± 0.8	380 ± 96	1198 215	8.21 ± 0.14	1322 ± 266	0.22 ± 0.86	4.03 ± 1.60	87 ± 6
	(5.1 / 30)	(27.3 / 31.8)	(309 / 668)	(747 / 1628)	(7.79 / 8.42)	(766 / 1846)	(−2.87 / 1.56)	(0.53 / 7.57)	(73 / 107)
> 30	33.7 ± 2.2	28.4 ± 0.5	439 ± 17	1895 ± 129	8.27 ± 0.01	2170 ± 160	2.08 ± 0.25	1.74 ± 1.09	88 ± 3
	(30.1 / 36.2)	(27.5 / 29.3)	(384 / 469)	(1765 / 2024)	(8.24 / 8.32)	(2010 / 2331)	(1.83 / 2.34)	(0.65 / 2.83)	(84 / 94)
Mangrove creek	0.6 ± 0.3	28.7 ± 0.2	8988 ± 2325	1555 ± 195	6.92 ± 0.09	1177 ± 356	−6.43 ± 1.79	22.70 ± 2.51	29 ± 16
	(0.1 / 2.1)	(28.3 / 30.1)	(3931 / 13,344)	(1071 / 2407)	(6.75 / 7.78)	(822 / 2055)	(−9.04 / −3.27)	(19.31 / 26.55)	(3 / 70)

158

$$\text{DICgain(sal)} = -FCO_2(sal). RT. H^{-1} \qquad (11)$$

where $FCO_2(sal)$ is the flux (mol m^{-2} h^{-1}) for every salinity unit, RT is the residence time (h) during mixing between salinity (sal) and (sal+1) and H is the water depth (m). $FCO_2(sal)$ is calculated with Eq.3, and the conservative mixing $pCO_2(sal)$. The new corrected DIC concentration at sal+1 is obtained by adding the DICgain(sal+1) to the DIC(sal+1) previously deduced from the conservative mixing of DIC(sal) with DIC_{marine}:

$$\text{Corrected DIC(sal+1)} = DIC(sal+1) + DICgain(sal) \qquad (12)$$

Then we recalculate the corrected $pCO_2(sal+1)$ from a new mixing lines between corrected DIC(sal+1) and DIC_{marine}, and TA(sal+1) and TA_{marine}. The next iteration consisted in calculating the $FCO_2(sal+1)$ from the corrected $pCO_2(n+1)$ and the DICgain(sal+2) using Eq.3. This model of incrementation allowed the building pCO_2 mixing curves corrected from gas exchange ($pCO_{2gas\ exchange}$). The difference between $pCO_{2gas\ exchange}$ and $pCO_{2mixing}$ ($\Delta pCO_{2gas\ exchange}$) is attributed to gas exchange.

The thermal influence on the pCO_2 (cooling or heating), was calculated from the TA and DIC conservative mixing, and this time by considering not the in situ measured temperature, but the temperature calculated as linearly conservative between the two endmembers. The difference between $pCO_{2mixing}$ (calculated with in situ temperature) and the pCO_2 calculated with the endmembers interpolation is attributed to the thermal pCO_2 along the mixing zone ($\Delta pCO_{2cooling/heating}$).
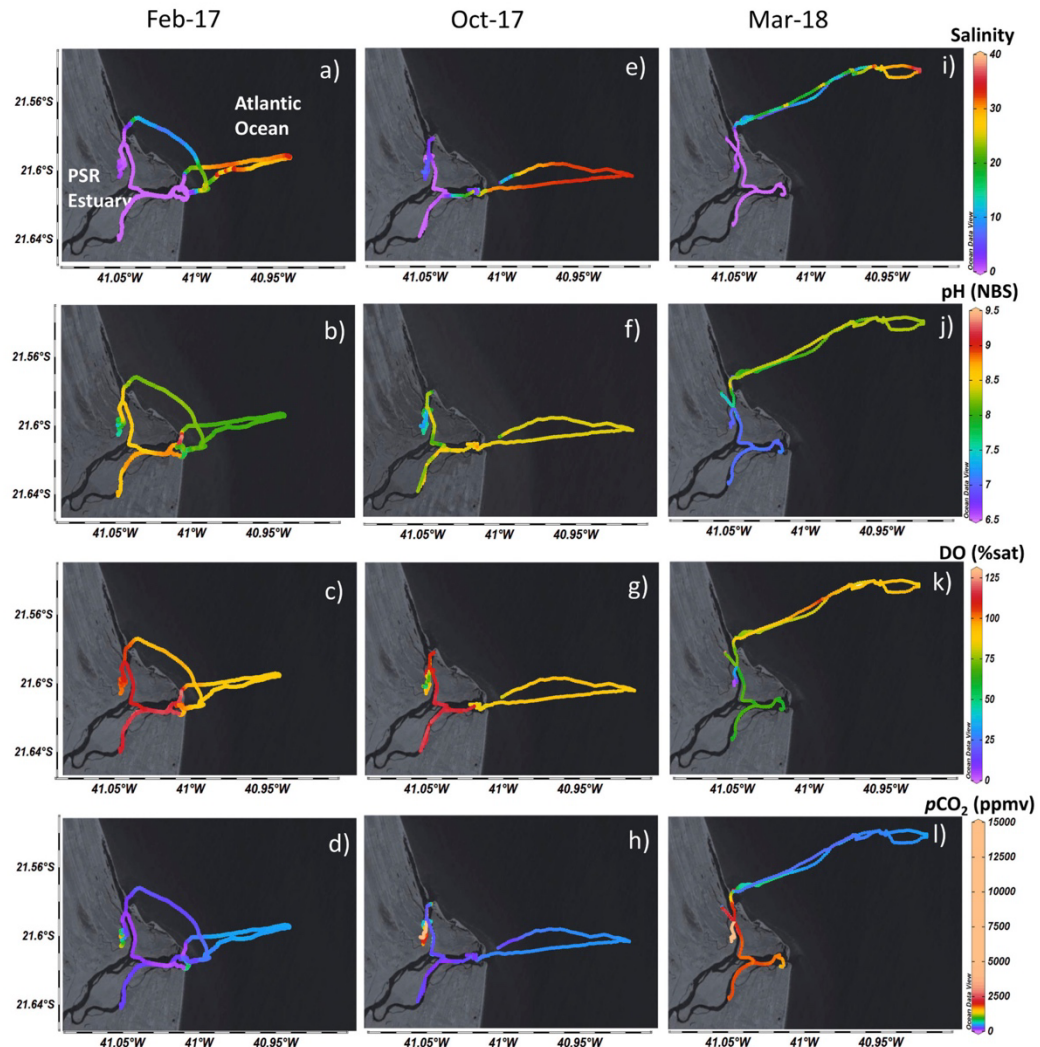
Fig. 2. Maps of continuous measurements of a) salinity, b) pH, c) DO, and d) pCO_2 in surface waters of the PSRE for all sampling campaigns.
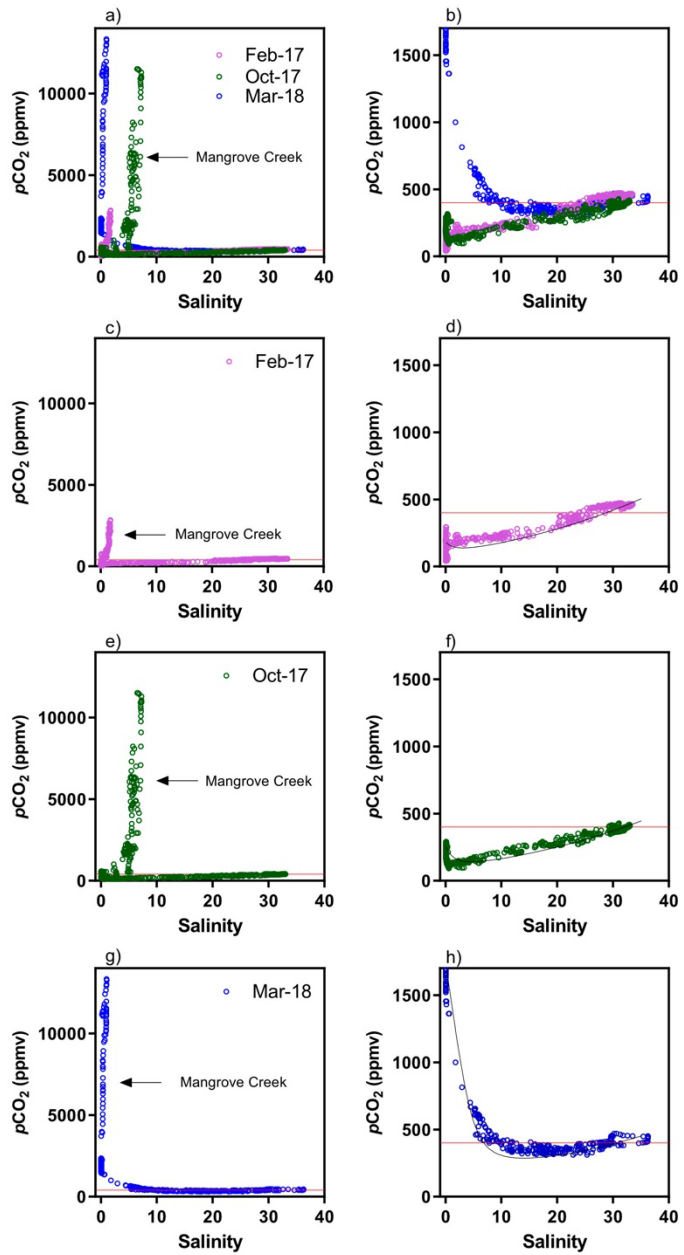
Fig. 3. Distribution of pCO$_2$ along the salinity gradient in the PSRE separated by sampling campaigns. Graphs a), c), e) and g) include all the data, with the main estuarine channel and the mangrove creek. Graphs b), d), f) and h) include only the data in the main estuarine channel.
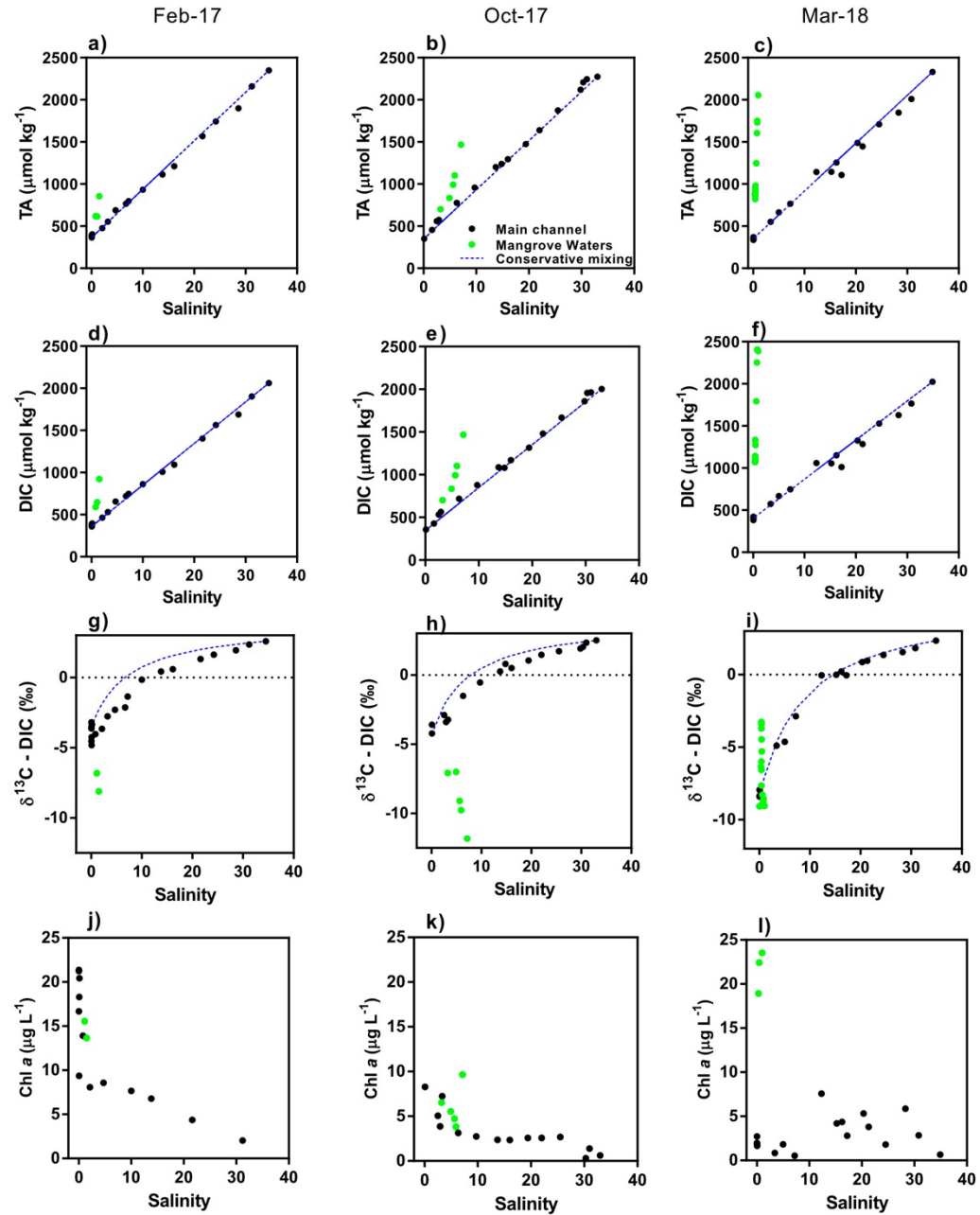
Fig. 4. Distributions of TA, DIC, δ^{13}C–DIC, and Chl a in discrete samples along the salinity gradient. The black dots are the main estuarine channel and the green dots are the mangrove creek. The dashed blue lines represent the theoretical models of conservative mixing endmembers. (For interpretation of the references to colour in this figure legend, the reader is referred to the web version of this article.)

9

2.6. Statistical analysis

We applied the Shapiro–Wilk test to investigate the normality of the data set. As the data did not follow normal distributions, we applied non–parametric statistics. To compare the differences between averages for the concentrations of biogeochemical parameters in water, we applied the Mann–Whitney test, which compares the distributions of un-matched groups. Linear and non–linear regressions were calculated to analyze the correlations between variables, providing the best–fit slope, the intercept and the goodness of fit (R^2). All statistical analyses were based on α = 0.05. The statistical tests and calculations were per-formed with the Graph Pad Prism 6 program.

3. Results

3.1. Spatial and temporal variations of carbonate chemistry and ancillary parameters

Spatial and temporal variations of pCO_2 and the main parameters analyzed in this study are presented in Table 1 for the four domains. Surface water temperature showed a marked seasonal trend between 26.2 and 31.8 °C in summer (Feb 17 and Mar 18 samplings) and be-tween 23.4 and 26.2 °C in winter (Oct 2017 sampling). The highest temperatures were found in freshwaters, with a cooling trend seaward. This decrease in water temperature was slight, with less than 2 °C dif-ference, on average, between the river and marine zones. However, this seaward temperature decrease trend was not linear during estuarine mixing. Intermediate salinities (values from 20 to 30) were generally sampled close to midday, when the solar irradiance is maximum. These intermediate salinities exhibited temperatures higher than that ex-pected for the conservative mixing because of the heating effect (> 0.8 °C, on average), reaching 2.2 °C during sampling on Mar 18. In contrast, waters with temperatures lower than that expected for the conservative mixing (cooling effect) were verified only on the Feb 17 sampling in low salinities.

The spatiotemporal salinity distribution in surface waters was gov-erned by the river water discharge (Fig. 2; Fig. S1 Supplementary in-formation). This figure shows the boat track for the three sampling campaigns. Note that the boat tracking was not the same for the sam-pling campaigns. The principal reason for these differences is that the main estuarine channel navigated in the first two trips (Feb 17 and Oct 17) became very shallow and dangerous for navigation. For safety reasons, we decided to navigate along the secondary channel during the trip of Ma 18. During the period of lowest freshwater discharge (178 m^3 s^{-1}), the mixing zone was located close to the river mouth, with an intrusion of brackish water (salinity ≤20) until approximately 4 km inside the internal estuary at high tide. Consequently, at low river discharge, the river plume covered a small area (~30 km^2) in the ad-jacent shelf waters, with the marine zone (salinity > 30) located closest to the river mouth (between 3 and 6 km from the river mouth) (Fig. S1). Contrastingly, during the Mar 18 sampling at high river flow (1240 m^3 s^{-1}), the mixing zone was located outside the limit of the coast, and no salinity intrusion occurred in the internal estuary (Fig. 2c). During this high flow period, the mixing zone covered the highest surface area (~63 km^2) in the adjacent shelf (extending to approximately 12 km from the river mouth), with the marine zone lo-cated far from the internal estuary (> 10 km) (Fig. S1).

Surface water pCO_2 in the estuary was strongly related to the sali-nity and followed a distribution close to that predicted for the mixing curve between the river and marine endmembers, with marked differ-ences between the dry and rainy seasons in the low salinity region (Figs. 2 and 3). During low river flow, the low salinity regions (0–5) presented undersaturated pCO_2 conditions compared with the equili-brium with atmosphere in all sampling campaigns, with mean values of 157 ± 47 ppmv and 192 ± 52 ppmv for the Feb 17 and Oct 17 samplings, respectively (Fig. 2a,b). In the seaward direction, pCO_2

increased with salinity, following a general trend close to the thermo-dynamic mixing curve (Figs. 2a,b and 3a,b). During the rainy period, the river zone presented high pCO_2 values with permanent over-saturation (mean of 1946 ± 252 ppmv). However, pCO_2 showed a sharp decline between salinities 0 and 5, and quickly reached under-saturated conditions at salinity higher than ~10, with a mean value of 380 ± 116 ppmv in the mixing zone (Figs. 2l and 3h). The marine zone (salinity > 30), during the rainy period, showed pCO_2 values close to those found during the dry period, 439 ± 17 ppmv, on average. Mangrove–dominated waters (mangrove creek) presented pCO_2 values much higher (up to 11,514 ppmv) than that found in the waters of the main estuarine channel in all sampling campaigns.

Strong relationships with salinity were also verified for carbonate chemistry parameters, including TA, DIC, and δ^{13}C–DIC (Fig. 4). The TA and DIC concentrations for the freshwater endmember presented small but statistically significant seasonal variation depending on the in-tensity of river flow (Mann–Whitney test, p < 0.0001). The TA and DIC concentrations in the freshwater endmember were 446 ± 89 (n = 4) and 435 ± 77 µmol kg^{-1} (n = 3) during the dry season and 428 ± 101 and 469 ± 86 µmol kg^{-1} during the wet season (n = 4), respectively. In the mangrove waters, the TA and DIC concentrations were much higher than those in the conservative mixing, and did not follow the linear pattern found in the main channel (Fig. 4a,b,c,d,e,f). Concerning the δ^{13}C–DIC signatures, the freshwater endmember showed important seasonal variation according to river discharge (Fig. 4). During low river flow (Feb 17 and Oct 17 samplings), fresh-water δ^{13}C–DIC values showed a mean of −3.55 ± 0.43‰, and the distributions along the salinity gradient showed slight ^{13}C depletion compared with the conservative mixing curve (Fig. 4). During high river flow, the stable isotope signature mean was −7.38 ± 1.49‰, and the δ^{13}C–DIC distributions along the salinity gradient showed only a minor deviation from the conservative mixing curve. δ^{13}C–DIC values in the mangrove creek were more negative than in the main channel during the two dry periods assessed, with mean and minimum values of −10.96 ± 1.23‰ and − 11.82‰, respectively (Fig. 4g,h). During the rainy period, the δ^{13}C–DIC values in the mangrove creek presented a mean of −6.43 ± 1.79‰, with enrichment in ^{13}C compared with that of the waters of the main channel, and above the conservative mixing curve (Fig. 4i).

During the dry period, Chl a concentrations were higher in fresh-waters (between 3.86 and 21.30 µg L^{-1}) and showed a marked decrease in the seaward direction (Fig. 4j,k). This decrease in Chl a concentra-tions with increasing salinity is coincident with an increase in pCO_2. Chl a and pCO_2 were negatively correlated in the main channel (R^2 = 0.59 on Feb 17; R^2 = 0.60 on Oct 17; p < 0.001) (Fig. 5). On the other hand, for the rainy period, the freshwaters presented the lowest Chl a concentrations, and the distributions did not follow a clear pattern along the salinity gradient, not presenting significant correlations with pCO_2 (Figs. 4 and 5). The Chl a concentrations in the mangrove tidal creek were high for all the sampling campaigns, reaching a maximum value of 26 µg L^{-1} on Feb 17.

3.2. Tidal and diurnal variations of carbonate chemistry in the mangrove creek

Results of diurnal variations of the carbonate chemistry parameters in the tidal creek are presented in Table 2 and Figs. 6 and 7. We sam-pled one ebb tide at daytime followed by one flood tide at nighttime and one ebb tide at nighttime. Tidal amplitude was 0.42 m for the first ebb phase (from ~12:00 pm to 06:30 pm) and 0.64 m for the second ebb phase (from ~00:30 am to 07:30 am). For the first tidal cycle, no statistically significant difference was observed between the ebb and flood tides (Mann Whitney Test; p > 0.05); however, the second ebb tide (nighttime) presented higher salinity values than those found in the other sampled periods (Mann Whitney Test; p < 0.01), following an atypical pattern. Daytime sampling presented higher average
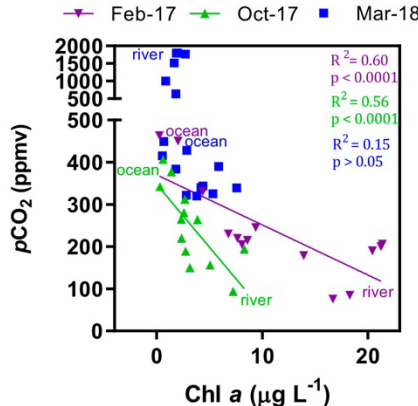
Fig. 5. Relationship between the concentrations of Chl a vs. pCO_2 along the main channel of the PSRE. The different symbols in the figure represent the sampling campaigns, as indicated in the caption. The terms "river" and "ocean" represent the values found in the river and ocean endmembers, respectively, for the different sampling campaigns.

Table 2

Results of the anchored station at the mangrove creek showing the diurnal variability (mean, standard deviation, minimum and maximum) for the principal physicochemical properties k, separated by time of sampling (ebb tide daytime, flood tide nighttime, ebb tide nighttime).

	Ebb tide	Flood tide	Ebb tide
	Daytime	Night time	Night time
Temperature (°C)	30.3 ± 0.3	29.0 ± 0.7	27.6 ± 0.03
	28.8-31.0	28.1-30.0	27.6-27.7
Salinity	0.38 ± 0.00	0.41 ± 0.02	0.72 ± 0.07
	0.38-0.42	0.39-0.44	0.58-0.80
pCO_2 (ppmv)	7439 ± 1390	$11{,}191 \pm 2264$	$18{,}276 \pm 3408$
	5318-11,600	7366 -13,919	6358-21,720
DIC (µmol kg-1)	1105 ± 32	1259 ± 77	2213 ± 210
	1071-1143	1103 -1335	1791-2407
TA (µmol kg-1)	860 ± 36	931 ± 34	1582 ± 169
	805-912	885-981	1246-1749
pH (NBS)	7.06 ± 0.06	6.92 ± 0.10	6.89 ± 0.03
	6.84-7.61	6.81-7.07	6.80-6.93
$\delta^{13}C$-DIC(‰)	-4.10 ± 0.95	-5.99 ± 1.12	-8.57 ± 0.15
	−6.00 to −3.27	−7.65 to −4.45	−8.79 to −8.28
Chl a (µmol kg-1)	66.7 ± 4.0	19.0 ± 3.4	-
	61.3-72.1	15.5-22.4	
DO (%sat)	59.8 ± 10.8	39.2 ± 14.2	4.9 ± 4.3
	5.2-80.3	23.9-62.0	0.2-13.1

temperature (30.0 $\pm$ 0.3 °C) than nighttime sampling (28.3 $\pm$ 0.3 °C).

In the mangrove creek, pCO_2 values varied drastically along the diurnal time scale, with means of 7439 $\pm$ 1390 ppmv during daytime ebb tide, 11,191 $\pm$ 2264 ppmv during nighttime flood tide, and 18,276 $\pm$ 3408 ppmv during nighttime ebb tide (Table 2). The maximum pCO_2 value (21,720 ppmv) occurred during nighttime ebb tide, whereas the minimum pCO_2 value (5318 ppmv) occurred during daytime ebb tide. The highest pCO_2 values during nighttime ebb tide were coincident with the highest TA, DIC and salinity concentrations and the lowest pH and $\delta^{13}C$-DIC values (Figs. 6 and 7). In this way, pCO_2 showed strong negative correlations with DO ($R^2 = 0.99$; p < 0.0001) and $\delta^{13}C$-DIC($R^2 = 0.97$; p < 0.0001) (Fig. 7d). Hypoxic and anoxic conditions occurred from the end of the nighttime period until sunrise (between approximately 00:30 am and 07:30 am) (Fig. 6c). DO concentrations were also strongly positively correlated with $\delta^{13}C$-DIC

values ($R^2 = 0.96$; p < 0.0001) (Fig. 7c). During the diurnal cycle in the mangrove creek, $\delta^{13}C$-DIC values varied between −8.79‰ (nighttime ebb tide) and − 3.27‰ (daytime flood tide). The TA and DIC distributions followed a nearly linear relationship with salinity (Fig. 7a). Increased TA concentrations followed decreased DO concentrations linearly, but only under hypoxic/anoxic conditions (Fig. 7b). As expected, E-DIC and AOU were well correlated in the mangrove creek, presenting positive concentrations and a high deviation above the line 1:1 in all sampling campaigns, which were different from the main channel pattern (Fig. 8a). The TA and DIC concentrations also showed strong deviation from the conservative mixing (ΔTA and ΔDIC), and different from the pattern observed in the main channel (Fig. 8b).

3.3. Gas transfer velocities and CO_2 exchanges at the air–water interface

The k–wind speed parameterization is one of the most critical parameters to compute the air-sea CO_2 fluxes between the pCO_2 gradients in the surface ocean and lower atmosphere (Borges and Abril, 2011; Wanninkhof, 2014; Call et al., 2015). Diverse formulations of k–wind parameterizations are available to estimate the main driving forces of turbulence at the air–sea interface, based on theoretical results from several studies that showed that their performance is more appropriate under certain conditions and environments (Wanninkhof, 2014). Thus, we computed the air–sea CO_2 fluxes using three different k–wind parameterizations: two appropriate for estuarine environments (Raymond and Cole, 2001; Abril et al., 2009) and one appropriate for open ocean waters (Wanninkhof, 1992), providing ranges of estimates (Table 3).

The calculated gas transfer velocities varied between 0.44 and 21.26 cm h^{-1} over the morning, afternoon and night periods (Table 3). The k_{600} values calculated from the equation of Abril et al. (2009) for estuarine waters, which account for wind velocity, estuarine size and current velocity, were higher than those calculated using the parameterizations proposed by Raymond and Cole (2001) and Wanninkhof (1992), except for wind speeds> 6 m s^{-1}, when the equation of Abril et al. (2009) provided lower gas transfer values. The inner estuary current velocities estimated for each estuarine region, considering the water discharge and the cross-sectional area, ranged from 0.1 m s^{-1}, during low river flow, to 1.2 m s^{-1}, during high river flow. For the outer estuary (river plume), the current velocities were measured according to Knoppers et al. (1999). The Oct 17 sampling presented higher gas transfer velocity values compared with those measured on February 17 and March 18 (p < 0.0001; t–test) as a result of the higher wind speed averages. Higher computed gas transfer velocities occurred during the afternoon, followed by night and morning (Table 3).

Calculated CO_2 fluxes showed high spatiotemporal variability (Table 3) related to salinity and distance from the mangrove forest. The freshwater endmember was a CO_2 sink during low discharge and a CO_2 source during high discharge. The highest values of air–water CO_2 uptake in the estuarine zone (between −26.23 and − 37.80 mmol C m^2 d^{-1}) were found during the afternoon, when wind speed was strongest. The mixing zone was also a CO_2 sink, but with smaller intensity compared with fresh and low–salinity waters. The air–water CO_2 fluxes in the mixing zone varied between −0.34 and − 18.41 mmol C m^2 d^{-1}. The marine zone acted as a slight CO_2 source, with emissions ranging from 0.12 to 5.78 mmol C m^2 d^{-1}. The mangrove creek waters were a strong CO_2 source, with values ranging from 1.97 to 216.14 mmol C m^2 d^{-1}.

Considering all the estuarine areas and time of sampling (morning, afternoon and night), the estuary was a slight CO_2 sink under dry conditions, with weighted surface fluxes ranging from −1.34 to −5.26 mmol C m^2 d^{-1} (Table 3), representing an uptake between 1.45 and 5.72 t C d^{-1}. During high river discharge (Mar 18), the low salinity region was a strong CO_2 source, with emissions ranging from 6.36 to 117.77 mmol C m^2 d^{-1}, but the mixing zone remained a slight CO_2
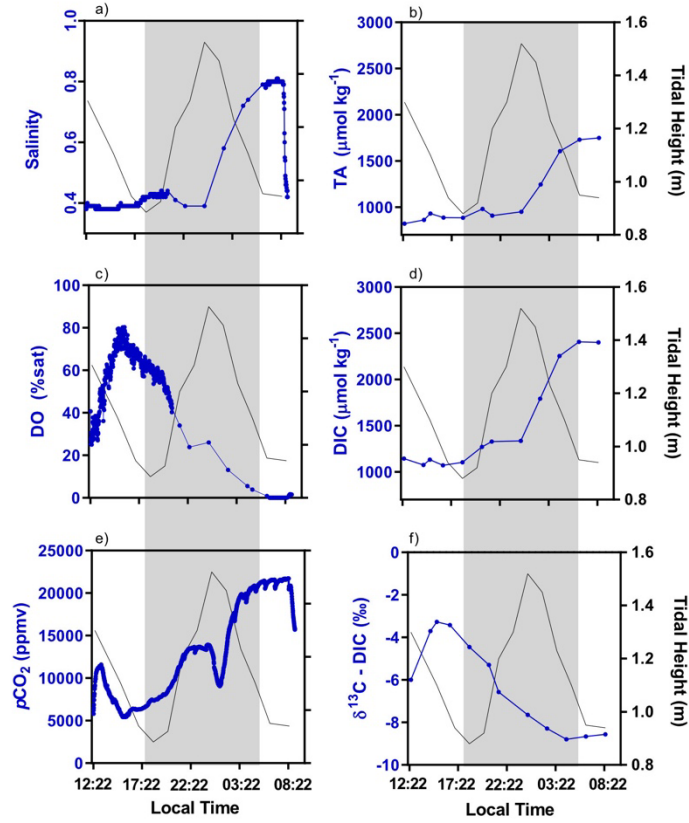
Fig. 6. Eulerian time-series data of the mangrove creek. The shaded area symbolizes the nighttime sampling.

sink, with fluxes varying between −0.12 and − 2.93 mmol m^2 d^{-1}. The marine zone was a CO_2 source, but with pCO_2 values very close to the equilibrium with the atmosphere and emissions ranging from 0.05 to 1.27 mmol m^2 d^{-1}. The mangrove tidal creek was a strong source of atmospheric CO_2, with degassing ranging from 9.34 to 358.39 mmol m^2 d^{-1}. Considering the estuary as a whole, the weighted CO_2 surface emissions during high river discharge ranged from 5.71 to 19.37 mmol C m^2 d^{-1}, representing an efflux between 6.21 and 21.09 t C d^{-1}.

The riverine inputs of DIC to the estuary calculated by multiplying the DIC concentrations at the river endmember by the river flow were 106 tC d^{-1}, 64 tC d^{-1} and 488 tC d^{-1} for the samplings conducted on February 17, October 17 and March 18, respectively. Considering the estuary as a whole, the mean net estuarine fluxes at the air–sea interface were − 3.32 tC d^{-1}, −5.72 tC d^{-1} and 15.88 tC d^{-1} for the Feb 17, Oct 17 and Mar 18 samplings, respectively. Consequently, the DIC inputs from the river to the estuary were between ~11 and 32 times higher than the carbon influx or efflux at the air-water interface.

4. Discussion

4.1. Predominance of thermodynamic processes on pCO_2 distributions in the main channel and CO_2 air–water fluxes

Oversaturated pCO_2 conditions are usually observed in river-dominated estuaries as a result of the net heterotrophic metabolism sustained by inputs of organic carbon from the catchment (Frankignoulle et al., 1998; Dai et al., 2009; Cai, 2011; Borges and Abril, 2011), river input of dissolved CO_2 (Abril et al., 2000; Jiang et al., 2008; Joesoef et al., 2015; Van Dam et al., 2018a), and of tidal pumping (Maher et al., 2015; Santos et al., 2018). The overall trend of pCO_2 decreasing seaward has mostly been described in rivers with moderate to high TA concentrations (≥1000 µmol kg^{-1}) and moderate to long water residence time (Frankignoulle et al., 1998; Borges and Abril, 2011). However, in the case of many tropical river deltas, TA concentrations are generally low at the riverine endmember (Cai et al., 2008), and these estuaries have relatively short water residence time (Ludwig et al., 1998). Under such conditions, thermodynamic changes during estuarine mixing generate strong pCO_2 undersaturation in the low salinity region (Whitfield and Turner, 1986; Cai et al., 2013) that can exceed CO_2 production and consumption by biological processes. Low TA concentrations in the river endmember provide low buffering
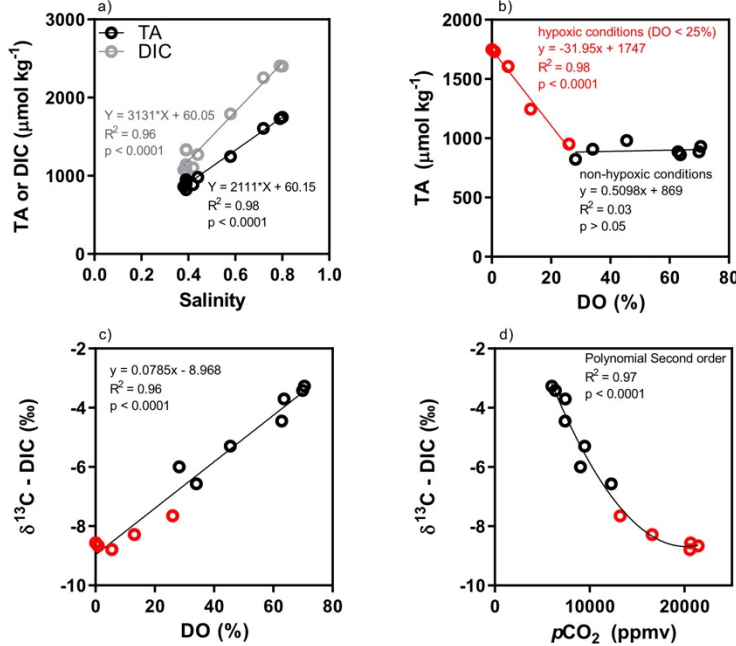
Fig. 7. Scatter plots between a) TA or DIC and salinity, b) TA and DO, c) $\delta^{13}C$–DIC and DO, d) $\delta^{13}C$–DIC and pCO_2 in the mangrove creek throughout the 20 h cycle on Mar 18. Red dots characterize hypoxic condition with $DO_{sat}\% < 25\%$ observed in early morning and low tide. (For interpretation of the references to colour in this figure legend, the reader is referred to the web version of this article.)
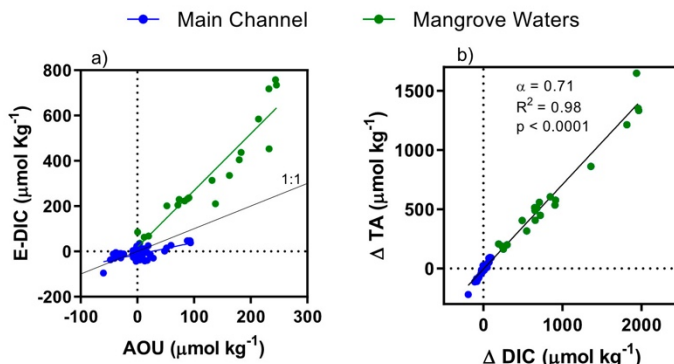
Fig. 8. Graph a shows the relationship between the excess dissolved inorganic carbon (E-DIC) and apparent oxygen utilization (AOU) in the PSRE main channel and mangrove creek for the three sampling campaigns. Green dots are the stations in the mangrove creek and blue dots are the stations in the main estuarine channel. The 1:1 line represents the quotient between CO_2 and O_2 during the processes of photosynthesis and respiration. Graph b) shows the deviations from conservative mixing lines of total alkalinity (ΔTA) as a function of dissolved inorganic carbon (ΔDIC), including the three sampling campaigns. Green dots are the stations in the mangrove creek and blue dots are the stations in the main estuarine channel. α indicates the slope of the linear regression. (For interpretation of the references to colour in this figure legend, the reader is referred to the web version of this article.)

capacity in fresh and low salinity waters (Egleston et al., 2010; Hu and Cai, 2013; Cai et al., 2013). We calculated the Revelle factor ($\gamma DIC = \partial ln(CO_2)/\partial DIC)^{-1}$ along the mixing zone of the PSRE to investigate its buffering capacity (Revelle and Suess, 1957; Egleston et al., 2010). The results corroborate this hypothesis, showing that waters with salinities < 10 presented the lowest buffering capacity in all sampling campaigns (Fig. S2; Supplementary information).

In the PSRE, pCO_2 distributions along the salinity gradient were very close to that predicted by theoretical thermodynamic changes during conservative mixing between the river and marine endmembers, including a pCO_2 minimum much lower than the atmospheric value (Fig. 3). During low river discharge (Feb–17 and Oct–17), the river endmember already presented CO_2 undersaturation with relation to the atmosphere (due to phytoplankton uptake). During high river flow, pCO_2 was high in freshwater, but showed a sharp decrease between salinities 0 and 5 and remained below the atmospheric value along the mixing zone (salinity 0–30). This marked pCO_2 decrease occurred in poorly buffered estuarine waters. The mixing of river water and seawater generates strong equilibrium displacements between species of the carbonate system and strongly alters water pCO_2 values and air-water CO_2 fluxes, creating pCO_2 undersaturation by inorganic processes (Whitfield and Turner, 1986; Cai et al., 2013). In the case of acidic freshwater with low TA and eventually high pCO_2, dissolved CO_2 is absorbed by the buffering capacity of the seawater and immediately incorporated into the HCO_3^- and CO_3^{2-} pools rather than totally emitted to the atmosphere. Because the displacement of chemical

Table 3

Calculated mean values for gas exchange coefficient (k_{600}) and CO_2 fluxes at the air–water interface in each estuarine regions of the PSRE, as well as, the spatial time–integrated fluxes for the whole system. The periods M, A, and N represents the morning, afternoon and night. W92 is the data calculated according to k600 of Wanninkhof (1992), RC01 is the data calculated according to k600 of Raymond and Cole (2001), and A09 is data calculated according to k600 of Abril et al. (2009).

	Period	FCO_2 (mmol C m^{-2} d^{-1})	FCO_2 (mmol C m^{-2} d^{-1})	FCO_2 (mmol C m^{-2} d^{-1})	K_{600} (cm h^{-1})	K_{600} (cm h^{-1})	K_{600} (cm h^{-1})
		W92	RC01	A09	W92	RC01	A09
Feb – 17							
0-5 (21.50 km^2)	M	−1.61	−7.44	−11.52	0.69	3.21	4.98
	A	−12.07	−18.46	−19.49	5.21	7.97	8.42
	N	−2.30	−8.18	−12.46	1.00	3.54	5.38
5-30 (49.00 km^2)	M	−0.34	−1.56	−2.78	0.69	3.21	5.76
	A	−2.52	−3.86	−5.11	5.21	7.97	10.56
	N	−0.48	−1.70	−3.05	1.00	3.54	6.32
> 30 (20.00 km^2)	M	0.38	1.75	3.14	0.69	3.21	5.76
	A	2.86	4.37	5.78	5.21	7.97	10.56
	N	0.55	1.94	3.46	1.00	3.54	6.32
Mangrove Creek (0.25 km^2)	M	1.97	28.56	34.92	0.17	2.47	3.02
	A	14.35	44.30	48.82	1.24	3.82	4.22
	N	2.88	30.07	41.18	0.25	2.6	3.56
All Estuary (90.75 km^2) are–averaged	M	−0.48	−2.14	−3.43			
	A	−3.55	−5.38	−5.98			
	N	−0.67	−2.35	−3.72			
		−1.34	**−3.05**	**−4.22**			
Oct – 17							
0-5 (12.90 km^2)	M	−5.64	−10.34	−12.86	3.17	5.82	7.23
	A	−26.23	−37.80	−21.55	14.75	21.26	12.12
	N	−9.26	−14.16	−14.98	5.21	7.97	8.42
5-30 (30.60 km^2)	M	−2.74	−5.04	−7.70	3.17	5.82	8.9
	A	−12.77	−18.41	−13.61	14.75	21.26	15.73
	N	−4.51	−6.91	−9.14	5.21	7.97	10.56
> 30 (47.00 km2)	M	0.12	0.22	0.34	3.17	5.82	8.9
	A	0.55	0.82	0.60	14.75	21.26	15.73
	N	0.19	0.31	0.41	5.21	7.97	10.56
Mangrove Creek (0.25 km^2)	M	23.09	107.40	131.16	0.69	3.21	3.92
	A	126.82	216.14	171.31	3.79	6.46	5.12
	N	41.50	127.80	141.19	1.24	3.82	4.22
All Estuary (90.75 km^2) area–averaged	M	−1.61	−2.76	−3.89			
	A	−7.39	−10.56	−6.86			
	N	−2.62	−3.84	−4.61			
		−3.55	**−5.26**	**−4.99**			
Mar – 18							
0-5 (21.50 km^2)	M	6.36	41.76	66.17	0.44	2.89	4.58
	A	68.06	107.35	117.77	4.71	7.43	8.15
	N	12.86	49.70	75.72	0.89	3.44	5.24
5-30 (62.00 km^2)	M	−0.12	−0.82	−1.49	0.44	2.89	5.21
	A	−1.34	−2.14	−2.93	4.71	7.43	10.19
	N	−0.26	−0.98	−1.75	0.89	3.44	6.13
> 30 (7.00 km^2)	M	0.05	0.36	0.65	0.44	2.89	5.21
	A	0.60	0.94	1.27	4.71	7.43	10.19
	N	0.12	0.43	0.77	0.89	3.44	6.13
Mangrove Creek (0.25 km^2)	M	9.34	198.72	219.84	0.11	2.34	3.38
	A	105.31	324.41	358.39	1.24	3.82	4.22
	N	26.33	228.46	289.08	0.31	2.69	3.63
All Estuary (90.75 km^2) area–averaged	M	1.46	9.91	15.50			
	A	15.55	24.94	26.98			
	N	2.95	11.76	17.64			
		5.71	**14.59**	**19.37**			

equilibriums is an almost instantaneous process, it can occur completely even with the short residence time of waters of few days in the estuary.

A previous study discussed these acid–base processes in a theoretically, suggesting that the Amazon River presents a CO_2 deficit along its mixing zone with relation to atmospheric conditions as a result of thermodynamic changes, and the pCO_2 variations are quickly dominated by seawater, sustaining a CO_2 sink along the river–ocean mixing (Cai et al., 2013). In the PSRE, these acid–base processes are confirmed along the mixing zone, showing strong agreement between the theoretical model and in situ data. For the three sampling campaigns, however, the pCO_2 values in the salinity gradient remained close but slightly above the theoretical dilution curve (pCO_2 $_{mixing}$). The slight deviations of measured pCO_2 compared with pCO_2 $_{mixing}$ are attributed to the influence of biological activities, gas exchange, and thermal variability during estuarine mixing, as discussed in the following section.

4.2. Origin of the observed pCO_2 deviation from conservative mixing

Deviations of measured pCO_2 compared with pCO_2 $_{mixing}$ are potentially related to gas exchange, thermal effect (heating/cooling), and ecosystem metabolism (estuarine autotrophy/heterotrophy plus tidal pumping) during estuarine mixing (Jiang et al., 2008; Joesoef et al., 2015; Van Dam et al., 2018a). In order to account for these processes, first we binned the measured pCO_2, calculating the means and standard deviations for each salinity increment. Then we calculated the effects of gas exchange and thermal variability on pCO_2 $_{mixing}$ as described in

material and methods (Section 2.5.5) for the same salinity intervals, assuming a constant and homogeneous residence time along the entire salinity gradient. This way we could calculate different pCO_2 curves during estuarine mixing: measured pCO_2 ($pCO_{2\ measured}$), conservative pCO_2 ($pCO_{2\ mixing}$), conservative pCO_2 corrected for gas exchange ($pCO_{2\ gas\ exchange}$), and conservative pCO_2 corrected for thermal effects ($pCO_{2\ heating/cooling}$) (Fig. 9). The difference between $pCO_{2\ gas\ exchange}$ and $pCO_{2\ mixing}$ ($\Delta pCO_{2\ gas\ exchange}$) was attributed to gas exchange, whereas the difference between $pCO_{2\ heating/cooling}$ and $pCO_{2\ mixing}$ ($\Delta pCO_{2\ heating/cooling}$) was attributed to thermal effects. Finally, the residual difference between $pCO_{2\ measured}$ and $pCO_{2\ gas\ exchange}$ + $pCO_{2\ heating/cooling}$ ($\Delta pCO_{2\ residual}$) was assigned to ecosystem metabolism (Fig. 9).

During low river flow, the values of $\Delta pCO_{2\ gas\ exchange}$ were positive along the entire salinity gradient in all sampling campaigns, with higher values at low salinities (< 10), indicating strong CO_2 invasion that increases the values of pCO_2 in the water (Fig. 9d,e). During the rainy period, the low salinities also showed the highest $\Delta pCO_{2\ gas\ exchange}$ deviations, but with negative values, indicating the influence of CO_2 evasion that decreases the values of pCO_2 (Fig. 9f). This shows that the maximal influence of gas exchange on pCO_2 variability during estuarine mixing occurs at low salinities. The influence of gas exchange on pCO_2 showed a marked decrease tendency seaward, with nearly negligible influence from salinities > 10, as a result of higher buffering capacity and lower air-water pCO_2 gradient. In addition, in intermediate and high salinity waters, pCO_2 values remain very close to air pCO_2 values, minimizing the effect of atmospheric gas exchange.
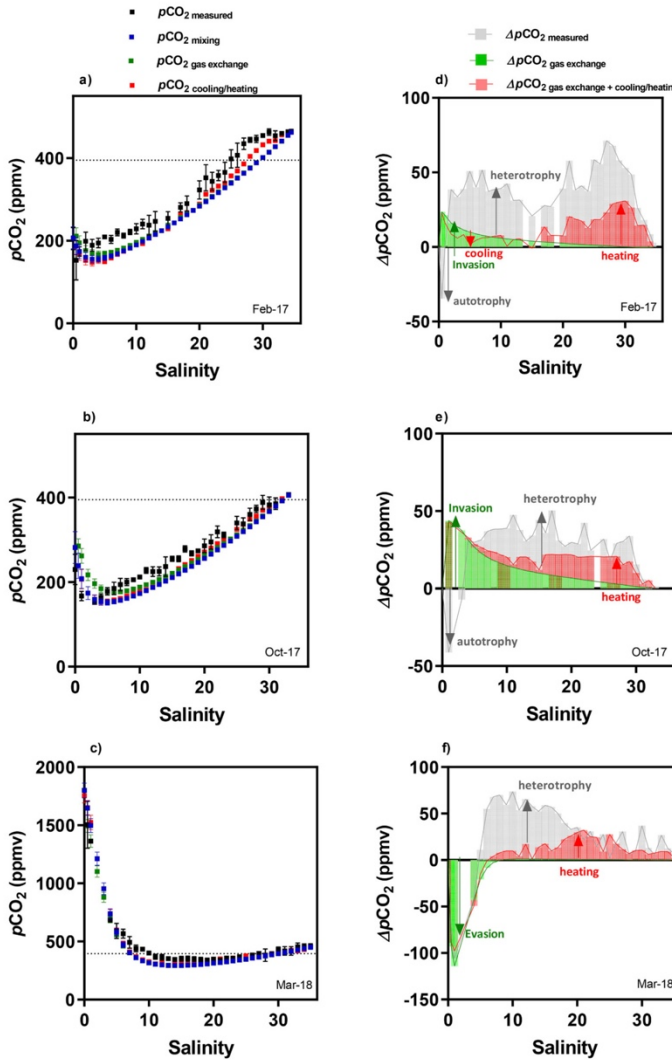
Fig. 9. Comparison between mixing model and $pCO_{2\ measured}$ in the mixing zone, including corrections performed for gas exchange and thermal variability and deviations from the conservative mixing. Graphs a), b) and c) show the means and standard deviations of $pCO_{2\ measured}$ (black dots), $pCO_{2\ mixing}$ (blue dots), $pCO_{2\ gas\ exchange}$ (green dots) and $pCO_{2\ cooling/heating}$ (red dots) for each salinity unit. Graphs d), e) and f) show the difference between $pCO_{2\ measured}$ and $pCO_{2\ mixing}$ ($\Delta pCO_{2\ measured}$), $pCO_{2\ gas\ exchange}$ and $pCO_{2\ mixing}$ ($\Delta pCO_{2\ gas\ exchange}$), and the cumulative difference between $pCO_{2\ gas\ exchange}$ + $pCO_{2\ cooling/heating}$ and $pCO_{2\ mixing}$ ($\Delta pCO_{2\ gas\ exchange+cooling/heating}$). The green arrow indicates the effect of gas exchange compared with $pCO_{2\ mixing}$ (influx or efflux of CO_2). The red arrow indicates the effect of thermal variability (cooling and heating). The grey arrow indicates the residual difference between $pCO_{2\ measured}$ and $pCO_{2\ mixing}$ attributed to biological activities. (For interpretation of the references to colour in this figure legend, the reader is referred to the web version of this article.)

15

Consequently, during estuarine mixing in the PSRE, the process of gas exchange has a significant impact on DIC concentrations, particularly in the low–buffered waters of the river domain (Fig. S2; Supplementary information). The highest influence of CO_2 invasion was verified on October 17, when the highest wind and gas transfer velocities were observed (Table 3) and ΔpCO_2 gas exchange reached a value of 50 ppmv (Fig. 9b,e). The highest influence of CO_2 evasion was verified on March 18, when the ΔpCO_2 gas exchange reached a value of −150 ppmv (Fig. 9f). For intermediate and high salinity waters, the influence of gas exchange on pCO_2 variability was minor and nearly negligible, close to that of the marine endmember. Indeed, previous studies have reported lower buffering capacities in regions dominated by freshwaters when the freshwater endmember present low TA concentrations (Hu and Cai, 2013; Cai et al., 2013).

The values of ΔpCO_2 cooling/heating were almost always positive, indicating that the water in the estuarine zone was warmed compared to expected behavior for two endmembers mixing. The highest values of ΔpCO_2 cooling/heating occurred in mid– to high–salinity waters (salinity values of 20-30). These salinities are generally sampled around midday, when solar irradiance is highest, thus causing this thermal effect. For these salinities of the PSRE, the increase of 1 °C in water temperature tend to increase pCO_2 by ~15 ppmv. As the difference between the temperature measured in situ and that predicted by the conservative mixing mean of approximately +0.8 °C, the influence of heating was 12 ppmv, on average; however, the heating effect could reach up ~30 ppmv of pCO_2 under conditions of high intensity solar irradiance during sampling in summer, particularly on the Mar 18 sampling (Fig. 9c,f). An exception occurred during sampling on February 17, when water cooling was observed at low salinities (Fig. 9a,d). In addition to local thermal effects occurring at the time scale of estuarine mixing, seasonal variation in temperature induced variations in pCO_2 mainly in waters with salinity > 30, resulting in approximately one half (30 ppmv) of the pCO_2 difference between summer and winter (Takahashi et al., 2002). Indeed, pCO_2 variability in the oligotrophic surface waters of the continental shelf of the Southwestern Subtropical Atlantic Ocean is mainly driven by temperature (Ito et al., 2005). The continental shelf of southeastern Brazil, where the river plume of the PSRE is located, is influenced by the Western Boundary Current, which flows southward along the Brazilian shelf as a section of the South Atlantic Ocean subtropical gyre (Campos et al., 2000). The Brazil Current carries the Tropical Water in the upper layers, the South Atlantic Central Water at intermediate depths, in addition to the Coastal Water in the inner portion of continental shelves, which compose the water masses in the region (Castro and Miranda, 1998).

In general, the differences between pCO_2 measured and pCO_2 mixing were positive for all sampling campaigns, with deviation means of +45 ppmv, +30 ppmv and + 32 ppmv for the Feb 17, Oct 17 and Feb 18 samplings, respectively (Fig. 9d,e,f). Together, the gas exchange and thermal effects accounted for nearly half of this difference (with gas exchange and water heating corresponding to approximately 18% and 36%, respectively), whereas the other half (residual difference, ΔpCO_2 residual) was attributed to the ecosystem metabolism along the mixing zone. These positive deviations reveal a CO_2 production along the mixing zone that is not linked to conservative mixing, gas exchange and thermal variability, but rather to net heterotrophy during estuarine mixing. However, some negative ΔpCO_2 residual values were also observed in low salinity waters under low river flow conditions, which shows a net biological CO_2 uptake by phytoplanktonic primary production. At low salinities in summer, some autotrophy decreases pCO_2 measured values in relation to those of pCO_2 mixing.

4.3. Impact of phytoplankton on the river and low salinity region

Phytoplankton had an important impact on pCO_2 in the low salinity region of the PSRE, as revealed by the Chl a concentrations (Fig. 4j,k,l), the δ^{13}C–DIC signatures (Fig. 4g,h,i), and by the mixing model

presented in the previous section (Fig. 9). During low river flow, the PSRE presented an atypical pattern of pCO_2 variability along the salinity gradient. In that period, Chl a concentrations were higher in the fresh and low salinity waters, with a strong negative correlation with water pCO_2, showing an uptake by planktonic primary production (Fig. 5). This inverse correlation between Chl a and pCO_2 occurred only during low river flow, when the lower hydrological model forcing provides favorable conditions for phytoplankton growth in freshwaters because of the high availability of nutrients, high incidence of photosynthetically active radiance, increased water residence time, and formation of vertical water column stratification (Souza et al., 2010; Cotovicz Jr. et al., 2013). The freshwater discharge contributes to maintaining low dilution and flushing potentials, changing the trophic status in the estuary from oligotrophic to mesotrophic (Cotovicz Jr. et al., 2013). Uptake of CO_2 by phytoplankton is also evidenced by the negative and significant relationship between pCO_2, DO, and δ^{13}C–DIC signatures (Fig. S3, Supplementary information). During low river flow, pCO_2 values were lower, whereas DO concentrations and δ^{13}C–DIC signatures were higher, indicating prevalence of net autotrophy. During photosynthesis, plants preferentially utilize the lighter carbon isotope (^{12}C) rather than the heavier carbon isotope (^{13}C), making the remaining DIC pool ^{13}C enriched (Finlay and Kendall, 2007; Cotovicz Jr. et al., 2019). A previous study showed that the stable isotope composition of the dissolved CO^2 (δ^{13}C–DOC) also presented a marked seasonal signal in the PSRE, with more ^{13}C depletion in the rainy season (minimum of −25.7‰) than in the dry season (maximum of −20.0‰) (Marques et al., 2017). These authors suggested that algae could be a potential source of isotopically heavier DOC to the river zone during the dry season, as our data of low pCO_2 values and high δ^{13}C–DIC signatures and Chl a concentrations also suggest.

The Paraiba do Sul River receives large amounts of domestic and industrial effluents along its course, which drains one of the most urbanized and industrialized regions of Brazil (Cotovicz et al., 2013). Low pCO_2 levels due to nutrient enrichment and phytoplankton blooms development has been previously shown for other coastal bays surrounded by large urban areas, e.g., the tropical Guanabara Bay (Cotovicz Jr. et al., 2015) and in the temperate Tokyo Bay (Kubo et al., 2017). However, this is very uncommon in river–dominated estuaries, which are considered important CO_2 sources globally (Borges and Abril, 2011). To the best of our knowledge, this pattern of low pCO_2 in freshwater was only reported in the temperate Merrimack Estuary, located in a highly industrialized region of the United States, which experienced a rapid population growth (Salisbury et al., 2008).

Large phytoplankton biomass is observed in the freshwaters of the PSRE during low river flow, but it shows a marked decline seaward (Fig. 4j,k,l). Indeed, estuarine deltas with short residence times are characterized by rapid salinity changes in water masses, which hinder the installation of phytoplankton communities because of osmotic stress (Lancelot and Muylaert, 2011). Salinity and turbulent mixing are often reported as the major factors determining phytoplankton distribution (Cloern, 1996; Lancelot and Muylaert, 2011). In addition to osmotic stress, the community structure, biomass production, species succession, and magnitude of the phytoplankton bloom along the estuary are also related to small availability and short residence time (Roubeix et al., 2008; Flöder et al., 2010). Thus, sharp salinity changes, high turbulence, turbidity, and short residence time create conditions unfavorable for phytoplankton production.

During high river flow, the phytoplankton community is probably flushed and dies in the main channel. The river discharge is stronger than the tidal prism, and the mixing occurs offshore. According to Lucas et al. (2009), the phytoplankton biomass can increase in an estuary only if the net specific growth rates exceed the water residence time and flushing time in the estuary. In general, development of phytoplankton blooms in estuaries is inversely correlated to river water discharge (Strayer et al., 2008). However, during the flood on May 18, part of the phytoplankton was apparently trapped in the low salinity mangrove

16

creeks, where the observed Chl a concentrations reached ~70 μg L^{-1} (Table 2). Mangrove creek provided ideal conditions for phytoplankton refuge due to low salinity stress. This created a special case in this estuary – a low salinity mangrove creek enriched with phytoplankton. Phytoplankton activity and the influence on DIC and δ^{13}C–DIC concentrations are evident in the mangrove creek within the diurnal variations (Fig. 6). During the diel sampling in the mangrove creek, phytoplankton biomass was high, and managed to drawdown pCO$_2$ during the afternoon compare with nighttime, making δ^{13}C–DIC less negative due to a preferential uptake of ^{12}C from the DIC pool during photosynthesis. Similar processes have been described in a hypertrophic lake (Lake Taihu, China; Van Dam et al., 2018b) and in a tropical eutrophic coastal embayment (Guanabara Bay, Brazil, Cotovicz Jr. et al., 2019), but not in mangrove creeks. During the rainy period, the mangrove creek presented more ^{13}C-enriched signatures than the expected for conservative mixing (Fig. 4g,h,i) and related to this phytoplankton activity. However, this pattern in the mangrove creek was not verified during the dry period, when Chl a concentration do not exceed 14.6 μg L^{-1}, and δ^{13}C–DIC signatures were ^{13}C-depleted more than would be expected for conservative mixing, a distribution generally found in mangrove-dominated waters because of enhanced respiratory processes (Bouillon et al., 2007, 2011; Miyajima et al., 2009; Sippo et al., 2016).

4.4. Evidence of heterotrophy in the mixing zone

Multiplication of the residual pCO$_2$ difference attributed to biological activities (ΔpCO$_{2 residual}$) with gas transfer velocity (Eq. (3)) provides an estimate of the community production (NCP) (Table 4). The gas transfer velocity parameterization of Raymond and Cole (2001), which resulted in intermediate values of air–water fluxes (Table 3), was chosen for this calculation. For the entire estuarine mixing zone, average NCP was −1.70 mmol m^{-2} d^{-1} on February 17, −1.13 mmol m^{-2} d^{-1} on October 17, and − 0.58 mmol m^{-2} d^{-1} on February 18. NCP values in the PSRE are in the lower range of NCP and ecosystem metabolism in the European coastal zone (Gazeau et al., 2004). These low NCP values observed along the mixing zone of the PSRE confirm the moderate influence of biological activities, with microbial respiration not being sufficient to create CO$_2$ oversaturation in relation to the atmosphere. During low river flow, the entire mixing zone was already undersaturated, and the net heterotrophy was also not sufficient to generate CO$_2$ outgassing. This created a very special condition in the mixing zone of the estuary, with concomitant pCO$_2$ undersaturation and heterotrophic metabolism. During high river flow, the heterotrophic metabolism was also apparent in the freshwater owing to pCO$_2$ values above the atmospheric equilibrium, DO concentrations below the atmospheric equilibrium, and more negative δ^{13}C–DIC signatures, all indicating prevalence of microbial respiration over primary production (Fig. S3, Supplementary information). However, as previously shown (Fig. 9f), heterotrophic metabolism was modest in the estuary during high discharge, and thus the river input was a major contributor to the high CO$_2$ concentrations, at least in the region dominated by freshwaters (0-5 salinity). Riverine CO$_2$ inputs represent the major CO$_2$ source in other river-dominated estuaries (Jiang et al., 2008; Joesoef et al., 2015; Van Dam et al., 2018a).

The covariations of Δδ^{13}C–DIC and ΔDIC, considering only the main river channel, also reveal net heterotrophy, with values of δ^{13}C–DIC showing slight ^{13}C-depleted signatures (negative Δδ^{13}C–DIC) compared with the conservative mixing (Fig. 10). This graph is divided in four quadrants that represent the processes of primary production/outgassing of CO$_2$ (quadrant PP/OG), carbonate precipitation (quadrant CP), organic carbon degradation (quadrant DC), and carbonate dissolution (quadrant CD) (Alling et al., 2012; Samanta et al., 2015; Cotovicz Jr. et al., 2019). The red arrows represent the directions of slopes in which data points would move in relation to a specific process, whereas the grey lines represent the directions in which samples would

move in relation to the effects of more than one process (see figure caption for further details). The data points of the PSRE are mostly located in the quadrant of organic carbon degradation (DC), and to a lesser extent in the quadrant of carbonate precipitation (CP). The process of organic carbon degradation increases the DIC concentrations in water (positive ΔDIC) and decreases the isotopic signature of DIC (negative Δδ^{13}C–DIC) (Alling et al., 2012; Samanta et al., 2015). The respiration of organic carbon produces CO$_2$ with approximately the same isotopic signature than that of the respired organic matter, which is generally ^{13}C depleted; consequently, the DIC pool tends to be more depleted in ^{13}C when the organic matter respiration rates are high and prevalent in phytoplankton uptake (Kendall et al., 2004; Bouillon et al., 2011; Borges et al., 2018). The process of carbonate precipitation is unlikely to occur, because this estuary is not known to host high levels of calcifying fauna and flora. However, as pointed out, DIC and δ^{13}C–DIC can be subjected to more than one process at same time. This means that if one sample was subjected to organic carbon degradation followed by CO$_2$ outgassing, it could also be located in the quadrant of carbonate precipitation (Samanta et al., 2015). This probably occurs in regions that are sources of CO$_2$ to the atmosphere: the mixing region with very low salinities on March 18 and in offshore waters on Feb 17 and Mar 18 (Figs. 9 and 10). These deviations of δ^{13}C–DIC signatures and DIC concentrations from the conservative mixing are thus very consistent with the approach, considering the differences between pCO$_2$ measured and pCO$_{2 mixing}$ (Fig. 9).

The marked seaward decrease of Chl a concentrations along the mixing zone in the main channel suggests that these phytoplankton cells are dying, providing labile organic material for decomposition by heterotrophic bacteria. However, heterotrophy remains weak probably because of the short water residence time in the mixing zone, a crucial factor for bacterial growth in estuaries (Del Giorgio and Bouvier, 2002; Crump et al., 2004), and because of salinity stress in the bacterioplankton, since that freshwater bacteria could remain active in the estuary, but at a reduced rate (Crump et al., 2004). The ΔTA and ΔDIC values along the salinity gradient in the main channel were low (generally < 50 μmol kg^{-1}; Fig. 8b), which correspond to less than 5% of the DIC and TA pools, confirming a modest biological influence in the main channel.

Table 4

Net Community Production (NCP; mmolC m^{-2} d^{-1}) estimated for the mixing zone. The NCP was estimated as the difference between (ΔFCO$_2$; mmolC m^{-2}d^{-1}), (ΔFCO$_2$mixing corrected; mmolC m^{-2} d^{-1}) and (ΔFCO$_2$cooling/heating; mmolC m^{-2} d^{-1}). FCO$_2$, FCO$_2$mixing corrected and FCO$_2$cooling/heating (mmolC m^{-2} d^{-1}) were calculated with the values of pCO$_2$ measured, pCO$_2$ mixing corrected and pCO$_2$ cooling/heating. See the section "2.5 calculations" in material and methods and section "4.4 evidence of heterotrophy in the mixing zone" in discussion for further details.

|	Mixing zone
Feb - 17	
ΔFCO$_2$ = FCO$_{2mixing}$ − FCO$_2$	−2.18
ΔFCO$_{2mixing\ corrected}$ = FCO$_{2mixing}$ − FCO$_{2mixing\ corrected}$	−0.18
ΔFCO$_{2cooling/heating}$ = FCO$_{2mixing}$ − FCO$_{2cooling/heating}$	−0.30
NCP = (ΔFCO$_2$) − (ΔFCO$_{2mixing\ corrected}$) − (ΔFCO$_{2cooling/heating}$)	−1.70
Oct - 17	
ΔFCO$_2$ = FCO$_{2mixing}$ − FCO$_2$	−2.95
ΔFCO$_{2mixing\ corrected}$ = FCO$_{2mixing}$ − FCO$_{2mixing\ corrected}$	−1.02
ΔFCO$_{2cooling/heating}$ = FCO$_{2mixing}$ − FCO$_{2cooling/heating}$	−0.79
NCP = (ΔFCO$_2$) − (ΔFCO$_{2mixing\ corrected}$) − (ΔFCO$_{2cooling/heating}$)	−1.13
Mar - 18	
ΔFCO$_2$ = FCO$_{2mixing}$ − FCO$_2$	−0.46
ΔFCO$_{2mixing\ corrected}$ = FCO$_{2mixing}$ − FCO$_{2mixing\ corrected}$	0.69
ΔFCO$_{2cooling/heating}$ = FCO$_{2mixing}$ − FCO$_{2cooling/heating}$	−0.57
NCP = (ΔFCO$_2$) − (ΔFCO$_{2mixing\ corrected}$) − (ΔFCO$_{2cooling/heating}$)	−0.58

17

169
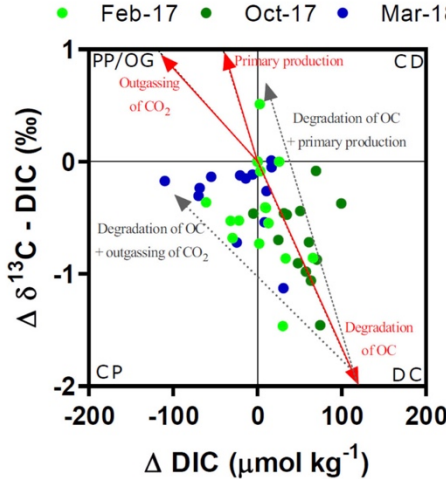
Fig. 10. Deviations from conservative mixing lines of stable isotope composition of DIC ($\Delta\delta^{13}$C-DIC) as a function of DIC (ΔDIC) for the main channel. Different colors represent the sampling campaigns. The origin represents the conservative mixing with sample values equal to the ocean endmember value. The four quadrants (PP/OG, CP, DC, and CD) in the graph indicate the processes that could influence the DIC and δ^{13}C–DIC distributions. Quadrant PP/OG represents the primary production/outgassing of CO_2, when DIC concentrations increase and δ^{13}C–DIC values decrease. Quadrant CP represents the carbonate precipitation, when DIC concentrations and δ^{13}C–DIC values decrease. Quadrant DC represents the degradation of organic carbon, when DIC concentrations increase and δ^{13}C–DIC decrease. Quadrant CD represents the carbonate dissolution, when the DIC concentrations and δ^{13}C–DIC values increase. The red vectors represent the slopes of specific processes affecting the DIC and δ^{13}C–DIC distributions: primary production (slope = −24.0‰), CO_2 outgassing (slope = −8.4‰), and organic carbon degradation using the δ^{13}C-DIC value of river water (−16.0‰). The grey arrows represent the direction that the samples will follow if they are subject to more than one process (organic matter degradation followed by primary production, which is drawn parallel to vector of primary production; and organic carbon degradation followed by CO_2 outgassing, which is drawn parallel to the vector of CO_2 outgassing). Details about the formulations and calculations of these vectors can be found in Alling et al. (2012), Samanta et al. (2015), and Cotovicz Jr. et al. (2019). (For interpretation of the references to colour in this figure legend, the reader is referred to the web version of this article.)

4.5. Tidal pumping in the mangrove creek

Water pCO_2 values in the mangrove creek were much higher than those in the main channel, as well as than those predicted by the conservative mixing curve (Fig. 3). In addition, the mean pCO_2 values observed in the mangrove creeks were within the high range of values reported in other mangroves worldwide. The maximum pCO_2 value reported here was 22,000 ppmv and, to the best of our knowledge, only one study reported a higher maximum pCO_2 value (27,000 ppmv; Australian micro–tidal system, Call et al., 2015). Our measured pCO_2 values are similar to those observed in some micro–, meso–(Koné and Borges, 2008; Call et al., 2015; Rosentreter et al., 2018) and macro–tidal (Call et al., 2019) mangrove creeks. The mangrove waters presented higher values of ΔTA and ΔDIC compared with those of the main channel (Fig. 8b). The slope of the linear regression of ΔTA vs. ΔDIC in the mangrove creek was 0.73, a value within the theoretical slopes of organic matter aerobic degradation (0.2), denitrification (0.8), sulfate reduction (0.9), and calcium carbonate ($CaCO_3$) dissolution (2.0) (Borges et al., 2003; Bouillon et al., 2007). Denitrification is likely to be

minor in mangrove ecosystems due to the low concentrations of inorganic N–species (Alongi et al., 2000; Maher et al., 2016). $CaCO_3$ dissolution is unlike to be important in this mangrove that does not receive important amounts of $CaCO_3$ from adjacent ecosystems. This slope is rather similar to those found in the mangrove tidal creeks of Papua New Guinea (Borges et al., 2003), Kenya (Bouillon et al., 2007) and Australia (Sippo et al., 2016) and in the secondary channels of the Mekong Delta (Borges et al., 2018), suggesting that the main processes responsible for TA and DIC production are sulphate reduction and aerobic degradation of organic matter. TA production occurs when DO presents saturation < 30% (Fig. 7b), and it is maximal under hypoxic/anoxic conditions. These results reveal that the mangrove creek in the PSRE is producing and exporting DIC and TA to mangrove surrounding waters, a process recently reported in a number of other mangroves that still needs precise quantification (Sippo et al., 2016; and references there in). Important correlations of radon (^{222}Rn) with DIC and TA in several mangrove creeks located at different coastal latitudes have evidenced an important production of TA and DIC in mangrove sediment pore waters with export mediated by tidally induced processes (Santos et al., 2018; Call et al., 2019 and references therein).

The relationship between E–DIC and AOU (Fig. 8a) exhibited important deviations above the 1:1 line that occurred almost exclusively in the mangrove creek. This high deviation above the 1:1 line in the mangrove creek could be associated with anaerobic organic matter degradation in sediments and lateral transfer via tidal pumping. Because the process of sulphate reduction is a dominant mineralization pathway of organic carbon in mangroves (Borges et al., 2003; Bouillon et al., 2007; Sippo et al., 2016), secondary metabolites such as Fe(II) and sulfides escape re-oxidation by oxygen through the formation of pyrite (Alongi et al., 2000; Hu and Cai, 2011), resulting in net consumption of protons and net production of TA.

Tidal variation also seems to be important considering the modulation of CO_2 production and consumption in the mangrove tidal creek (Figs. 6 and 7). On May 2017, CO_2 uptake occurred during daytime, making the waters enriched in δ^{13}C-DIC, with drawdown of pCO_2 and production of DO, even during ebb tide. This explains the low pCO_2 values at ebb tide (daytime), which are not common in mangrove waters (Bouillon et al., 2011; Sippo et al., 2016). The maximal CO_2 concentrations were found during ebb tide in early morning, concomitant with the highest concentrations of TA and DIC and the highest ^{13}C depletion, evidencing the carbon respiration accumulated overnight and the influence of diagenetic processes. Tidal pumping is facilitated, during ebb tide, by the semi–diurnal flushing of crab burrows that are considerably enriched in dissolved carbon due to the diffusion and advection of pore water from the soils (Borges et al., 2003; Call et al., 2015; Maher et al., 2015). This pCO_2 pattern peaking at the nighttime ebb tide is consistent with findings of previous studies that suggest a pore water source of surface water pCO_2 (Bouillon et al., 2007; Kristensen et al., 2008; Linto et al., 2014; Call et al., 2019).

4.6. CO_2 fluxes in the PSRE compared with those of other estuaries

Estuarine systems and mangrove surrounding waters are sources of CO_2 to the atmosphere and significant for regional and global carbon budgets (Bouillon et al., 2008; Maher et al., 2013; Chen et al., 2013; Laruelle et al., 2013). According to the most recent global compilation of estuarine CO_2 emissions propose by Chen et al. (2013), upper estuaries are CO_2 sources of the order of 106 mmol C m^{-2} d^{-1}, mid-estuaries emit 47 mmol C m^{-2} d^{-1}, and lower estuaries with salinities > 25 emit 23 mmol C m^{-2} d^{-1}. These values are much higher than those found in the PSRE, which partially acts as a CO_2 sink, with annual CO_2 emission of only 1.63 to 11.98 mmol C m^{-2} d^{-1} (Table 3). The low CO_2 fluxes in the PSRE are consistent with those found in the continental shelf of the subtropical Atlantic Ocean (0.3-9.8 mmol C m^{-2} d^{-1}; Ito et al., 2005). Considering only the dry period, the estuary as a whole was a CO_2 sink, with fluxes ranging from −0.34 to −5.26 mmol C m^2

d^{-1}. These values are close to those reported in the tropical Aby Lagoon (-7.39 mmolC m^{-2} d^{-1}; Koné et al., 2008), subtropical southeast Australian estuaries (-3.28 to -12.05 mmolC m^{-2} d^{-1}; Maher and Eyre, 2012), the tropical eutrophic Guanabara Bay (-26.3 to -50.1 mmolC m^{-2} d^{-1}; Cotovicz Jr. et al., 2015), the temperate Tokyo Bay (-8.8 mmolC m^{-2} d^{-1}; Kubo et al., 2017) and the Liminganlahti Bay (-2.46 mmolC m^{-2} d^{-1}; Silvennoinen et al., 2008), in addition to some fjords (Takahashi et al., 2012). All these systems are marine-dominated estuaries, different from the PSRE, which is a river–dominated estuary. To the best of our knowledge, only the temperate Kennebec River (-1.36 mmol C m^{-2} d^{-1}; Takahashi et al., 2012) and the New River/USA (-0.5 to 5.4 mmolC m^{-2} d^{-1}; Crosswell et al., 2017) are river–dominated estuaries that exhibited CO$_2$ sink at least in certain periods of the year. Recent findings in the mixing zone of the Amazon River estuary also calculated a net CO$_2$ sink (maximum of -9.2 mmol C m^{-2}d^{-1}), attributed to mixing and biological activity, although the Amazon River and the tropical Atlantic are net sources (Lefèvre et al., 2017). Considering only the rainy period, the PSRE was a CO$_2$ source of approximately 5.71 to 19.37 mmol C m^{-2} d^{-1}. These CO$_2$ emissions are much lower than the average global emissions in estuaries (Chen et al., 2013) due to the fact that, even under high river flow conditions, the mixing zone of the PSRE is a permanent CO$_2$ sink due to the prevalence of thermodynamic processes. However, considering only the river domain during the rainy season, the PSRE presents emission of approximately 60 mmol C m^{-2} d^{-1}, a degassing rate close to those reported in other river–dominated estuaries (Frankignoulle et al., 1998; Chen et al., 2013).

The CO$_2$ degassing rate in the mangrove tidal creek (average of 135 mmol C m^{-2} d^{-1}) is above global average of CO$_2$ flux emissions from surrounding mangrove waters (56 mmol C m^{-2} d^{-1}; Rosentreter et al., 2018). Our mean values and ranges of CO$_2$ degassing are close to those found in mangroves in Vietnam (Kiên Vàng and Tam Giang mangroves, 32 to 155 mmol C m^{-2} d^{-1}; Koné and Borges, 2008), Andaman Islands (Kalighat mangrove, 23 to 173 mmol C m^{-2} d^{-1}; Linto et al., 2014), Australia (Moreton Bay mangrove tidal creek, 202 mmol C m^{-2} d^{-1}; Call et al., 2015), and the Amazon region (62 to 437 mmol C m^{-2} d^{-1}; Call et al., 2019). These high CO$_2$ emissions in mangrove tidal creeks, in addition to the mangrove production of TA and DIC and transport to surrounding waters, can represent an important fraction of the carbon that is fixed by mangrove vegetation, with high significance in mangrove carbon budgets on a global scale (Bouillon et al., 2008; Maher et al., 2013; Call et al., 2015).

Comparison between the amount of DIC delivered by the river and the CO$_2$ exchanges at the air–sea interface in the mixing zone shows that the river contributes ~18 to 520 times more inorganic carbon to the adjacent continental shelf compared with the estuarine carbon sink. This means that the air–water exchange of CO$_2$ is much slower than the acid–base equilibration of DIC during mixing in the estuary, increasing the importance of thermodynamic processes and decreasing the importance of air–water exchanges and biological activities. It is worth highlighting that many of the world's largest river systems are located in tropical regions, which provide ~40% of global freshwater discharge to the oceans (Dai and Trenberth, 2002). Overall, large tropical rivers present low TA concentrations, such as the Amazon, Congo and Orinoco Rivers (Cai et al., 2008; Moore–Maley et al., 2018). Consequently, the CO$_2$ concentrations at the estuarine mixing zone of large and poorly buffered rivers can be largely overestimated due to this still overlooked process.

5. Conclusions

Overall, the ecosystem showed aquatic sources and sinks of CO$_2$ considering specific estuarine regions, which were modulated by carbonate thermodynamics, gas exchange, thermal effects, and biological activities. The pCO$_2$ and carbonate chemistry parameters in the PSRE showed marked spatiotemporal variations governed by processes somewhat different from those reported so far in the literature:

i). In the freshwater domain, biological effects were prevalent. During high river flow, the waters presented higher pCO$_2$ values and lower DO concentrations and δ^{13}C-DIC signatures, as a result of heterotrophic processes in the river. In contrast, under dry conditions, the waters presented low pCO$_2$ values and high δ^{13}C-DIC signatures as a result of phytoplankton growth.

ii). In the mixing zone, the thermodynamic processes during estuarine mixing was the most important driver of pCO$_2$ variations, with measured pCO$_2$ following a distribution close to the theoretical conservative curve predicted by the mixing of the river and marine endmembers. During the rainy period, the pCO$_2$ values decreased sharply as a result of rapid absorption by the acid–base buffering capacity of high TA seawaters. During the dry period, the pCO$_2$ values were below the atmospheric pCO$_2$ in freshwater and increased in seaward, also consistent with the theoretical thermodynamic mixing.

iii). The δ^{13}C-DIC signatures were slightly below the conservative mixing curve, indicating a heterotrophic metabolism at intermediate to high salinities. The biological activity contributed to approximately half of the deviation of measured pCO$_2$ from pCO$_2$ $_{mixing}$. The other half was attributed to gas exchange (~18%) and water heating (~36%) during estuarine mixing.

iv). In the mangrove creek, the waters presented high CO$_2$ values in all sampling campaigns, with strong oversaturation attributed to production of DIC and TA in the water and pore waters by aerobic and anaerobic processes, and transport by diffusion and convection via tidal pumping. Interesting to point out that, during high river flow, the mangrove–dominated waters presented higher δ^{13}C-DIC signatures than the main estuarine channel, attributed to phytoplankton growth and fractionation of DIC.

Considering the entire area of the PSRE, the estuary was a CO$_2$ sink at low freshwater discharge (air–water CO$_2$ fluxes ranging from -0.34 to -5.26 mmol C m^{-2} d^{-1}) and a CO$_2$ source at high freshwater discharge (5.71-19.37 mmol C m^{-2} d^{-1}). These fluxes are lower and different from those reported in other river–dominated estuaries worldwide, which are normally strong CO$_2$ sources. The construction of dams in the upper sections of Paraiba do Sul River has decreased its water flow and, associated with increased anthropogenic–derived nutrient inputs to the river, can potentially change the functioning of this ecosystem, from an annual CO$_2$ source to an annual CO$_2$ sink. These results also have implications on global carbon budgets, showing that tropical river–dominated estuaries could absorb CO$_2$ along the river and mixing domains as a result of the poor buffering capacity during estuarine mixing. Low TA concentrations are a property of many large tropical rivers (Amazon, Congo, Orinoco), suggesting that this process can be important globally and needs further investigation.

Declaration of Competing Interest

None.

Appendix A. Supplementary data

Supplementary data to this article can be found online at https://doi.org/10.1016/j.marchem.2020.103869.

References

Abril, G., Borges, A.V., 2004. Carbon dioxide and methane emissions from estuaries. In: Tremblay, A., Varfalvy, L., Roehm, C., Garneau, M. (Eds.), Greenhouse Gases Emissions from Natural Environments and Hydroelectric Reservoirs: Fluxes and Processes. Springer, Berlin, pp. 187–207.

Abril, Gwenaël, Etcheber, Henry, Borges, Alberto, Frankignoulle, Michel, 2000. Excess atmospheric carbon dioxide transported by rivers into the Scheldt estuary. Comptes Rendus de l'Académie des Sciences 330, 761–768. https://doi.org/10.1016/S1251-8050(00)00231-7.

Abril, G., Etcheber, H., Delille, B., Frankignoulle, M., Borges, A.V., 2003. Carbonate dissolution in the turbid and eutrophic Loire estuary. Mar. Ecol–Prog. Ser. 259, 129–138. https://doi.org/10.3354/meps259129.

Abril, G., Commarieu, M.–V., Sottolichio, A., Bretel, P., Guérin, F., 2009. Turbidity limits gas exchange in a large macrotidal estuary. Estuar. Coast. Shelf Sci. 83, 342–348. https://doi.org/10.1016/j.ecss.2009.03.006.

Abril, G., Martinez, J.–M., Artigas, L.F., Moreira–Turcq, P., Benedetti, M.F., Vidal, L., Meziane, T., Kim, J.–H., Bernardes, M.C., Savoye, N., Deborde, J., Albéric, P., Souza, M.F.L., Souza, E.L., Roland, F., 2014. Amazon River carbon dioxide outgassing fueled by wetlands. Nature 505, 395–398. https://doi.org/10.1038/nature12797.

Alling, V., Porcelli, D., Mörth, C.M., Anderson, L.G., Sanchez–Garcia, L., Gustafsson, Ö., Andersson, P.S., Humborg, C., 2012. Degradation of terrestrial organic carbon, primary production and out–gassing of CO_2 in the Laptev and east Siberian seas as inferred from ^{13}C values of DIC. Geochim. Cosmochim. Acta 95, 143–159. https://doi.org/10.1016/j.gca.2012.07.028.

Alongi, D.M., Tirendi, F., Trott, L.A., Xuan, T.T., 2000. Benthic decomposition rates and pathways in plantations of the mangrove Rhizophora apiculata in the Mekong delta, Vietnam. Mar. Ecol–Prog. Ser. 194, 87–101. https://doi.org/10.3354/meps194087.

Amarante, O.A., Silva, F.J., Rios Filho, L.G., 2002. Atlas Eólico, Estado do Rio de Janeiro. Secretaria de Estado da Energia. da Indústria Naval e do Petróleo, Rio de Janeiro. http://www.cresesb.cepel.br/publicacoes/download/atlas_eolico/AtlasEolicoRJ.pdf (accessed 15 April 2019).

Bauer, J.E., Cai, W.–J., Raymond, P., Bianchi, T.S., Hopkinson, C.S., Regnier, P.G., 2013. The changing carbon cycle of the coastal ocean. Nature 504, 61–70. https://doi.org/10.1038/nature12857.

Benson, B.B., Krause, D., 1984. The concentration and isotopic fractionation of oxygen dissolved in freshwater and seawater in equilibrium with the atmosphere. Limnol. Oceanogr. 29, 620–632. https://doi.org/10.4319/lo.1984.29.3.0620.

Borges, A.V., Abril, G., 2011. Carbon dioxide and methane dynamics in estuaries. In: Wolanski, E., McLusky, D. (Eds.), Treatise on Estuarine and Coastal Science. vol. 5. Academic Press, Amsterdam, pp. 119–161.

Borges, A.V., Djenidi, S., Lacroix, G., Theate, J., Delille, B., Frankignoulle, M., 2003. Atmospheric CO_2 flux from mangrove surrounding waters. Geophys. Res. Lett. 30, 1558. https://doi.org/10.1029/2003GL017143.

Borges, A.V., Abril, G., Bouillon, S., 2018. Carbon dynamics and CO_2 and CH_4 outgassing in the Mekong delta. Biogeosciences 15, 1093–1114. https://doi.org/10.5194/bg–15–1093–2018.

Bouillon, S., Dehairs, F., Schiettecatte, L.–S., Borges, A.V., 2007. Biogeochemistry of the Tana estuary and delta (northern Kenya). Limnol. Oceanogr. 52, 46–59. https://doi.org/10.4319/lo.2007.52.1.0046.

Bouillon, S., Borges, A.V., Castañeda–Moya, E., Diele, K., Dittmar, T., Duke, N.C., Kristensen, E., Lee, S.Y., Marchand, C., Middelburg, J.J., Rivera–Monroy, V., Smith, T.J., Twilley, R.R., 2008. Mangrove production and carbon sinks: a revision of global budget estimates. Glob. Biogeochem. Cy. 22 https://doi.org/10.1029/2007GB003052. GB2013.

Bouillon, S., Connolly, R.M., Gillikin, D.P., 2011. Use of stable isotopes to understand food webs and ecosystem functioning in estuaries. In: Wolanski, E., McLusky, D. (Eds.), Treatise on Estuarine and Coastal Science. Academic Press, Amsterdam, pp. 143–173.

Cai, W.–J., 2011. Estuarine and coastal ocean carbon paradox: CO_2 sinks or sites of terrestrial carbon incineration? Annu. Rev. Mar. Sci. 3, 123–145. https://doi.org/10.1146/annurev–marine–120709–142723.

Cai, W.–J., Pomeroy, L.R., Moran, M.A., Wang, Y., 1999. Oxygen and carbon dioxide mass balance for the estuarine–intertidal marsh complex of five rivers in the southeastern U.S. Limnol. Oceanogr. 44, 639–649. https://doi.org/10.4319/lo.1999.44.3.0639.

Cai, W.–J., Guo, X., Chen, C.–T.A., Dai, M., Zhang, L., Zhai, W., Lohrenz, S.E., Yin, K., Harrison, P.J., Wang, Y., 2008. A comparative overview of weathering intensity and HCO_3^- flux in the world's major rivers with emphasis on the Changjiang, Huanghe, Zhujiang (pearl) and Mississippi Rivers. Cont. Shelf Res. 28, 1538–1549. https://doi.org/10.1016/j.csr.2007.10.014.

Cai, W.–J., Hu, X., Huang, W.–J., Murrell, M.C., Lehrter, J.C., Lohrenz, S.E., Chou, W.–C., Zhai, W., Hollibaugh, J.T., Wang, Y., 2011. Acidification of subsurface coastal waters enhanced by eutrophication. Nat. Geosci. 4, 766–770. https://doi.org/10.1038/ngeo1297.

Cai, W.–J., Chen, C.–T.A., Borges, A.V., 2013. Carbon dioxide dynamics and fluxes in coastal waters influenced by river plumes. In: Bianchi, T., Allison, M., Cai, W.–J. (Eds.), Biogeochemical Dynamics at Major River–Coastal Interfaces: Linkages with Global Change. Cambridge University Press, Cambridge, pp. 155–173.

Call, M., Maher, D.T., Santos, I.R., Ruiz–Halpern, S., Mangion, P., Sanders, C.J., Erler, D.V., Oakes, J.M., Rosentreter, J., Murray, R., Eyre, B.D., 2015. Spatial and temporal variability of carbon dioxide and methane fluxes over semi–diurnal and spring––neap-spring timescales in a mangrove creek. Geochim. Cosmochim. Acta 150, 211–225. https://doi.org/10.1016/j.gca.2014.11.023.

Call, M., Santos, I.R., Dittmar, T., Rezende, C.E., Asp, N.E., Maher, D.T., 2019. High pore–water derived CO_2 and CH_4 emissions from a macro–tidal mangrove creek in the Amazon region. Geochim. Cosmochim. Acta 247, 106–120. https://doi.org/10.1016/j.gca.2018.12.029.

Campos, E.J.D., Velhote, D., Silveira, I.C.A., 2000. Shelf break upwelling driven by Brazil current cyclonic meanders. Geophys. Res. Lett. 27, 751–754. https://doi.org/10.1029/1999GL010502.

Castro, B.M., Miranda, L.B., 1998. Physical oceanography of the western Atlantic continental shelf located between 4°N and 34°S. In: Robinson, A.R., Brink, K.H. (Eds.), The Sea. John Wiley, Hoboken, pp. 209–251.

Chen, C.T.A., Borges, A.V., 2009. Reconciling opposing views on carbon cycling in the coastal ocean: continental shelves as sinks and near–shore ecosystems as sources of atmospheric CO_2. Deep Sea res. Part 2 top. Stud. Oceanogr. 56, 578–590. https://doi.org/10.1016/j.dsr2.2009.01.001.

Chen, C.–T.A., Huang, T.–H., Chen, Y.–C., Bai, Y., He, X., Kang, Y., 2013. Air-sea exchanges of CO_2 in the world's coastal seas. Biogeosciences 10, 6509–6544. https://doi.org/10.5194/bg–10–6509–2013.

Cloern, J.E., 1996. Phytoplankton bloom dynamics in coastal ecosystems: a review with some general lessons from sustained investigation of San Francisco Bay, California. Rev. Geophys. 2, 127–168. https://doi.org/10.1029/96RG00986.

Cohen, J.E., Small, C., Mellinger, A., Gallup, J., Sachs, J., Vitousek, P.M., Mooney, H.A., 1997. Estimates of coastal populations. Science 278, 1209–1213. https://doi.org/10.1126/science.278.5341.1209c.

Cotovicz Jr., L.C., Brandini, N., Knoppers, B.A., Mizerkowski, B.D., Sterza, J.M., Ovalle, A.R.C., Medeiros, P.R.P., 2013. Assessment of the trophic status of four coastal lagoons and one estuarine delta, eastern Brazil. Environ. Monit. Assess. 185, 3297–3311. https://doi.org/10.1007/s10661–012–2791–x.

Cotovicz Jr., L.C., Knoppers, B.A., Brandini, N., Costa Santos, S.J., Abril, G., 2015. A strong CO_2 sink enhanced by eutrophication in a tropical coastal embayment (Guanabara Bay, Rio de Janeiro, Brazil). Biogeosciences 12, 6125–6146. https://doi.org/10.5194/bg–12–6125–2015.

Cotovicz Jr., L.C., Libardoni, B., Brandini, N., Knoppers, B., Abril, G., 2016. Comparações entre medições em tempo real da pCO_2 aquática com estimativas indiretas em dois estuários tropicais contrastantes: o estuário eutrofizado da Baia de Guanabara (RJ) e o estuário oligotrofico do Rio São Francisco (AL). Quím. Nova 39, 1206–1214. https://doi.org/10.21577/0100–4042.20160145.

Cotovicz Jr., L.C., Knoppers, B.A., Deirmendjian, L., Abril, G., 2019. Sources and sinks of dissolved inorganic carbon in an urban tropical coastal bay revealed by $\delta^{13}C$-DIC signals. Estuar. Coast. Shelf Sci. 220, 185–195. https://doi.org/10.1016/j.ecss.2019.02.048.

Crosswell, J.R., Anderson, I.C., Stanhope, J.W., Van Dam, B., Brush, M.J., Ensign, S., Piehler, M.F., McKee, B., Bost, M., Paerl, H.W., 2017. Carbon budget of a shallow, lagoonal estuary: transformations and source–sink dynamics along the river–estuary–ocean continuum. Limnol. Oceanogr. 62, S29–S45. https://doi.org/10.1002/lno.10631.

Crump, B.C., Hopkinson, C.S., Sogin, M.L., Hobbie, J.E., 2004. Microbial biogeography along an estuarine salinity gradient: combined influences of bacterial growth and residence time. Appl. Environ. Microbiol. 70, 1494–1505.2. https://doi.org/10.1128/aem.70.3.1494–1505.2004.

Dai, A., Trenberth, K.E., 2002. Estimates of freshwater discharge from continents: latitudinal and seasonal variations. J. Hydrometeorol. 3, 660–687. https://doi.org/10.1175/1525–7541(2002)003<0660:EOFDFC>2.0.CO;2.

Dai, M., Lu, Z., Zhai, W., Chen, B., Cao, Z., Zhou, K., Cai, W.–J., Chen, C.A., 2009. Diurnal variations of surface seawater pCO_2 in contrasting coastal environments. Limnol. Oceanogr. 54, 735–745. https://doi.org/10.4319/lo.2009.54.3.0735.

Deirmendjian, L., Abril, G., 2018. Carbon dioxide degassing at the groundwater–stream–atmosphere interface: isotopic equilibration and hydrological mass balance in a sandy watershed. J. Hydrol. 558, 129–143. https://doi.org/10.1016/j.jhydrol.2018.01.003.

Del Giorgio, P.A., Bouvier, T., 2002. Linking the physiologic and phylogenetic successions in free–living bacterial communities along an estuarine salinity gradient. Limnol. Oceanogr. 47, 471–486. https://doi.org/10.4319/lo.2002.47.2.0471.

Dickson, A.G., 1990. Thermodynamics of the dissociation of boric acid in synthetic seawater from 273.15 to 318.15 K. Deep–Seares. I Oceanogr. Res. Pap. 37, 755–766. https://doi.org/10.1016/0198–0149(90)90004–F.

Dickson, A.G., Millero, F.J., 1987. A comparison of the equilibrium constants for the dissociation of carbonic acid in seawater media. Deep–Sea Res. 34, 1733–1743. https://doi.org/10.1016/0198–0149(87)90021–5.

Dinauer, A., Mucci, A., 2017. Spatial variability in surface–water pCO_2 and gas exchange

172

in the world's largest semi–enclosed estuarine system: St. Lawrence estuary (Canada). Biogeosciences 14, 3221–3237. https://doi.org/10.5194/bg–14–3221–2017.

Eggleston, E.S., Sabine, C.L., Morel, F.M., 2010. Revelle revisited: Buffer factors that quantify the response of ocean chemistry to changes in DIC and alkalinity. Glob. Biogeochem. Cy. 24, 2010. https://doi.org/10.1029/2008GB003407. GB1002.

Finlay, J.C., Kendall, C., 2007. Stable isotope tracing of temporal and spatial variability in organic matter sources to freshwater ecosystems. In: Michener, R., Lajtha, K. (Eds.), Stable Isotopes in Ecology and Environmental Science. Blackwell Publishing, Hong Kong, pp. 283–333.

Flöder, S., Jaschinski, S., Wells, G., Burns, C.W., 2010. Dominance and compensatory growth in phytoplankton communities under salinity stress. J. Exp. Mar. Biol. Ecol. 395, 223–231. https://doi.org/10.1016/j.jembe.2010.09.006.

Frankignoulle, M., Abril, G., Borges, A., Bourge, I., Canon, C., Delille, B., Libert, E., Theate, J.M., 1998. Carbon dioxide emission from European estuaries. Science 282, 434–436. https://doi.org/10.1126/science.282.5388.434.

Frankignoulle, M., Borges, A., Biondo, R., 2001. A new design of equilibrator to monitor carbon dioxide in highly dynamic and turbid environments. Water Res. 35, 1344–1347. https://doi.org/10.1016/S0043–1354(00)00369–9.

Gattuso, J.–P., Magnan, A., Billé, R., Cheung, W.W.L., Howes, E.L., Joos, F., Allemand, D., Bopp, L., Cooley, S.R., Eakin, C.M., Hoegh–Guldberg, O., Kelly, R.P., Pörtner, H.–O., Rogers, A.D., Baxter, J.M., Laffoley, D., Osborn, D., Rankovic, A., Rochette, J., Sumaila, U.R., Treyer, S., Turley, C., 2015. Contrasting futures for ocean and society from different anthropogenic CO$_2$ emissions scenarios. Science 349 https://doi.org/10.1126/science.aac4722. aac4722.

Gazeau, F., Smith, S.V., Gentili, B., Frankignoulle, M., Gattuso, J.–P., 2004. The European coastal zone: characterization and first assessment of ecosystem metabolism. Estuar. Coast. Shelf Sci. 60, 673–694. https://doi.org/10.1016/j.ecss.2004.03.007.

Gran, G., 1952. Determination of the equivalence point in potentiometric titrations–part II. Analyst 77, 661–671.

Guérin, F., Abril, G., Serça, D., Delon, C., Richard, S., Delmas, R., Tremblay, A., Varfalvy, L., 2007. Gas transfer velocities of CO$_2$ and CH$_4$ in a tropical reservoir and its river downstream. J. Mar. Syst. 66, 161–172. https://doi.org/10.1016/j.jmarsys.2006.03.019.

Hu, X., Cai, W.–J., 2011. An assessment of ocean margin anaerobic processes on oceanic alkalinity budget. Global Biogeochem. Cy. 25, GB3003. https://doi.org/10.1029/2010GB003859.

Hu, X., Cai, W.–J., 2013. Estuarine acidification and minimum buffer zone—A conceptual study. Geophys. Res. Lett. 40, 5176–5181. https://doi.org/10.1002/grl.51000.

IBGE, 2018. Instituto Brasileiro de Geografia e Estatistica. https://cidades.ibge.gov.br/brasil/rj/panorama/ (Accessed December 13, 2018).

IPCC, 2013. Climate change 2013: the physical science basis. In: Stocker (Ed.), Contribution of Working Group I to the Fifth Assessment Report of the Intergovernmental Panel on Climate Change. Cambridge Univ. Press, Cambridge. https://doi.org/10.1017/CBO9781107415324.

Ito, R.G., Scheider, B., Thomas, H., 2005. Distribution of surface fCO$_2$ and air–sea fluxes in the southwestern subtropical Atlantic and adjacent continental shelf. J. Mar. Syst. 56, 227–242. https://doi.org/10.1016/j.jmarsys.2005.02.005.

Jähne, B., Munnich, K.O., Bosinger, R., Dutzi, A., Huber, W., Libner, P., 1987. On para–meters influencing air–water exchange. J. Geophys. Res. 92, 1937–1949. https://doi.org/10.1029/JC092iC02p01937.

Jiang, L.–Q., Cai, W.–J., Wang, Y., 2008. A comparative study of carbon dioxide degassing in river–and marine–dominated estuaries. Limnol. Oceanogr. 53, 2603–2615. https://doi.org/10.4319/lo.2008.53.6.2603.

Joesoef, A., Huang, W.–J., Gao, Y., Cai, W.–J., 2015. Air–water fluxes and sources of carbon dioxide in the Delaware estuary: spatial and seasonal variability. Biogeosciences 12, 6085–6101. https://doi.org/10.5194/bg–12–6085–2015.

Joos, F., Spahni, R., 2008. Rates of change in natural and anthropogenic radiative forcing over the past 20,000 years. Proc. Natl. Acad. Sci. 105, 1425–1430. https://doi.org/10.1073/pnas.0707386105.

Kendall, C., Doctor, D.H., Holland, H.D., Turekian, K.K., 2004. Stable isotope applications in hydrologic studies. Surf. Gr. Water Weather. Soils 5, 319–364. https://doi.org/10.1016/B0–08–043751–6/05081–7.

Knoppers, B.A., Ekau, W., Figueiredo, A.G., 1999. The coast and shelf of east and Northeast Brazil and material transport. Geo–Mar. Lett. 19, 171–178. https://doi.org/10.1007/s003670050106.

Koné, Y.J.M., Borges, A.V., 2008. Dissolved inorganic carbon dynamics in the waters surrounding forested mangroves of the Ca Mau Province (Vietnam). Estuar. Coast. Shelf Sci. 77, 409–421. https://doi.org/10.1016/j.ecss.2007.10.001.

Koné, Y.J.M., Abril, G., Kouadio, K.N., Delille, B., Borges, A.V., 2008. Seasonal variability of carbon dioxide in the Rivers and lagoons of Ivory Coast (West Africa). Estuar. Coasts 32, 246–260. https://doi.org/10.1007/s12237–008–9121–0.

Körtzinger, A., 2003. A significant sink of CO$_2$ in the tropical Atlantic Ocean associated with the Amazon River plume. Geophys. Res. Lett. 30, 2287. https://doi.org/10.1029/2003GL018841.

Kristensen, E., Flindt, M.R., Ulomi, S., Borges, A.V., Abril, G., Bouillon, S., 2008. Emission of CO$_2$ and CH$_4$ to the atmosphere by sediments and open waters in two Tanzanian mangrove forests. Mar. Ecol. Prog. Ser. 370, 53–67. https://doi.org/10.3354/meps07642.

Kubo, A., Maeda, Y., Kanda, J., 2017. A significant net sink for CO$_2$ in Tokyo Bay. Sci. Rep. 7, 44355. https://doi.org/10.1038/srep44355.

Lancelot, C., Muylaert, K., 2011. Trends in estuarine phytoplankton ecology. In: McLusky, D.S., Wolanski, E. (Eds.), Treatise on Estuarine and Coastal Science. Academic Press, Amsterdam, pp. 5–15.

Laruelle, G.G., Dürr, H.H., Lauerwald, R., Hartmann, J., Slomp, C.P., Goossens, N., Regnier, P., 2013. Global multi–scale segmentation of continental and coastal waters from the watersheds to the continental margins. Hydrol. Earth Syst. Sci. 17,

2029–2051. https://doi.org/10.5194/hess–17–2029–2013.

Le Quéré, C., Andrew, R.M., Friedlingstein, P., Sitch, S., Hauck, J., Pongratz, J., Pickers, P.A., Korsbakken, J.I., Peters, G.P., Canadell, J.G., Arneth, A., Arora, V.K., Barbero, L., Bastos, A., Bopp, L., Chevallier, F., Chini, L.P., Ciais, P., Doney, S.C., Gkritzalis, T., Goll, D.S., Harris, I., Haverd, V., Hoffman, F.M., Hoppema, M., Houghton, R.A., Hurtt, G., Ilyina, T., Jain, A.K., Johannessen, T., Jones, C.D., Kato, E., Keeling, R.F., Goldewijk, K.K., Landschützer, P., Lefèvre, N., Lienert, S., Liu, Z., Lombardozzi, D., Metzl, N., Munro, D.R., Nabel, J.E.M.S., Nakaoka, S.–I., Neill, C., Olsen, A., Ono, T., Patra, P., Peregon, A., Peters, W., Peylin, P., Pfeil, B., Pierrot, D., Poulter, B., Rehder, G., Resplandy, L., Robertson, E., Rocher, M., Rödenbeck, C., Schuster, U., Schwinger, J., Séférian, R., Skjelvan, I., Steinhoff, T., Sutton, A., Tans, P.P., Tian, H., Tilbrook, B., Tubiello, F.N., van der Laan–Luijkx, I.T., van der Werf, G.R., Viovy, N., Walker, A.P., Wiltshire, A.J., Wright, R., Zaehle, S., Zheng, B., 2018. Global carbon budget 2018. Earth Syst. Sci. Data 10, 2141–2194. https://doi.org/10.5194/essd–10–2141–2018.

Lee, K., Kim, T.W., Byrne, R.H., Millero, F.J., Feely, R.A., Liu, Y.M., 2010. The universal ratio of boron to chlorinity for the North Pacific and North Atlantic oceans. Geochim. Cosmochim. Acta 74, 1801–1811. https://doi.org/10.1016/j.gca.2009.12.027.

Lefèvre, N., Montes, M.F., Gaspar, F.L., Rocha, C., Jiang, S., Araujo, M., Ibanhez, S., 2017. Net heterotrophy in the Amazon continental shelf changes rapidly to a sink of CO$_2$ in the outer Amazon plume. Front. Mar. Sci. 4, 1–16. https://doi.org/10.3389/fmars.2017.00278.

Linto, N., Barnes, J., Ramachandran, R., Divia, J., Ramachandran, P., Upstill–Goddard, R.C., 2014. Carbon dioxide and methane emissions from mangrove–associated waters of the Andaman Islands, bay of Bengal. Estuar. Coasts 37, 381–398. https://doi.org/10.1007/s12237–013–9674–4.

Lucas, L.V., Thompson, J.K., Brown, L.R., 2009. Why are diverse relationships observed between phytoplankton biomass and transport time? Limnol. Oceanogr. 54, 381–390. https://doi.org/10.4319/lo.2009.54.1.0381.

Ludwig, W., Amiotte–Suchet, P., Munhoven, G., Probst, J.–L., 1998. Atmospheric CO$_2$ consumption by continental erosion: present–day controls and implications for the last glacial maximum global planet. Change 17, 107–120. https://doi.org/10.1016/S0921–8181(98)00016–2.

Maher, D.T., Eyre, B.D., 2012. Carbon budgets for three autotrophic Australian estuaries: implications for global estimates of the coastal air–water CO$_2$ flux. Global Biogeochem. Cy. 26, GB1032. https://doi.org/10.1029/2011GB004075.

Maher, D.T., Santos, I.R., Golsby–Smith, L., Gleeson, J., Eyre, B.D., 2013. Groundwater–derived dissolved inorganic and organic carbon exports from a mangrove tidal creek: the missing mangrove carbon sink? Limnol. Oceanogr. 58, 475–488. https://doi.org/10.4319/lo.2013.58.2.0475.

Maher, D.T., Cowley, K., Santos, I.R., Macklin, P., Eyre, B.D., 2015. Methane and carbon dioxide dynamics in a subtropical estuary over a diel cycle: insights from automated in situ radioactive and stable isotope measurements. Mar. Chem. 168, 69–79. https://doi.org/10.1016/j.marchem.2014.10.017.

Maher, D.T., Sippo, J., Tait, D., Holloway, C., Santos, I.R., 2016. Pristine mangrove creek waters are a sink of nitrous oxide. Sci. Rep. 6, 25701. https://doi.org/10.1038/srep25701.

Marques, J.S.J., Dittmar, T., Niggemann, J., Almeida, M.G., Gomez–Saez, G.V., Rezende, C.E., 2017. Dissolved black carbon in the Headwaters–To–Ocean continuum of Paraíba Do Sul River, Brazil. Front. Earth Sci. 5, 1–12. https://doi.org/10.3389/feart.2017.00011.

Mehrbach, C., Cuberson, C.H., Hawley, J.E., Pytkowicz, R.M., 1973. Measurements of the apparent dissociation constants of carbonic acid in seawater at atmospheric pressure. Limnol. Oceanogr. 18, 897–907. https://doi.org/10.4319/lo.1973.18.6.0897.

Miyajima, T., Miyajima, Y., Hanba, Y.T., Yoshii, K., Koitabashi, T., Wada, E., 1995. Determining the stable isotope ratio of total dissolved inorganic carbon in lake water by GC/C/IIRMS. Limnol. Oceanogr. 40, 994–1000. https://doi.org/10.4319/lo.1995.40.5.0994.

Miyajima, T., Tsuboi, Y., Tanaka, Y., Koike, I., 2009. Export of inorganic carbon from two southeast Asian mangrove forests to adjacent estuaries as estimated by the stable isotope composition of dissolved inorganic carbon. J. Geophys. Res. Biogeosci. 114, 1–12. https://doi.org/10.1029/2008JG000861.

Mook, W.G., Koene, B.K., 1975. Chemistry of dissolved inorganic carbon in estuarine and coastal brackish waters. Estuar. Coast. Mar. Sci. 3, 325–336.

Mook, W.G., Tan, F.C., 1991. Stable carbon isotopes in rivers and estuaries. In: Degens, E.T., Kempe, S., Richey, J.E. (Eds.), Biogeochemistry of Major World Rivers. John Wiley and Sons, Chichester, pp. 245–264.

Moore–Maley, B., Ianson, D., Allen, S.E., 2018. The sensitivity of estuarine aragonite sa–turation state and pH to the carbonate chemistry of a freshet–dominated river. Biogeosciences 15, 3743–3760. https://doi.org/10.5194/bg–15–3743–2018.

NOAA, 2019. National Oceanic and Atmospheric Administration. Earth System Research Laboratory. Global Monitoring Division. https://www.esrl.noaa.gov/gmd/ccgg/trends/graph.html (Accessed 24 July 2019).

Orr, J.C., Epitalon, J.–M., Dickson, A.G., Gattuso, J.–P., 2018. Routine uncertainty pro–pagation for the marine carbon dioxide system. Mar. Chem. 207, 84–107. https://doi.org/10.1016/j.marchem.2018.10.006.

Ovalle, A.R.C., Silva, C.F., Rezende, C.E., Gatts, C.E.N., Suzuki, M.S., Figueiredo, R.O., 2013. Long–term trends in hydrochemistry in the Paraíba do Sul River, southeastern Brazil. J. Hydrol. 481, 191–203. https://doi.org/10.1016/j.jhydrol.2012.12.036.

Raymond, P.A., Cole, J.J., 2001. Gas exchange in Rivers and estuaries: choosing a gas transfer velocity. Estuaries 24, 312–317. https://doi.org/10.2307/1352954.

Revelle, R., Suess, H.E., 1957. Carbon dioxide exchange between atmosphere and ocean and the question of an increase of atmospheric CO2 during the past decades. Tellus 9, 18–27.

Robbins, L.L., Hansen, M.E., Kleypas, J.A., Meylan, S.C., 2010. CO$_2$ Calc: a user–friendly seawater carbon calculator for Windows, Max OS X, and iOS (iPhone), U.S. Geological Survey Open–File Report, 2010–1280, 1–17. http://pubs.usgs.gov/of/

2010/1280/ (accessed 07 November 2018).

Rosentreter, J.A., Maher, D.T., Erler, D.V., Murray, R., Eyre, B.D., 2018. Seasonal and temporal CO_2 dynamics in three tropical mangrove creeks – a revision of global mangrove CO_2 emissions. Geochim. Cosmochim. Acta 222, 729–745. https://doi.org/10.1016/j.gca.2017.11.026.

Roubeix, V., Rousseau, V., Lancelot, C., 2008. Diatom succession and silicon removal from freshwater in estuarine mixing zones: from experiment to modelling. Estuar. Coast. Shelf Sci. 78, 14–26.

Rudorff, N.M., Kampel, M., Rezende, C.E., 2011. Spectral mapping of the Paraíba do Sul River plume (Brazil) using multitemporal Landsat images. J. Appl. Remote. Sens. 5 https://doi.org/10.1117/1.3630220. 053550–053550–19.

Salisbury, J.E., 2008. Coastal acidification by Rivers: a threat to shellfish? Eos 89, 513–528. https://doi.org/10.1029/2008EO500001.

Salisbury, J.E., Vandemark, D., Hunt, C.W., Campbell, J.W., McGillis, W.R., McDowell, W.H., 2008. Seasonal observations of surface waters in two gulf of Maine estuary–plume systems: relationships between watershed attributes, optical measurements and surface pCO_2. Estuar. Coast. Shelf Sci. 77, 245–252. https://doi.org/10.1016/j.ecss.2007.09.033.

Samanta, S., Dalai, T.K., Pattanaik, J.K., Rai, S.K., Mazumdar, A., 2015. Dissolved inorganic carbon (DIC) and its ^{13}C in the ganga (Hooghly) river estuary, India: Evidence of DIC generation via organic carbon degradation and carbonate dissolution. Geochim. Cosmochim. Acta 165, 226–248. https://doi.org/10.1016/j.gca.2015.05.040.

Santos, I.R., Maher, D.T., Larkin, R., Webb, J., Sanders, C.J., 2018. Carbon outwelling and outgassing vs. burial in an estuarine tidal creek surrounded by mangrove and salt-marsh wetlands. Limnol. Oceangr. 64, 996–1013. https://doi.org/10.1002/lno.11090.

Silvennoinen, H., Liikanen, A., Rintala, J., Martikainen, P.J., 2008. Greenhouse gas fluxes from the eutrophic Temmesjoki River and its estuary in the Liminganlahti Bay (the Baltic Sea). Biogeochemistry 90, 193–208. https://doi.org/10.1007/s10533-008-9244-1.

Sippo, J.Z., Maher, D.T., Tait, D.R., Holloway, C., Santos, I.R., 2016. Are mangroves drivers or buffers of coastal acidification? Insights from alkalinity and dissolved inorganic carbon export estimates across a latitudinal transect. Global Biogeochem. Cy. 30, 753–766. https://doi.org/10.1002/2015GB005324.

Souza, T.A., Godoy, J.M., Godoy, M.L.D.P., Moreira, I., Carvalho, Z.L., Salomão, M.S.M.B., Rezende, C.E., 2010. Use of multitracers for the study of water mixing in the Paraíba do Sul River estuary. J. Environ. Radioact. 101, 564–570. https://doi.org/10.1016/j.jenvrad.2009.11.001.

Sterza, J.M., Fernandes, L.L., 2006. Distribution and abundance of cladocera (brachiopoda) in the Paraíba do Sul River estuary, Rio de Janeiro, Brazil. Braz. J. Oceanogr.

54, 193–204. https://doi.org/10.1590/S1679-87592006000300003.

Strayer, D.L., Pace, M.L., Caraco, N.F., Cole, J.J., Findlay, S., 2008. Hydrology and grazing jointly control a large-river food web. Ecology 89, 12–18. https://doi.org/10.1890/07-0979.1.

Strickland, J.D.H., Parsons, T.R., 1972. A Practical Handbook of Seawater Analysis. Fisheries Research Board of Canada Bulletin, Ottawa.

Takahashi, T., Sutherland, S.C., Sweeney, C., Poisson, A., Metzl, N., Tilbrook, B., Bates, N., Wanninkhof, R., Feely, R.A., Sabine, C., Olafsson, J., Nojiri, Y., 2002. Global sea-air CO_2 flux based on climatological surface ocean pCO_2, and seasonal biological and temperature effects. Deep-Sea Res. II Top. Stud. Oceanogr. 49, 1601–1622. https://doi.org/10.1016/S0967-0645(02)00003-6).

Takahashi, T., Sutherland, S.C., Kozyr, A., 2012. Global ocean surface water partial pressure of CO_2 database: Measurements performed during 1957–2011 (Version 2011). In: Oak Ridge, Tennessee, https://doi.org/10.3334/CDIAC/OTG.NDP088(V2013.

Ternon, J.F., Oudot, C., Dessier, A., Diverrès, D., 2000. A seasonal tropical sink for atmospheric CO_2 in the Atlantic Ocean: the role of the Amazon River discharge. Mar. Chem. 68, 183–201. https://doi.org/10.1016/S0304-4203(99)00077-8.

Van Dam, B.R., Crosswell, J.R., Anderson, I.C., Paerl, H.W., 2018a. Watershed-scale drivers of air-water CO_2 exchange in two lagoonal North Carolina (USA) estuaries. J. Geophys. Res. Biogeosci. 123, 1–17. https://doi.org/10.1002/2017JG004243.

Van Dam, B.R., Tobias, C., Holbach, A., Paerl, H.W., Zhu, G., 2018b. CO_2 limited conditions favor cyanobacteria in a hypereutrophic lake: an empirical and theoretical stable isotope study. Limnol. Oceanogr. 63, 1643–1659. https://doi.org/10.1002/lno.10798.

Wanninkhof, R., 1992. Relationship between wind speed and gas exchange. J. Geophys. Res. 97, 7373–7382. https://doi.org/10.1029/92JC00188.

Wanninkhof, R., 2014. Relationship between wind speed and gas exchange over the ocean revisited. Limnol. Oceanogr. Methods 12, 351–362. https://doi.org/10.4319/lom.2014.12.351.

Weiss, R.F., 1974. Carbon dioxide in water and seawater: the solubility of a non-ideal gas. Mar. Chem. 2, 203–215. https://doi.org/10.1016/0304-4203(74)90015-2.

Whitfield, M., Turner, D.R., 1986. The carbon dioxide system in estuaries – an inorganic perspective. Sci. Total Environ. 49, 235–255. https://doi.org/10.1016/0048-9697(86)90243-3.

Willeit, M., Ganopolski, A., Calov, R., Brovkin, V., 2019. Mid-Pleistocene transition in glacial cycles explained by declining CO_2 and regolith removal. Sci. Adv. 5, 1–9. https://doi.org/10.1126/sciadv.aav7337.

Zhai, W., Dai, M., Guo, X., 2007. Carbonate system and CO_2 degassing fluxes in the inner estuary of Changjiang (Yangtze) river, China. Mar. Chem. 107, 342–356. https://doi.org/10.1016/j.marchem.2007.02.011.

174

RÉFÉRENCES BIBLIOGRAPHIQUES

Abril, G., Borges, A. V., 2019. Ideas and perspectives: Carbon leaks from flooded land: do we need to replumb the inland water active pipe? Biogeosciences 16, 769–784. https://doi.org/10.5194/bg-16-769-2019

Abril, G., Bouillon, S., Darchambeau, F., Teodoru, C.R., Marwick, T.R., Tamooh, F., Ochieng Omengo, F., Geeraert, N., Deirmendjian, L., Polsenaere, P., Borges, A. V., 2015. Technical note: Large overestimation of pCO2 calculated from pH and alkalinity in acidic, organic-rich freshwaters. Biogeosciences 12, 67–78. https://doi.org/10.5194/bg-12-67-2015

Aguiar Jr., T.R., Rasera, K., Parron, L.M., Brito, A.G., Ferreira, M.T., 2015. Nutrient removal effectiveness by riparian buffer zones in rural temperate watersheds: The impact of no-till crops practices. Agric. Water Manag. 149, 74–80. https://doi.org/10.1016/j.agwat.2014.10.031

Anbumozhi, V., Radhakrishnan, J., Yamaji, E., 2005. Impact of riparian buffer zones on water quality and associated management considerations. Ecol. Eng. 24, 517–523. https://doi.org/10.1016/j.ecoleng.2004.01.007

Assante, M., Candela, L., Castelli, D., Tani, A., 2016. Are Scientific Data Repositories Coping with Research Data Publishing? Data Sci. J. 15, 1–24. https://doi.org/10.5334/dsj-2016-006

Baillieux, A., Campisi, D., Jammet, N., Bucher, S., Hunkeler, D., 2014. Regional water quality patterns in an alluvial aquifer: Direct and indirect influences of rivers. J. Contam. Hydrol. 169, 123–131. https://doi.org/10.1016/j.jconhyd.2014.09.002

Baker, J.L., Mickelson, S.K., 1994. Application Technology and Best Management Practices for Minimizing Herbicide Runoff. Weed Technol. 8, 862–869.

Baskaran, S., Ransley, T., Brodie, R.S., Baker, P., 2009. Investigating groundwater-river interactions using environmental tracers. Aust. J. Earth Sci. 56, 13–19. https://doi.org/10.1080/08120090802541887

Battin, T.J., Kaplan, L.A., Findlay, S., Hopkinson, C.S., Marti, E., Packman, A.I., Newbold, J.D., Sabater, F., 2008. Biophysical controls on organic carbon fluxes in fluvial networks. Nat. Geosci. 1, 95–100. https://doi.org/10.1038/ngeo101

Baudron, P., Cockenpot, S., Lopez-Castejon, F., Radakovitch, O., Gilabert, J., Mayer, A., Garcia-Arostegui, J.L., Martinez-Vicente, D., Leduc, C., Claude, C., 2015. Combining radon, short-lived radium isotopes and hydrodynamic modeling to assess submarine groundwater discharge from an anthropized semiarid watershed to a Mediterranean lagoon (Mar Menor, SE Spain). J. Hydrol. 525, 55–71. https://doi.org/10.1016/j.jhydrol.2015.03.015

Bayani Cardenas, M., 2008. The effect of river bend morphology on flow and timescales of surface water-groundwater exchange across pointbars. J. Hydrol. 362, 134–141. https://doi.org/10.1016/j.jhydrol.2008.08.018

Bencala, K.E., Gooseff, M.N., Kimball, B.A., 2011. Rethinking hyporheic flow and transient storage to advance understanding of stream-catchment connections. Water Resour. Res. 47, 1–9. https://doi.org/10.1029/2010WR010066

Bencala, K.E., McKnight, D.M., Zellweger, G.W., 1990. Characterization of transport in an acidic and metal-rich mountain stream based on a lithium tracer injection and simulations of transient storage. Water Resour. Res. 26, 989–1000. https://doi.org/10.1029/WR026i005p00989

Biehler, A., Chaillou, G., Buffin-Bélanger, T., Baudron, P., 2020. Hydrological connectivity in the aquifer–river continuum: Impact of river stages on the geochemistry of groundwater floodplains. J. Hydrol. 590, 125379. https://doi.org/10.1016/j.jhydrol.2020.125379

Biron, P., Buffin-bélanger, T., Larocque, M., Demers, S., Olsen, T., Ouellet, M.-A., Choné, G., Cloutier, C., Needelman, M., 2013. Espace de liberté : un cadre de gestion intégrée pour la conservation des cours d'eau dans un contexte de changements climatiques.

Biron, P.M., Buffin-Bélanger, T., Larocque, M., Choné, G., Cloutier, C.A., Ouellet, M.A., Demers, S., Olsen, T., Desjarlais, C., Eyquem, J., 2014. Freedom space for rivers: a sustainable management approach to enhance river resilience. Environ. Manage. 54, 1056–1073. https://doi.org/10.1007/s00267-014-0366-z

Bohlke, J.K., Denver, J.M., 1995. Combined use of groundwater dating, chemical, and isotopic analyses to resolve the history and fate of nitrate contamination in two agricultural watersheds, atlantic coastal Plain, Maryland. Water Resour. Res. 31, 2319–2339. https://doi.org/10.1029/95WR01584

Boulton, A.J., Findlay, S., Marmonier, P., Stanley, E.H., Valett, H.M., 1998. The functional significance of the hyporheic zone in streams and rivers. Annu. Rev. Ecol. Syst. 29, 59–81. https://doi.org/10.1146/annurev.ecolsys.29.1.59

Broder, T., Biester, H., 2017. Linking major and trace element concentrations in a headwater stream to DOC release and hydrologic conditions in a bog and peaty riparian zone. Appl.

Geochemistry 87, 188–201. https://doi.org/10.1016/j.apgeochem.2017.11.003

Brunke, M., Gonser, T., 1997. The ecological significance of exchange processes between rivers and groundwater. Freshw. Biol. 37, 1–33. https://doi.org/10.1046/j.1365-2427.1997.00143.x

Brunner, P., Therrien, R., Renard, P., Simmons, C.T., Franssen, H.-J.H., 2017. Advances in understanding river-groundwater interactions. Rev. Geophys. 55, 818–854. https://doi.org/10.1002/2017RG000556

Buffin-Bélanger, T., Biron, P., Larocque, M., Demers, S., Olsen, T., Choné, G., Ouellet, M.-A., Cloutier, C.-A., Desjarlais, C., Eyquem, J., 2015a. Freedom space for rivers: An economically viable river management concept in a changing climate. Geomorphology 251, 137–148. https://doi.org/10.1016/j.geomorph.2015.05.013

Buffin-Bélanger, T., Chaillou, G., Cloutier, C.-A., Touchette, M., Roy, M.-A., Hétu, B., Lewis, N., 2015b. Programme d'acquisition de connaissances sur les eaux souterraines du nord-est du Bas-Saint-Laurent (PACES-NEBSL) : Rapport final. Rimouski.

Buffin-Bélanger, T., Cloutier, C.A., Tremblay, C., Chaillou, G., Larocque, M., 2015c. Dynamics of groundwater floodwaves and groundwater flood events in an alluvial aquifer. Can. Water Resour. J. 41, 469–483. https://doi.org/10.1080/07011784.2015.1102651

Burnett, W.C., Dulaiova, H., 2003. Estimating the dynamics of groundwater input into the coastal zone via continuous radon-222 measurements. J. Environ. Radioact. 69, 21–35. https://doi.org/10.1016/S0265-931X(03)00084-5

Burnett, W.C., Kim, G., Lane-Smith, D., 2001. A continuous monitor for assessment of 222Rn in the coastal ocean. J. Radioanal. Nucl. Chemestry 249, 167–172. https://doi.org/10.1023/A:1013217821419

Burnett, W.C., Peterson, R.N., Santos, I.R., Hicks, R.W., 2010. Use of automated radon measurements for rapid assessment of groundwater flow into Florida streams. J. Hydrol. 380, 298–304. https://doi.org/10.1016/j.jhydrol.2009.11.005

Butman, D., Raymond, P. a., 2011. Significant efflux of carbon dioxide from streams and rivers in the United States. Nat. Geosci. 4, 839–842. https://doi.org/10.1038/ngeo1294

Calver, A., 2001. Riverbed Permeabilities: Information from Pooled Data. Ground Water 39, 546–553. https://doi.org/10.1111/j.1745-6584.2001.tb02343.x

Campeau, A., del Giorgio, P.A., 2014. Patterns in CH4 and CO2 concentrations across boreal rivers: Major drivers and implications for fluvial greenhouse emissions under climate change scenarios. Glob. Chang. Biol. 20, 1075–1088.

https://doi.org/10.1111/gcb.12479

Campeau, A., Lapierre, J.-F., Vachon, D., del Giorgio, P.A., 2014. Regional contribution of CO2 and CH4 fluxes from the fluvial network in a lowland boreal landscape of Québec. Global Biogeochem. Cycles 28, 57–69. https://doi.org/10.1002/2013GB004685

Candela, L., Castelli, D., Manghi, P., Tani, A., 2015. Data journals: A survey. J. Assoc. Inf. Sci. Technol. 66, 1747–1762. https://doi.org/10.1002/asi.23358

Cartwright, I., Hofmann, H., Gilfedder, B., Smyth, B., 2014. Understanding parafluvial exchange and degassing to better quantify groundwater inflows using 222Rn: The King River, southeast Australia. Chem. Geol. 380, 48–60. https://doi.org/10.1016/j.chemgeo.2014.04.009

Cecil, L.D., Green, J.R., 2000. Radon-222, in: Cook, P.G., Herczeg, A.L. (Eds.), Environmental Tracers in Subsurface Hydrology. Springer, Boston, MA, pp. 175–194. https://doi.org/10.1007/978-1-4615-4557-6_6

Centre d'expertise hydrique du Québec, 2022. Débit à la station 021601 - Matane [WWW Document]. Ministère l'Environnement la Lutte contre les Chang. Clim. URL http://www.cehq.gouv.qc.ca/suivihydro/tableau.asp?NoStation=021601&Zone=&Secteur= (accessed 6.5.22).

Chah, B., Zikovsky, L., 1990. Nouvelle méthode de dosage du radon dans l'eau par scintillation dans l'ortho-xylène. Rev. des Sci. l'eau 3, 343. https://doi.org/10.7202/705079ar

Chaillou, G., Lemay-Borduas, F., Couturier, M., 2016. Transport and transformations of groundwater-borne carbon discharging through a sandy beach to a coastal ocean. Can. Water Resour. J. / Rev. Can. des ressources hydriques 41, 455–468. https://doi.org/10.1080/07011784.2015.1111775

Chaillou, G., Lemay-Borduas, F., Larocque, M., Couturier, M., Biehler, A., Tommi-Morin, G., 2018. Flow and discharge of groundwater from a snowmelt-affected sandy beach. J. Hydrol. 557, 4–15. https://doi.org/10.1016/j.jhydrol.2017.12.010

Chaillou, G., Touchette, M., Buffin-Bélanger, T., Cloutier, C.-A., Hétu, B., Roy, M.-A., 2017. Hydrogeochemical evolution and groundwater mineralization of shallow aquifers in the Bas-Saint-Laurent region, Québec, Canada. Can. Water Resour. J. / Rev. Can. des ressources hydriques 43, 136–151. https://doi.org/10.1080/07011784.2017.1387817

Chapman, A., Simperl, E., Koesten, L., Konstantinidis, G., Ibáñez, L.-D., Kacprzak, E., Groth, P., 2020. Dataset search: a survey. VLDB J. 29, 251–272. https://doi.org/10.1007/s00778-019-00564-x

Clark, J.F., Schlosser, P., Stute, M., Simpson, H.J., 1996. SF6 − 3He Tracer Release Experiment: A New Method of Determining Longitudinal Dispersion Coefficients in Large Rivers. Environ. Sci. Technol. 30, 1527–1532. https://doi.org/10.1021/es9504606

Clausen, J.C., Guillard, K., Sigmund, C.M., Martin Dors, K., 2000. Water quality changes from riparian buffer restoration in Connecticut. J. Environ. Qual. 29, 1751–1761. https://doi.org/10.2134/jeq2000.00472425002900060004x

Cloutier, C., 2013. Analyse à haute résolution spatiale et temporelle de la connectivité entre la rivière matane et son aquifère alluvial lors d'événements de crue. Université du Québec à Rimouski, Master's Thesis.

Cloutier, C.A., Buffin-Bélanger, T., Larocque, M., 2014. Controls of groundwater floodwave propagation in a gravelly floodplain. J. Hydrol. 511, 423–431. https://doi.org/10.1016/j.jhydrol.2014.02.014

Cole, J.J., Caraco, N.F., 2001. Carbon in catchments: connecting terrestrial carbon losses with aquatic metabolism. Mar. Freshw. Res. 52, 101. https://doi.org/10.1071/MF00084

Cole, J.J., Prairie, Y.T., Caraco, N.F., McDowell, W.H., Tranvik, L.J., Striegl, R.G., Duarte, C.M., Kortelainen, P., Downing, J.A., Middelburg, J.J., Melack, J., 2007. Plumbing the global carbon cycle: Integrating inland waters into the terrestrial carbon budget. Ecosystems 10, 171–184. https://doi.org/10.1007/s10021-006-9013-8

Constantz, J., Cox, M.H., Su, G.W., 2003. Comparison of Heat and Bromide as Ground Water Tracers Near Streams. Ground Water 41, 647–656. https://doi.org/10.1111/j.1745-6584.2003.tb02403.x

Cook, P.G., 2015. Quantifying river gain and loss at regional scales. J. Hydrol. 531, 749–758. https://doi.org/10.1016/j.jhydrol.2015.10.052

Cook, P.G., Favreau, G., Dighton, J.C., Tickell, S., 2003. Determining natural groundwater influx to a tropical river using radon, chlorofluorocarbons and ionic environmental tracers. J. Hydrol. 277, 74–88. https://doi.org/10.1016/S0022-1694(03)00087-8

Cook, P.G., Lamontagne, S., Berhane, D., Clark, J.F., 2006. Quantifying groundwater discharge to Cockburn River, southeastern Australia, using dissolved gas tracers 222Rn and SF6. Water Resour. Res. 42, 1–12. https://doi.org/10.1029/2006WR004921

Cook, P.G., Wood, C., White, T., Simmons, C.T., Fass, T., Brunner, P., 2008. Groundwater inflow to a shallow, poorly-mixed wetland estimated from a mass balance of radon. J. Hydrol. 354, 213–226. https://doi.org/10.1016/j.jhydrol.2008.03.016

COPDESS, 2018. Commitment Statement in the earth, space, and environmental sciences [WWW Document]. Earth Sciece Inf. Partn. URL https://copdess.org/enabling-fair-

data-project/commitment-statement-in-the-earth-space-and-environmental-sciences/ (accessed 5.25.22).

CoreTrustSeal Standards and Certification Board, 2019. CoreTrustSeal Requirements Core Trustworthy Data Repositories Requirements 2020 – 2022. Zenodo. https://doi.org/doi.org/10.5281/zenodo.3638211

Correll, D.L., Jordan, T.E., Weller, D.E., 1997. Failure of agricultural riparian buffers to protect surface waters from groundwater nitrate contamination., in: J. Gibert and others (Ed.), Groundwater/Surface Water Ecotones: Biological and Hydrological Interactions and Management Options. Cambridge University Press, Cambridge, UK, pp. 162–165.

Cotovicz, L.C., Vidal, L.O., de Rezende, C.E., Bernardes, M.C., Knoppers, B.A., Sobrinho, R.L., Cardoso, R.P., Muniz, M., dos Anjos, R.M., Biehler, A., Abril, G., 2020. Carbon dioxide sources and sinks in the delta of the Paraíba do Sul River (Southeastern Brazil) modulated by carbonate thermodynamics, gas exchange and ecosystem metabolism during estuarine mixing. Mar. Chem. 226, 103869. https://doi.org/10.1016/j.marchem.2020.103869

Crawford, J.T., Lottig, N.R., Stanley, E.H., Walker, J.F., Hanson, P.C., Finlay, J.C., Striegl, R.G., 2014. CO2 and CH4 emissions from streams in a lake-rich landscape: Patterns, controls, and regional significance. Global Biogeochem. Cycles 28, 197–210. https://doi.org/10.1002/2013GB004661

Daniel, J.A., Staricka, J.A., 2000. Frozen soil impact on ground water - surface water interaction. J. Am. Water Resour. Assoc. 36, 151–160. https://doi.org/10.1111/j.1752-1688.2000.tb04256.x

Deirmendjian, L., Abril, G., 2018. Carbon dioxide degassing at the groundwater-stream-atmosphere interface: isotopic equilibration and hydrological mass balance in a sandy watershed. J. Hydrol. 558, 129–143. https://doi.org/10.1016/j.jhydrol.2018.01.003

Diepenbroek, M., Grobe, H., Reinke, M., Schlitzer, R., Sieger, R., 1999. Data Management of Proxy Parameters with PANGAEA, in: Use of Proxies in Paleoceanography. Springer Berlin Heidelberg, Berlin, Heidelberg, pp. 715–727. https://doi.org/10.1007/978-3-642-58646-0_29

Diepenbroek, M., Schindler, U., Huber, R., Pesant, S., Stocker, M., Felden, J., Buss, M., Weinrebe, M., 2017. Terminology supported archiving and publication of environmental science data in PANGAEA. J. Biotechnol. 261, 177–186. https://doi.org/10.1016/j.jbiotec.2017.07.016

Digital Science, Simons, N., Goodey, G., Hardeman, M., Clare, C.; Gonzales, S., Strange, D., Smith, G., Kipnis, D., Lida, K., Miyairi, N., Tshetsha, V., Ramokgola, M., Makhera, P., Barbour, G., 2021. The State of Open Data 2021.

https://doi.org/10.6084/m9.figshare.17061347.v1

Dionne, J., Coll, D., 1995. Le niveau marin relatif dans la région de Matane (Québec), de la déglaciation à nos jours. Géographie Phys. Quat. 49, 363–380. https://doi.org/10.7202/033060ar

Downs, R.R., 2021. Improving Opportunities for New Value of Open Data: Assessing and Certifying Research Data Repositories. Data Sci. J. 20, 1–11. https://doi.org/10.5334/dsj-2021-001

Dragon, K., Marciniak, M., Szpikowski, J., Szpikowska, G., Wawrzyniak, T., 2015. The hydrochemistry of glacial Ebba River (Petunia Bay, Central Spitsbergen): Groundwater influence on surface water chemistry. J. Hydrol. 529, 1499–1510. https://doi.org/10.1016/j.jhydrol.2015.08.031

Duarte, C.M., Prairie, Y.T., 2005. Prevalence of Heterotrophy and Atmospheric CO2 Emissions from Aquatic Ecosystems. Ecosystems 8, 862–870. https://doi.org/10.1007/s10021-005-0177-4

Dugdale, S.J., Bergeron, N.E., St-Hilaire, A., 2013. Temporal variability of thermal refuges and water temperature patterns in an Atlantic salmon river. Remote Sens. Environ. 136, 358–373. https://doi.org/10.1016/j.rse.2013.05.018

Dulaiova, H., Peterson, R., Burnett, W.C., Lane-Smith, D., 2005. A multi-detector continuous monitor for assessment of 222Rn in the coastal ocean. J. Radioanal. Nucl. Chem. 263, 361–363. https://doi.org/10.1007/s10967-005-0063-8

Duvert, C., Bossa, M., Tyler, K.J., Wynn, J.G., Munksgaard, N.C., Bird, M.I., Setterfield, S.A., Hutley, L.B., 2019. Groundwater-Derived DIC and Carbonate Buffering Enhance Fluvial CO 2 Evasion in Two Australian Tropical Rivers. J. Geophys. Res. Biogeosciences 124, 312–327. https://doi.org/10.1029/2018JG004912

Duvert, C., Butman, D.E., Marx, A., Ribolzi, O., Hutley, L.B., 2018. CO2 evasion along streams driven by groundwater inputs and geomorphic controls. Nat. Geosci. 11, 813–818. https://doi.org/10.1038/s41561-018-0245-y

Dyke, A.S., 2004. An outline of North American deglaciation with emphasis on central and northern Canada, in: Developments in Quaternary Science. pp. 373–424. https://doi.org/10.1016/S1571-0866(04)80209-4

Environnement et Changement climatique Canada, 2021. Données historiques quotidiennes enregistrées aux stations AMQUI et RIMOUSKI [WWW Document]. URL https://climat.meteo.gc.ca/historical_data/search_historic_data_f.html (accessed 10.18.21).

European Inventory of Groundwater Research, 2021. Kindra - Knowledge Inventory for hydrogeology research [WWW Document]. URL https://kindraproject.eu (accessed 10.18.21).

Exner-Kittridge, M., Strauss, P., Blöschl, G., Eder, A., Saracevic, E., Zessner, M., 2016. The seasonal dynamics of the stream sources and input flow paths of water and nitrogen of an Austrian headwater agricultural catchment. Sci. Total Environ. 542, 935–945. https://doi.org/10.1016/j.scitotenv.2015.10.151

Fischer, R.A., Martin, C.O., Fischenich, J.C., 2000. Improving Riparian Strips and Corridors for Water Quality and Wildlife, in: International Conference on Riparian Ecology and Management in Multi-Land Use Watersheds. American water resources association, pp. 1–7.

Fleckenstein, J.H., Krause, S., Hannah, D.M., Boano, F., 2010. Groundwater-surface water interactions: New methods and models to improve understanding of processes and dynamics. Adv. Water Resour. 33, 1291–1295. https://doi.org/10.1016/j.advwatres.2010.09.011

Gagnon, E., Gangbazo, G., 2007. Efficacité des bandes riveraines : analyse de la documentation scientifique et perspectives. Québec.

Garnett, A., Leahey, A., Savard, D., Towell, B., Wilson, L., 2017. Open Metadata for Research Data Discovery in Canada. J. Libr. Metadata 17, 201–217. https://doi.org/10.1080/19386389.2018.1443698

Genereux, D.P., Hemond, H.F., 1990. Naturally Occurring Radon 222 as a Tracer for Streamflow Generation: Steady State Methodology and Field Example. Water Resour. Res. 26, 3065–3075. https://doi.org/10.1029/WR026i012p03065

Gerardin, V., McKenney, D., 2001. Une classification climatique du Québec à partir de modèles de distribution spatiale de données climatiques mensuelles : vers une définition des bioclimats du Québec. Direction du patrimoine écologique et du développement durable, ministère de l'Environnement.

Gilfedder, B.S., Frei, S., Hofmann, H., Cartwright, I., 2015. Groundwater discharge to wetlands driven by storm and flood events: Quantification using continuous Radon-222 and electrical conductivity measurements and dynamic mass-balance modelling. Geochim. Cosmochim. Acta 165, 161–177. https://doi.org/10.1016/j.gca.2015.05.037

Golkowska, K., Rugani, B., Koster, D., Van Oers, C., 2016. Environmental and economic assessment of biomass sourcing from extensively cultivated buffer strips along water bodies. Environ. Sci. Policy 57, 31–39. https://doi.org/10.1016/j.envsci.2015.11.014

Gómez-Gener, L., Rocher-Ros, G., Battin, T., Cohen, M.J., Dalmagro, H.J., Dinsmore, K.J.,

Drake, T.W., Duvert, C., Enrich-Prast, A., Horgby, Å., Johnson, M.S., Kirk, L., Machado-Silva, F., Marzolf, N.S., McDowell, M.J., McDowell, W.H., Miettinen, H., Ojala, A.K., Peter, H., Pumpanen, J., Ran, L., Riveros-Iregui, D.A., Santos, I.R., Six, J., Stanley, E.H., Wallin, M.B., White, S.A., Sponseller, R.A., 2021. Global carbon dioxide efflux from rivers enhanced by high nocturnal emissions. Nat. Geosci. 14, 289–294. https://doi.org/10.1038/s41561-021-00722-3

Gonfiantini, R., 1978. Standards for stable isotope measurments in natural compounds. Nature 271, 534–536. https://doi.org/doi.org/10.1038/271534a0

Gooseff, M.N., 2010. Defining hyporheic zones - advancing our conceptual and operational definitions of where stream water and groundwater meet. Geogr. Compass 4, 945–955. https://doi.org/10.1111/j.1749-8198.2010.00364.x

Gurrieri, J.T., Furniss, G., 2004. Estimation of groundwater exchange in alpine lakes using non-steady mass-balance methods. J. Hydrol. 297, 187–208. https://doi.org/10.1016/j.jhydrol.2004.04.021

Halbedel, S., Koschorreck, M., 2013. Regulation of CO2 emissions from temperate streams and reservoirs. Biogeosciences 10, 7539–7551. https://doi.org/10.5194/bg-10-7539-2013

Hall, P.O.J., Aller, R.C., 1992. Rapid, small-volume, flow injection analysis for SCO2, and NH4+ in marine and freshwaters. Limnol. Oceanogr. 37, 1113–1119. https://doi.org/10.4319/lo.1992.37.5.1113

Hartmann, J., Lauerwald, R., Moosdorf, N., 2019. GLORICH - Global river chemistry database. PANGAEA. https://doi.org/https://doi.org/10.1594/PANGAEA.902360,

Hatch, C.E., Fisher, A.T., Revenaugh, J.S., Constantz, J., Ruehl, C., 2006. Quantifying surface water-groundwater interactions using time series analysis of streambed thermal records: Method development. Water Resour. Res. 42, 1–14. https://doi.org/10.1029/2005WR004787

Haycock, N.E., Pinay, G., 1993. Groundwater nitrate dynamics in grass and poplar vegetated riparian buffer strips during the winter. J. Environ. Qual. 22, 273–278.

Herczeg, A.L., Edmunds, W.M., 2000. Inorganic Ions as Tracers, in: Cook, P.G., Herczeg, A.L. (Eds.), Environmental Tracers in Subsurface Hydrology. Springer US, Boston, MA, pp. 31–77. https://doi.org/10.1007/978-1-4615-4557-6_2

Hill, A.R., 1996. Nitrate removal in stream riparian zones. J. Environ. Qual. 25, 743–755. https://doi.org/10.2134/jeq1996.00472425002500040014x

Hoehn, E., Von Gunten, H.R., 1989. Radon in groundwater: A tool to assess infiltration from

surface waters to aquifers. Water Resour. Res. 25, 1795–1803. https://doi.org/10.1029/WR025i008p01795

Hofmann, A.F., Soetaert, K., Meysman, F.J.R., Hagens, M., 2016. Integrated Development Toolbox for Aquatic Chemical Model Generation.

Hofmann, H., Gilfedder, B.S., Cartwright, I., 2011. A novel method using a silicone diffusion membrane for continuous 222Rn measurements for the quantification of groundwater discharge to streams and rivers. Environ. Sci. Technol. 45, 8915–8921. https://doi.org/10.1021/es202683z

Hook, D.W., Porter, S.J., Herzog, C., 2018. Dimensions: Building Context for Search and Evaluation. Front. Res. Metrics Anal. 3, 1–11. https://doi.org/10.3389/frma.2018.00023

Hope, D., Billett, M.F., Cresser, M.S., 1994. A review of the export of carbon in river water: Fluxes and processes. Environ. Pollut. 84, 301–324. https://doi.org/10.1016/0269-7491(94)90142-2

Hotchkiss, E.R., Hall Jr, R.O., Sponseller, R.A., Butman, D., Klaminder, J., Laudon, H., Rosvall, M., Karlsson, J., 2015. Sources of and processes controlling CO2 emissions change with the size of streams and rivers. Nat. Geosci. 8, 696–699. https://doi.org/10.1038/ngeo2507

Hotchkiss, E.R., Sadro, S., Hanson, P.C., 2018. Toward a more integrative perspective on carbon metabolism across lentic and lotic inland waters. Limnol. Oceanogr. Lett. 3, 57–63. https://doi.org/10.1002/lol2.10081

Huhta, C., Sloat, J., 2007. Discharge Uncertainty Calculations Using a SonTek FlowTracker. San Diego (CA), USA.

Hunt, C.W., Salisbury, J.E., Vandemark, D., 2011. Contribution of non-carbonate anions to total alkalinity and overestimation of PCO2 in New England and New Brunswick rivers. Biogeosciences 8, 3069–3076. https://doi.org/10.5194/bg-8-3069-2011

Hunt, R.J., Krabbenhoft, D.P., Anderson, M.P., 1996. Groundwater Inflow Measurements in Wetland Systems. Water Resour. Res. 32, 495–507. https://doi.org/10.1029/95WR03724

Hvorslev, M.J., 1951. Time lag and soil permeability in ground-water observations. Vicksburg, MS, U.S. Army Waterways Experiment Station.

Interagency research funding, 2021. Tri-Agency Research Data Management Policy [WWW Document]. Gov. Canada. URL https://www.ic.gc.ca/eic/site/063.nsf/eng/h_97610.html (accessed 6.20.22).

International Science Council, 2021. Trusted Data Services for Global Science [WWW Document]. URL https://www.worlddatasystem.org/organization (accessed 10.19.21).

IPCC, 2022. Terrestrial and Freshwater Ecosystems and their Services, in: Climate Change 2022 Impacts, Adaptation and Vulnerability.

Jarvis, N., Koestel, J., Messing, I., Moeys, J., Lindahl, A., 2013. Influence of soil, land use and climatic factors on the hydraulic conductivity of soil. Hydrol. Earth Syst. Sci. 17, 5185–5195. https://doi.org/10.5194/hess-17-5185-2013

Johnson, M.S., Lehmann, J., Riha, S.J., Krusche, A. V., Richey, J.E., Ometto, J.P.H.B., Couto, E.G., 2008. CO_2 efflux from Amazonian headwater streams represents a significant fate for deep soil respiration. Geophys. Res. Lett. 35, L17401. https://doi.org/10.1029/2008GL034619

Jones, J.B., Mulholland, P.J., 1998. Carbon Dioxide Variation in a Hardwood Forest Stream: An Integrative Measure of Whole Catchment Soil Respiration. Ecosystems 1, 183–196. https://doi.org/10.1007/s100219900014

Jung, M., Burt, T.P., Bates, P.D., 2004. Toward a conceptual model of floodplain water table response. Water Resour. Bull. 40, 1–13. https://doi.org/10.1029/2003WR002619

Käser, D.H., Binley, A., Krause, S., Heathwaite, A.L., 2014. Prospective modelling of 3D hyporheic exchange based on high-resolution topography and stream elevation. Hydrol. Process. 28, 2579–2594. https://doi.org/10.1002/hyp.9758

Kempe, S., 1991. Biogeochemistry of European Rivers, in: Biogeochemistry of Major World Rivers. pp. 1–24.

Kennedy, C.D., Genereux, D.P., Mitasova, H., Corbett, D.R., Leahy, S., 2008. Effect of sampling density and design on estimation of streambed attributes. J. Hydrol. 355, 164–180. https://doi.org/10.1016/j.jhydrol.2008.03.018

Khadka, M.B., Martin, J.B., Kurz, M.J., 2017. Synoptic estimates of diffuse groundwater seepage to a spring-fed karst river at high spatial resolution using an automated radon measurement technique. J. Hydrol. 544, 86–96. https://doi.org/10.1016/j.jhydrol.2016.11.013

Kling, G.W., Kipphut, G.W., Miller, M.C., 1991. Arctic Lakes and Streams as Gas Conduits to the Atmosphere: Implications for Tundra Carbon Budgets. Science (80-.). 251, 298–301. https://doi.org/10.1126/science.251.4991.298

Kluge, T., Ilmberger, J., von Rohden, C., Aeschbach-Hertig, W., 2007. Tracing and quantifying groundwater inflow into lakes using a simple method for radon-222 analysis. Hydrol. Earth Syst. Sci. 11, 1621–1631. https://doi.org/10.5194/hessd-4-1519-

2007

Kuglerová, L., Ågren, A., Jansson, R., Laudon, H., 2014. Towards optimizing riparian buffer zones: Ecological and biogeochemical implications for forest management. For. Ecol. Manage. 334, 74–84. https://doi.org/10.1016/j.foreco.2014.08.033

L'Hours, H., Kleemola, M., De Leeuw, L., 2019. CoreTrustSeal: From academic collaboration to sustainable services. IASSIST Q. 43, 1–17. https://doi.org/10.29173/iq936

Larocque, M., Biron, P.M., Buffin-Bélanger, T., Needelman, M., Cloutier, C.-A., Mckenzie, J.M., 2016a. Role of the geomorphic setting in controlling groundwater – surface water exchanges in riverine wetlands : A case study from two southern Québec rivers (Canada). Can. Water Resour. J. / Rev. Can. des ressources hydriques 41, 528–542. https://doi.org/10.1080/07011784.2015.1128360

Larocque, M., Biron, P.M., Buffin-Bélanger, T., Needelman, M., Cloutier, C.-A., Mckenzie, J.M., 2016b. SUPPR Role of the geomorphic setting in controlling groundwater – surface water exchanges in riverine wetlands : A case study from two southern Québec. Can. Water Resour. J. / Rev. Can. des ressources hydriques 41, 528–542. https://doi.org/10.1080/07011784.2015.1128360

Lebuis, J., David, P.P., 1977. Quaternary stratigraphy and events in the western part of the Gaspé Peninsula, Québec. Géographie Phys. Quat. 31, 275–296. https://doi.org/10.7202/1000278ar

Ledesma, J.L., Grabs, T., Futter, M.N., Bishop, K.H., Laudon, H., Köhler, S.J., 2013. Riparian zone control on base cation concentration in boreal streams. Biogeosciences 10, 3849–3868. https://doi.org/10.5194/bg-10-3849-2013

Leopold, L.B., Wolman, M.G., Miller, J.P., 1964. Fluvial Processes in Geomorphology. San Francisco, California (US).

Lewandowski, J., Arnon, S., Banks, E., Batelaan, O., Betterle, A., Broecker, T., Coll, C., Drummond, J., Gaona Garcia, J., Galloway, J., Gomez-Velez, J., Grabowski, R., Herzog, S., Hinkelmann, R., Höhne, A., Hollender, J., Horn, M., Jaeger, A., Krause, S., Löchner Prats, A., Magliozzi, C., Meinikmann, K., Mojarrad, B., Mueller, B., Peralta-Maraver, I., Popp, A., Posselt, M., Putschew, A., Radke, M., Raza, M., Riml, J., Robertson, A., Rutere, C., Schaper, J., Schirmer, M., Schulz, H., Shanafield, M., Singh, T., Ward, A., Wolke, P., Wörman, A., Wu, L., 2019. Is the Hyporheic Zone Relevant beyond the Scientific Community? Water 11, 2230. https://doi.org/10.3390/w11112230

Lewandowski, J., Lischeid, G., Nützmann, G., 2009. Drivers of water level fluctuations and hydrological exchange between grundwater and surface water at the lowland River Spree (Germany): field study and statistical analyses. Hydrol. Process. 23, 2117–2128.

https://doi.org/10.1002/hyp.7277

Li, S., Gu, S., Tan, X., Zhang, Q., 2009. Water quality in the upper Han River basin , China : The impacts of land use / land cover in riparian buffer zone. J. Hazard. Mater. 165, 317–324. https://doi.org/10.1016/j.jhazmat.2008.09.123

Lin, J., Strasser, C., 2014. Recommendations for the Role of Publishers in Access to Data. PLoS Biol. 12, e1001975. https://doi.org/10.1371/journal.pbio.1001975

Löffler, F., Wesp, V., König-Ries, B., Klan, F., 2021. Dataset search in biodiversity research: Do metadata in data repositories reflect scholarly information needs? PLoS One 16, e0246099. https://doi.org/10.1371/journal.pone.0246099

Lovell, S.T., Sullivan, W.C., 2006. Environmental benefits of conservation buffers in the United States : Evidence, promise, and open questions. Agric. Ecosyst. Environ. 112, 249–260. https://doi.org/10.1016/j.agee.2005.08.002

Lyle, J., 2017. Making the Case for Disciplinary Data Repositories, in: Curating Research Data. Volume Two: A Handbook of Current Practice. Chicago, Illinois, pp. 162–164. https://doi.org/10.29173/jchla29404

Maberly, S.C., Barker, P.A., Stott, A.W., De Ville, M.M., 2013. Catchment productivity controls CO_2 emissions from lakes. Nat. Clim. Chang. 3, 391–394. https://doi.org/10.1038/nclimate1748

Macdonald, D., Dixon, A., Newell, A., Hallaways, A., 2012. Groundwater flooding within an urbanised flood plain. J. Flood Risk Manag. 5, 68–80. https://doi.org/10.1111/j.1753-318X.2011.01127.x

Macklin, P.A., Maher, D.T., Santos, I.R., 2014. Estuarine canal estate waters: Hotspots of CO_2 outgassing driven by enhanced groundwater discharge? Mar. Chem. 167, 82–92. https://doi.org/10.1016/j.marchem.2014.08.002

Malcolm, I.A., Youngson, A.F., Soulsby, C., 2003. Survival of salmonid eggs in a degraded gravel-bed stream: effects of groundwater-surface water interactions. River Res. Appl. 19, 303–316. https://doi.org/10.1002/rra.706

Mander, Ü., Kuusemets, V., Hayakawa, Y., 2005. Purification processes , ecological functions , planning and design of riparian buffer zones in agricultural watersheds. Ecol. Eng. 24, 421–432. https://doi.org/10.1016/j.ecoleng.2005.01.015

Mander, Ü., Kuusemets, V., Lõhmus, K., Mauring, T., 1997. Efficiency and dimensioning of riparian buffer zones in agricultural catchments. Ecol. Eng. 8, 299–324. https://doi.org/https://doi.org/10.1016/S0925-8574(97)00025-6

Marchand, J.-P., 2013. Stratigraphie holocène et application d'un modèle séquentiel de vallée de fjord pour la vallée de la rivière Matane, Est-du-Québec, Canada. Université du Québec à Rimouski, Master's Thesis.

Marchand, J., Biron, P., Buffin-Bélanger, T., Larocque, M., 2022. High-resolution spatiotemporal analysis of hydrologic connectivity in the historical floodplain of straightened lowland agricultural streams. River Res. Appl. 1–19. https://doi.org/10.1002/rra.3990

Marchand, J., Buffin-Bélanger, T., Hétu, B., St-Onge, G., 2014. Stratigraphy and infill history of the glacially eroded Matane River Valley, eastern Quebec, Canada. Can. J. Earth Sci. 51, 105–124. https://doi.org/10.1139/cjes-2013-0054

Martin, J.B., Cable, J.E., Smith, C., Roy, M., Cherrier, J., 2007. Magnitudes of submarine groundwater discharge from marine and terrestrial sources: Indian River Lagoon, Florida. Water Resour. Res. 43, 1–15. https://doi.org/10.1029/2006WR005266

Marx, A., Dusek, J., Jankovec, J., Sanda, M., Vogel, T., van Geldern, R., Hartmann, J., Barth, J.A.C., 2017. A review of CO_2 and associated carbon dynamics in headwater streams: A global perspective. Rev. Geophys. 55, 560–585. https://doi.org/10.1002/2016RG000547

Masse-Dufresne, J., Baudron, P., Barbecot, F., Patenaude, M., Pontoreau, C., Proteau-Bédard, F., Menou, M., Pasquier, P., Veuille, S., Barbeau, B., 2019. Anthropic and Meteorological Controls on the Origin and Quality of Water at a Bank Filtration Site in Canada. Water 11, 2510. https://doi.org/10.3390/w11122510

Mayer, P.M., Reynolds, S.K., McCutchen, M.D., Canfield, T.J., 2007. Meta-analysis of nitrogen removal in riparian buffers. J. Environ. Qual. 36, 1172. https://doi.org/10.2134/jeq2006.0462

Mayorga, E., Aufdenkampe, A.K., Masiello, C.A., Krusche, A. V., Hedges, J.I., Quay, P.D., Richey, J.E., Brown, T.A., 2005. Young organic matter as a source of carbon dioxide outgassing from Amazonian rivers. Nature 436, 538–541. https://doi.org/10.1038/nature03880

McClain, M.E., Boyer, E.W., Dent, C.L., Gergel, S.E., Grimm, N.B., Groffman, P.M., Hart, S.C., Harvey, J.W., Johnston, C. a., Mayorga, E., McDowell, W.H., Pinay, G., 2003. Biogeochemical Hot Spots and Hot Moments at the Interface of Terrestrial and Aquatic Ecosystems. Ecosystems 6, 301–312. https://doi.org/10.1007/s10021-003-0161-9

MDDELCC, 2015. Guide d'interprétation, Politique de protection des rives, du littoral et des plaines inondables.

MDDELCC - Ministère du Développement durable de l'Environnement et de la Lutte contre

les changements climatiques, 2018. Stratégie québécoise de L'Eau 2018-2030.

Meals, D.W., Dressing, S.A., Davenport, T.E., 2010. Lag Time in Water Quality Response to Best Management Practices: A Review. J. Environ. Qual. 39, 85–96. https://doi.org/10.2134/jeq2009.0108

Meisner, J.D., Rosenfeld, J.S., Regier, H.A., 1988. The Role of Groundwater in the Impact of Climate Warming on Stream Salmonines. Fisheries 13, 2–8. https://doi.org/10.1577/1548-8446(1988)013<0002:TROGIT>2.0.CO;2

MELCC - Ministère de l'Environnement et de la Lutte contre les changements climatiques, 2020. Rapport sur l'état des ressources en eau et des écosystèmes aquatiques du Québec 2020. Bibliothèque et Archives nationales du Québec.

MELCC - Ministère de l'Environnement et de la Lutte contre les changements climatiques, 2018. Politique de protection des rives, du littoral et des plaines inondables, Loi sur la qualité de l'environnement, Q-2, a. 2.1.

Meybeck, M., 1982. Carbon, Nitrogen, and phosphorus transport by world rivers. Am. J. Sci. 282, 401–450.

Millero, F.J., Graham, T.B., Huang, F., Bustos-Serrano, H., Pierrot, D., 2006. Dissociation constants of carbonic acid in seawater as a function of salinity and temperature. Mar. Chem. 100, 80–94. https://doi.org/10.1016/j.marchem.2005.12.001

Milly, P.C.D., Dunne, K.A., Vecchia, A. V., 2005. Global pattern of trends in streamflow and water availability in a changing climate. Nature 438, 347–350. https://doi.org/10.1038/nature04312

Ministère des Forêts de la Faune et des Parcs, 1986. Loi sur les forêts. Éditeur officiel du Québec.

Molloy, J.C., 2011. The Open Knowledge Foundation: Open Data Means Better Science. PLoS Biol. 9, e1001195. https://doi.org/10.1371/journal.pbio.1001195

Montevecchi, F., Stickler, T., Hintemann, R., Hinterholzer, S., 2020. Energy-efficient Cloud Computing Technologies and Policies for an Eco-friendly Cloud Market. Final Study Report. Vienna. https://doi.org/10.2759/3320

Murtagh, F., Legendre, P., 2014. Ward's hierarchical agglomerative clustering method: Which algorithms implement Ward's criterion? J. Classif. 31, 274–295. https://doi.org/10.1007/s00357-014-9161-z

National Academies of Sciences Engineering and Medicine, Flannagan, C.A., Lyle, J., Carlson, J., University of Michigan and Georgetown University Denise Bedford,

National Cooperative Highway Research Program, Transportation Research Board, 2020. Managing Research Data, in: Guide to Ensuring Access to the Publications and Data of Federally Funded Transportation Research. Washington, DC, p. 138. https://doi.org/10.17226/25704

National Science Foundation, 2021. Publications Output: U.S. and International Comparisons, Science and Engineering Indicators 2022. Alexandria, VA.

O'Brien, C., Hendershot, W.H., 1993. Separating streamflow into groundwater, solum and upwelling flow and its implications for hydrochemical modelling. J. Hydrol. 146, 1–12. https://doi.org/10.1016/0022-1694(93)90266-C

Observatoire Global du Saint-Laurent, 2021. About the St. Lawrence Global Observatory [WWW Document]. URL https://ogsl.ca/en/about-slgo/ (accessed 10.18.21).

Oksanen, J., Blanchet, F.G., Friendly, M., Kindt, R., Legendre, P., Mcglinn, D., Minchin, P.R., Hara, R.B.O., Simpson, G.L., Solymos, P., Stevens, M.H.H., Szoecs, E., Wagner, H., 2019. Package "vegan": Community ecology package, R package version 2.5-4.

Ollerenshaw, N.C., 1967. Cuoq-Langis area, Matane and Matapédaia counties. Geological report 121. Department of Natural Resources. Québec.

Öquist, M.G., Wallin, M., Seibert, J., Bishop, K., Laudon, H., 2009. Dissolved Inorganic Carbon Export Across the Soil/Stream Interface and Its Fate in a Boreal Headwater Stream. Environ. Sci. Technol. 43, 7364–7369. https://doi.org/10.1021/es900416h

Organisation des Nations Unies, 2019. Rapport sur les objectifs de développement durable 2019. New-York.

Organisation des Nations Unies, 2008. Objectifs du Millénaire pour le développement - Rapport 2008. New York.

Ortega, L., Manzano, M., Custodio, E., Hornero, J., Rodríguez-Arévalo, J., 2015. Using 222Rn to identify and quantify groundwater inflows to the Mundo River (SE Spain). Chem. Geol. 395, 67–79. https://doi.org/10.1016/j.chemgeo.2014.12.002

Pampel, H., Vierkant, P., Scholze, F., Bertelmann, R., Kindling, M., Klump, J., Goebelbecker, H.-J., Gundlach, J., Schirmbacher, P., Dierolf, U., 2013. Making Research Data Repositories Visible: The re3data.org Registry. PLoS One 8, e78080. https://doi.org/10.1371/journal.pone.0078080

Patenaude, M., Baudron, P., Labelle, L., Masse-Dufresne, J., 2020. Evaluating Bank-Filtration Occurrence in the Province of Quebec (Canada) with a GIS Approach. Water 12, 662. https://doi.org/10.3390/w12030662

Peterjohn, W.T., Correll, D.L., 1984. Nutrient dynamics in an agricultural watershed: Observations on the role of a riparian forest. Ecology 5, 1466–1475.

Peterson, E.W., Sickbert, T.B., 2006. Stream water bypass through a meander neck, laterally extending the hyporheic zone. Hydrogeol. J. 14, 1443–1451. https://doi.org/10.1007/s10040-006-0050-3

Pinti, D.L., Retailleau, S., Barnetche, D., Moreira, F., Moritz, A.M., Larocque, M., Gélinas, Y., Lefebvre, R., Hélie, J.F., Valadez, A., 2014. 222Rn activity in groundwater of the St. Lawrence Lowlands, Quebec, eastern Canada: Relation with local geology and health hazard. J. Environ. Radioact. 136, 206–217. https://doi.org/10.1016/j.jenvrad.2014.05.021

Piwowar, H.A., Day, R.S., Fridsma, D.B., 2007. Sharing Detailed Research Data Is Associated with Increased Citation Rate. PLoS One 2, e308. https://doi.org/10.1371/journal.pone.0000308

Polsenaere, P., Abril, G., 2012. Modelling CO2 degassing from small acidic rivers using water pCO2, DIC and δ13C-DIC data. Geochim. Cosmochim. Acta 91, 220–239. https://doi.org/10.1016/j.gca.2012.05.030

Power, G., Brown, R.S., Imhof, J.G., 1999. Groundwater and fish — insights from northern North America. Hydrol. Process. 13, 401–422. https://doi.org/10.1002/(SICI)1099-1085(19990228)13:3<401::AID-HYP746>3.0.CO;2-A

Raanan Kiperwas, H., 2011. Radium Isotopes as Tracers of Groundwater-Surface Water Interactions in Inland Environments. Duke University.

Ran, L., Li, L., Tian, M., Yang, X., Yu, R., Zhao, J., Wang, L., Lu, X.X., 2017. Riverine CO2 emissions in the Wuding River catchment on the Loess Plateau: Environmental controls and dam impoundment impact. J. Geophys. Res. Biogeosciences 122, 1439–1455. https://doi.org/10.1002/2016JG003713

Rasilo, T., Hutchins, R.H.S., Ruiz-González, C., del Giorgio, P.A., 2017. Transport and transformation of soil-derived CO2, CH4 and DOC sustain CO2 supersaturation in small boreal streams. Sci. Total Environ. 579, 902–912. https://doi.org/10.1016/j.scitotenv.2016.10.187

Ratnasingham, S., Hebert, P.D.N., 2007. BOLD: The Barcode of Life Data System (http://www.barcodinglife.org). Mol. Ecol. Notes 7, 355–364. https://doi.org/10.1111/j.1471-8286.2007.01678.x

Raymond, P.A., Hartmann, J., Lauerwald, R., Sobek, S., McDonald, C.P., Hoover, M., Butman, D., Striegl, R., Mayorga, E., Humborg, C., Kortelainen, P., Durr, H., Meybeck, M., Ciais, P., Guth, P., 2013. Global carbon dioxide emissions from inland waters.

Nature 503, 355–359. https://doi.org/10.1038/nature12760

Raymond, P.A., Zappa, C.J., Butman, D., Bott, T.L., Potter, J., Mulholland, P., Laursen, a. E., McDowell, W.H., Newbold, D., 2012. Scaling the gas transfer velocity and hydraulic geometry in streams and small rivers. Limnol. Oceanogr. Fluids Environ. 2, 41–53. https://doi.org/10.1215/21573689-1597669

re3data.org, 2012. Registry of Research Data Repositories [WWW Document]. https://doi.org/https://doi.org/10.17616/R3D

Regnier, P., Friedlingstein, P., Ciais, P., Mackenzie, F.T., Gruber, N., Janssens, I. a., Laruelle, G.G., Lauerwald, R., Luyssaert, S., Andersson, A.J., Arndt, S., Arnosti, C., Borges, A. V., Dale, A.W., Gallego-Sala, A., Goddéris, Y., Goossens, N., Hartmann, J., Heinze, C., Ilyina, T., Joos, F., LaRowe, D.E., Leifeld, J., Meysman, F.J.R., Munhoven, G., Raymond, P. a., Spahni, R., Suntharalingam, P., Thullner, M., 2013. Anthropogenic perturbation of the carbon fluxes from land to ocean. Nat. Geosci. 6, 597–607. https://doi.org/10.1038/ngeo1830

Richey, J.E., Melack, J.M., Aufdenkampe, A.K., Ballester, V.M., Hess, L.L., 2002. Outgassing from Amazonian rivers and wetlands as a large tropical source of atmospheric CO2. Nature 416, 617–620. https://doi.org/10.1038/416617a

Roireau, N., Zikovsky, L., 1989. Determination of radon in groundwater of Quebec. J. Radioanal. Nucl. Chem. Lett. 137, 79–85. https://doi.org/10.1007/BF02164562

Rose, S., Fullagar, P.D., 2005. Strontium isotope systematics of base flow in Piedmont Province watersheds, Georgia (USA). Appl. Geochemistry 20, 1571–1586. https://doi.org/10.1016/j.apgeochem.2005.04.015

Ruehl, C., Fisher, A.T., Hatch, C., Huertos, M.L., Stemler, G., Shennan, C., 2006. Differential gauging and tracer tests resolve seepage fluxes in a strongly-losing stream. J. Hydrol. 330, 235–248. https://doi.org/10.1016/j.jhydrol.2006.03.025

Sadat-Noori, M., Santos, I.R., Sanders, C.J., Sanders, L.M., Maher, D.T., 2015. Groundwater discharge into an estuary using spatially distributed radon time series and radium isotopes. J. Hydrol. 528. https://doi.org/10.1016/j.jhydrol.2015.06.056

Santos, I.R., Maher, D.T., Eyre, B.D., 2012. Coupling automated radon and carbon dioxide measurements in coastal waters. Environ. Sci. Technol. 46, 7685–7691. https://doi.org/10.1021/es301961b

Schelker, J., Singer, G.A., Ulseth, A.J., Hengsberger, S., Battin, T.J., 2016. CO2 evasion from a steep, high gradient stream network: importance of seasonal and diurnal variation in aquatic pCO2 and gas transfer. Limnol. Oceanogr. 61, 1826–1838. https://doi.org/10.1002/lno.10339

Schindler, J.E., Krabbenhoft, D.P., 1998. The hyporheic zone as a source of dissolved organic carbon gases to a temperate forest stream. Biogeochemistry 43, 157–174. https://doi.org/10.1023/A:1006005311257

Schmadel, N.M., Neilson, B.T., Stevens, D.K., 2010. Approaches to estimate uncertainty in longitudinal channel water balances. J. Hydrol. 394, 357–369. https://doi.org/10.1016/j.jhydrol.2010.09.011

Schmidt, A., Schlueter, M., Melles, M., Schubert, M., 2008. Continuous and discrete on-site detection of radon-222 in ground- and surface waters by means of an extraction module. Appl. Radiat. Isot. 66, 1939–1944. https://doi.org/10.1016/j.apradiso.2008.05.005

Schmidt, B., Gemeinholzer, B., Treloar, A., 2016. Open Data in Global Environmental Research: The Belmont Forum's Open Data Survey. PLoS One 11, e0146695. https://doi.org/10.1371/journal.pone.0146695

Sophocleous, M.A., 1991. Stream-floodwave propagation through the Great Bend alluvial aquifer, Kansas: Field measurements and numerical simulations. J. Hydrol. 124, 207–228. https://doi.org/10.1016/0022-1694(91)90015-A

St Jacques, J.-M., Sauchyn, D.J., 2009. Increasing winter baseflow and mean annual streamflow from possible permafrost thawing in the Northwest Territories, Canada. Geophys. Res. Lett. 36. https://doi.org/10.1029/2008GL035822

Stanford, J.A., Ward, J. V., 1993. An ecosystem perspective of alluvial rivers: connectivity and the hyporheic corridor. J. North Am. Benthol. Soc. 12, 48–60. https://doi.org/10.2307/1467685

Stuart, D., Baynes, G., Hrynaszkiewicz, I., Allin, K., Penny, D., Lucraft, M., Astell, M., 2018. Practical Challenges for Researchers in Data Sharing., figshare. Journal contribution. https://doi.org/10.6084/m9.figshare.5975011.v1

Syversen, N., 2005. Effect and design of buffer zones in the Nordic climate: The influence of width, amount of surface runoff, seasonal variation and vegetation type on retention efficiency for nutrient and particle runoff. Ecol. Eng. 24, 483–490. https://doi.org/10.1016/j.ecoleng.2005.01.016

Taillardat, P., Willemsen, P., Marchand, C., Friess, D.A., Widory, D., Baudron, P., Truong, V.V., Nguyễn, T.-N., Ziegler, A.D., 2018. Assessing the contribution of porewater discharge in carbon export and CO2 evasion in a mangrove tidal creek (Can Gio, Vietnam). J. Hydrol. 563, 303–318. https://doi.org/10.1016/j.jhydrol.2018.05.042

Tang, Q., Kurtz, W., Schilling, O.S., Brunner, P., Vereecken, H., Hendricks Franssen, H.-J., 2017. The influence of riverbed heterogeneity patterns on river-aquifer exchange fluxes under different connection regimes. J. Hydrol. 554, 383–396.

https://doi.org/10.1016/j.jhydrol.2017.09.031

Teodoru, C.R., del Giorgio, P.A., Prairie, Y.T., Camire, M., 2009. Patterns in pCO2 in boreal streams and rivers of northern Quebec, Canada. Global Biogeochem. Cycles 23. https://doi.org/10.1029/2008GB003404

Thelwall, M., Kousha, K., 2017. Do journal data sharing mandates work? Life sciences evidence from Dryad. Aslib J. Inf. Manag. 69, 36–45. https://doi.org/10.1108/AJIM-09-2016-0159

Tiwari, T., Lidman, F., Laudon, H., Lidberg, W., Ågren, A., 2017. GIS-based prediction of stream chemistry using landscape composition, wet areas, and hydrological flow pathways. J. Geophys. Res. Biogeosciences 122, 65–79. https://doi.org/10.1002/2016JG003399

Tomaszewska, B., Tyszer, M., Dendys, M., 2018. The availability of groundwater information sources in relation to the transposition of the WFD into Polish law. Project KINDRA. Therm. Sci. Eng. Prog. 5, 437–443. https://doi.org/10.1016/j.tsep.2018.01.018

Touchette, M., Cloutier, C.-A., McGrath-Pompon, M., Buffin-Bélanger, T., Chaillou, G., McCormack, R., 2013. Programme d ' acquisition de connaissances sur les eaux souterraines du nord-est du Bas-Saint- Rapport d ' étape phase 1 .

Triska, F.J., Kennedy, V.C., Avanzino, R.J., Zellweger, G.W., Bencala, K.E., 1989. Retention and transport of nutrients in a third-order stream in northwestern California: Hyporheic processes. Ecology 70, 1893–1905. https://doi.org/10.2307/1938120

Ullman, W.J., Aller, R.C., 1982. Diffusion coefficients in nearshore marine sediments1. Limnol. Oceanogr. 27, 552–556. https://doi.org/10.4319/lo.1982.27.3.0552

UNESCO, 2021. UNESCO Recommendation on Open Science.

United Nations, 2015. World Urbanization Prospects: The 2014 Revision. New York.

Uusi-Kämppä, J., Jauhiainen, L., 2010. Long-term monitoring of buffer zone efficiency under different cultivation techniques in boreal conditions. Agric. , Ecosyst. Environ. 137, 75–85. https://doi.org/10.1016/j.agee.2010.01.002

Valett, H.M., Fisher, S.G., Grimm, N.B., Camill, P., 1994. Vertical Hydrologic Exchange and Ecological Stability of a Desert Stream Ecosystem. Ecology 75, 548–560. https://doi.org/10.2307/1939557

Van Noorden, R., 2013. Data-sharing: Everything on display. Nature 500, 243–245. https://doi.org/10.1038/nj7461-243a

Vekerdy, Z., Meijerink, A.M.., 1998. Statistical and analytical study of the propagation of flood-induced groundwater rise in an alluvial aquifer. J. Hydrol. 205, 112–125. https://doi.org/10.1016/S0022-1694(97)00148-0

Venkiteswaran, J.J., Schiff, S.L., Wallin, M.B., 2014. Large Carbon Dioxide Fluxes from Headwater Boreal and Sub-Boreal Streams. PLoS One 9, e101756. https://doi.org/10.1371/journal.pone.0101756

Vidon, P., 2012. Towards a better understanding of riparian zone water table response to precipitation: Surface water infiltration, hillslope contribution or pressure wave processes? Hydrol. Process. 26, 3207–3215. https://doi.org/10.1002/hyp.8258

Vidon, P., Allan, C., Burns, D., Duval, T.P., Gurwick, N., Inamdar, S., Lowrance, R., Okay, J., Scott, D., Sebestyen, S., 2010. Hot spots and hot moments in riparian zones: Potential for improved water quality management. J. Am. Water Resour. Assoc. 46, 278–298. https://doi.org/10.1111/j.1752-1688.2010.00420.x

Vines, T.H., Andrew, R.L., Bock, D.G., Franklin, M.T., Gilbert, K.J., Kane, N.C., Moore, J., Moyers, B.T., Renaut, S., Rennison, D.J., Veen, T., Yeaman, S., 2013. Mandated data archiving greatly improves access to research data. FASEB J. 27, 1304–1308. https://doi.org/10.1096/fj.12-218164

Wallin, M.B., Grabs, T., Buffam, I., Laudon, H., Ågren, A., Öquist, M.G., Bishop, K., 2013. Evasion of CO2 from streams - The dominant component of the carbon export through the aquatic conduit in a boreal landscape. Glob. Chang. Biol. 19, 785–797. https://doi.org/10.1111/gcb.12083

Wanninkhof, R., 1992. Relationship between wind speed and gas exchange over the ocean. J. Geophys. Res. 97, 7373–7382. https://doi.org/10.1029/92JC00188

White, D.S., 1993. Perspectives on defining and delineating hyporheic zones. J. North Am. Benthol. Soc. 12, 61–69. https://doi.org/10.2307/1467686

Wilkinson, M.D., Dumontier, M., Aalbersberg, Ij.J., Appleton, G., Axton, M., Baak, A., Blomberg, N., Boiten, J.-W., da Silva Santos, L.B., Bourne, P.E., Bouwman, J., Brookes, A.J., Clark, T., Crosas, M., Dillo, I., Dumon, O., Edmunds, S., Evelo, C.T., Finkers, R., Gonzalez-Beltran, A., Gray, A.J.G., Groth, P., Goble, C., Grethe, J.S., Heringa, J., 't Hoen, P.A.., Hooft, R., Kuhn, T., Kok, R., Kok, J., Lusher, S.J., Martone, M.E., Mons, A., Packer, A.L., Persson, B., Rocca-Serra, P., Roos, M., van Schaik, R., Sansone, S.-A., Schultes, E., Sengstag, T., Slater, T., Strawn, G., Swertz, M.A., Thompson, M., van der Lei, J., van Mulligen, E., Velterop, J., Waagmeester, A., Wittenburg, P., Wolstencroft, K., Zhao, J., Mons, B., 2016. The FAIR Guiding Principles for scientific data management and stewardship. Sci. Data 3, 160018. https://doi.org/10.1038/sdata.2016.18

Williams, D.D., 1989. Towards a biological and chemical definition of the hyporheic zone in two Canadian rivers. Freshw. Biol. 22, 189–208. https://doi.org/10.1111/j.1365-2427.1989.tb01095.x

Williams, P.J., Burt, T.P., 1974. Measurement of Hydraulic Conductivity of Frozen Soils. Can. Geotech. J. 11, 647–650. https://doi.org/10.1139/t74-066

Winterdahl, M., Wallin, M.B., Karlsen, R.H., Laudon, H., Öquist, M., Lyon, S.W., 2016. Decoupling of carbon dioxide and dissolved organic carbon in boreal headwater streams. J. Geophys. Res. Biogeosciences 121, 2630–2651. https://doi.org/10.1002/2016JG003420

Wondzell, S.M., Gooseff, M.N., 2013. Geomorphic controls on hyporheic exchange across scales: Watersheds to particles, in: Treatise on Geomorphology. Elsevier, pp. 203–218. https://doi.org/10.1016/B978-0-12-374739-6.00238-4

World Commission on Environment and Development, 1987. Our Common Future, From One Earth to One World. https://doi.org/10.1080/07488008808408783

Xafis, V., Labude, M.K., 2019. Openness in Big Data and Data Repositories. Asian Bioeth. Rev. 11, 255–273. https://doi.org/10.1007/s41649-019-00097-z

Xu, M., Wang, Z., Pan, B., Zhao, N., 2012. Distribution and species composition of macroinvertebrates in the hyporheic zone of bed sediment. Int. J. Sediment Res. 27, 129–140. https://doi.org/10.1016/S1001-6279(12)60022-5

Xue, X., Pang, Y., Landis, A.E., 2014. Evaluating agricultural management practices to improve the environmental footprint of corn-derived ethanol. Renew. Energy 66, 454–460. https://doi.org/10.1016/j.renene.2013.12.026

Zaharescu, D.G., Palanca-Soler, A., Hooda, P.S., Tanase, C., Burghelea, C.I., Lester, R.N., 2017. Riparian vegetation in the alpine connectome: Terrestrial-aquatic and terrestrial-terrestrial interactions. Sci. Total Environ. 602, 247–259.